Hybridised Mimetic Discretisation and Variational Multiscale Theory for Advection-Dominated Problems

M.Sc. Thesis

Suyash Shrestha

Delft University of Technology

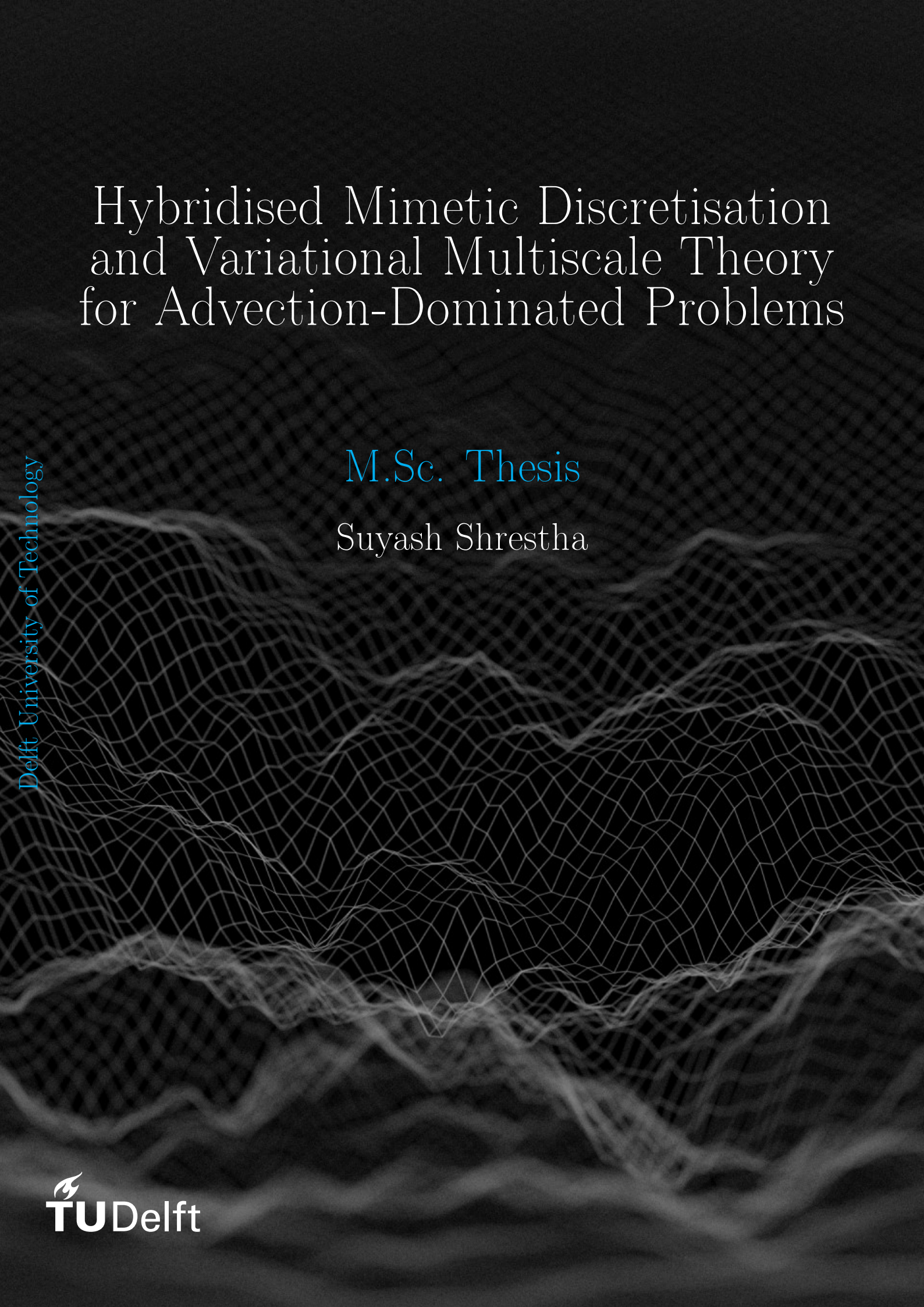

TU Delft

In loving memory of my late father Prashanta Shrestha and his father before him Krishna Bhakta Ranjitkar.

Gone yet not forgotten

Hybridised Mimetic Discretisation and Variational Multiscale Theory for Advection-Dominated Problems

M.Sc. Thesis

by

Suyash Shrestha

to obtain the degree of Master of Science
in Aerospace Engineering at Delft University of Technology,
to be defended publicly on 3rd November 2022.

Student number:	4677846	
Project duration:	15th December 2021 – 25th October 2022	
Thesis committee:	Dr. ir. M. I. Gerritsma,	TU Delft, supervisor
	Dr. S. J. Hulshoff,	TU Delft, supervisor
	Dr. B. Chen,	TU Delft, examiner
	Dr. ir. I. Akkerman,	TU Delft, examiner

TU Delft

Preface

This thesis project has been a remarkable journey where I got the chance and freedom to explore a variety of interesting aspects related to numerical methods. Before starting my thesis, I knew well upfront that I wanted to do something related to mimetic methods and multiscale theory as these were the two topics that, in my opinion, really stood out in comparison to the other things I learned during my master's. Given that there were no open thesis topics addressing both the mimetic and multiscale theory, my ambitious self came up with the idea to combine these two different things. Needless to say that my idea had many different challenges along the way, nonetheless, I was absolutely delighted to spend all this time doing the things I am truly passionate about.

I would now like to take this opportunity to extend my gratitude and thank Dr.ir. Marc Gerritsma and Dr. Steven Hulshoff for their guidance and supervision throughout this thesis project. They were the ones who initially introduced me to mimetic methods and multiscale theory during the CFD-II and CFD-III lectures, and this project would not have been possible without their support. I have thoroughly enjoyed working together with both of them and I will always remember those times in our meetings when none of us knew exactly what was going wrong and we would just stare at our screens trying to make sense of some results.

I would also like to give my special thanks to my aunt Prarthana Shrestha and uncle Bahman Zafarifar. They were the ones who went out of their way and took my 14-year-old self into their home after the passing of my father. They brought me to The Netherlands and raised me as their own and I am who I am because of them. I would also like to thank their 7-year-old son (my cousin) Ashkan Shrestha, who supported me in his own unique way. Additionally, I would like to thank my family back in Nepal, most notably my grandmother Rajeshwori Ranjitkar and of course my mother Rusha Shrestha. Despite being so far away, they have always supported me through everything and I am forever grateful for that. Last but not least I would like to thank my loving girlfriend Giulia Di Teodoro who has supported me and helped me power through my studies.

Suyash Shrestha
Delft, Friday 4th November, 2022

Contents

List of Figures

1

Introduction

The utilisation of Computational Fluid Dynamics (CFD) to address complex flow-related problems has become increasingly customary in both academic and industrial settings. While the academic perspective entails research into the development of new and improved methods for CFD and the development of turbulence models, some notable industrial applications of CFD include the design and optimisation of aircraft, rocket nozzles, cars, and even microprocessors [1, 2]. This increase in the employment of CFD is coupled with the growth in the world's computing resources in terms of the number of cores being used, however, not necessarily in terms of the core speeds [1]. Despite this gain in prevalence, it is worth noting that a majority of commercial CFD software packages currently employ rudimentary numerical techniques developed around the seventies, such as the Finite-Volume Method. While these methods are well adapted for advection-dominated problems their extension to higher order methods is not trivial as Spectral Element methods. This constitutes the method requiring excessive amounts of computational cost when attempting to capture complex flow phenomena (for example turbulent boundary layers). Moreover, the methods tend to diverge when dealing with particularly complex problems [3, 4] which require the addition of numerical dissipation for stabilisation. This thus motivates the development of more advanced and robust numerical methods which are not susceptible to such shortcomings.

One family of such advanced methods are *structure-preserving or mimetic discretisations*. These discretisation techniques are derived by employing the concepts from differential geometry which thereby enables the discretisation to attain specific conservation properties. For any given physical problem, the (model) governing equations are often expressed in terms of partial differential equations that describe the conservation of physical properties. The Navier-Stokes equations, for example, describe the conservation of mass (density), momentum, and energy. It has been well established that traditional discretisation techniques fail to preserve these continuous level symmetries at the discrete level. Mimetic methods on the other hand have been designed to have the ability to preserve or mimic certain structures of the continuous equations at the discrete level, hence the name 'mimetic'. The works presented in [5, 6] highlight some examples of such discretisation techniques. Mimetic discretisation techniques have the tendency to reflect the true physical behaviour of the governing equations, thereby helping to improve the stability/robustness and accuracy of the numerical solution. However, like traditional techniques, they are not entirely robust in specific multiscale cases such as under-resolved simulations or cases involving discontinuities in the flow.

The concept of under-resolved simulations ties into the idea of Large Eddy Simulations (LES) that is often encountered in industrial applications. Such applications involve flow cases where highly refined meshes are required to capture the full flow physics, however, the use of such meshes is unpractical/infeasible given the associated cost. There exist numerous methods/approaches for LES, howbeit, the one method that emerges from the concept of discretisation is the Variational Multiscale (VMS) method where the discrete solution is regarded as a projection of the exact solution. The VMS employs an a priori scale separation, essentially splitting the solution into a resolved and un-resolved part, whereby the resolved scales are solved by taking into account the effect of the un-resolved scales. This approach thus offers a stabilisation technique for under-resolved simulations.

The two frameworks, mimetic methods and VMS, have been extensively studied independently, however, their combination offers the potential of achieving a favourable robust solver capable of handling complicated

[1] `https://www.karlrupp.net/2018/02/42-years-of-microprocessor-trend-data/`

industrial problems. Moreover, the extension of the hybridised variant of mimetic methods towards advection-dominated problems is an interesting avenue yet to be explored. Therefore, this thesis focuses on the extension of the hybridised mimetic method and its combination with the VMS theory. Subsequently, the thesis goal has been formulated as follows:

> *"To extend the hybrid mimetic Spectral Element framework for advection-dominated problems and further equip the method with the ability to incorporate Variational Multiscale theory."*

In order to fulfil this objective, the following research questions and sub questions have been posed:

1. What do the discrete equations look like for advection-dominated PDEs discretised using the hybrid mimetic method?
    a. What are the terms in the discrete equations and are they metric-free?
    b. What do the Lagrange multipliers physically represent for advection-dominated problems in 1D and 2D?
    c. Does the hybrid formulation conserve continuous-level invariants?
2. What does the multiscale formulation integrated within the hybrid mimetic method for linear PDEs look like?
    a. What is the additional term introduced into the equations with VMS theory?
    b. What is the effect of the multiscale formulation on the discrete solution?
    c. Does the multiscale formulation preserve structures of the continuous equations?

This report addresses the work carried out for answering the above research questions. First Chapter 2 addresses some of the relevant theoretical fundamentals of differential geometry necessary for deriving the mimetic discretisation framework. The framework itself is subsequently presented in Chapter 3 in the form of the mimetic Spectral Element Method. Thereafter, the fundamentals and implementation approaches for the VMS are shown in Chapter 4. This chapter is then followed by the implementation of the established mimetic and multiscale theories for linear problems in Chapter 5. The linear problems addressed in this chapter include the 1D steady and unsteady linear advection-diffusion equation. Thereafter, mimetic approaches for non-linear problems are presented in Chapter 6 which addresses the 1D Burgers' equation and the 2D incompressible Navier-Stokes/Euler equations. The chapter on non-linear problems does not include multiscale theory as developing sub-scale models for such cases goes out of the scope of the present study. Lastly, Chapter 7 and Chapter 8, respectively present the conclusions and future recommendations of this research.

2

Differential geometry

This chapter addresses various core concepts of differential geometry which set up the foundation for formulating mimetic discretisation techniques. The theory presented in this chapter encompasses some fundamental definitions of spaces, the objects that reside in them, and the different operators that can be applied to these objects.

2.1. Manifold

Definition 2.1 ([7, 8])**.** *An n-dimensional manifold comprises of a* ***topological space*** $\boldsymbol{\mathcal{M}}$ *along with a set of* ***local coordinate neighborhoods*** $\{\boldsymbol{\mathcal{U}}_0, \boldsymbol{\mathcal{U}}_1, \ldots\}$ *whereby each point of* $\boldsymbol{\mathcal{M}}$ *exists in at least one of these* $\boldsymbol{\mathcal{U}}$*, (*$\boldsymbol{\mathcal{M}} = \boldsymbol{\mathcal{U}}_0 \cup \boldsymbol{\mathcal{U}}_1 \cup \ldots$*). Moreover, there exists a bijective coordinate mapping* $\boldsymbol{\phi}_{\boldsymbol{\mathcal{U}}_i} : \boldsymbol{\mathcal{U}}_i \to \mathbb{R}^n$ *which maps* $\boldsymbol{\mathcal{U}}_i$ *to an n-dimensional Euclidean space such that* $\boldsymbol{\phi}_{\boldsymbol{\mathcal{U}}_i}(\boldsymbol{\mathcal{U}}_i) \subset \mathbb{R}^n$ *is open.*

Generally speaking, a manifold is described as the most generic space wherein one can apply differential and integral calculus in roughly the same manner as in Euclidean space [7]. Consequently, a manifold is commonly referred to as a space that locally resembles Euclidean space at each point of the manifold. Furthermore, the topological attribute of the space $\boldsymbol{\mathcal{M}}$ highlights the fact that there is no natural measure of distances between points, nor a measure of angles on a manifold.

2.2. Objects on manifolds

Having established the fundamental definition of a manifold, the various types of objects that live on manifolds are described in this section.

2.2.1. Tangent vectors

Defining an n-dimensional vector space that is tangent to $\boldsymbol{\mathcal{M}}$ at an arbitrary point is not entirely trivial as defining a tangent basis in Euclidean space. In order to define a tangent space to an n-dimensional manifold $\boldsymbol{\mathcal{M}}$, the Euclidean vectors are identified with directional differentiation as shown in Definition 2.2.

Definition 2.2 ([7])**.** *Let* $\boldsymbol{p}$ *be a point on an n-dimensional manifold* $\boldsymbol{\mathcal{M}}$ *and f be a real-valued smooth function in the vicinity of* $\boldsymbol{p}$*. The derivative of f with respect to a vector* $\boldsymbol{X}$ *located at point* $\boldsymbol{p}$ *is given by:*

$$\boldsymbol{X}_p(f) := \sum_j X_j \frac{\partial f}{\partial x_j}\bigg|_{\boldsymbol{p}}, \tag{2.1}$$

where X_j are the components of the vector $\boldsymbol{X}$*. Any arbitrary vector at point* $\boldsymbol{p}$ *may be seen as a differential operator that can be applied to real-valued smooth functions near* $\boldsymbol{p}$*. Therefore, the operation generalises to the form:*

$$\boldsymbol{X}_p := \sum_j X_j \frac{\partial}{\partial x_j}\bigg|_{\boldsymbol{p}}. \tag{2.2}$$

*It is noted that $\boldsymbol{X}_p$ assigns a real number to each smooth function on $\boldsymbol{\mathcal{M}}$. Furthermore, there exist a set of vectors at point $\boldsymbol{p}$, namely $\left[\left.\frac{\partial}{\partial x_1}\right|_{\boldsymbol{p}}, \left.\frac{\partial}{\partial x_2}\right|_{\boldsymbol{p}}, \ldots, \left.\frac{\partial}{\partial x_n}\right|_{\boldsymbol{p}}\right]$, which form a basis for the **tangent space** to $\boldsymbol{\mathcal{M}}$ at point $\boldsymbol{p}$ and is denoted by $\boldsymbol{\mathcal{T}_{\mathcal{M}}}$.*

2.2.2. Dual space

Definition 2.3 ([7]). *A **linear functional** α defined on a vector space $\boldsymbol{\mathcal{E}}$ is a real-valued linear function that is a mapping $\alpha : \boldsymbol{\mathcal{E}} \to \mathbb{R}$ from $\boldsymbol{\mathcal{E}}$ to the one dimensional vector space.*

$$\alpha(a\boldsymbol{u} + b\boldsymbol{v}) = a\alpha(\boldsymbol{u}) + b\alpha(\boldsymbol{v}), \qquad \forall\, \boldsymbol{u}, \boldsymbol{v} \in \boldsymbol{\mathcal{E}} \text{ and } \forall\, a, b \in \mathbb{R}. \tag{2.3}$$

If $\boldsymbol{\mathcal{E}}$ is a finite-dimensional vector space with n dimensions which has $\boldsymbol{e}_1, \boldsymbol{e}_2, \ldots, \boldsymbol{e}_n$ as its basis, any arbitrary vector $\boldsymbol{v} \in \boldsymbol{\mathcal{E}}$ can be expanded as a linear combination of the basis vectors $\boldsymbol{v} = \sum_j v_j \boldsymbol{e}_j$. Subsequently, applying the functional α to $\boldsymbol{v}$ yields:

$$\alpha(\boldsymbol{v}) = \alpha\left(\sum_j v_j \boldsymbol{e}_j\right) = \sum_j v_j \alpha(\boldsymbol{e}_j). \tag{2.4}$$

Note that the linear functional α does **not** live in the vector space $\boldsymbol{\mathcal{E}}$, much like the Dirac Delta Functional does not live in the space of continuous real-valued functions [7]. Instead, the linear functional lives in a different space defined as follows:

Definition 2.4 ([7]). *The set of all the linear functionals on the vector space $\boldsymbol{\mathcal{E}}$ form a separate vector space referred to as the **dual space** denoted by $\boldsymbol{\mathcal{E}^*}$. If $\boldsymbol{\mathcal{E}}$ is n-dimensional, then so is $\boldsymbol{\mathcal{E}^*}$, which enables one to define the **dual basis** $\sigma_1, \sigma_2, \ldots, \sigma_n$. Every linear vector space has its dual space and the elements in the dual space are referred to as **covectors**. Furthermore, the canonical dual basis satisfies the property:*

$$\sigma_i(\boldsymbol{e}_j) = \delta_{ij}, \tag{2.5}$$

which, along with the linearity of σ, can be used to show that applying σ_i to a vector $\boldsymbol{v} \in \boldsymbol{\mathcal{E}}$ simply extracts the i^{th} component of $\boldsymbol{v}$

$$\sigma_i\left(\sum_j v_j \boldsymbol{e}_j\right) = \sum_j \sigma_i(\boldsymbol{e}_j) v_j = \sum_j \delta_{ij} v_j = v_i. \tag{2.6}$$

Having established the notion of the dual space, it can then be applied to the aforementioned tangent space in Definition 2.2 to construct the **cotangent space** denoted by $\boldsymbol{\mathcal{T}^*_{\mathcal{M}}}$. Given that the basis vectors of the tangent space are the linear differentials $\left[\left.\frac{\partial}{\partial x_1}\right|_{\boldsymbol{p}}, \left.\frac{\partial}{\partial x_2}\right|_{\boldsymbol{p}}, \ldots, \left.\frac{\partial}{\partial x_n}\right|_{\boldsymbol{p}}\right]$, the basis of the cotangent space must be $[\mathrm{d}x_1, \mathrm{d}x_2, \ldots, \mathrm{d}x_n]$ in order to satisfy the Kronecker Delta property in Equation (2.5).

2.2.3. Differential forms

Definition 2.5 ([8]). *The real-valued smooth functions that are defined on the n-dimensional manifold $\boldsymbol{\mathcal{M}}$ are referred to as the **0-forms**.*

Definition 2.6 ([8]). *Let $\boldsymbol{p}$ be a point on an n-dimensional manifold $\boldsymbol{\mathcal{M}}$. The **1-forms**, $\alpha^{(1)}$, at $\boldsymbol{p}$ are expressed by a linear combination of the basis vectors of the cotangent space at $\boldsymbol{p}$*

$$\alpha^{(1)} := \sum_i \alpha_i \mathrm{d}x_i, \qquad \forall\, \alpha_i \in \mathbb{R}. \tag{2.7}$$

As such, the 1-forms are seen as a linear functional $\alpha^{(1)} : \boldsymbol{\mathcal{T}_{\mathcal{M}}} \to \mathbb{R}$. In general. the space of k-forms on $\boldsymbol{\mathcal{M}}$ is denoted by $\Lambda^{(k)}(\boldsymbol{\mathcal{M}})$.

One way of interpreting the differential form is that it is a means of measuring k-dimensional objects that live in the manifold. This idea comes from the fact that applying the *1-form* to a vector in $\boldsymbol{\mathcal{T}_{\mathcal{M}}}$ is analogous to the vector inner (dot) product in Euclidean space.

Proof 2.1. *Consider a vector and covector (1-form) pair which live in the tangent and cotangent spaces respectively,* $\boldsymbol{v} \in \mathcal{T}_{\mathcal{M}}$, $\alpha^{(1)} \in \mathcal{T}^*_{\mathcal{M}}$. *The vector and the covector may be expressed as a linear combination of the basis vectors of their respective spaces which, although are known from Section 2.2.2, are represented by* $\boldsymbol{e}_1, \boldsymbol{e}_2, \ldots, \boldsymbol{e}_n$ *and* $\sigma_1, \sigma_2, \ldots, \sigma_n$ *respectively for the sake of clarity*

$$\boldsymbol{v} = \sum_j v_j \boldsymbol{e}_j, \qquad \alpha^{(1)} = \sum_i \alpha_i \sigma_i. \tag{2.8}$$

Applying the linear functional $\alpha^{(1)}$ *to* $\boldsymbol{v}$ *and using the relations in Equation (2.4) and Equation (2.5) yields:*

$$\alpha^{(1)}(\boldsymbol{v}) = \sum_j v_j \alpha^{(1)}(\boldsymbol{e}_j) = \sum_j \sum_i v_j \alpha_i \sigma_i(e_j) = \sum_j \sum_i v_j \alpha_i \delta_{ij} = \sum_i v_i \alpha_i \in \mathbb{R}. \tag{2.9}$$

An important aspect to note here is that the duality paring implied by the vector inner product of α_i and v_j is independent of the choice of basis. The expansion coefficients α_i and v_j will change when using a different set of basis, however, the duality paring is unchanged. This is the major distinction to the classic inner product where a change of basis generally leads to a different metric tensor.

An alternative interpretation of the differential form is that it is any quantity that occurs under the integral sign [8]. To demonstrate this notion, consider the expanded version of the *1-form* from Equation (2.7).

$$\alpha^{(1)} = \alpha_1 \mathrm{d}x_1 + \alpha_2 \mathrm{d}x_2 + \ldots + \alpha_n \mathrm{d}x_n \tag{2.10}$$

By integrating Equation (2.10), one obtains:

$$\int \alpha^{(1)} = \int \alpha_1 \mathrm{d}x_1 + \alpha_2 \mathrm{d}x_2 + \ldots + \alpha_n \mathrm{d}x_n, \tag{2.11}$$

where the integral on the right can be identified as the line integral.

The presented proof and analogy of the *1-form* can be generalised to any *k-form*, wherein a *k-form* is constructed by taking the sums of the **exterior products** of the *1-forms*.

Definition 2.7 ([7, 8])**.** *For an n-dimensional manifold* $\boldsymbol{\mathcal{M}}$, *the* ***exterior product*** *or* ***wedge product*** *is the mapping* $\wedge : \Lambda^{(k)}(\boldsymbol{\mathcal{M}}) \times \Lambda^{(l)}(\boldsymbol{\mathcal{M}}) \to \Lambda^{(k+l)}(\boldsymbol{\mathcal{M}})$ *which maps two differential forms of lower degree to differential forms of higher degree. The mapping satisfies the following properties for* $\alpha^{(k)} \in \Lambda^{(k)}(\boldsymbol{\mathcal{M}})$, $\beta^{(l)} \in \Lambda^{(l)}(\boldsymbol{\mathcal{M}})$, $\gamma^{(m)} \in \Lambda^{(m)}(\boldsymbol{\mathcal{M}})$, *and* $f \in \Lambda^{(0)}(\boldsymbol{\mathcal{M}})$*:*

$$\alpha^{(k)} \wedge \beta^{(l)} = (-1)^{kl} \beta^{(l)} \wedge \alpha^{(k)} \tag{2.12}$$

$$\left(\alpha^{(k)} + \beta^{(l)}\right) \wedge \gamma^{(m)} = \alpha^{(k)} \wedge \gamma^{(m)} + \beta^{(l)} \wedge \gamma^{(m)} \tag{2.13}$$

$$\left(\alpha^{(k)} \wedge \beta^{(l)}\right) \wedge \gamma^{(m)} = \alpha^{(k)} \wedge \left(\beta^{(l)} \wedge \gamma^{(m)}\right) \tag{2.14}$$

$$f(\alpha^{(k)} \wedge \beta^{(l)}) = f(\alpha^{(k)}) \wedge \beta^{(l)} = \alpha^{(k)} \wedge f(\beta^{(l)}). \tag{2.15}$$

A *2-form* in a 2-dimensional manifold can be found by taking the exterior product of two *1-forms*.

Proof 2.2. *Consider the 1-forms* $\alpha^{(1)}$ *and* $\beta^{(1)}$ *on a 2-dimensional manifold* $\boldsymbol{\mathcal{M}} \subset \mathbb{R}^2$

$$\alpha^{(1)} = \alpha_1 \mathrm{d}x_1 + \alpha_2 \mathrm{d}x_2, \qquad \beta^{(1)} = \beta_1 \mathrm{d}x_1 + \beta_2 \mathrm{d}x_2.$$

The exterior product of $\alpha^{(1)}$ *and* $\beta^{(1)}$ *is then given by:*

$$\begin{aligned}
\alpha^{(1)} \wedge \beta^{(1)} &= (\alpha_1 \mathrm{d}x_1 + \alpha_2 \mathrm{d}x_2) \wedge (\beta_1 \mathrm{d}x_1 + \beta_2 \mathrm{d}x_2) \\
&= \cancelto{0}{\alpha_1\beta_1 \mathrm{d}x_1 \wedge \mathrm{d}x_1} + \alpha_1\beta_2 \mathrm{d}x_1 \wedge \mathrm{d}x_2 + \alpha_2\beta_1 \underbrace{\mathrm{d}x_2 \wedge \mathrm{d}x_1}_{=-\mathrm{d}x_1 \wedge \mathrm{d}x_2} + \cancelto{0}{\alpha_2\beta_2 \mathrm{d}x_2 \wedge \mathrm{d}x_2} \\
&= (\alpha_1\beta_2 - \alpha_2\beta_1)\, \mathrm{d}x_1 \wedge \mathrm{d}x_2.
\end{aligned}$$

One can recognise that the presented operation resembles the vector product in $\mathbb{R}^2$. However, unlike in vector calculus where the 2D vector product produces a scalar, the wedge product of two *1-forms* produces a *2-form*.

2.3. Operators on manifolds

2.3.1. Exterior derivative

The concept of derivatives is extensively used in the context of vector calculus where operators such as the gradient ($\vec{\nabla}$), divergence ($\vec{\nabla}\cdot$), and the curl ($\vec{\nabla}\times$) are constructed using different combinations of the differentials. In the context of differential geometry, however, these operators are unified into a single operator referred to as the **exterior derivative**.

Definition 2.8 ([7])**.** *The **exterior derivative** on an n-dimensional manifold $\boldsymbol{\mathcal{M}}$ is a unique mapping $\mathrm{d}:\ \Lambda^{(k)}(\boldsymbol{\mathcal{M}})\to\Lambda^{(k+1)}(\boldsymbol{\mathcal{M}})$ which maps differential k-forms into differential (k + 1)-forms. This operator satisfies the following properties:*

$$\mathrm{d}\left(\alpha^{(k)}+\beta^{(k)}\right)=\mathrm{d}\alpha^{(k)}+\mathrm{d}\beta^{(k)},\qquad\forall\alpha^{(k)},\beta^{(k)}\in\Lambda^{(k)}(\boldsymbol{\mathcal{M}}) \tag{2.16}$$

$$\mathrm{d}f=\sum_j\frac{\partial f}{\partial x_j}\mathrm{d}x_j,\qquad\forall f\in\Lambda^{(0)}(\boldsymbol{\mathcal{M}}) \tag{2.17}$$

$$\mathrm{d}\left(\alpha^{(k)}\wedge\beta^{(l)}\right)=\mathrm{d}\alpha^{(k)}\wedge\beta^{(l)}+(-1)^k\alpha^{(k)}\wedge\mathrm{d}\beta^{(l)},\qquad\forall\alpha^{(k)}\in\Lambda^{(k)}(\boldsymbol{\mathcal{M}}),\beta^{(l)}\in\Lambda^{(l)}(\boldsymbol{\mathcal{M}}) \tag{2.18}$$

$$\mathrm{d}\left(\mathrm{d}\alpha^{(k)}\right)=0,\qquad\forall\alpha^{(k)}\in\Lambda^{(k)}(\boldsymbol{\mathcal{M}}). \tag{2.19}$$

Example 2.9. *Consider a 0-form f (smooth function) defined on a 3-dimensional manifold $\boldsymbol{\mathcal{M}}\subset\mathbb{R}^3$. Applying the exterior derivative to f using the property defined in Equation (2.17) yields:*

$$\mathrm{d}f=\left(\frac{\partial f}{\partial x_1}\right)\mathrm{d}x_1+\left(\frac{\partial f}{\partial x_2}\right)\mathrm{d}x_2+\left(\frac{\partial f}{\partial x_3}\right)\mathrm{d}x_3\in\Lambda^{(1)}(\boldsymbol{\mathcal{M}}). \tag{2.20}$$

*Hence, applying the exterior derivative to a 0-form results in a 1-form of which the components correspond to the derivative of the function in each of the three directions. In Cartesian coordinates, these components correspond to the **gradient** of f ($\vec{\nabla}f$).*

Example 2.10. *Let $\alpha^{(1)}$ be a 1-form defined on a 3-dimensional manifold $\boldsymbol{\mathcal{M}}\subset\mathbb{R}^3$.*

$$\alpha^{(1)}=\alpha_1\mathrm{d}x_1+\alpha_2\mathrm{d}x_2+\alpha_3\mathrm{d}x_3 \tag{2.21}$$

The exterior derivative of $\alpha^{(1)}$ is thus given by:

$$\begin{aligned}
\mathrm{d}\alpha^{(1)}&=\mathrm{d}\alpha_1\wedge\mathrm{d}x_1+\mathrm{d}\alpha_2\wedge\mathrm{d}x_2+\mathrm{d}\alpha_3\wedge\mathrm{d}x_3\\
&=\left[\left(\frac{\partial\alpha_1}{\partial x_1}\right)\mathrm{d}x_1+\left(\frac{\partial\alpha_1}{\partial x_2}\right)\mathrm{d}x_2+\left(\frac{\partial\alpha_1}{\partial x_3}\right)\mathrm{d}x_3\right]\wedge\mathrm{d}x_1\\
&\quad+\left[\left(\frac{\partial\alpha_2}{\partial x_1}\right)\mathrm{d}x_1+\left(\frac{\partial\alpha_2}{\partial x_2}\right)\mathrm{d}x_2+\left(\frac{\partial\alpha_2}{\partial x_3}\right)\mathrm{d}x_3\right]\wedge\mathrm{d}x_2\\
&\quad+\left[\left(\frac{\partial\alpha_3}{\partial x_1}\right)\mathrm{d}x_1+\left(\frac{\partial\alpha_3}{\partial x_2}\right)\mathrm{d}x_2+\left(\frac{\partial\alpha_3}{\partial x_3}\right)\mathrm{d}x_3\right]\wedge\mathrm{d}x_3\\
&=\cancel{\left(\frac{\partial\alpha_1}{\partial x_1}\right)\mathrm{d}x_1\wedge\mathrm{d}x_1}+\left(\frac{\partial\alpha_1}{\partial x_2}\right)\mathrm{d}x_2\wedge\mathrm{d}x_1+\left(\frac{\partial\alpha_1}{\partial x_3}\right)\mathrm{d}x_3\wedge\mathrm{d}x_1\\
&\quad+\left(\frac{\partial\alpha_2}{\partial x_1}\right)\mathrm{d}x_1\wedge\mathrm{d}x_2+\cancel{\left(\frac{\partial\alpha_2}{\partial x_2}\right)\mathrm{d}x_2\wedge\mathrm{d}x_2}+\left(\frac{\partial\alpha_2}{\partial x_3}\right)\mathrm{d}x_3\wedge\mathrm{d}x_2\\
&\quad+\left(\frac{\partial\alpha_3}{\partial x_1}\right)\mathrm{d}x_1\wedge\mathrm{d}x_3+\left(\frac{\partial\alpha_3}{\partial x_2}\right)\mathrm{d}x_2\wedge\mathrm{d}x_3+\cancel{\left(\frac{\partial\alpha_3}{\partial x_3}\right)\mathrm{d}x_3\wedge\mathrm{d}x_3}\\
&=\left(\frac{\partial\alpha_3}{\partial x_2}-\frac{\partial\alpha_2}{\partial x_3}\right)\mathrm{d}x_2\wedge\mathrm{d}x_3+\left(\frac{\partial\alpha_1}{\partial x_3}-\frac{\partial\alpha_3}{\partial x_1}\right)\mathrm{d}x_3\wedge\mathrm{d}x_1+\left(\frac{\partial\alpha_2}{\partial x_1}-\frac{\partial\alpha_1}{\partial x_2}\right)\mathrm{d}x_1\wedge\mathrm{d}x_2.
\end{aligned}$$

*Therefore, the exterior derivative of a 1-form returns a 2-form of which the components can be unidentified to be the components of the **curl** of $\boldsymbol{\alpha}$ ($\vec{\nabla}\times\boldsymbol{\alpha}$) in Cartesian coordinates.*

Example 2.11. *Let $\omega^{(2)}$ be a 2-form defined on a 3-dimensional manifold $\boldsymbol{\mathcal{M}}\subset\mathbb{R}^3$.*

$$\omega^{(2)}=\omega_1\mathrm{d}x_2\wedge\mathrm{d}x_3+\omega_2\mathrm{d}x_3\wedge\mathrm{d}x_1+\omega_3\mathrm{d}x_1\wedge\mathrm{d}x_2. \tag{2.22}$$

Subsequently, applying the exterior derivative to $\omega^{(2)}$ gives:

$$\begin{aligned}\mathrm{d}\omega^{(2)} &= \mathrm{d}\omega_1 \mathrm{d}x_2 \wedge \mathrm{d}x_3 + \mathrm{d}\omega_2 \mathrm{d}x_3 \wedge \mathrm{d}x_1 + \mathrm{d}\omega_3 \mathrm{d}x_1 \wedge \mathrm{d}x_2 \\ &= \left(\frac{\partial \omega_1}{\partial x_1}\right) \mathrm{d}x_1 \wedge \mathrm{d}x_2 \wedge \mathrm{d}x_3 + \left(\frac{\partial \omega_2}{\partial x_2}\right) \mathrm{d}x_2 \wedge \mathrm{d}x_3 \wedge \mathrm{d}x_1 + \left(\frac{\partial \omega_3}{\partial x_3}\right) \mathrm{d}x_3 \wedge \mathrm{d}x_1 \wedge \mathrm{d}x_2 \\ &= \left(\frac{\partial \omega_1}{\partial x_1} + \frac{\partial \omega_2}{\partial x_2} + \frac{\partial \omega_3}{\partial x_3}\right) \mathrm{d}x_1 \wedge \mathrm{d}x_2 \wedge \mathrm{d}x_3.\end{aligned}$$

*As apparent through the above expression, the exterior derivative of a 2-form results in a 3-form which has a single component pertaining the sum of the derivatives of the components of ω in each direction. This single component corresponds to the **divergence** of $\boldsymbol{\omega}$ ($\vec{\nabla} \cdot \boldsymbol{\omega}$) in Cartesian coordinates.*

Lastly, it is intriguing to focus on the property of the exterior derivative given in Equation (2.19) which states that applying the exterior derivative twice returns a zero for all *k-forms*. Going back to the $\boldsymbol{\mathcal{M}} \subset \mathbb{R}^3$ case considered in the prior examples shows that the property in Equation (2.19) reflects the well known vector calculus relations which state that the ***curl of the gradient is zero*** $\vec{\nabla} \times (\vec{\nabla}\,[\cdot]) = 0$ and the ***divergence of the curl is zero*** $\vec{\nabla} \cdot (\vec{\nabla} \times [\vec{\cdot}]) = 0$. Moreover, an important remark can be made about the exterior derivative regarding its generality. While the exterior derivative can be interpreted with the ***gradient***, ***curl*** and ***div*** in Cartesian coordinates, the identities extend to curvilinear domains.

2.3.2. Interior product

Contrary to the exterior derivative, there exists an operator that acts to decrease the degree of a given differential form. This operator is referred to as the **interior product** and it is applied to a *k-form* through the means of a vector field.

Definition 2.12 ([7])**.** *For an n-dimensional manifold $\boldsymbol{\mathcal{M}}$, let $\boldsymbol{v} \in \boldsymbol{\mathcal{T}}_{\boldsymbol{\mathcal{M}}}$ be a vector field. The **interior product** is defined as the mapping $i_{\boldsymbol{v}} : \Lambda^{(k)}(\boldsymbol{\mathcal{M}}) \to \Lambda^{(k-1)}(\boldsymbol{\mathcal{M}})$ that transforms a differential k-form to a (k - 1)-form under the vector field $\boldsymbol{v}$, such that:*

$$i_{\boldsymbol{v}} f = 0, \qquad \forall f \in \Lambda^{(0)}(\boldsymbol{\mathcal{M}}) \tag{2.23}$$

$$i_{\boldsymbol{v}} \alpha^{(1)} = \alpha(\boldsymbol{v}), \qquad \forall \alpha^{(1)} \in \Lambda^{(1)}(\boldsymbol{\mathcal{M}}) \tag{2.24}$$

$$i_{\boldsymbol{v}} \gamma^{(k)} = \gamma^{(k)}\left(\boldsymbol{v}, \boldsymbol{w}_1, \boldsymbol{w}_2, \ldots, \boldsymbol{w}_{k-1}\right), \qquad \forall \gamma^{(k)} \in \Lambda^{(k)}(\boldsymbol{\mathcal{M}}) \text{ with } \boldsymbol{w}_1, \boldsymbol{w}_2, \ldots, \boldsymbol{w}_{k-1} \in \boldsymbol{\mathcal{T}}_{\boldsymbol{\mathcal{M}}}. \tag{2.25}$$

The interior product satisfies the following properties:

$$i_{a\boldsymbol{v}+b\boldsymbol{w}} \alpha^{(k)} = (a i_{\boldsymbol{v}} + b i_{\boldsymbol{w}}) \alpha^{(k)}, \qquad \forall \alpha^{(k)} \in \Lambda^{(k)}(\boldsymbol{\mathcal{M}}), a, b \in \mathbb{R} \tag{2.26}$$

$$i_{\boldsymbol{v}} \circ i_{\boldsymbol{w}} \alpha^{(k)} = -i_{\boldsymbol{w}} \circ i_{\boldsymbol{v}} \alpha^{(k)}, \qquad \forall \alpha^{(k)} \in \Lambda^{(k)}(\boldsymbol{\mathcal{M}}) \tag{2.27}$$

$$i_{\boldsymbol{v}} \left(\alpha^{(k)} \wedge \beta^{(l)}\right) = i_{\boldsymbol{v}} \alpha^{(k)} + (-1)^k \alpha^{(k)} \wedge i_{\boldsymbol{v}} \beta^{(l)}, \qquad \forall \alpha^{(k)} \in \Lambda^{(k)}(\boldsymbol{\mathcal{M}}), \beta^{(l)} \in \Lambda^{(l)}(\boldsymbol{\mathcal{M}}). \tag{2.28}$$

Note that, while the interior product maps differential forms in the direction opposite that of the exterior derivative, the two are **not** inverses of each other as they describe fundamentally different aspects.

2.3.3. Lie derivative

Definition 2.13 ([7, 8])**.** *The **Lie derivative** is an operator defined on an n-dimensional manifold $\boldsymbol{\mathcal{M}}$ that measures the change of a vector or differential k-form as it is transported by a vector field $\boldsymbol{v}$ generating a local flow. The Lie derivative of a k-form $\alpha^{(k)}$ along a vector field $\boldsymbol{v}$ is a mapping $\mathcal{L}_{\boldsymbol{v}} : \Lambda^{(k)}(\boldsymbol{\mathcal{M}}) \to \Lambda^{(k)}(\boldsymbol{\mathcal{M}})$ from a k-form to another k-form and is defined as follows:*

$$\mathcal{L}_{\boldsymbol{v}} \alpha^{(k)} := i_{\boldsymbol{v}} \circ \mathrm{d}\alpha^{(k)} + \mathrm{d} \circ i_{\boldsymbol{v}} \alpha^{(k)}. \tag{2.29}$$

This operator satisfies the following properties:

$$\mathcal{L}_{\boldsymbol{v}} \circ \mathrm{d}\alpha^{(k)} = \mathrm{d} \circ \mathcal{L}_{\boldsymbol{v}} \alpha^{(k)}, \qquad \forall \alpha^{(k)} \in \Lambda^{(k)}(\boldsymbol{\mathcal{M}}) \tag{2.30}$$

$$\mathcal{L}_{\boldsymbol{v}} \circ i_{\boldsymbol{v}} \alpha^{(k)} = i_{\boldsymbol{v}} \circ \mathcal{L}_{\boldsymbol{v}} \alpha^{(k)}, \qquad \forall \alpha^{(k)} \in \Lambda^{(k)}(\boldsymbol{\mathcal{M}}) \tag{2.31}$$

$$\mathcal{L}_{\boldsymbol{v}} \left(\alpha^{(k)} \wedge \beta^{(l)}\right) = \mathcal{L}_{\boldsymbol{v}} \alpha^{(k)} \wedge \beta^{(l)} + \alpha^{(k)} \wedge \mathcal{L}_{\boldsymbol{v}} \beta^{(l)}, \qquad \forall \alpha^{(k)} \in \Lambda^{(k)}(\boldsymbol{\mathcal{M}}), \beta^{(l)} \in \Lambda^{(l)}(\boldsymbol{\mathcal{M}}). \tag{2.32}$$

Applying the Lie derivative to the different differential forms associates with it certain vector proxies (v.p.) as described by [9]:

$$\alpha^{(0)} \in \Lambda^{(0)}(\boldsymbol{\mathcal{M}}): \quad \mathcal{L}_{\boldsymbol{v}}\alpha^{(0)} \overset{\text{v.p.}}{=} \boldsymbol{v} \cdot \vec{\nabla}\, \alpha \tag{2.33}$$

$$\alpha^{(1)} \in \Lambda^{(1)}(\boldsymbol{\mathcal{M}}): \quad \mathcal{L}_{\boldsymbol{v}}\alpha^{(1)} \overset{\text{v.p.}}{=} \vec{\nabla}\,(\boldsymbol{v} \cdot \boldsymbol{\alpha}) + \vec{\nabla} \times \boldsymbol{\alpha} \times \boldsymbol{v} \tag{2.34}$$

$$\alpha^{(2)} \in \Lambda^{(2)}(\boldsymbol{\mathcal{M}}): \quad \mathcal{L}_{\boldsymbol{v}}\alpha^{(2)} \overset{\text{v.p.}}{=} \vec{\nabla} \times (\boldsymbol{v} \times \boldsymbol{\alpha}) + \boldsymbol{v}\, \vec{\nabla} \cdot \boldsymbol{\alpha} \tag{2.35}$$

$$\alpha^{(3)} \in \Lambda^{(3)}(\boldsymbol{\mathcal{M}}): \quad \mathcal{L}_{\boldsymbol{v}}\alpha^{(3)} \overset{\text{v.p.}}{=} \vec{\nabla} \cdot (\boldsymbol{v}\alpha). \tag{2.36}$$

2.3.4. Hodge $\star$ operator

It was noted in Section 2.2.2 that vectors and differential *1-forms* (covectors) were related via the dual space. Similarly, the *1-forms* on an n-dimensional manifold are associated with *(n - 1)-forms*. This association between the *1-form* and *(n - 1)-form* generalises to any *k-form* and *(n - k)-form* through the means of the **Hodge $\star$ operator**.

Definition 2.14 ([7, 9])**.** *Let $\boldsymbol{\mathcal{M}}$ be an n-dimensional manifold. The Hodge $\star$ operator is defined as the linear mapping $\star: \Lambda^{(k)}(\boldsymbol{\mathcal{M}}) \to \Lambda^{(n-k)}(\boldsymbol{\mathcal{M}})$ that transforms a differential k-form to its dual (n - k)-form. Some examples of applying the Hodge operator in $\mathbb{R}^3$ to different k-forms are:*

$$\Lambda^{(0)}(\boldsymbol{\mathcal{M}}) \to \Lambda^{(3)}(\boldsymbol{\mathcal{M}}): \qquad \star\, 1 = \mathrm{d}x_1 \wedge \mathrm{d}x_2 \wedge \mathrm{d}x_3 \tag{2.37}$$

$$\Lambda^{(3)}(\boldsymbol{\mathcal{M}}) \to \Lambda^{(1)}(\boldsymbol{\mathcal{M}}): \qquad \star\, \mathrm{d}x_1 \wedge \mathrm{d}x_2 \wedge \mathrm{d}x_3 = 1 \tag{2.38}$$

$$\Lambda^{(1)}(\boldsymbol{\mathcal{M}}) \to \Lambda^{(2)}(\boldsymbol{\mathcal{M}}): \qquad \star\, \mathrm{d}x_1 = \mathrm{d}x_2 \wedge \mathrm{d}x_3 \tag{2.39}$$

$$\Lambda^{(2)}(\boldsymbol{\mathcal{M}}) \to \Lambda^{(1)}(\boldsymbol{\mathcal{M}}): \qquad \star\, \mathrm{d}x_2 \wedge \mathrm{d}x_3 = \mathrm{d}x_1. \tag{2.40}$$

Furthermore, applying the operator twice satisfies the following relation:

$$\star \star \alpha^{(k)} = (-1)^{k(n-k)}\alpha^{(k)}, \qquad \forall \alpha^{(k)} \in \Lambda^{(k)}(\boldsymbol{\mathcal{M}}). \tag{2.41}$$

One major thing to note is that, while all the other operators introduced in this section are purely topological, the Hodge $\star$ operator is not, and is therefore metric dependent. The metric dependence originates from the inclusion of the determinant of the metric tensor in the definition of the canonical form [9]. This metric dependent factor exists to account for the curvature of the manifold. On a different note, there exists a geometric interpretation for the Hodge operator which namely deals with the aforementioned notion of different geometric orientations. To demonstrate this, consider the illustration shown in Figure 2.1 which shows the different orientations assigned to each geometric object (differential forms) in $\mathbb{R}^3$. There namely two sets of orientations, the outer and the inner. The outer orientation considers the points and lines to have a sense of rotation, the surfaces having a flux, and the volumes having a source or sink like behaviour. The inner orientation, on the other hand, considers the points to have a source or sink like behaviour, the lines to have a circulation, and the surfaces and volumes having a sense of rotation within the plane and volume respectively. Notice that the inner orientations of the *k-forms* directly match with the outer orientations of the *(3 - k)-forms*. It is exactly this likeness between the two forms that the Hodge operator is based on. When applying the Hodge, the orientation of a differential form is preserved under the operation, whereas the geometric object is transformed.

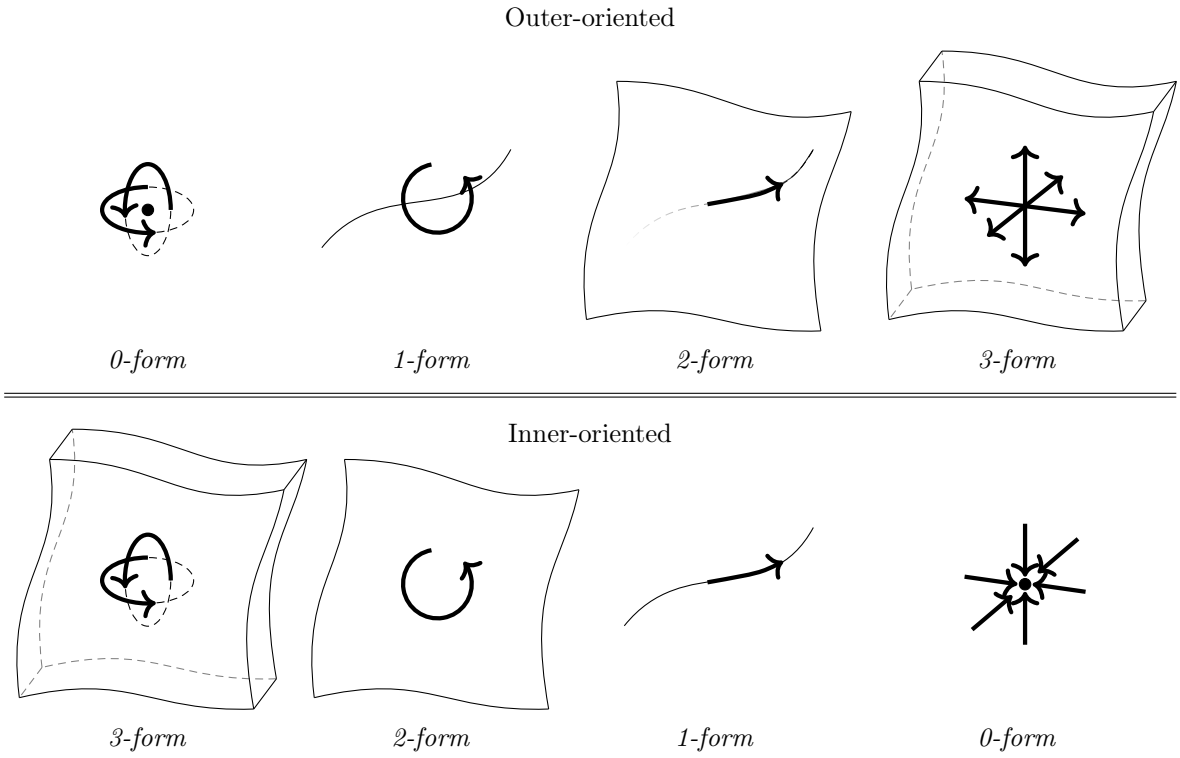

Figure 2.1: Outer and Inner oriented forms in $\mathbb{R}^3$

2.4. De Rham complex

A common theme that can be recognised from the behaviour of the different operators introduced in Section 2.3, is that they connect the different spaces of differential forms to one another. The exact sequence of mapping between differential forms can be summarised by the double De Rham complex which is shown in Figure 2.2 for $\mathbb{R}^3$.

$$\begin{array}{ccccccccccccc}
\mathbb{R} & \longrightarrow & \Lambda^{(0)}(\boldsymbol{\mathcal{M}}) & \xrightarrow[\vec{\nabla}]{\mathrm{d}} & \Lambda^{(1)}(\boldsymbol{\mathcal{M}}) & \xrightarrow[\vec{\nabla}\times]{\mathrm{d}} & \Lambda^{(2)}(\boldsymbol{\mathcal{M}}) & \xrightarrow[\vec{\nabla}\cdot]{\mathrm{d}} & \Lambda^{(3)}(\boldsymbol{\mathcal{M}}) & \longrightarrow & 0 \\
 & & \updownarrow\star & & \updownarrow\star & & \updownarrow\star & & \updownarrow\star & & \\
0 & \longleftarrow & \tilde{\Lambda}^{(3)}(\boldsymbol{\mathcal{M}}) & \xleftarrow[\vec{\nabla}\cdot]{\mathrm{d}} & \tilde{\Lambda}^{(2)}(\boldsymbol{\mathcal{M}}) & \xleftarrow[\vec{\nabla}\times]{\mathrm{d}} & \tilde{\Lambda}^{(1)}(\boldsymbol{\mathcal{M}}) & \xleftarrow[\vec{\nabla}]{\mathrm{d}} & \tilde{\Lambda}^{(0)}(\boldsymbol{\mathcal{M}}) & \longleftarrow & \mathbb{R}
\end{array}$$

Figure 2.2: The double de Rham complex in $\mathbb{R}^3$

The top row of this complex represents the space of differential forms in $\mathbb{R}^3$, and the bottom row represents the corresponding dual space of differential forms denoted by $\tilde{\Lambda}^{(k)}(\boldsymbol{\mathcal{M}})$. Moreover, the mapping along the horizontal direction is done by the exterior derivative which is a purely topological operator that links to the gradient, divergence, and curl operators in $\mathbb{R}^3$. The mapping along the vertical direction is done by the Hodge $\star$ operator, which is metric dependent as highlighted in Section 2.3.4.

3

Mimetic Spectral Element Method

Having discussed the mathematical concepts in the previous chapter, this chapter presents the framework of the 1D and 2D mimetic Spectral Element Method (SEM). Moreover, this chapter discusses the approach through which the numerical method employs the concepts of differential geometry introduced in the previous chapter. Firstly, Section 3.1 briefly explains the types of meshes used for the SEM. Subsequently, Section 3.2 presents the different basis functions defined on the mesh for 1D and 2D cases. Section 3.3 thereafter, show the derivation of the discrete operators which establishes a connection to the previous chapter on differential geometry. Lastly, Section 3.4 presents the discrete representation of the De Rham sequence.

3.1. Mesh

As in any numerical method, the SEM requires a computational mesh which holds the discrete representation of the physical quantities of a given model problem. As the discrete equations for the SEM are derived from the weak (or variational) formulation of the governing equations, the nodes of the mesh are taken to integration points of quadrature rules so as to aid numerical integration. A common quadrature rule applied in the SEM is the Gauss-Lobatto quadrature given that it includes the endpoints. Moreover, it is quite common to use two meshes for the mimetic SEM where the two meshes are referred to as the primal and the dual mesh. The two meshes are staggered as depicted in Figure 3.1 and Figure 3.2 which show the primal and dual meshes using 4 Gauss-Lobatto points in 1D and 2D respectively.

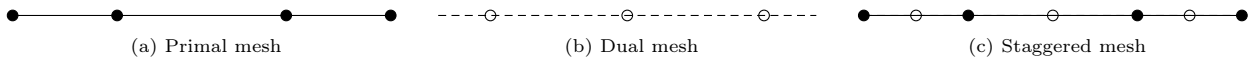

(a) Primal mesh (b) Dual mesh (c) Staggered mesh

Figure 3.1: Computational mesh in $\mathbb{R}^1$

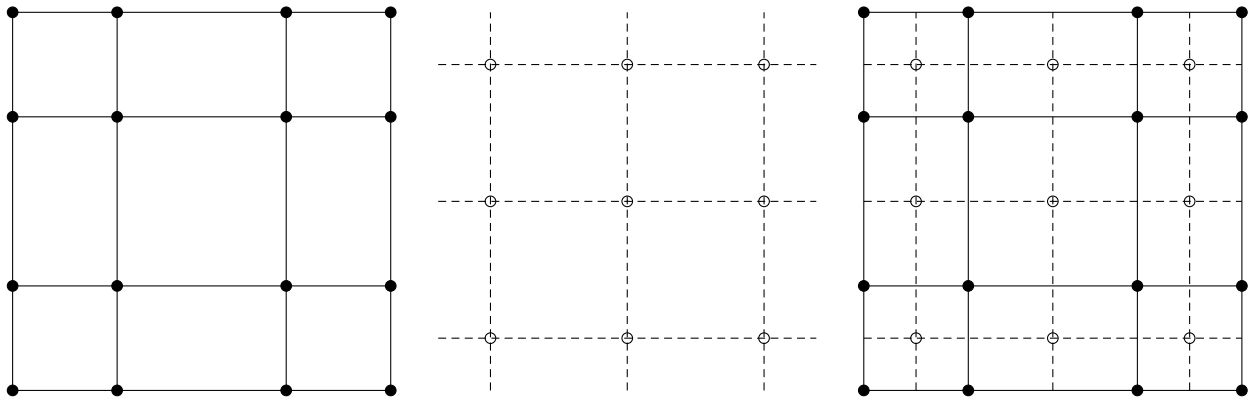

(a) Primal mesh (b) Dual mesh (c) Staggered mesh

Figure 3.2: Computational mesh in $\mathbb{R}^2$

This nomenclature employed for naming the meshes is not arbitrary, as it relates to the concept of dual spaces introduced in Chapter 2 and will be later explained in Section 3.3. The degrees of freedom that are defined

Figure 3.3: 1D inner oriented cell complex

on the two meshes are discrete differential forms. In $\mathbb{R}^1$, there are namely two differential forms, the *0-form* defined in points (nodes) and the *1-form* defined in edges (between two nodes). Similarly in $\mathbb{R}^2$, there are three different differential forms, namely the *0-form* defined in points, the *1-forms* defined along lines, and the *2-forms* defined in surfaces. Subsequently, the different differential forms are assigned a set of orientations, namely, the *outer-orientation* and the *inner-orientation* previously discussed in Section 2.3.4. For the 1D cases in the present work, the sole inner-oriented forms shown in Figure 3.3 are sufficient for the discretisation. The 2D case, on the other hand, requires both inner and outer orientations where the differential forms on primal mesh have an outer-orientation and the differential forms on dual mesh have an inner-orientation. The depiction of the two orientations is shown in Figure 3.4.

(a) Outer-oriented cell complex

(b) Inner-oriented cell complex

Figure 3.4: Orientation of cell complexes in $\mathbb{R}^2$

The outer oriented primal mesh, as depicted in Figure 3.4a, entails the points (*0-forms*) having a sense of rotation, the edges (*1-forms*) having the notion of flux through the edge, and the surfaces (*2-forms*) having a source like orientation. On top of the orientations, the nodes, edges, and surfaces on both primal and dual meshes are numbered.

3.2. Basis functions

Having established the concepts of the computational mesh, a description of the different function spaces used for the mimetic SEM is presented in this section. There are a vast number of function spaces that could be used as basis functions for the SEM such as the Fourier basis, or even B-splines. In the mimetic SEM, there are namely two classes of bases, the nodal basis, and the edge basis [10]. The description of the two is presented in the subsequent subsections.

3.2.1. 1D Nodal basis

As the name suggests, the nodal bases are the functions that are defined by a set of nodes or points. In the 1D case, these nodes are taken to be the points of the computational mesh $(\xi_0, \xi_1, \ldots, \xi_p)$, where the 1D nodal basis $(h_i(\xi))$ satisfies the following property:

$$h_i(\xi_j) = \delta_{ij}. \tag{3.1}$$

A function space that satisfies the above property is the space of Lagrange polynomials:

$$h_i(\xi) := \prod_{\substack{j=0 \\ j\neq i}}^{p} \frac{\xi - \xi_j}{\xi_i - \xi_j}, \qquad i = 0, 1, \ldots, p. \tag{3.2}$$

Equation (3.2) describes a set of $p+1$ 1D polynomials of order p. The essence of this basis is that if a quantity ϕ^h is expanded as a linear combination of the nodal basis as shown in Equation (3.3):

$$\phi_h = [h_0, h_1, \dots, h_p] \begin{bmatrix} \phi_0 \\ \phi_1 \\ \vdots \\ \phi_p \end{bmatrix}, \tag{3.3}$$

then ϕ_h represents a discrete differential *0-form* and the expansion coefficients ϕ_i correspond to the evaluation of ϕ at the nodes ξ_i due to the property in Equation (3.1).

$$\phi_i = \phi(\xi_i). \tag{3.4}$$

3.2.2. 1D Edge basis

The edge basis functions $e_i(\xi)$ are a separate set of functions that satisfy the following property:

$$\int_{\xi_{j-1}}^{\xi_j} e_i(\xi)\, \mathrm{d}\xi = \delta_{ij}. \tag{3.5}$$

The edge basis functions can be computed in terms of the nodal basis as shown below [10]:

$$e_i(\xi) := -\sum_{j=0}^{i-1} \frac{\mathrm{d}h_j}{\mathrm{d}\xi}, \qquad i = 1, 2, \dots, p. \tag{3.6}$$

Given the property in Equation (3.5), if a quantity is expanded using the edge basis functions as shown in Equation (3.7):

$$\varphi_h = [e_1, e_2, \dots, e_p] \begin{bmatrix} \varphi_1 \\ \varphi_2 \\ \vdots \\ \varphi_p \end{bmatrix}, \tag{3.7}$$

then ϕ_h represents a discrete differential *1-form* and the coefficients φ_i correspond to the integrated value between two nodes

$$\varphi_i = \int_{\xi_{i-1}}^{\xi_i} \varphi\, \mathrm{d}\xi. \tag{3.8}$$

The plots of the 1D nodal and edge Lagrange polynomials for $p = 4$ are shown in Figure 3.5 where the nodes are taken to be the Gauss Lobatto points.

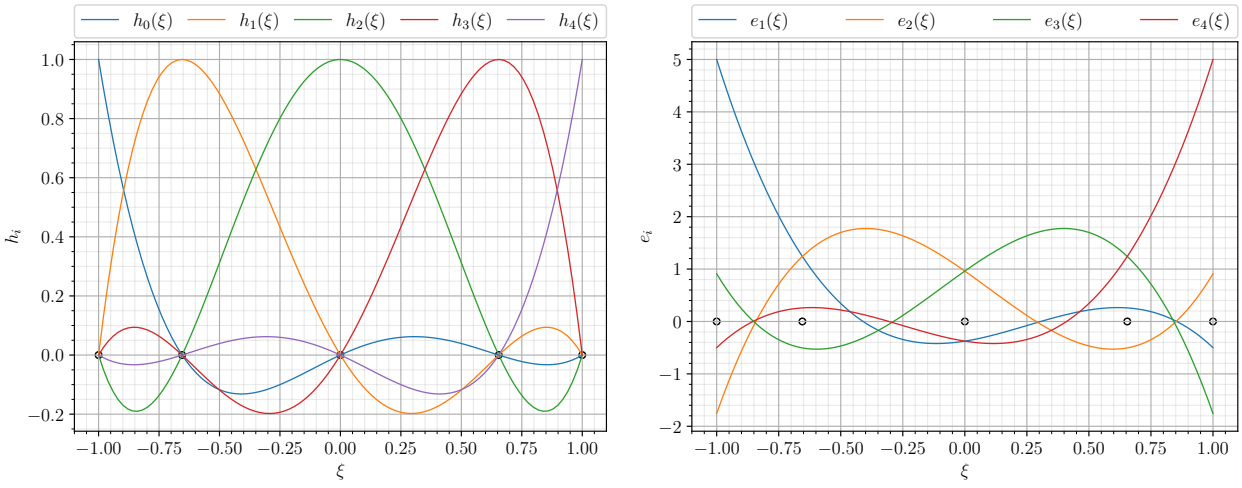

(a) Nodal Lagrange basis functions

(b) Edge basis functions

Figure 3.5: 1D nodal and edge basis functions for $p = 4$

3.2.3. Multi-dimensional Basis

The extension of the above mentioned 1D bases to higher dimensions is naturally done by taking the tensor product of the 1D polynomials. The exact combination of the 1D bases used in the tensor product for generating the 2D bases is shown in Table 3.1.

Table 3.1: Basis functions in 1D and 2D

***k-form* basis**	**1D**	**2D**
$\boldsymbol{\psi}^{(0)}$	$h(\xi)$	$h(\xi) \otimes h(\eta)$
$\boldsymbol{\psi}^{(1)}$	$e(\xi)$	$[h(\xi) \otimes e(\eta) \cdot \hat{\boldsymbol{n}}_{\boldsymbol{\xi}},\ h(\eta) \otimes e(\xi) \cdot \hat{\boldsymbol{n}}_{\boldsymbol{\eta}}]$
$\boldsymbol{\psi}^{(2)}$	N.A	$e(\xi) \otimes e(\eta)$

The multidimensional *k-form* basis functions corresponding to polynomial degree of 2 ($p = 2$) are shown in Appendix .1.

As highlighted before, there are three distinct differential forms that can be represented on a 2D mesh. As such, there are three sets of basis functions for the 2D case. The basis functions $\boldsymbol{\psi}^{(k)}$ are referred to as the *k-form* basis functions stemming from their property that a quantity expanded using these bases represents a discrete differential *k-form*. The *k-form* basis functions satisfy Korneker Delta properties similar to those of their 1D constituents. As such, the *0-form* basis satisfies the following property:

$$\psi_i^{(0)}(p_j) = \delta_{ij}, \tag{3.9}$$

with p_j being the j^{th} node of the mesh. The *1-form* basis satisfies:

$$\int_{l_j} \psi_i^{(1)}\, \mathrm{d}l_j = \delta_{ij}, \tag{3.10}$$

where l_j corresponds to the j^{th} edge of the mesh. Lastly, the *2-form* basis satisfies:

$$\int_{s_j} \psi_i^{(2)}\, \mathrm{d}s_j = \delta_{ij}, \tag{3.11}$$

where s_j is the j^{th} surface of the mesh. Subsequently, the discrete *k-forms* on the 2D computational mesh can be expressed as follows:

$$\alpha_h^{(0)} = \left[\psi_0^{(0)}, \psi_1^{(0)}, \ldots, \psi_n^{(0)}\right] \begin{bmatrix} \alpha_0 \\ \alpha_1 \\ \vdots \\ \alpha_n \end{bmatrix} \tag{3.12}$$

$$\beta_h^{(1)} = \left[\psi_0^{(1)}, \psi_1^{(1)}, \ldots, \psi_m^{(1)}\right] \begin{bmatrix} \beta_0 \\ \beta_1 \\ \vdots \\ \beta_m \end{bmatrix} \tag{3.13}$$

$$\omega_h^{(2)} = \left[\psi_0^{(2)}, \psi_1^{(2)}, \ldots, \psi_l^{(2)}\right] \begin{bmatrix} \omega_0 \\ \omega_1 \\ \vdots \\ \omega_l \end{bmatrix}, \tag{3.14}$$

where the expansion coefficients α_i correspond to the nodal values of α_h, β_i correspond to the fluxes of β_h over the edges of the mesh, and lastly, ω_i correspond to the integral value of ω_h over the surfaces of the mesh. These expansion coefficients are also commonly referred to as the *degrees of freedom*. It is worth noting that the basis function presented thus far have all been constructed on the primal mesh. The procedure for constructing the basis on the dual mesh is the same where one would use the dual nodes instead of the primal ones. However, the explicit construction of the dual basis functions is not needed as there exists a unique mapping between the primal and dual function spaces as shown in [11] and re-iterated in Section 3.3.2.

3.3. Discrete operators

The derivation of the discrete operators that can be applied to the discrete differential forms is presented in this section. The operators presented in this section correspond to the discrete counterparts of the operators shown in Section 2.3.

3.3.1. Exterior derivative

To start off, the discrete counterpart of the exterior derivative is introduced in this section. The underlying theorem behind all the derivations presented in this section is the Generalised Stokes' theorem [11]:

$$\int_{\Omega} \mathrm{d}\omega^{(k)} = \int_{\partial\Omega} \omega^{(k)}. \tag{3.15}$$

Firstly, consider an inner oriented 1D domain with the points and edges numbered as shown in Figure 3.6.

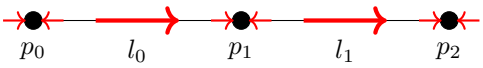

Figure 3.6: 1D inner oriented mesh

Suppose that a quantity ϕ is expanded/represented using the *0-form* (nodal) basis as follows:

$$\phi_h := \boldsymbol{\psi^{(0)}}\boldsymbol{\phi}. \tag{3.16}$$

Here, ϕ_h is the discrete representation of ϕ, $\boldsymbol{\psi^{(0)}}$ is the row vector containing the *0-form* basis functions, and $\boldsymbol{\phi}$ is the column vector containing the expansion coefficients (degrees of freedom). To derive the discrete exterior derivative for this 1D case, consider the 1D gradient theorem applied between two neighbouring nodes p_i and p_{i-1}:

$$\int_{p_{i-1}}^{p_i} \frac{\partial \phi}{\partial x}\,\mathrm{d}x = \phi\Big|_{p_i} - \phi\Big|_{p_{i-1}}. \tag{3.17}$$

Recalling that expansion coefficients, $\boldsymbol{\phi}$, of a discrete *0-form* correspond to the nodal evaluation of ϕ based on the property in Equation (3.4). As such, the gradient theorem can be expressed *exactly* as follows:

$$\int_{p_{i-1}}^{p_i} \frac{\partial \phi}{\partial x}\,\mathrm{d}x = \phi_i - \phi_{i-1} \tag{3.18}$$

Writing out this differencing operation for the simple 1D mesh shown in Figure 3.6 yields:

$$\begin{bmatrix} \int_{p_0}^{p_1} \frac{\partial \phi}{\partial x}\,\mathrm{d}x \\ \int_{p_1}^{p_2} \frac{\partial \phi}{\partial x}\,\mathrm{d}x \end{bmatrix} = \begin{bmatrix} -1 & 1 & 0 \\ 0 & -1 & 1 \end{bmatrix} \begin{bmatrix} \phi_0 \\ \phi_1 \\ \phi_2 \end{bmatrix}. \tag{3.19}$$

Now recall the property of the 1D *1-form* (edge) basis function given in Equation (3.8) which states that the expansion coefficients of a quantity expanded using the *1-form* basis corresponds to the integral values of the quantities between two neighbouring nodes. The differencing operation shown in Equation (3.19) yields the *exact* integrated value of the gradient of ϕ over two mesh nodes and can thus be considered to be the expansion coefficients of the *1-form* basis function expanding the gradient of ϕ.

$$\frac{\partial \phi_h}{\partial x} = \begin{bmatrix} \psi_1^{(1)}, \psi_2^{(1)} \end{bmatrix} \begin{bmatrix} \int_{p_0}^{p_1} \frac{\partial \phi}{\partial x}\,\mathrm{d}x \\ \int_{p_1}^{p_2} \frac{\partial \phi}{\partial x}\,\mathrm{d}x \end{bmatrix} \tag{3.20}$$

$$\frac{\partial \phi_h}{\partial x} = \begin{bmatrix} \psi_1^{(1)}, \psi_2^{(1)} \end{bmatrix} \begin{bmatrix} -1 & 1 & 0 \\ 0 & -1 & 1 \end{bmatrix} \begin{bmatrix} \phi_0 \\ \phi_1 \\ \phi_2 \end{bmatrix} \tag{3.21}$$

$$\frac{\partial \phi_h}{\partial x} = \boldsymbol{\psi^{(1)}}\mathbb{E}^{1,0}\boldsymbol{\phi}. \tag{3.22}$$

The differencing operator is written as $\mathbb{E}^{1,0}$ and is referred to as the *incidence matrix*. Following the shown derivation, it is evident that this incidence matrix is a linear transformation that maps the degrees of freedom

of discrete *0-forms* to the degrees of freedom of discrete *1-forms*, $\mathbb{E}^{1,0} : \Lambda_h^{(0)}(\boldsymbol{\mathcal{M}}) \rightarrow \Lambda_h^{(1)}(\boldsymbol{\mathcal{M}})$ and is therefore the discrete counterpart of the exterior derivative in 1D.

$$\mathbb{E}^{1,0} = \begin{bmatrix} -1 & 1 & 0 \\ 0 & -1 & 1 \end{bmatrix} \tag{3.23}$$

The construction of this incidence matrix can also be done geometrically following the orientations and numbering of the mesh shown in Figure 3.6. Considering the edge l_0, it can be seen that its orientation points to the right which is aligned with the direction of the left arrow of p_1 but opposite to the right arrow of p_0. Assigning a $+1$ for the point that is aligned, a -1 for the miss-aligned point, and 0 for all the non-enclosing points of l_0 yields a vector $[-1, 1, 0]$ which is equivalent to the first row of $\mathbb{E}^{1,0}$. Applying the same algorithm for l_1 yields $[0, -1, 1]$ which is equivalent to the second row of $\mathbb{E}^{1,0}$. This algorithm can be generalised to 1D meshes with an arbitrary number of points which are oriented and numbered as in Figure 3.6.

The constructed incidence matrix is for the primal mesh, however, following the De Rham sequence, there exists an adjoint or dual operator, $\widetilde{\mathbb{E}}^{1,0}$, which can be applied to the quantities defined on the dual mesh. The exact relation between $\mathbb{E}^{1,0}$ and $\widetilde{\mathbb{E}}^{1,0}$ can be found by considering the operator that is dual to the derivative operator. Consider two real-valued functions u and v defined in a 1D domain Ω with boundary $\partial\Omega$. The derivative of the product of the two functions can be expanded using the product rule:

$$\frac{\partial uv}{\partial x} = v\frac{\partial u}{\partial x} + \frac{\partial v}{\partial x}u. \tag{3.24}$$

Now integrating the above equation over the domain Ω yields:

$$\int_\Omega \frac{\partial uv}{\partial x}\,\mathrm{d}x = \int_\Omega v\frac{\partial u}{\partial x}\,\mathrm{d}x + \int_\Omega \frac{\partial v}{\partial x}u\,\mathrm{d}x \tag{3.25}$$

$$uv\Big|_{\partial\Omega} = \int_\Omega v\frac{\partial u}{\partial x}\,\mathrm{d}x + \int_\Omega \frac{\partial v}{\partial x}u\,\mathrm{d}x \tag{3.26}$$

$$\int_\Omega v\frac{\partial u}{\partial x}\,\mathrm{d}x = uv\Big|_{\partial\Omega} - \int_\Omega \frac{\partial v}{\partial x}u\,\mathrm{d}x. \tag{3.27}$$

The resulting expression shows that the dual operator of the 1D gradient is the negative gradient. More specifically, although not apparent in the 1D case, the dual gradient operator is the negative of the transpose of the gradient[1]. The found relation for the 1D gradient and its dual operator translates to the discrete setting too, therefore,

$$\widetilde{\mathbb{E}}^{1,0} = -\mathbb{E}^{1,0^T} + \mathbb{N}_1\mathcal{B}^{(0)}. \tag{3.28}$$

Similar to the 1D case, the incidence matrices for the 2D case are constructed by employing the geometric notions of the differential operators such as the gradient ($\vec{\nabla}$), divergence ($\vec{\nabla}\cdot$), and curl ($\vec{\nabla}\times$) which relate back to the Generalised Stokes' theorem in Equation (3.15). To demonstrate this, consider a simple 2×2 staggered mesh with the orientations and numbering as shown in Figure 3.7.

Firstly, the incidence matrix $\mathbb{E}^{1,0}$ is derived on this mesh. For the construction of this operator, consider a quantity defined in the points of the primal mesh, for instance the 2D vorticity field $\boldsymbol{\omega} = [0,\ 0,\ \omega_z]^T$ where:

$$\omega_{z_h} := \boldsymbol{\psi^{(0)}}\boldsymbol{\omega_z}, \tag{3.29}$$

is the discrete representation of ω_z using the *0-form* basis. Integrating the normal component curl of this quantity over an edge l_i of the primal mesh can be expressed as:

$$\int_{l_i} (\vec{\nabla}\times\boldsymbol{\omega})\cdot\hat{\boldsymbol{n}}\,\mathrm{d}l_i = \int_{l_i}\left[\frac{\partial\omega_z}{\partial y}, -\frac{\partial\omega_z}{\partial x}, 0\right]^T\cdot\hat{\boldsymbol{n}}_{l_i}\,\mathrm{d}l_i = \pm\left[\omega_z\right]_{\partial l_i}, \tag{3.30}$$

where $\hat{\boldsymbol{n}}_{l_i}$ is the unit vector normal to l_i and $[\omega_z]_{\partial l_i}$ is difference of ω_z at the end points of l_i. To elaborate on the expression in Equation (3.30), consider the integral over the edge l_0:

$$\int_{l_0} (\vec{\nabla}\times\boldsymbol{\omega})\cdot\hat{\boldsymbol{n}}_{l_0}\,\mathrm{d}l_0 = \int_{l_0}\left[\frac{\partial\omega_z}{\partial y}, -\frac{\partial\omega_z}{\partial x}, 0\right]^T\cdot[1,\ 0,\ 0]^T\,\mathrm{d}y \tag{3.31}$$

$$= \int_{l_0}\frac{\partial\omega_z}{\partial y}\,\mathrm{d}y \tag{3.32}$$

$$= \omega_z\Big|_{p_3} - \omega_z\Big|_{p_0} = [\omega_z]_{\partial l_0}. \tag{3.33}$$

[1]The origin of the transpose is more apparent when Equation (3.27) is expressed in a discrete setting

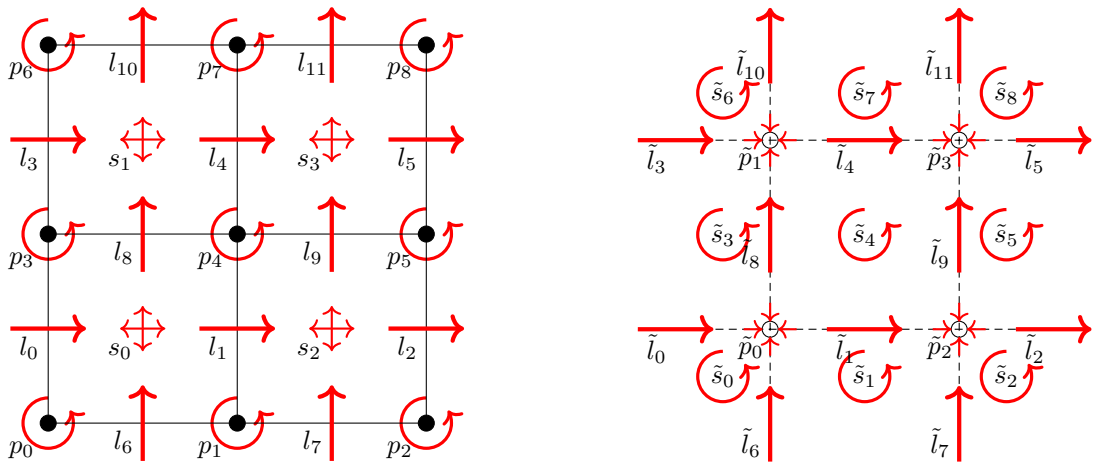

(a) Outer oriented primal mesh (b) Inner oriented dual mesh

Figure 3.7: 2×2 Primal and Dual meshes

Similarly, consider the integral over l_6:

$$\int_{l_6} (\vec{\nabla} \times \boldsymbol{\omega}) \cdot \hat{\boldsymbol{n}}_{l_6} \, \mathrm{d}l_6 = \int_{l_6} \left[\frac{\partial \omega_z}{\partial y}, -\frac{\partial \omega_z}{\partial x}, 0 \right]^T \cdot [0, 1, 0]^T \, \mathrm{d}x \tag{3.34}$$

$$= -\int_{l_0} \frac{\partial \omega_z}{\partial x} \, \mathrm{d}x \tag{3.35}$$

$$= -\left(\omega_z \Big|_{p_1} - \omega_z \Big|_{p_0} \right) = -\left[\omega_z \right]_{\partial l_6} . \tag{3.36}$$

In short, Equation (3.30) states that taking the difference of the neighbouring nodal values on the primal mesh yields the integrated value of the curl of the quantity normal to the edge connecting the two points. Alike the 1D case, applying this differencing operation to all the edges and incorporating the difference operator in a matrix yields the following:

$$\begin{bmatrix} \int_{l_0} (\vec{\nabla} \times \boldsymbol{\omega}) \cdot \hat{\boldsymbol{n}}_{l_0} \, \mathrm{d}l_0 \\ \int_{l_1} (\vec{\nabla} \times \boldsymbol{\omega}) \cdot \hat{\boldsymbol{n}}_{l_1} \, \mathrm{d}l_1 \\ \vdots \\ \int_{l_{11}} (\vec{\nabla} \times \boldsymbol{\omega}) \cdot \hat{\boldsymbol{n}}_{l_{11}} \, \mathrm{d}l_{11} \end{bmatrix} = \begin{bmatrix} -1 & 0 & 0 & 1 & 0 & 0 & 0 & 0 & 0 \\ 0 & -1 & 0 & 0 & 1 & 0 & 0 & 0 & 0 \\ 0 & 0 & -1 & 0 & 0 & 1 & 0 & 0 & 0 \\ 0 & 0 & 0 & -1 & 0 & 0 & 1 & 0 & 0 \\ 0 & 0 & 0 & 0 & -1 & 0 & 0 & 1 & 0 \\ 0 & 0 & 0 & 0 & 0 & -1 & 0 & 0 & 1 \\ 1 & -1 & 0 & 0 & 0 & 0 & 0 & 0 & 0 \\ 0 & 1 & -1 & 0 & 0 & 0 & 0 & 0 & 0 \\ 0 & 0 & 0 & 1 & -1 & 0 & 0 & 0 & 0 \\ 0 & 0 & 0 & 0 & 1 & -1 & 0 & 0 & 0 \\ 0 & 0 & 0 & 0 & 0 & 0 & 1 & -1 & 0 \\ 0 & 0 & 0 & 0 & 0 & 0 & 0 & 1 & -1 \end{bmatrix} \begin{bmatrix} \omega_{z_0} \\ \omega_{z_1} \\ \vdots \\ \omega_{z_8} \end{bmatrix} . \tag{3.37}$$

Recalling the property of the 2D *1-form* basis from Equation (3.10), one can show that[2]:

$$(\vec{\nabla} \times \boldsymbol{\omega}) = \left[\psi_0^{(1)}, \psi_1^{(1)}, \dots \psi_{11}^{(1)} \right] \begin{bmatrix} \int_{l_0} (\vec{\nabla} \times \boldsymbol{\omega}) \cdot \hat{\boldsymbol{n}}_{l_0} \, \mathrm{d}l_0 \\ \int_{l_1} (\vec{\nabla} \times \boldsymbol{\omega}) \cdot \hat{\boldsymbol{n}}_{l_1} \, \mathrm{d}l_1 \\ \vdots \\ \int_{l_{11}} (\vec{\nabla} \times \boldsymbol{\omega}) \cdot \hat{\boldsymbol{n}}_{l_{11}} \, \mathrm{d}l_{11} \end{bmatrix} \tag{3.38}$$

[2]Note that while the example was shown for a Cartesian mesh, the approach is not limited to that. The described method can be applied to other meshes which may be skewed, stretched, sheared, etc.

$$\left(\vec{\nabla} \times \boldsymbol{\omega}\right) = \left[\psi_0^{(1)},\ \psi_1^{(1)},\ \dots \psi_{11}^{(1)}\right] \begin{bmatrix} -1 & 0 & 0 & 1 & 0 & 0 & 0 & 0 & 0 \\ 0 & -1 & 0 & 0 & 1 & 0 & 0 & 0 & 0 \\ 0 & 0 & -1 & 0 & 0 & 1 & 0 & 0 & 0 \\ 0 & 0 & 0 & -1 & 0 & 0 & 1 & 0 & 0 \\ 0 & 0 & 0 & 0 & -1 & 0 & 0 & 1 & 0 \\ 0 & 0 & 0 & 0 & 0 & -1 & 0 & 0 & 1 \\ 1 & -1 & 0 & 0 & 0 & 0 & 0 & 0 & 0 \\ 0 & 1 & -1 & 0 & 0 & 0 & 0 & 0 & 0 \\ 0 & 0 & 0 & 1 & -1 & 0 & 0 & 0 & 0 \\ 0 & 0 & 0 & 0 & 1 & -1 & 0 & 0 & 0 \\ 0 & 0 & 0 & 0 & 0 & 0 & 1 & -1 & 0 \\ 0 & 0 & 0 & 0 & 0 & 0 & 0 & 1 & -1 \end{bmatrix} \begin{bmatrix} \omega_{z_0} \\ \omega_{z_1} \\ \vdots \\ \omega_{z_8} \end{bmatrix} \tag{3.39}$$

$$\left(\vec{\nabla} \times \boldsymbol{\omega}\right) = \boldsymbol{\psi}^{(1)} \mathbb{E}^{1,0} \boldsymbol{\omega_z}. \tag{3.40}$$

$$\mathbb{E}^{1,0} = \begin{bmatrix} -1 & 0 & 0 & 1 & 0 & 0 & 0 & 0 & 0 \\ 0 & -1 & 0 & 0 & 1 & 0 & 0 & 0 & 0 \\ 0 & 0 & -1 & 0 & 0 & 1 & 0 & 0 & 0 \\ 0 & 0 & 0 & -1 & 0 & 0 & 1 & 0 & 0 \\ 0 & 0 & 0 & 0 & -1 & 0 & 0 & 1 & 0 \\ 0 & 0 & 0 & 0 & 0 & -1 & 0 & 0 & 1 \\ 1 & -1 & 0 & 0 & 0 & 0 & 0 & 0 & 0 \\ 0 & 1 & -1 & 0 & 0 & 0 & 0 & 0 & 0 \\ 0 & 0 & 0 & 1 & -1 & 0 & 0 & 0 & 0 \\ 0 & 0 & 0 & 0 & 1 & -1 & 0 & 0 & 0 \\ 0 & 0 & 0 & 0 & 0 & 0 & 1 & -1 & 0 \\ 0 & 0 & 0 & 0 & 0 & 0 & 0 & 1 & -1 \end{bmatrix} \tag{3.41}$$

The differencing operator is thus the incidence matrix which maps the degrees of freedom of discrete differential *0-forms* into the degrees of freedom of discrete *1-forms*, $\mathbb{E}^{1,0} : \Lambda_h^{(0)}(\boldsymbol{\mathcal{M}}) \to \Lambda_h^{(1)}(\boldsymbol{\mathcal{M}})$, and can be viewed as the discrete curl operator.

The relation described in Equation (3.30) naturally translates to a geometric interpretation which can be used to construct the incidence matrix $\mathbb{E}^{1,0}$. Following the numbering and orientations of the points and edges in Figure 3.7a, one can observe that the direction of the flux over l_0 has a negative contribution (-1) coming from the rotation of p_0 and a positive contribution (+1) coming from p_3, given that the former has an induced direction opposite to the flux, and the latter has an induced direction aligned to the flux. Similarly, p_0 has a positive contribution to the flux at l_6 and p_1 has a negative contribution to l_6. Applying this procedure to every edge of the mesh and its confining nodes and collecting the entries (± 1) into a matrix where the rows correspond to the edge number and columns correspond to the point number, yields the matrix $\mathbb{E}^{1,0}$.

For the derivation of the second incidence matrix on the primal mesh, consider a vector field $\tilde{\boldsymbol{u}}$ defined as a *1-form*[3]:

$$\boldsymbol{u}_h := \boldsymbol{\psi^{(1)}} \boldsymbol{u}. \tag{3.42}$$

The Gauss Divergence theorem states that the integral of the divergence of $\tilde{\boldsymbol{u}}$ over a surface is equal to the flux of $\tilde{\boldsymbol{u}}$ over the boundary:

$$\int_{s_i} \vec{\nabla} \cdot \tilde{\boldsymbol{u}}\, \mathrm{d}s_i = \oint_{\partial s_i} \tilde{\boldsymbol{u}} \cdot \hat{\boldsymbol{n}}\, \mathrm{d}l. \tag{3.43}$$

Given that the expansion coefficients of the discrete *1-form* (u_i) correspond to the fluxes over the edges, the integral of the divergence of $\tilde{\boldsymbol{u}}$ can be exactly written as follows:

$$\begin{bmatrix} \int_{s_0} \vec{\nabla} \cdot \tilde{\boldsymbol{u}}\, \mathrm{d}s_0 \\ \int_{s_1} \vec{\nabla} \cdot \tilde{\boldsymbol{u}}\, \mathrm{d}s_1 \\ \int_{s_2} \vec{\nabla} \cdot \tilde{\boldsymbol{u}}\, \mathrm{d}s_2 \\ \int_{s_3} \vec{\nabla} \cdot \tilde{\boldsymbol{u}}\, \mathrm{d}s_3 \end{bmatrix} = \begin{bmatrix} -u_0 + u_1 - u_6 + u_8 \\ -u_1 + u_2 - u_7 + u_9 \\ -u_3 + u_4 - u_8 + u_{10} \\ -u_4 + u_5 - u_9 + u_{11} \end{bmatrix} \tag{3.44}$$

[3]The tilde is added to make the distinction between the quantity ($\tilde{\boldsymbol{u}}$) and the vector of expansion coefficients of the *1-form* basis ($\boldsymbol{u}$)

$$\begin{bmatrix} \int_{s_0} \vec{\nabla} \cdot \tilde{\boldsymbol{u}} \, \mathrm{d}s_0 \\ \int_{s_1} \vec{\nabla} \cdot \tilde{\boldsymbol{u}} \, \mathrm{d}s_1 \\ \int_{s_2} \vec{\nabla} \cdot \tilde{\boldsymbol{u}} \, \mathrm{d}s_2 \\ \int_{s_3} \vec{\nabla} \cdot \tilde{\boldsymbol{u}} \, \mathrm{d}s_3 \end{bmatrix} = \begin{bmatrix} -1 & 1 & 0 & 0 & 0 & 0 & -1 & 0 & 1 & 0 & 0 & 0 \\ 0 & 0 & 0 & -1 & 1 & 0 & 0 & 0 & -1 & 0 & 1 & 0 \\ 0 & -1 & 1 & 0 & 0 & 0 & 0 & -1 & 0 & 1 & 0 & 0 \\ 0 & 0 & 0 & 0 & -1 & 1 & 0 & 0 & 0 & -1 & 0 & 1 \end{bmatrix} \begin{bmatrix} u_0 \\ u_1 \\ \vdots \\ u_{11} \end{bmatrix}. \tag{3.45}$$

Following the same procedure as for $\mathbb{E}^{1,0}$ by using the property of the *2-form* basis:

$$\vec{\nabla} \cdot \tilde{\boldsymbol{u}} = \begin{bmatrix} \psi_0^{(2)}, \, \psi_1^{(2)}, \, \psi_2^{(2)}, \, \psi_3^{(2)} \end{bmatrix} \begin{bmatrix} \int_{s_0} \vec{\nabla} \cdot \tilde{\boldsymbol{u}} \, \mathrm{d}s_0 \\ \int_{s_1} \vec{\nabla} \cdot \tilde{\boldsymbol{u}} \, \mathrm{d}s_1 \\ \int_{s_2} \vec{\nabla} \cdot \tilde{\boldsymbol{u}} \, \mathrm{d}s_2 \\ \int_{s_3} \vec{\nabla} \cdot \tilde{\boldsymbol{u}} \, \mathrm{d}s_3 \end{bmatrix} \tag{3.46}$$

$$\vec{\nabla} \cdot \tilde{\boldsymbol{u}} = \begin{bmatrix} \psi_0^{(2)}, \, \psi_1^{(2)}, \, \psi_2^{(2)}, \, \psi_3^{(2)} \end{bmatrix} \begin{bmatrix} -1 & 1 & 0 & 0 & 0 & 0 & -1 & 0 & 1 & 0 & 0 & 0 \\ 0 & 0 & 0 & -1 & 1 & 0 & 0 & 0 & -1 & 0 & 1 & 0 \\ 0 & -1 & 1 & 0 & 0 & 0 & 0 & -1 & 0 & 1 & 0 & 0 \\ 0 & 0 & 0 & 0 & -1 & 1 & 0 & 0 & 0 & -1 & 0 & 1 \end{bmatrix} \begin{bmatrix} u_0 \\ u_1 \\ \vdots \\ u_{11} \end{bmatrix} \tag{3.47}$$

$$\vec{\nabla} \cdot \tilde{\boldsymbol{u}} = \boldsymbol{\psi^{(2)}} \mathbb{E}^{2,1} \boldsymbol{u} \tag{3.48}$$

$$\mathbb{E}^{2,1} = \begin{bmatrix} -1 & 1 & 0 & 0 & 0 & 0 & -1 & 0 & 1 & 0 & 0 & 0 \\ 0 & 0 & 0 & -1 & 1 & 0 & 0 & 0 & -1 & 0 & 1 & 0 \\ 0 & -1 & 1 & 0 & 0 & 0 & 0 & -1 & 0 & 1 & 0 & 0 \\ 0 & 0 & 0 & 0 & -1 & 1 & 0 & 0 & 0 & -1 & 0 & 1 \end{bmatrix}. \tag{3.49}$$

Thus, the incidence matrix $\mathbb{E}^{2,1}$ maps the degrees of freedom of discrete differential *1-forms* into the degrees of freedom of discrete *2-forms* $\mathbb{E}^{2,1} : \Lambda_h^{(1)}(\boldsymbol{\mathcal{M}}) \to \Lambda_h^{(2)}(\boldsymbol{\mathcal{M}})$ and is the discrete divergence operator.

Having concluded the derivations for the discrete exterior derivatives on the primal mesh ($\mathbb{E}^{1,0}$ and $\mathbb{E}^{2,1}$), the next step is to derive the discrete exterior derivatives on the dual mesh ($\widetilde{\mathbb{E}}^{1,0}$ and $\widetilde{\mathbb{E}}^{2,1}$). The derivation/construction of these incidence matrices on the dual mesh can be done in two ways. The first approach is the one which has been previously employed, namely, using the geometric notion of the generalised Stokes' theorem where the Gradient theorem in Equation (3.50) over the nodes and edges of the dual mesh yields the discrete gradient operator $\widetilde{\mathbb{E}}^{1,0}$, and similarly, Stokes' theorem in Equation (3.51) over the edges and surfaces of the dual mesh results in the discrete dual curl operator $\widetilde{\mathbb{E}}^{2,1}$.

$$\int_{\tilde{l}_i} \vec{\nabla} \, \varphi \, \mathrm{d}\tilde{l}_i = [\varphi]_{\partial \tilde{l}_i} \tag{3.50}$$

$$\int_{\tilde{s}_i} \vec{\nabla} \times \boldsymbol{\varphi} \, \mathrm{d}\tilde{s}_i = \oint_{\partial \tilde{s}_i} \boldsymbol{\varphi} \cdot \hat{\boldsymbol{t}} \, \mathrm{d}\tilde{l}. \tag{3.51}$$

The alternative approach is to use the idea that the operators on the dual mesh are the adjoint or dual of the operators on the primal. Consider a scalar function f and a vector field $\boldsymbol{u}$ defined in an arbitrary domain Ω that has a boundary $\partial\Omega$. The divergence of the product of f and $\boldsymbol{u}$ can be expressed as follows:

$$\vec{\nabla} \cdot (f\boldsymbol{u}) = (\vec{\nabla} \, f)^T \boldsymbol{u} + f \, \vec{\nabla} \cdot \boldsymbol{u}. \tag{3.52}$$

Now integrating the above equation over the domain Ω yields:

$$\int_\Omega \vec{\nabla} \cdot (f\boldsymbol{u}) \, \mathrm{d}\Omega = \int_\Omega (\vec{\nabla} \, f)^T \boldsymbol{u} \, \mathrm{d}\Omega + \int_\Omega f \, \vec{\nabla} \cdot \boldsymbol{u} \, \mathrm{d}\Omega. \tag{3.53}$$

Applying the Gauss Divergence theorem to the left hand side term:

$$\int_{\partial\Omega} (f\boldsymbol{u}) \cdot \hat{\boldsymbol{n}} \, \mathrm{d}\Gamma = \int_\Omega (\vec{\nabla} \, f)^T \boldsymbol{u} \, \mathrm{d}\Omega + \int_\Omega f \, \vec{\nabla} \cdot \boldsymbol{u} \, \mathrm{d}\Omega \tag{3.54}$$

$$\int_\Omega f \, \vec{\nabla} \cdot \boldsymbol{u} \, \mathrm{d}\Omega = -\int_\Omega (\vec{\nabla} \, f)^T \boldsymbol{u} \, \mathrm{d}\Omega - \int_{\partial\Omega} (f\boldsymbol{u}) \cdot \hat{\boldsymbol{n}} \, \mathrm{d}\Gamma. \tag{3.55}$$

Equation (3.55) thus shows that the *adjoint/dual of the divergence operator is negative the transpose of the gradient operator plus the boundary term.*

Similarly, consider two vector fields $\boldsymbol{u}$ and $\boldsymbol{v}$ defined in the domain Ω with boundary $\partial\Omega$. The divergence of the cross product of the two vectors can be written as follows:

$$\vec{\nabla} \cdot (\boldsymbol{v} \times \boldsymbol{u}) = \left(\vec{\nabla} \times \boldsymbol{u}\right)^T \boldsymbol{v} - \boldsymbol{u}^T \left(\vec{\nabla} \times \boldsymbol{v}\right). \tag{3.56}$$

Alike the previous case, integrating the above equation over Ω and applying the Gauss Divergence theorem gives:

$$\int_\Omega \vec{\nabla} \cdot (\boldsymbol{v} \times \boldsymbol{u}) \, \mathrm{d}\Omega = \int_\Omega \left(\vec{\nabla} \times \boldsymbol{u}\right)^T \boldsymbol{v} \, \mathrm{d}\Omega - \int_\Omega \boldsymbol{u}^T \left(\vec{\nabla} \times \boldsymbol{v}\right) \, \mathrm{d}\Omega \tag{3.57}$$

$$\int_{\partial\Omega} (\boldsymbol{v} \times \boldsymbol{u}) \cdot \hat{\boldsymbol{n}} \, \mathrm{d}\Gamma = \int_\Omega \left(\vec{\nabla} \times \boldsymbol{u}\right)^T \boldsymbol{v} \, \mathrm{d}\Omega - \int_\Omega \boldsymbol{u}^T \left(\vec{\nabla} \times \boldsymbol{v}\right) \, \mathrm{d}\Omega \tag{3.58}$$

$$\int_\Omega \left(\vec{\nabla} \times \boldsymbol{u}\right)^T \boldsymbol{v} \, \mathrm{d}\Omega = \int_\Omega \boldsymbol{u}^T \left(\vec{\nabla} \times \boldsymbol{v}\right) \, \mathrm{d}\Omega - \int_{\partial\Omega} (\boldsymbol{v} \times \boldsymbol{u}) \cdot \hat{\boldsymbol{n}} \, \mathrm{d}\Gamma. \tag{3.59}$$

Thus, Equation (3.59) shows that the *dual of the curl operator is the transpose of itself again with an additional boundary term.*

The found (continuous) relation for the dual divergence and dual curl operator translate to their discrete counterparts which gives the following expressions for $\widetilde{\mathbb{E}}^{1,0}$ and $\widetilde{\mathbb{E}}^{2,1}$:

$$\begin{aligned} \widetilde{\mathbb{E}}^{1,0} &= -\mathbb{E}^{2,1^T} + \mathbb{N}_1 \mathcal{B}^{(0)} \\ \widetilde{\mathbb{E}}^{2,1} &= \mathbb{E}^{1,0^T} + \mathbb{N}_0 \mathcal{B}^{(1)}. \end{aligned} \tag{3.60}$$

Having constructed all the incidence matrices for the 2D case, one can show a very important property of these operators, namely that applying the exterior derivative twice to any *0-form* yields a zero.

$$\mathrm{d} \circ \mathrm{d}\omega^{(0)} = 0, \qquad \forall \omega^{(0)} \in \Lambda^{(0)}(\boldsymbol{\mathcal{M}}) \tag{3.61}$$

This relation effectively reflects that the ***divergence*** of the ***curl*** of a quantity in the nodes of the primal mesh is zero, and that the ***curl*** of the ***gradient*** of a quantity on the nodes of the dual mesh is zero.

$$\vec{\nabla} \cdot \vec{\nabla} \times \boldsymbol{u} = 0, \quad \forall \boldsymbol{u} \in \mathbb{R}^n \tag{3.62}$$

$$\vec{\nabla} \times \vec{\nabla} \, f = 0, \quad \forall f \in \mathbb{R} \tag{3.63}$$

The property of the ***gradient***, ***divergence***, and ***curl*** operator is encapsulated by the incidence matrices whose product must yield exactly zero. Taking the product of the two incidence matrices on the primal mesh defined in Equation (3.41) and Equation (3.49) gives a matrix with zeros in all its entries.

$$\mathbb{E}^{2,1}\mathbb{E}^{1,0} = \mathbf{0} \tag{3.64}$$

Applying the same idea to the incidence matrices on the dual mesh is not as straightforward given the presence of the boundary terms. In the case where the boundary terms vanish, for instance when using periodic boundaries, the following identity hold:

$$\widetilde{\mathbb{E}}^{2,1}\widetilde{\mathbb{E}}^{1,0} = -\mathbb{E}^{1,0^T}\mathbb{E}^{2,1^T} = \mathbf{0}. \tag{3.65}$$

For the more general case where the boundary terms do not vanish, the product $\widetilde{\mathbb{E}}^{2,1}\widetilde{\mathbb{E}}^{1,0}$ is more involved but in the end it is found to be zero as shown in [11].

3.3.2. Hodge operator

A number of different works that employ the Finite/Spectral element method, resort to deriving the weak form of the governing equations. To demonstrate the weak form, consider a generic governing equation given below where $\mathscr{L}$ is a linear differential operator.

$$\mathscr{L}\alpha^{(k)} = 0, \qquad \alpha^{(k)} \in \Lambda^{(k)}(\boldsymbol{\mathcal{M}}) \tag{3.66}$$

The weak form of the governing equation is found by taking the wedge product of the equation with the Hodge of a test function v and integrating over the domain. This wedge Hodge operation is denotes the L^2 inner

product of the two quantities. For the Galerkin method, the test function is taken from the same function space as the solution space leading to the following:

$$\int_{\Omega} \mathscr{L}\alpha^{(k)} \wedge \star\, v^{(k)} = 0, \qquad \forall v^{(k)} \in \Lambda^{(k)}(\boldsymbol{\mathcal{M}}), \tag{3.67}$$

Now expressing the solution $\alpha^{(k)}$ and test function $v^{(k)}$ in a discrete finite-dimensional space using the *k-form* basis gives:

$$\alpha_h^{(k)} := \left[\psi_0^{(k)}, \psi_1^{(k)}, \ldots, \psi_p^{(k)}\right] \begin{bmatrix} \alpha_0 \\ \alpha_1 \\ \vdots \\ \alpha_p \end{bmatrix} = \boldsymbol{\psi}^{(k)}\boldsymbol{\alpha} \tag{3.68}$$

$$v_h^{(k)} := \left[\psi_0^{(k)}, \psi_1^{(k)}, \ldots, \psi_p^{(k)}\right] \begin{bmatrix} v_0 \\ v_1 \\ \vdots \\ v_p \end{bmatrix} = \boldsymbol{\psi}^{(k)}\boldsymbol{v}. \tag{3.69}$$

Substituting these discrete forms into Equation (3.67) yields the following:

$$v_i \alpha_j \int_{\Omega} \mathscr{L}\psi_j^{(k)} \wedge \star\, \psi_i^{(k)} = 0 \tag{3.70}$$

where the summation notation is implied over index i and j. Since the above equation holds for all $v_h \in \Lambda_h^{(k)}(\boldsymbol{\mathcal{M}})$, the coefficients v_i can be omitted, resulting in the following algebraic equation that can be solved to find the unknown α_js:

$$\alpha_j \int_{\Omega} \mathscr{L}\psi_j^{(k)} \wedge \star\, \psi_i^{(k)} = 0. \tag{3.71}$$

The solution to the algebraic system in Equation (3.71) will be the one that weakly satisfies $\mathscr{L}\alpha_h^{(k)} = 0$.

While the exact form the differential operator $\mathscr{L}$ will vary for different physical problems, it is still quite common that one will encounter the integral of the wedge product of the *k-form* basis with its Hodge when deriving the weak form. This integral term is referred to as the *k-form mass matrix* $\mathbb{M}^{(k)}$ and is defined as follows:

$$\mathbb{M}^{(k)} := \int_{\Omega} \left[\boldsymbol{\psi}^{(k)^T} \mathrm{d}x_1 \wedge \mathrm{d}x_2 \wedge \ldots \wedge \mathrm{d}x_k\right] \wedge \star \left[\boldsymbol{\psi}^{(k)} \mathrm{d}x_1 \wedge \mathrm{d}x_2 \wedge \ldots \wedge \mathrm{d}x_k\right]. \tag{3.72}$$

The Hodge operator in Equation (3.72) is considered to act as its continuous form, namely, that it maps *k-forms* to *(n-k)-forms* while leaving the point-wise values of the *k-form* unaffected. In other words, taking the dual of a *1-form* in 1D for instance, gives a *0-form*:

$$\star\, \boldsymbol{\psi^{(1)}\omega} = \tilde{\boldsymbol{\psi}}^{\boldsymbol{(0)}}\tilde{\boldsymbol{\omega}}, \tag{3.73}$$

however, the relation $\boldsymbol{\psi^{(1)}\omega} = \tilde{\boldsymbol{\psi}}^{\boldsymbol{(0)}}\tilde{\boldsymbol{\omega}}$ still holds in a point-wise sense. Using this idea, the Hodge of the *k-form* in Equation (3.72) need not be computed and the original *k-form* can be used instead with the inclusion of the metric tensor stemming from the definition of the Hodge operator [9]. The resulting expression for the *k-form* mass matrix is then given by:

$$\mathbb{M}^{(k)} = \sqrt{\det(g)} \int_{\Omega} \left[\boldsymbol{\psi}^{(k)^T} \mathrm{d}x_1 \wedge \mathrm{d}x_1 \wedge \ldots \wedge \mathrm{d}x_k\right] \wedge \left[\boldsymbol{\psi}^{(k)} \mathrm{d}x_{k+1} \wedge \mathrm{d}x_{k+2} \wedge \ldots \wedge \mathrm{d}x_n\right] \tag{3.74}$$

$$\mathbb{M}^{(k)} = \pm\sqrt{\det(g)} \int_{\Omega} \boldsymbol{\psi}^{(k)^T} \boldsymbol{\psi}^{(k)} \mathrm{d}x_1 \wedge \mathrm{d}x_2 \wedge \ldots \wedge \mathrm{d}x_k, \tag{3.75}$$

where $\sqrt{\det(g)}$ is the square root of the determinant of the metric tensor and the $\pm$ is there to account for the sign of the product of the basis vectors $(\mathrm{d}x_i)$. These *k-form* mass matrices essentially map discrete *k-forms* to discrete *(n-k)-forms*, $\mathbb{M}^{(k)} : \Lambda_h^{(k)}(\boldsymbol{\mathcal{M}}) \to \tilde{\Lambda}_h^{(n-k)}(\boldsymbol{\mathcal{M}})$. Therefore, the mass matrices act as the discrete Hodge operators. One important thing to note is that, unlike the incidence matrices, the mass matrices include metric dependence and are therefore subjected to the approximations/errors coming from the domain discretisation.

As previously mentioned in Section 3.2.3, the dual mesh and dual basis functions need not be explicitly constructed. The reason for this is highlighted in [11] which in short relates to the mass matrices. Consider a discrete *k-form* $\alpha_h^{(k)}$ defined in an n-dimensional manifold:

$$\alpha_h^{(k)} := \boldsymbol{\psi^{(k)}\alpha}. \tag{3.76}$$

Its dual $\tilde{\alpha}_h^{(n-k)}$ lives in the space of discrete *(n-k)-forms*:

$$\tilde{\alpha}_h^{(n-k)} := \tilde{\boldsymbol{\psi}}^{(\boldsymbol{n-k})}\tilde{\boldsymbol{\alpha}}. \tag{3.77}$$

The dual degrees of freedom $\tilde{\boldsymbol{\alpha}}$ can be computed using the *k-form* mass matrix as follows:

$$\tilde{\boldsymbol{\alpha}} = \mathbb{M}^{(k)}\boldsymbol{\alpha}. \tag{3.78}$$

Furthermore, as previously highlighted, $\boldsymbol{\alpha}$ and $\tilde{\alpha}_h^{(n-k)}$ must be equal in a strong (point-wise) sense.

$$\boldsymbol{\psi}^{(\boldsymbol{k})}\boldsymbol{\alpha} = \tilde{\boldsymbol{\psi}}^{(\boldsymbol{n-k})}\tilde{\boldsymbol{\alpha}} \tag{3.79}$$

$$\boldsymbol{\psi}^{(\boldsymbol{k})}\boldsymbol{\alpha} = \tilde{\boldsymbol{\psi}}^{(\boldsymbol{n-k})}\mathbb{M}^{(k)}\boldsymbol{\alpha}. \tag{3.80}$$

For the above expression to be equal, the dual basis functions $\tilde{\boldsymbol{\psi}}^{(\boldsymbol{n-k})}$ must be:

$$\tilde{\boldsymbol{\psi}}^{(\boldsymbol{n-k})} = \boldsymbol{\psi}^{(\boldsymbol{k})}\mathbb{M}^{(k)^{-1}}. \tag{3.81}$$

3.3.3. Interior product

To obtain a discrete interior product operator, it was noted in [9] that the interior product is adjoint/dual to the wedge product. This duality paring implied the following relation $\forall\alpha_h^{(k)} \in \Lambda_h^{(k)}(\boldsymbol{\mathcal{M}})$, $\forall\beta_h^{(k-1)} \in \Lambda_h^{(k-1)}(\boldsymbol{\mathcal{M}}), \forall \boldsymbol{v}_h \in \boldsymbol{\mathcal{T}}_{\boldsymbol{\mathcal{M}}_h}$:

$$\int_{\Omega_h}\left(i_{\boldsymbol{v}_h}\alpha_h^{(k)}\right)\wedge\star\beta_h^{(k-1)} = \int_{\Omega_h}\alpha_h^{(k)}\wedge\star\left(\beta_h^{(k-1)}\wedge\boldsymbol{v}_h^{\flat}\right). \tag{3.82}$$

The $\flat$ superscript on the vector $\boldsymbol{v}_h$ is referring to the musical operator which maps vectors from the tangent space to a *1-form*, $\flat : \boldsymbol{\mathcal{T}}_{\boldsymbol{\mathcal{M}}} \to \Lambda^{(1)}(\boldsymbol{\mathcal{M}})$. Now defining a new variable $\gamma_h^{(k-1)}$ to be the interior product of $\alpha_h^{(k)}$ under vector $\boldsymbol{v}_h$:

$$i_{v_h}\alpha_h^{(k)} = \gamma_h^{(k-1)} = \boldsymbol{\psi}^{(k-1)}\boldsymbol{\gamma}, \tag{3.83}$$

and substituting it into Equation (3.82) yields:

$$\int_{\Omega_h}\gamma_h^{(k-1)}\wedge\star\beta_h^{(k-1)} = \int_{\Omega}\alpha_h^{(k)}\wedge\star\left(\beta_h^{(k-1)}\wedge\boldsymbol{v}_h^{\flat}\right). \tag{3.84}$$

Expanding all the discrete differential forms using their respective *k-form* basis functions results in the following:

$$\boldsymbol{\beta}^T\int_{\Omega_h}\boldsymbol{\psi}^{(k-1)^T}\boldsymbol{\psi}^{(k-1)}\boldsymbol{\gamma} = \boldsymbol{\beta}^T\int_{\Omega_h}\boldsymbol{v}_h^{\flat}\boldsymbol{\psi}^{(k-1)^T}\boldsymbol{\psi}^{(k)}\boldsymbol{\alpha} \tag{3.85}$$

One can recognise that the integral on the left side of the above equation corresponds to the *(k-1)-form* mass matrix. The integral on the right, however, is not quite the mass matrix as it contains the product of the *(k-1)-form* basis with the *k-form* basis. This matrix acts as a projection matrix with the vector field and is expressed as $\mathbb{M}_{\boldsymbol{v}_h}^{(k-1,k)}$.

$$\boldsymbol{\beta}^T\mathbb{M}^{(k-1)}\boldsymbol{\gamma} = \boldsymbol{\beta}^T\mathbb{M}_{\boldsymbol{v}_h}^{(k-1,k)}\boldsymbol{\alpha}. \tag{3.86}$$

Since the above equation holds for all $\boldsymbol{\beta}$, it can be eliminated which results in the following expression for $\boldsymbol{\gamma}$:

$$\boldsymbol{\gamma} = \left(\mathbb{M}^{(k-1)}\right)^{-1}\mathbb{M}_{\boldsymbol{v}_h}^{(k-1,k)}\boldsymbol{\alpha}. \tag{3.87}$$

Therefore, the discrete interior product may be written as follows:

$$i_{\boldsymbol{v}_h}\alpha_h^{(k)} = \gamma_h^{(k-1)} = \boldsymbol{\psi}^{(k-1)^T}\left[\left(\mathbb{M}^{(k-1)}\right)^{-1}\mathbb{M}_{\boldsymbol{v}_h}^{(k-1,k)}\boldsymbol{\alpha}\right]. \tag{3.88}$$

The interior product in its continuous form is metric free, however, the discrete form derived above proves to have strong metric dependencies coming from the mass matrix ($\mathbb{M}^{(k-1)^{-1}}$) and the projection matrix ($\mathbb{M}_k^{(\boldsymbol{v}_h,k-1)}$). There are, however, certain cases where at least the projection matrix can be metric-free which will be later discussed in Section 5.1.2. Concerning the mappings involved in the discrete interior product, it can be seen that the projection matrix maps the *k-form* to a dual *(k - 1)-form* under the weight of the vector $\boldsymbol{v}$, and the mass matrix acts as the discrete Hodge operator mapping the dual quantity to the primal space.

3.3.4. Lie derivative

As highlighted in Section 2.3.3, the Lie derivative of a *k-form* can be expressed by some combination of the exterior derivative and the interior product. Having derived the discrete counterparts of both the exterior derivative and the interior product in the previous sections, the discrete Lie derivative can be readily found by simply re-writing Equation (2.29) using the discrete operators. The resulting discrete Lie derivative is given as follows:

$$\mathcal{L}_{\boldsymbol{v}_h}\alpha_h^{(k)} := \underbrace{\mathbb{E}^{k,k-1}\left(\mathbb{M}^{(k-1)}\right)^{-1}\mathbb{M}_{\boldsymbol{v}_h}^{(k-1,k)}}_{\mathrm{d}\circ i_{\boldsymbol{v}_h}}\alpha_h^{(k)} + \underbrace{\left(\mathbb{M}^{(k)}\right)^{-1}\mathbb{M}_{\boldsymbol{v}_h}^{(k,k+1)}\mathbb{E}^{k+1,k}}_{i_{\boldsymbol{v}_h}\circ \mathrm{d}}\alpha_h^{(k)}. \tag{3.89}$$

3.4. Discrete De Rham complex

As previously shown in Section 2.4, the sequence of applying the various operators on a manifold can be elegantly summarised by the De Rham sequence. Naturally, there also exists a discrete version of the De Rham complex which is shown in Figure 3.8 and Figure 3.9 for 1D and 2D respectively. The concept of the De Rham complexes shown here for the discrete cases are the same as the continuous case only difference being that the continuous operators are replaced by their discrete counterparts.

$$\begin{array}{ccccccccc}
\mathbb{R} & \longrightarrow & \Lambda_h^{(0)}(\boldsymbol{\mathcal{M}}) & \xrightarrow{\mathbb{E}^{1,0}} & \Lambda_h^{(1)}(\boldsymbol{\mathcal{M}}) & \longrightarrow & 0 \\
 & & \downarrow{\scriptstyle \mathbb{M}^{(0)}} & & \downarrow{\scriptstyle \mathbb{M}^{(1)}} & & \\
0 & \longleftarrow & \tilde{\Lambda}_h^{(1)}(\boldsymbol{\mathcal{M}}) & \xleftarrow{\widetilde{\mathbb{E}}^{1,0}} & \tilde{\Lambda}_h^{(0)}(\boldsymbol{\mathcal{M}}) & \longleftarrow & \mathbb{R}
\end{array}$$

Figure 3.8: Discrete De Rham complex in $\mathbb{R}^1$

$$\begin{array}{ccccccccc}
\mathbb{R} & \longrightarrow & \Lambda_h^{(0)}(\boldsymbol{\mathcal{M}}) & \xrightarrow{\mathbb{E}^{1,0}} & \Lambda_h^{(1)}(\boldsymbol{\mathcal{M}}) & \xrightarrow{\mathbb{E}^{2,1}} & \Lambda_h^{(2)}(\boldsymbol{\mathcal{M}}) & \longrightarrow & 0 \\
 & & \downarrow{\scriptstyle \mathbb{M}^{(0)}} & & \downarrow{\scriptstyle \mathbb{M}^{(1)}} & & \downarrow{\scriptstyle \mathbb{M}^{(2)}} & & \\
0 & \longleftarrow & \tilde{\Lambda}_h^{(2)}(\boldsymbol{\mathcal{M}}) & \xleftarrow{\widetilde{\mathbb{E}}^{2,1}} & \tilde{\Lambda}_h^{(1)}(\boldsymbol{\mathcal{M}}) & \xleftarrow{\widetilde{\mathbb{E}}^{1,0}} & \tilde{\Lambda}_h^{(0)}(\boldsymbol{\mathcal{M}}) & \longleftarrow & \mathbb{R}
\end{array}$$

Figure 3.9: Discrete De Rham complex in $\mathbb{R}^2$

3.5. Hybrid Spectral Element Method

The derivations and concepts presented in this chapter thus far have primarily tackled the Spectral method, that is, a mesh with only a single element. A single element alone can be quite restrictive, thus, it is customary to extend to multiple elements giving rise to the SEM. This extension to the multi element case is discussed in this section.

3.5.1. Mesh

The mesh for the multi element setting is simply constructed by adding a number of single elements like Figure 3.1 (for 1D) or Figure 3.2 (for 2D) in a sequence. Each element has its respective set of basis functions used for expressing the various (nodal, edge, etc) degrees of freedom. For ease of generalisation, the basis functions are define in a reference element, $\xi \in [-1, 1]$ in 1D and $(\xi, \eta) \in [-1, 1]^2$ in 2D. Thus the computations involving the basis functions are executed in the reference element and then transform to each physical element. The transformation is done via a mapping Φ which is expressed as follows for the 1D case:

$$\Phi(\xi) := \frac{a}{2}(1-\xi) + \frac{b}{2}(1+\xi), \qquad \xi \in [-1, 1], \tag{3.90}$$

the depiction of which is shown in Figure 3.10. An important quantity used in the transformations is the Jacobian $J = \dfrac{\partial \Phi}{\partial \xi}$ which acts to scale the quantities when moving from the reference element to the physical one. This approach can be generalised for multi-dimensional cases as well, see [11] for details.

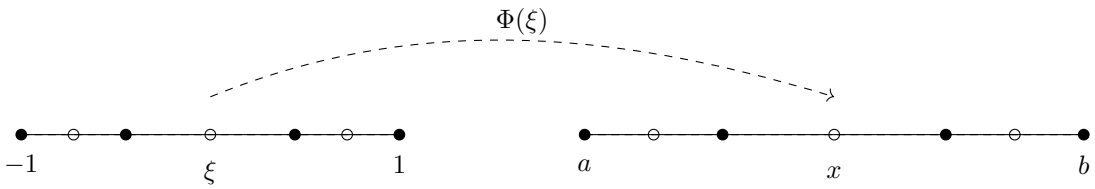

Figure 3.10: Illustration of mapping between the 1D reference and physical element

The mapping between the reference and physical elements is one key component of the multi-element case. The other key component relates to the manner by which information is passed between the elements. This is associated to enforcing some level of continuity between the elements. There are primarily two approaches to enforce said continuity amongst the elements, namely by either employing the gathering matrix approach or using the hybrid method. The latter is the approach considered in the present work. The hybrid method involves introducing additional degrees of freedom at the element interfaces which are used to enforce the desired continuity constraints. Examples of this hybrid setup for the 1D and 2D cases are shown in Figure 3.11 and Figure 3.12 respectively. Note that since only periodic problems are considered in the 2D case, the depicted 2D mesh in Figure 3.12 shows the Lagrange multipliers specific to the periodic case. The example 1D mesh

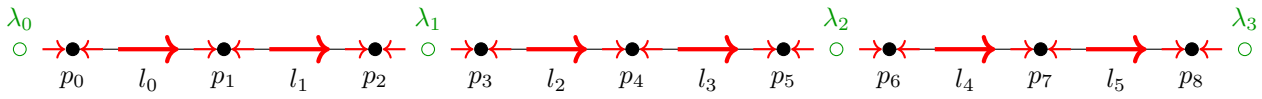

Figure 3.11: Example hybrid 1D mesh with $p = 2$ and $N = 3$ elements

in Figure 3.11 depicts a mesh with $N = 3$ elements with each element containing three (transformed Gauss-Lobatto) points leading to every element containing three quadratic $p = 2$ polynomials. Hereforth, for any given 1D mesh, the variables p and N are used to refer to the degree of the polynomial and number of elements respectively. The numbering shown in the figure highlight the global numbering of the degrees of freedom on the mesh where the λs are the additional Lagrange multipliers used to enforce inter element continuity and boundary conditions. Note that for case of periodic boundary conditions, λ_3 is redundant as periodicity between point 8 and 0 can be enforced using only λ_0.

Moving on to the 2D case, the example hybrid mesh in Figure 3.12 shows the global numbering of the degrees of freedom for a mesh comprised of 3×3 elements which each element containing quadratic ($p = 2$) polynomials for the nodal degrees of freedom. The extension of the hybrid formulation to the 2D case involves the addition of a few more Lagrange multipliers as shown in Figure 3.12. The desired continuity in the 2D case is the continuity between the nodal degrees of freedom and the continuity between the edge degrees of freedom, that is, continuity of the pointwise quantities and the continuity of the fluxes over the elements. For this reason, there are three set of Lagrange multipliers introduced, namely λ, γ, and θ. The λs map out to enforce continuity of the fluxes between the elements, whereas the γs are used to enforce continuity of the pointwise quantity. The γs on their own are in fact insufficient to obtain a unique solution to the constrained problem, hence the addition of θ. The θs are designed to enforce a constraint on the Lagrange multipliers λ themselves which in the end guarantee uniqueness of the solution to the constrained problem.

3.5.2. Constraints with Lagrange multipliers

With the Lagrange multipliers introduced, the approach for using them to enforce the desired constraints to a discrete algebraic system is discussed in this subsection. Consider an algebraic problem in the following form constructed on the 1D example mesh from Figure 3.11:

$$\boldsymbol{A}\boldsymbol{u} = \boldsymbol{f}, \tag{3.91}$$

where $\boldsymbol{u}$ is a vector containing the nodal degrees of freedom organised based on the global numbering of the nodes shown in Figure 3.11. Now suppose one wishes to enforce the solution to be equal to zero at the domain boundaries and pointwise continuous at the elements. Then the constraints on the degrees of freedom read as

Figure 3.12: Example hybrid 2D periodic mesh with $p = 2$ and 3×3 elements

follows:

$$\begin{aligned} u_0 &= 0 \\ u_3 - u_2 &= 0 \\ u_6 - u_5 &= 0 \\ u_8 &= 0. \end{aligned} \tag{3.92}$$

These constraints may be imposed using the Lagrange multipliers λ as the boundary variables as follows:

$$\int_{\partial\Omega_k} \lambda[u] \, \mathrm{d}\Gamma_k = 0, \tag{3.93}$$

where $[u]$ represents the jump in the value of u at the element boundary between neighbouring elements. The above expression may be rewritten as follows:

$$\boldsymbol{\lambda}^T \mathbb{E}^{\lambda,0} \boldsymbol{u} = \mathbf{0}, \tag{3.94}$$

where the jump operator is replaced by a differencing matrix $\mathbb{E}^{\lambda,0}$ and $\boldsymbol{\lambda}$ and $\boldsymbol{u}$ are the vectors containing the Lagrange multipliers and nodal degrees of freedom respectively. This $\mathbb{E}^{\lambda,0}$ shares a similarity with the previously described incidence matrices in the sense that they are both topological operators which simply include ± 1 as their entries.

Going back to the original algebraic problem, reformulating the problem with the inclusion of the constraints using the Lagrange multipliers yields the following system:

$$\boldsymbol{A}\boldsymbol{u} + \mathbb{E}^{\lambda,0^T} \boldsymbol{\lambda} = \boldsymbol{f} \tag{3.95}$$

$$\mathbb{E}^{\lambda,0} \boldsymbol{u} = 0 \tag{3.96}$$

$$\begin{bmatrix} \boldsymbol{A} & \mathbb{E}^{\lambda,0^T} \\ \mathbb{E}^{\lambda,0} & \varnothing \end{bmatrix} \begin{bmatrix} \boldsymbol{u} \\ \boldsymbol{\lambda} \end{bmatrix} = \begin{bmatrix} \boldsymbol{f} \\ \mathbf{0} \end{bmatrix}. \tag{3.97}$$

This concept can be further extended to the 2D case using the same procedure which will lead to additional topological operators, namely $\mathbb{E}^{\lambda,1}$, $\mathbb{E}^{\gamma,0}$, and $\mathbb{E}^{\theta,\gamma}$ [12]. Further details on this 2D case are explored for the case of the 2D Navier-Stokes equations in Section 6.2. In addition to that, all subsequent sections pertaining the discussion on the hybrid method also include the discussion on the physical representation of the Lagrange multipliers for the specific problem.

3.6. Time march

As the goal of this study is targeted towards advection problems, the choice of temporal discretisation is an important aspect to consider. Using the concepts introduced earlier in this chapter, one can discretise the spatial terms of any given time dependent PDE and arrive at semi-discrete equation which describes the time evolution of the degrees of freedom. This semi-discrete system can be discretised using any given time marching scheme to arrive at a fully discrete system. The choice of the time march scheme employed in this thesis is the Crank-Nicolson scheme which shall be elaborated within this section.

As the Crank-Nicolson scheme is a subset of a broader class of multistage Runge-Kutta methods, the focus is first set on multistage methods. Consider a generic time dependent problem describing the time evolution of a variable u as follows:

$$\frac{\partial u}{\partial t} = F(t, u). \tag{3.98}$$

If t^n represents the time at the n^{th} time level, $\Delta t = t^{n+1} - t^n$, and $u^n = u(t^n)$, then an s-stage Runge-Kutta predicts the solution at the new time level ($u(t^{n+1}) = u^{n+1}$) using the previous time level as follows:

$$u^{n+1} = u^n + \Delta t \sum_{i=1}^{s} b_i k_i, \tag{3.99}$$

where k_i is given by:

$$k_i = F\left(t + c_i \Delta t, u^n + \Delta t \sum_{j=1}^{s} a_{ij} k_j\right), \tag{3.100}$$

and the coefficients a_{ij}, b_i, c_i are real numbers typically taken from the Butcher Tableau of the given s-stage scheme as follows:

c_1	a_{11}	a_{12}	$\dots$	a_{1s}
c_2	a_{21}	a_{22}	$\dots$	a_{2s}
$\vdots$	$\vdots$	$\vdots$	$\vdots$	$\vdots$
c_s	a_{s1}	a_{s2}	$\dots$	a_{ss}
	b_1	b_2	$\dots$	b_s

Implicit methods include a full table whereas explicit methods generate lower triangular structure for the table (a_{ij}).

The Butcher Tableau for the Crank-Nicolson scheme is given by:

0	0	0
1	0.5	0.5
	0.5	0.5

Which gives the following for the 1 step update equation that is second order accurate:

$$u^{n+1} = u^n + \Delta t\, F\left(\frac{1}{2}(t^n + t^{n+1}), \frac{1}{2}(u^n + u^{n+1})\right) = u^n + \Delta t\, F\left(t^{n+\frac{1}{2}}, u^{n+\frac{1}{2}}\right). \tag{3.101}$$

This Crank-Nicolson scheme has been employed in many different mimetic discretisation techniques, see for example [4, 13]. The reason for its popularity within the class of mimetic methods is attributed to the fact that it is a sub-set of Gauss methods which are proven to be energy-conserving, reversible, and algebraically stable [14].

4

Variational Multiscale

This chapter presents a description of the VMS theory including its theoretical background and its applications. The focus of this study is on the residual-based algebraic VMS method, thus, this chapter focuses on that method in particular. Firstly, Section 4.1 discusses the origin and the mathematical foundation of the multiscale method. Subsequently, Section 4.2 addresses some examples of the applications of VMS in the context of LES including a brief discussion on discontinuity-capturing.

4.1. Residual Based Variational Multiscale theory

Many different problems in physics and engineering have a multiscale nature where the behaviour of the small scales has a significant influence on the larger scales. In the context of fluid flows, the multiscale nature appears in the dynamics of turbulent flows wherein the small turbulent scales drain energy from the large scales. This behaviour poses issues for under-resolved numerical simulations as the absence of the small scales in the numerical solution deprives the system of the energy drain mechanism leading to incorrect/nonphysical time evolution of the solution. Residual-based VMS theory offers a consistent stabilisation method for such multiscale problems. The manner by which the residual-based VMS method is incorporated into a weak form in the framework of Finite/Spectral Element methods is presented in this section.

4.1.1. Formulating the VMS method

The first stabilisation approach for Finite-Element methods was the Streamline Upwind Petrov Galerkin (SUPG) formulation. The essence of SUPG was that it would include a stabilisation term/parameter into the discrete equations that introduced diffusion in the streamwise direction and also helped in eliminating spurious oscillations in the numerical solution [15]. The VMS method itself originates from the re-interpretation of SUPG formulation stemming from the series of works in [16–25] as well as [26], and was first introduced in [27]. The essence of VMS is that it employs an a priori scale separation thereby differentiating the so-called resolved scales which are directly computed in the simulation, and the un-resolved (small) scales whose effect on the resolved scales needs to be accounted for. This concept of scale separation is applied to the variational form of the governing equations leading to the weak form being split into two separate formulations [28]. To demonstrate this, consider a generic form of a PDE shown below:

$$\mathscr{L}\boldsymbol{\phi} = f, \qquad \boldsymbol{x} \in \Omega \in \mathbb{R}^n \tag{4.1}$$

The weak form of the above PDE can be found by multiplying the equation with a test function v and integrating it over the domain. Note that while this approach does produce the weak form of the PDE, it is not the formal way of arriving at it. The formal approach for obtaining the weak form employs the minimisation of an energy functional. However, such a functional may not exist for any generic case, which is the reason for not applying the formal approach. In any case, employing the aforementioned approach of multiplying with a test function and integrating over the domain yields:

$$\int_\Omega \mathscr{L}\boldsymbol{\phi} \wedge \star\, v = \int_\Omega f \wedge \star\, v, \qquad \forall v \in \mathcal{V}. \tag{4.2}$$

Another important remark is that the test space should be from the same space as the residual of the PDE. This leads to the test space being the same as the trial space for elliptic problems, which is in fact the Galerkin

formulation. This formulation, however, is no longer valid for general hyperbolic problems. Nevertheless, the adaptation to this hyperbolic case is a separate challenging task in itself. Hence the classic Galerkin approach is employed for hyperbolic problems as well. In the traditional Galerkin Finite/Spectral element method, the solution and test space would be taken to be some finite-dimensional function space and it was precisely this finite-dimensional function space that was the origin of the multiscale problem. Thus, [27] proposed the following split of the function spaces:

$$\mathcal{V} := \mathcal{V}_h \oplus \mathcal{V}' \tag{4.3}$$
$$v := v_h + v' \tag{4.4}$$
$$\phi := \phi_h + \phi', \tag{4.5}$$

where the subscript h refers to the finite-dimensional space where the resolved (large) scales live, and the superscript $'$ refers to the infinite-dimensional space where the un-resolved (small) scales live. This approach was formally introduced in [29] where the VMS theory was further expanded upon. Inserting this split into the weak form in Equation (4.2) yields the following expression:

$$\int_\Omega \mathscr{L}\left(\phi_h + \phi'\right) \wedge \star \left(v_h + v'\right) = \int_\Omega f \wedge \star \left(v_h + v'\right). \tag{4.6}$$

Noting that the two function spaces emerging from the split are linearly independent, one can obtain two separate weak forms where one corresponds to the so-called resolved scale equation ($v' = 0$) and the other is the so-called un-resolved scale equation ($v_h = 0$).

$$\int_\Omega \mathscr{L}\left(\phi_h + \phi'\right) \wedge \star v_h = \int_\Omega f \wedge \star v_h \tag{4.7}$$
$$\int_\Omega \mathscr{L}\left(\phi_h + \phi'\right) \wedge \star v' = \int_\Omega f \wedge \star v' \tag{4.8}$$

The resolved scale equation in Equation (4.7) yields a finite-dimensional system that can be solved to find the resolved scales provided that there is (at least some) information on the un-resolved scales. On the contrary, the un-resolved scale equation in Equation (4.8) is infinite-dimensional meaning that has to be solved analytically provided some simplifying assumptions thus yielding a small scale model.

4.1.2. Residual based small scales

Considering the case of turbulent fluid flow, for instance, it would be ideal that the small (or sub-grid) scale model be residual-driven such that the model would "turn off" when the solution is well resolved. The small scale weak form in Equation (4.8) can actually be shown to be residual driven. For example, assuming $\mathscr{L}$ is a linear operator allows for Equation (4.7) to be written as follows:

$$\int_\Omega \mathscr{L}\phi_h \wedge \star v_h + \int_\Omega \mathscr{L}\phi' \wedge \star v_h = \int_\Omega f \wedge \star v_h \tag{4.9}$$
$$\int_\Omega \mathscr{L}\phi_h \wedge \star v_h + \int_\Omega \phi' \wedge \star \tilde{\mathscr{L}} v_h = \int_\Omega f \wedge \star v_h, \tag{4.10}$$

where $\tilde{\mathscr{L}}$ is the dual of the linear operator $\mathscr{L}$. Similarly, Equation (4.8) can be rewritten as follows:

$$\int_\Omega \mathscr{L}\phi_h \wedge \star v' + \int_\Omega \mathscr{L}\phi' \wedge \star v' = \int_\Omega f \wedge \star v' \tag{4.11}$$
$$\int_\Omega \mathscr{L}\phi' \wedge \star v' = \int_\Omega (f - \mathscr{L}\phi_h) \wedge \star v' \tag{4.12}$$
$$\int_\Omega \phi' \wedge \star \tilde{\mathscr{L}} v' = -\int_\Omega \mathscr{R}\phi_h \wedge \star v'. \tag{4.13}$$

One can observe that the right-hand side of Equation (4.12) corresponds to the residual of the resolved scales which is denoted by $\mathscr{R}\phi_h$. This structure of the un-resolved scale problem is not limited to linear problems, as the weak form of non-linear PDEs also produces a very similar structure, albeit with some additional terms [28] involving both the resolved and un-resolved components. Since the present work only focuses on the incorporation of multiscale theory for linear problems, the treatment for non-linear operators is excluded from the discussion.

4.1.3. Small scale Green's function

Having shown the elegant property that the un-resolved scale equation is driven by the residual of the resolved scales, the subsequent step is to come up with an approach to solve it. This subsection presents a brief discussion on Greens' function approach to arrive at an algebraic expression for the un-resolved scales. One can easily recognise that the un-resolved scale problem in Equation (4.13) is a global problem as the integral spans the entire domain. This global nature of the small scales poses issues in terms of the practical implementation of the VMS method. As such, the problem is localised to an element level problem where one seeks an estimate of $\boldsymbol{\phi}'$ over each element of the mesh [30]. This is thus an approximation applied to generate a small scale model suitable for practical applications. The process of applying such a approximation can be seen as selecting a *projection* $\mathscr{P}$ that maps the exact infinite-dimensional solution $\boldsymbol{\phi}$ to a finite-dimensional $\boldsymbol{\phi}_h$, $\mathscr{P} : \boldsymbol{\phi} \in \mathcal{V} \rightarrow \boldsymbol{\phi}_h \in \mathcal{V}_h$. The choice of the value imposed at the element boundaries for $\boldsymbol{\phi}'$ determines the projection type. While explicit relations of the boundary interface values for $\boldsymbol{\phi}'$ can only be found for a handful of cases, there are some distinguished cases where imposing $\boldsymbol{\phi}' = 0$ at the element boundaries gives the H^1 projector [28].

With the H^1 projector in mind, the element's Greens' function can be set up as follows:

$$\tilde{\mathscr{L}} g_e(\boldsymbol{x}, \boldsymbol{s}) = \delta(\boldsymbol{x} - \boldsymbol{s}), \qquad \boldsymbol{x}, \boldsymbol{s} \in \Omega_{e_k} \tag{4.14}$$

$$g_e(\boldsymbol{x}, \boldsymbol{s}) = 0, \qquad \boldsymbol{x} \in \partial\Omega_{e_k} \tag{4.15}$$

where Ω_{e_k} is the k^{th} element of the discretised domain, $\bigcup_{k=0}^{n} \Omega_{e_k} = \Omega_h$. The element's Green's function satisfying the element-wise boundary condition can generally be computed analytically for the adjoint operator $\tilde{\mathscr{L}}$ and can be directly substituted into Equation (4.13) which gives[1]:

$$\int_{\Omega_{e_k}} \tilde{\mathscr{L}} g_e(\boldsymbol{x}, \boldsymbol{s})\, \boldsymbol{\phi}' \, \mathrm{d}\Omega^s_{e_k} = -\int_{\Omega_{e_s}} g_e(\boldsymbol{x}, \boldsymbol{s})\, \mathscr{R}\boldsymbol{\phi}_h \, \mathrm{d}\Omega^s_{e_k} \tag{4.16}$$

$$\int_{\Omega_{e_k}} \delta(\boldsymbol{x} - \boldsymbol{s})\, \boldsymbol{\phi}' \, \mathrm{d}\Omega^s_{e_k} = -\int_{\Omega_{e_k}} g_e(\boldsymbol{x}, \boldsymbol{s})\, \mathscr{R}\boldsymbol{\phi}_h \, \mathrm{d}\Omega^s_{e_k} \tag{4.17}$$

$$\boldsymbol{\phi}'(\boldsymbol{x}) = -\int_{\Omega_{e_k}} g_e(\boldsymbol{x}, \boldsymbol{s})\, \mathscr{R}\boldsymbol{\phi}_h \, \mathrm{d}\Omega^s_{e_k} \tag{4.18}$$

Equation (4.18) thus gives an explicit equation which can be solved to find the exact (pointwise) $\boldsymbol{\phi}'$ under the approximations imposed through the projection. However, solving the exact integral equation can be rather expensive and impractical. In addition to that, the exact $\boldsymbol{\phi}'$ values are unnecessary given that pointwise values are undefined in Sobolev spaces where everything is defined in an L^2 sense. Thus, to avoid computing the pointwise values of u', the Greens' function appearing in the integral may be simplified such that it only contains the terms necessary to obtain the correct integral of u' in the resolved scale equation. This simplification step is designed to reduce Equation (4.18) into an algebraic expression in the following form:

$$\boldsymbol{\phi}'(\boldsymbol{x}) \approx -\tau\, \mathscr{R}\boldsymbol{\phi}_h, \tag{4.19}$$

where τ is commonly referred to as the stabilising parameter that encapsulates the necessary effects of the Greens' function, see [30] for further details. Several different approaches for this algebraic VMS method employ different techniques to obtain the required (approximate) u' for their desired projection. Some examples and applications of the use of VMS theory are presented in the subsequent section.

4.2. Application of the multiscale theory

The first use of VMS in the context of LES can be found in [31, 32] where the small scale model was tuned to capture the physical behaviour of the small-scales. This process did not use the residual-based approach nor the Green's function as previously described and instead treated the small scale model as a scaled diffusion term. This concept emerged from the classical LES and RANS turbulence modelling techniques. The residual-based approach using the Greens' function was first applied in [33] and was further elaborated in [34]. Additionally, the works on the VMS method focused on the construction of the stabilisation parameter τ. The work presented in [27] suggested that the element-averaged Greens' function can be a suitable approximation of τ for low-ordered basis functions. Furthermore, the paper suggested an extension to higher-order methods by

[1] Note the integration variable is switched to s as the goal is to obtain $\boldsymbol{\phi}'$ as a function of x and not s

employing bubble functions. Alternatively, other works arrive at an approximation of τ by using asymptotic scaling arguments [28, 35]. Other examples of VMS being used in the LES framework can be found in [36–38].

The stabilisation that the VMS method offers is not just limited to the field of under-resolved simulations. The use of VMS methods in the context of capturing discontinuities is also something found in the literature. Unlike shock (discontinuity) fitting, the underlying principle behind discontinuity-capturing methods is to (locally) add artificial viscosity to the solution, thereby suppressing the unwanted oscillations [39]. The first approach for eliminating such spurious oscillations in Finite-Element methods was to employ the SUPG formulation [15]. As such, the subsequent approaches for discontinuity-capturing introduce their stabilisation (discontinuity-capturing) operator in a similar manner. For instance, [40] uses the so-called $YZ\beta$ shock capturing approach which is a residual-driven operator introduced in [41]. Moreover, the works in [35] proposed a discontinuity-capturing framework that employs the Variational Multiscale analysis in combination with the Variational Entropy theory [42]. This proposed discontinuity-capturing method employs a residual-based approach whereby Variational Entropy viscosity (artificial viscosity) is introduced in the discrete solution in the regions where the conservation of Variational Entropy is violated. While this concept of discontinuity-capturing is a compelling topic to explore, it falls out of the scope of the present study.

The vast majority of the aforementioned applied examples of the multiscale theory focus on methods such as (low order) Finite-elements or Isogeometric analysis. The present study, on the other hand, addresses the incorporation/extension of the VMS into the high-order mimetic SEM. The exact approach for achieving this extension is described in the subsequent chapters.

5

Linear problems

This chapter presents the work carried out on applying the hybrid mimetic discretisation technique and multiscale theory on 1D linear advection problems. Firstly, Section 5.1 addresses the approach for discretising and incorporating multiscale theory for the steady advection-diffusion problem where the results of the numerical experiments performed are presented at the end of the section. Subsequently, Section 5.2 presents similar discussions for the unsteady case wherein both parabolic and hyperbolic cases are considered.

5.1. 1D steady advection-diffusion

The steady advection-diffusion equation is one of the simplest model equations exhibiting advection and diffusion phenomenon, as suggested by the name. For the considered 1D case, the governing equation is characterised as a linear second-order boundary value problem which reads:

$$c\frac{\partial u}{\partial x} - \nu\frac{\partial^2 u}{\partial x^2} = f, \qquad x \in \Omega \in [0,1] \tag{5.1}$$

$$u(0) = u(1) = 0, \tag{5.2}$$

where c and ν are positive constants representing the advection speed and diffusion coefficient respectively, and f is some given real-valued function acting as a source term. For the test cases considered in this section, f is taken to be a constant function equal to 1. Moreover, the considered problem is subject to homogeneous Dirichlet boundary conditions as highlighted by Equation (5.2), for which the exact solution with $f = 1$ can be found to be:

$$u_{exact}(x) = -\frac{-e^{\frac{c}{\nu}}x + x + e^{\frac{c}{\nu}x} - 1}{c\left(e^{\frac{c}{\nu}} - 1\right)}. \tag{5.3}$$

The second-order boundary value problem in Equation (5.1) can be expressed as two first-order equations by defining a new quantity q as follows:

$$q - \frac{\partial u}{\partial x} = 0 \tag{5.4}$$

$$c\frac{\partial u}{\partial x} - \nu\frac{\partial q}{\partial x} = f. \tag{5.5}$$

This reformulation yields the mixed formulation of Equation (5.1) which will be used in the subsequent subsection alongside Equation (5.1) itself. In Section 5.1.1, the model equation is reformulated at the continuous level by expressing it in a weak form. Thereafter, the equation is discretised using the mimetic framework in Section 5.1.2 and the numerical tests of the scheme are presented in Section 5.1.3. Subsequently, the integration of multiscale theory and its results are presented in Section 5.1.4 and Section 5.1.5 respectively.

5.1.1. Continuous form

To derive the weak form, it is convenient to consider the mixed formulation through which the geometric representation of the physical quantities can be more easily recognised. Equation (5.4) states that q is the derivative of u, where if u is expressed as a *0-form* ($u \in \Lambda^{(0)}(\boldsymbol{\mathcal{M}})$) then q must be a *1-form* ($q \in \Lambda^{(1)}(\boldsymbol{\mathcal{M}})$).

Employing this representation, the Galerkin weak form of Equation (5.4) is found by testing the equation with $\eta^{(1)}$ as follows:

$$\int_\Omega q^{(1)} \wedge \star\, \eta^{(1)} - \int_\Omega \mathrm{d}u^{(0)} \wedge \star\, \eta^{(1)} = 0, \qquad \forall \eta^{(1)} \in \Lambda^{(1)}(\boldsymbol{\mathcal{M}}) \tag{5.6}$$

Subsequently, the (Galerkin) weak form of Equation (5.5) is found by testing the equation with $v^{(0)}$. Note, however, that the exterior derivative of the *1-form* q does not exist in 1D. Thus the exterior derivative is moved to the test function which yields the adjoint operator where the additional emerging boundary terms are ignored given the *essential* boundary conditions in Equation (5.2).

$$c \int_\Omega \mathrm{d}u^{(0)} \wedge \star\, v^{(0)} + \nu \int_\Omega q^{(1)} \wedge \star\, \mathrm{d}v^{(0)} = \int_\Omega f^{(0)} \wedge \star\, v^{(0)}, \qquad \forall v^{(0)} \in \Lambda^{(0)}(\boldsymbol{\mathcal{M}}) \tag{5.7}$$

Alternatively, one can derive the Galerkin weak form by directly testing Equation (5.1) with test function $v^{(0)}$ which gives:

$$\int_\Omega \mathscr{L} u^{(0)} \wedge \star\, v^{(0)} = \int_\Omega f^{(0)} \wedge \star\, v^{(0)}, \qquad \forall v^{(0)} \in \Lambda^{(0)}(\boldsymbol{\mathcal{M}}), \quad \text{with } \mathscr{L} := c\frac{\partial}{\partial x} - \nu\frac{\partial^2}{\partial x^2}. \tag{5.8}$$

For this direct approach, the advection term simply involves taking the derivative of $u^{(0)}$ by applying the exterior derivative. The diffusion term on the other hand requires the exterior derivative to be applied twice on $u^{(0)}$ which is not possible. Thus, the derivative is once again moved to the test function and boundary terms are ignored given the essential boundary conditions.

$$c \int_\Omega \mathrm{d}u^{(0)} \wedge \star\, v^{(0)} + \nu \int_\Omega \mathrm{d}u^{(0)} \wedge \star\, \mathrm{d}v^{(0)} = \int_\Omega f^{(0)} \wedge \star\, v^{(0)} \tag{5.9}$$

The two approaches for deriving the weak form inevitably lead to expressions that are mathematically identical. This fact is reiterated in the subsequent subsection where the weak forms are discretised.

5.1.2. Discrete form

With the weak forms derived in the previous subsection, the discrete algebraic system can be derived by substituting the respective continuous *k-forms* for their discrete representations shown below:

$$u_h := \boldsymbol{\psi}^{(0)}\boldsymbol{u}, \quad \in \Lambda_h^{(0)}(\boldsymbol{\mathcal{M}}) \tag{5.10}$$
$$q_h := \boldsymbol{\psi}^{(1)}\boldsymbol{q}, \quad \in \Lambda_h^{(1)}(\boldsymbol{\mathcal{M}}) \tag{5.11}$$
$$f_h := \boldsymbol{\psi}^{(0)}\boldsymbol{f}, \quad \in \Lambda_h^{(0)}(\boldsymbol{\mathcal{M}}) \tag{5.12}$$
$$v_h := \boldsymbol{\psi}^{(0)}\boldsymbol{v}, \quad \in \Lambda_h^{(0)}(\boldsymbol{\mathcal{M}}) \tag{5.13}$$
$$\eta_h := \boldsymbol{\psi}^{(1)}\boldsymbol{\eta}, \quad \in \Lambda_h^{(0)}(\boldsymbol{\mathcal{M}}) \tag{5.14}$$

Starting with the weak form of the mixed formulation, the discrete algebraic system of Equation (5.6) reads:

$$\boldsymbol{\eta}^T \left[\int_{\Omega_h} \boldsymbol{\psi}^{(1)^T}\boldsymbol{\psi}^{(1)}\,\mathrm{d}\Omega_h\right] \boldsymbol{q} - \boldsymbol{\eta}^T \left[\int_{\Omega_h} \boldsymbol{\psi}^{(1)^T}\boldsymbol{\psi}^{(1)}\,\mathrm{d}\Omega_h\right] \mathbb{E}^{1,0}\boldsymbol{u} = 0 \tag{5.15}$$

$$\mathbb{M}^{(1)}\boldsymbol{q} - \mathbb{M}^{(1)}\mathbb{E}^{1,0}\boldsymbol{u} = 0. \tag{5.16}$$

Similarly the discrete system for Equation (5.7) reads:

$$c\,\boldsymbol{v}^T \left[\int_{\Omega_h} \boldsymbol{\psi}^{(0)^T}\boldsymbol{\psi}^{(1)}\,\mathrm{d}\Omega_h\right] \mathbb{E}^{1,0}\boldsymbol{u} + \nu\,\boldsymbol{v}^T\mathbb{E}^{1,0^T} \left[\int_{\Omega_h} \boldsymbol{\psi}^{(1)^T}\boldsymbol{\psi}^{(1)}\,\mathrm{d}\Omega_h\right] \boldsymbol{q} = \boldsymbol{v}^T \left[\int_{\Omega_h} \boldsymbol{\psi}^{(0)^T}\boldsymbol{\psi}^{(0)}\,\mathrm{d}\Omega_h\right] \boldsymbol{f} \tag{5.17}$$

$$c\,\mathbb{M}^{(0,1)}\mathbb{E}^{1,0}\boldsymbol{u} + \nu\,\mathbb{E}^{1,0^T}\mathbb{M}^{(1)}\boldsymbol{q} = \mathbb{M}^{(0)}\boldsymbol{f}. \tag{5.18}$$

The two discrete systems in Equation (5.16) and Equation (5.18) can be combined together in a matrix form as follows:

$$\begin{bmatrix} \mathbb{M}^{(1)} & -\mathbb{M}^{(1)}\mathbb{E}^{1,0} \\ \nu\,\mathbb{E}^{1,0^T}\mathbb{M}^{(1)} & c\,\mathbb{M}^{(0,1)}\mathbb{E}^{1,0} \end{bmatrix} \begin{bmatrix} \boldsymbol{q} \\ \boldsymbol{u} \end{bmatrix} = \begin{bmatrix} \boldsymbol{0} \\ \mathbb{M}^{(0)}\boldsymbol{f} \end{bmatrix}. \tag{5.19}$$

Employing the same substitution approach for Equation (5.9) gives:

$$c\,\boldsymbol{v}^T \left[\int_{\Omega_h} \boldsymbol{\psi}^{(0)^T}\boldsymbol{\psi}^{(1)}\,\mathrm{d}\Omega_h\right] \mathbb{E}^{1,0}\boldsymbol{u} + \nu\,\boldsymbol{v}^T\mathbb{E}^{1,0^T} \left[\int_{\Omega_h} \boldsymbol{\psi}^{(1)^T}\boldsymbol{\psi}^{(1)}\,\mathrm{d}\Omega_h\right] \mathbb{E}^{1,0}\boldsymbol{u} = \boldsymbol{v}^T \left[\int_{\Omega_h} \boldsymbol{\psi}^{(0)^T}\boldsymbol{\psi}^{(0)}\,\mathrm{d}\Omega_h\right] \boldsymbol{f} \tag{5.20}$$

$$c\,\mathbb{M}^{(0,1)}\mathbb{E}^{1,0}\boldsymbol{u} + \nu\,\mathbb{E}^{1,0^T}\mathbb{M}^{(1)}\mathbb{E}^{1,0}\boldsymbol{u} = \mathbb{M}^{(0)}\boldsymbol{f}. \tag{5.21}$$

One can easily recognise the equivalence between Equation (5.19) and Equation (5.21) where term $\mathbb{E}^{1,0}\boldsymbol{u}$ in the diffusion term has been treated separately as q in the mixed formulation[1]. On a more intriguing note, the nature of the advection and diffusion operators can be assessed by considering their constituent matrices. The advection term comprises of the incidence matrix $\mathbb{E}^{1,0}$ along with the matrix $\mathbb{M}^{(0,1)}$. As discussed in Section 3.3 the $\mathbb{E}^{1,0}$ incidence matrix is the discrete exterior derivative and is a topological operator. On the other hand, the $\mathbb{M}^{(0,1)}$ matrix is constructed via the L^2 inner product of the *0-form* basis and the *1-form* basis:

$$\mathbb{M}^{(0,1)} := \left[\int_{\Omega_h} \boldsymbol{\psi}^{(0)^T} \boldsymbol{\psi}^{(1)} \, \mathrm{d}\Omega_h\right]. \tag{5.22}$$

Since both the bases are defined on a reference domain $\xi \in [-1, 1]$, the above integral reads as follows when transformed to the physical domain using the concepts described in Section 3.5:

$$\mathbb{M}^{(0,1)} := \left[\int_{\Omega_h} \boldsymbol{\psi}^{(0)^T}(\xi(x)) \frac{1}{\cancel{J}} \boldsymbol{\psi}^{(1)}(\xi(x)) \cancel{J} \mathrm{d}\xi\right]. \tag{5.23}$$

As the *1-form* basis involves the derivative of the *0-form* basis, it needs to be scaled by the inverse Jacobian of the transformation ($\frac{1}{J}$) when expressing it in physical coordinates (x). Similarly, the integral must also be scaled, not by the inverse but by the Jacobian itself. This then leads to the cancellation of the Jacobian term from the integral. This cancellation means that the matrix $\mathbb{M}^{(0,1)}$ is unaffected by the stretching of the physical domain. Therefore, it can be concluded that this matrix is metric-independent much like the incidence matrix. For the diffusion term, on the other hand, the operators include the incidence matrices on the primal and dual which are metric independent, along with the discrete metric-dependent Hodge operator in the form of the *1-form* mass matrix $\mathbb{M}^{(1)}$. The sequence of applying the said operators for the advection and diffusion terms can be visually summarised by considering the path followed in the De Rham sequence shown in Figure 5.1.

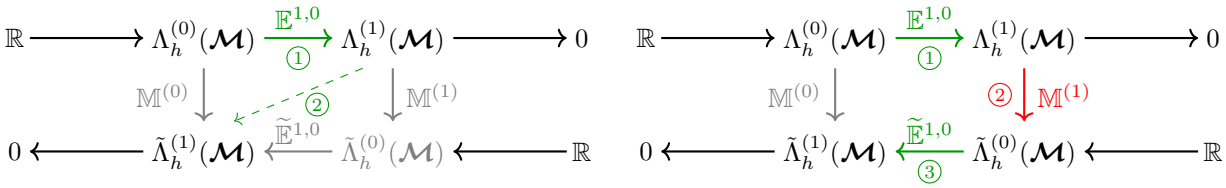

(a) Advection operator

(b) Diffusion operator

Figure 5.1: The path followed in the discrete De Rham sequence for advection and diffusion terms for the steady advection-diffusion problem

The green links shown in Figure 5.1 are metric-free mappings whereas the red links are metric-dependent. Looking at Figure 5.1a, the advection operator consists of an initial mapping of the *0-form* u to a *1-form*, followed by a projection to the dual *1-form*. The diffusion operator also initially maps u from a *0-form* to a *1-form*, then maps the *1-form* to its dual *0-form*, and finally maps the solution to the dual *1-form*.

Thus far, the discrete systems in Equation (5.19) and Equation (5.21) have been derived for individual elements. To impose element-wise continuity and the essential Dirichlet boundary conditions, Lagrange multipliers $\boldsymbol{\lambda}$ are introduced as discussed in Section 3.5. For the example 1D mesh shown in Figure 3.11, the constraints read:

$$\begin{aligned} u_0 &= 0 \\ u_3 - u_2 &= 0 \\ u_6 - u_5 &= 0 \\ u_8 &= 0, \end{aligned} \tag{5.24}$$

which reads as follows when expressed in a matrix form:

$$\mathbb{E}^{\lambda,0}\boldsymbol{u} = 0. \tag{5.25}$$

Here $\mathbb{E}^{\lambda,0}$ is a topological operator containing ± 1 that enforces the desired constraint which has the following structure for the mesh in Figure 3.11:

$$\mathbb{E}^{\lambda,0} = \begin{bmatrix} 1 & 0 & 0 & 0 & 0 & 0 & 0 & 0 & 0 \\ 0 & 0 & -1 & 1 & 0 & 0 & 0 & 0 & 0 \\ 0 & 0 & 0 & 0 & 0 & -1 & 1 & 0 & 0 \\ 0 & 0 & 0 & 0 & 0 & 0 & 0 & 0 & 1 \end{bmatrix}. \tag{5.26}$$

[1] Both discrete systems are mathematically equivalent, and the experiments in the subsequent subsection employ the form in Equation (5.21)

Both systems in Equation (5.19) and Equation (5.21) can be expressed as a generic linear system in the form of $\boldsymbol{A}\hat{\boldsymbol{u}} = \hat{\boldsymbol{f}}$, and adding the constraint to the system through the Lagrange multipliers yields the following:

$$\boldsymbol{A}\hat{\boldsymbol{u}} + \mathbb{E}^{\lambda,0^T}\boldsymbol{\lambda} = \hat{\boldsymbol{f}} \tag{5.27}$$

$$\mathbb{E}^{\lambda,0}\hat{\boldsymbol{u}} = 0 \tag{5.28}$$

$$\begin{bmatrix} \boldsymbol{A} & \mathbb{E}^{\lambda,0^T} \\ \mathbb{E}^{\lambda,0} & \varnothing \end{bmatrix} \begin{bmatrix} \hat{\boldsymbol{u}} \\ \boldsymbol{\lambda} \end{bmatrix} = \begin{bmatrix} \hat{\boldsymbol{f}} \\ \boldsymbol{0} \end{bmatrix}. \tag{5.29}$$

The Lagrange multipliers are additional degrees of freedom which undoubtedly increases the size of the linear system, thereby increasing the cost of the computation. However, these Lagrange multipliers do carry a physical meaning which can thus give some additional information about the numerical solution. To obtain the physical representation of $\boldsymbol{\lambda}$, consider Equation (5.21) in its complete form where the boundary terms are not excluded:

$$c\,\mathbb{M}^{(0,1)}\mathbb{E}^{1,0}\boldsymbol{u} + \nu\,\mathbb{E}^{1,0^T}\mathbb{M}^{(1)}\mathbb{E}^{1,0}\boldsymbol{u} - \nu\,\mathbb{N}_1\mathbb{B}\,\mathbb{E}^{1,0}\boldsymbol{u} = \mathbb{M}^{(0)}\boldsymbol{f}. \tag{5.30}$$

Here, $\mathbb{N}_1$ is the discrete trace operator introduced in Equation (3.28) and $\mathbb{B}$ is a sampling matrix which returns the gradient of the solution times the test function value at the element boundaries when applied to $\mathbb{E}^{1,0}\boldsymbol{u}$. Given that the test function's value at the element boundaries is simply 1, the boundary term solely comprises the diffusive flux $\left(\nu\dfrac{\partial u}{\partial x}\right)$. Furthermore, it can be noted that the manner by which the Lagrange multipliers are introduced in Equation (5.27) is reminiscent of this boundary term. Therefore, the Lagrange multipliers' physical representation is found to be the diffusive flux.

5.1.3. Numerical experiments

With the discrete system in place, a set of numerical experiments were carried out and their results are presented in this subsection. All the cases considered have the same problem setup with the advection speed $c = 1$, the aforementioned source term of $f = 1$, and diffusion coefficient $\nu = 0.01$ with the exception of the convergence tests where a value of $\nu = 0.025$ was used in order to improve the clarity of the figures. Before moving on to the results, it is worth noting that the solution that is being sought lives in the H_0^1 space. In other words, the exact solution and its derivative are square integrable in the domain. This fact implies that the best possible numerical (finite-dimensional) solution is the H_0^1 projection of the exact solution. The approach for obtaining this projection is described in Appendix .2, where the exact solution is given by Equation (5.3). All the results presented in this subsection are accompanied by this H_0^1 projection for comparison.

To start off, the derived algebraic system was first verified by comparing the numerical solution to the exact solution. The error of the numerical solution and of the H_0^1 projection with respect to the exact solution was computed in the L^2 and H^1 error norms for different mesh refinements using different polynomial degrees and number of elements. The corresponding error curves are shown in Figure 5.2 where the variation of the error is plotted against the number of degrees of freedom ($nDOF$) which includes the number of Lagrange multipliers.

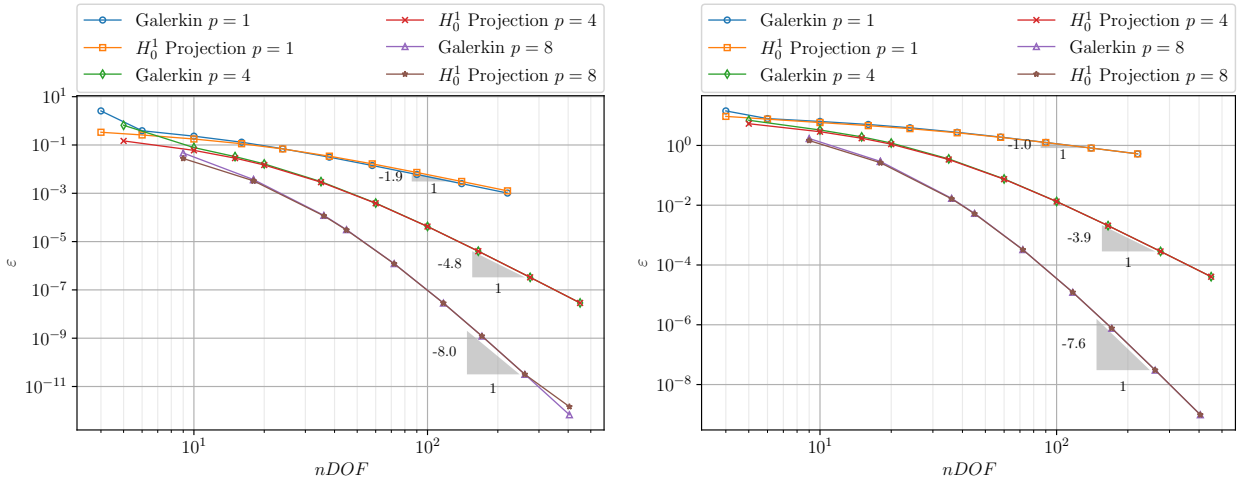

(a) h-convergence in the L^2 error norm

(b) h-convergence in the H^1 error norm

Figure 5.2: h-convergence of the Galerkin scheme and the H_0^1 Projection computed in the L^2 and H^1 error norms using the exact solution

It is observed that the slopes of the different curves in the range of large number of degrees of freedom are approximately one higher than the degree of the polynomial used in the discretisation when computing the error using the L^2 norm. There is the exception for the $p = 8$ case where the error reaches values in the order of 1×10^{-12} where round-off errors come into play before the slope is allowed to settle. This observed rate of convergence is in line with the expected rate wherein the L^2 error of an approximation using p^{th} degree polynomials converges at a rate of $p+1$. In the H^1 norm, however, the slopes of error curves are approximately the same as the degree of the polynomial. The reason for this slower rate of convergence in the H^1 error norm is attributed to the fact that the L^2 error of the derivative of the numerical solution decreases at p^{th} order given that the derivative of a polynomial of degree p, is a polynomial of degree $p-1$. Moreover, the absolute error values in the H^1 norm are considerably larger than the L^2 error which clearly indicates that the error in the gradient of the solution is the dominant error term.

On another note, it is evident that both the Galerkin scheme and the H_0^1 Projection behave very similarly when the mesh is highly refined. The difference between the two is more pronounced for particularly coarse meshes where the Galerkin scheme yields a poorer solution as compared to the H_0^1 Projection. To further assess the behaviour of the Galerkin scheme, the discrete solution and its derivative are plotted alongside the H_0^1 Projection and the exact solution for different mesh refinements in Figure 5.3 and Figure 5.4. Considering the behaviour of the Galerkin solution on coarse meshes shown in Figure 5.3a and Figure 5.3b, it is evident that the discrete solution has an oscillatory behaviour. This behaviour is attributed to the fact that the mesh is too coarse to capture the sharp layer of the solution around $x = 1$. Once the mesh is sufficiently refined to capture the sharp layer, the oscillations are greatly reduced and the solution closely follows the exact solution. In contrast to the Galerkin solution, the H_0^1 Projection yields an interpolant that closely follows the exact solution which is nodally exact for the $p = 1$ case and produces minor oscillations at the last element for larger degree polynomials.

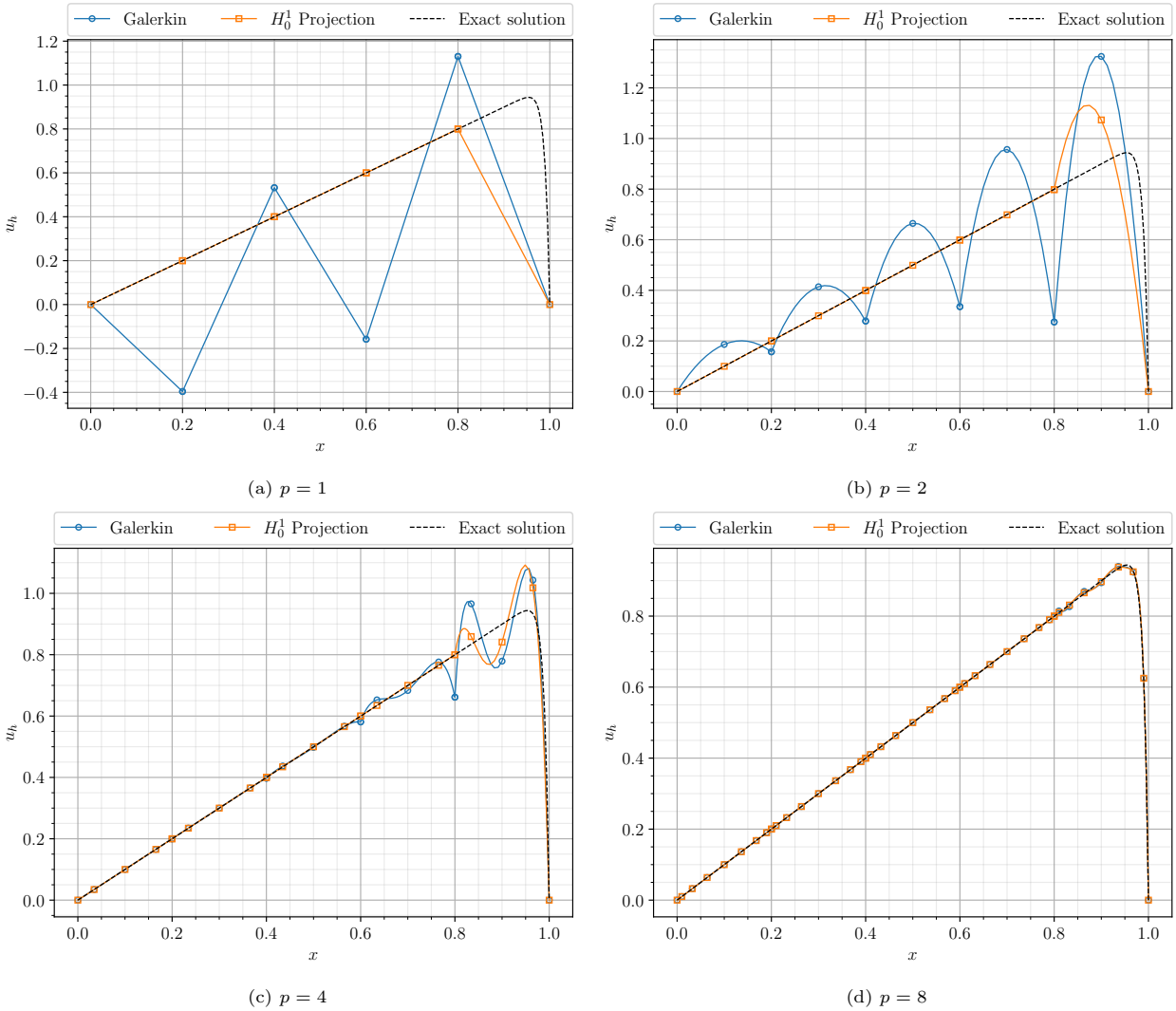

(a) $p = 1$

(b) $p = 2$

(c) $p = 4$

(d) $p = 8$

Figure 5.3: Solution to the steady advection-diffusion equation for different order polynomials with $N = 5$ uniform elements

Considering the derivative of the numerical solution, the source of the large errors in the H^1 norm becomes more apparent. As seen through Figure 5.4a, Figure 5.4b, and Figure 5.4c there is generally a large miss match between the derivative of the numerical and exact solutions. The first point to address is the discontinuous jumps in the solution gradient. This is attributed to the fact that the applied Lagrange multiplier approach for enforcing continuity only ensures C^0 continuity meaning that the solution is continuous but the derivatives are not. Secondly, the large gradient at $x = 1$ is something that both the Galerkin and H_0^1 Projection methods naturally fail to capture on coarse meshes. However, it can be noted that the H_0^1 Projection does smoothly capture the constant part of the solution gradient for all meshes while only producing a slight jump when transitioning to the final element. Lastly, given that the numerical schemes are consistent, both methods tend to closely approach the exact solution when sufficiently many degrees of freedom are used as apparent through Figure 5.3d and Figure 5.4d.

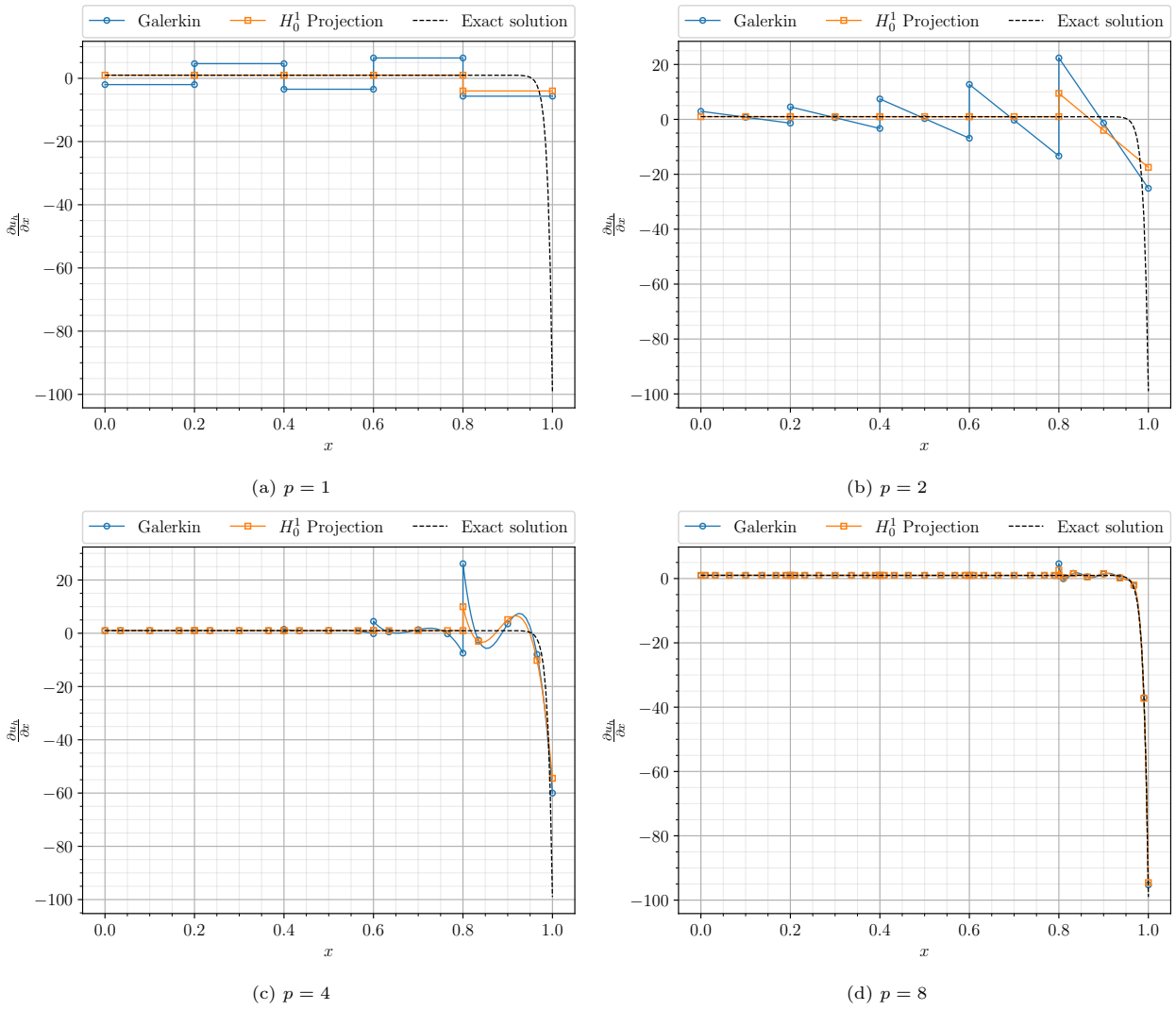

(a) $p = 1$ (b) $p = 2$

(c) $p = 4$ (d) $p = 8$

Figure 5.4: Derivative of the solution to the steady advection-diffusion for different order polynomials with $N = 5$ uniform elements

All things considered, the distinct differences in the coarse meshes between the Galerkin and the optimal H_0^1 Projection, suggest that the Galerkin scheme is sub-optimal. In order to improve the Galerkin solution in the said coarse meshes, one must account for the un-resolved components of the solution. The succeeding subsection describes the approach to do exactly that by employing multiscale theory.

5.1.4. Variational Multiscale

In order to incorporate multiscale theory into the Galerkin approach, consider the following multiscale split of the function spaces:

$$\Lambda^{(k)}(\boldsymbol{\mathcal{M}}) = \Lambda_h^{(k)}(\boldsymbol{\mathcal{M}}) \oplus \Lambda^{(k)'}(\boldsymbol{\mathcal{M}}) \tag{5.31}$$

$$u^{(k)} = u_h + u' \tag{5.32}$$

$$v^{(k)} = v_h + v', \tag{5.33}$$

where $\Lambda_h^{(k)}(\boldsymbol{\mathcal{M}})$ is the finite-dimensional resolved space and $\Lambda^{(k)'}(\boldsymbol{\mathcal{M}})$ is the infinite-dimensional un-resolved space. Plugging this split into Equation (5.8) gives:

$$\int_\Omega \mathscr{L}(u_h + u') \wedge \star\,(v_h + v') = \int_\Omega f^{(0)} \wedge \star\,(v_h + v'), \tag{5.34}$$

which simplifies to the following given the linearity of $\mathscr{L}$:

$$\int_\Omega \mathscr{L}u_h \wedge \star\,(v_h + v') + \int_\Omega \mathscr{L}u' \wedge \star\,(v_h + v') = \int_\Omega f^{(0)} \wedge \star\,(v_h + v'). \tag{5.35}$$

Using the linear independence of the resolved and un-resolved function spaces, the resolved scale equation can be derived by setting $v' = 0$ which gives:

$$\int_\Omega \mathscr{L}u_h \wedge \star\, v_h + \int_\Omega \mathscr{L}u' \wedge \star\, v_h = \int_\Omega f^{(0)} \wedge \star\, v_h. \tag{5.36}$$

It is more convenient to move the linear operator to the test function instead of applying it to u'. By moving the operator to the test function the adjoint operator is introduced where the emerging boundary terms involving the boundary evaluation of u' are neglected given that the essential Dirichlet boundary conditions in Equation (5.2) result in $u' = 0$ at the (domain) boundaries. The resulting resolved scale equation is thus:

$$\int_\Omega \mathscr{L}u_h \wedge \star\, v_h + \int_\Omega u' \wedge \star\, \tilde{\mathscr{L}} v_h = \int_\Omega f^{(0)} \wedge \star\, v_h, \qquad \text{where } \tilde{\mathscr{L}} := -c\frac{\partial}{\partial x} - \nu\frac{\partial^2}{\partial x^2}. \tag{5.37}$$

In a similar manner, the un-resolved scale equation is derived by setting $v_h = 0$ and then applying the adjoint operator where the boundary evaluation of u' is again neglected. The un-resolved scale equation is thus given by:

$$\int_\Omega \mathscr{L}u_h \wedge \star\, v' + \int_\Omega \mathscr{L}u' \wedge \star\, v' = \int_\Omega f^{(0)} \wedge \star\, v' \tag{5.38}$$

$$\int_\Omega \mathscr{L}u' \wedge \star\, v' = -\int_\Omega \left(\mathscr{L}u_h - f^{(0)}\right) \wedge \star\, v' \tag{5.39}$$

$$\int_\Omega \mathscr{L}u' \wedge \star\, v' = -\int_\Omega \mathscr{R}u_h \wedge \star\, v' \tag{5.40}$$

$$\int_\Omega u' \wedge \star\, \tilde{\mathscr{L}} v' = -\int_\Omega \mathscr{R}u_h \wedge \star\, v', \tag{5.41}$$

where $\mathscr{R}u_h$ is the residual of the resolved equation. Naturally, the un-resolved scale problem is a global problem as can be seen through Equation (5.41) where the integral spans the entire domain Ω. In order to simplify this global problem into a problem that is more practical to implement, an approximation is applied where u' is assumed to be zero at the element boundaries. This approximation step reduces the global un-resolved scale problem into a local problem in each element at the cost of only obtaining an estimate of u' over each element. Applying the said simplification can be seen as selecting the H^1 projector as the scale separation projector. This means that the multiscale solution must coincide with the H^1 Projection of the exact solution provided the correct u' is obtained. Obtaining the correct u' for arbitrary cases (arbitrary basis functions for example) is by no means a straightforward approach to generalise. Nonetheless, a generalised approach for obtaining an approximate u' by solving the local un-resolved scale problem in Equation (5.41) is presented in this section.

To solve the local problem for u', the elements Greens' function $g_e(x, s)$ is computed as follows:

$$\tilde{\mathscr{L}} g_e(x, s) = \delta(x - s), \qquad x \in \Omega_e \tag{5.42}$$

$$g_e(x, s) = 0, \qquad x \in \partial\Omega_e \tag{5.43}$$

The imposed homogeneous Dirichlet boundary condition on $g_e(x,s)$ follows from the approximation where $u'=0$ at the element boundaries. The exact element Greens' function can be computed analytically for the linear advection-diffusion operator which reads:

$$g_e(x,s) = \begin{cases} C_1(s)\left(1-e^{-2\alpha\frac{x}{h}}\right), & x \leq s \\ C_2(s)\left(e^{-2\alpha\frac{x}{h}}-e^{-2\alpha}\right), & x \geq s \end{cases} \tag{5.44}$$

$$C_1(s) = \frac{1-e^{-2\alpha\left(1-\frac{s}{h}\right)}}{c\left(1-e^{-2\alpha}\right)} \tag{5.45}$$

$$C_2(s) = \frac{e^{2\alpha\frac{s}{h}}-1}{c\left(1-e^{-2\alpha}\right)} \tag{5.46}$$

$$\alpha = \frac{ch}{2\nu}, \tag{5.47}$$

where, h is the element width and α is the element Péclet number. Substituting this elements Greens' function as the test function into Equation (5.41) ($v' = g_e(x,s)$) yields the following integral expression for u':

$$u'(x) = -\int_{\Omega_e} g_e(x,s)\mathscr{R}u_h \, \mathrm{d}s. \tag{5.48}$$

The above equation is capable of returning the point-wise estimate of u', however, as discussed in Section 4.1.3, Finite/Spectral element methods only deal with Sobolev spaces where pointwise values are not required as apparent through Equation (5.37) where u' only appears as a weighted integral. As such, u' only needs to be correct in an integral sense. For *piecewise linear* ($p=1$) basis functions, most commonly used in Finite-Element methods, u' only needs to be a constant given that the advection-diffusion operator applied to a polynomial of degree one is a constant function. This constant approximation for u' is found by computing the 0^{th} moment of the element Greens' function, τ, and multiplying it with the residual.

$$\tau = \frac{1}{h}\int_{\Omega_e}\int_{\Omega_e} g_e(x,s)\,\mathrm{d}x\mathrm{d}s \tag{5.49}$$

$$\tau = \frac{h}{2c}\left(\coth(\alpha) - \frac{1}{\alpha}\right) \tag{5.50}$$

$$u' \approx -\tau\mathscr{R}u_h \tag{5.51}$$

This is a common approach employed for obtaining the estimate u' for many cases in the literature. In the results that follow in the subsequent subsection, this approach is referred to as the 'Classical VMS'.

While this element-averaged approach is elegant, it does not generalise to arbitrary high-ordered basis functions. The definition of τ must be adjusted in order to generalise this form for obtaining u' in Equation (5.51). To arrive at a new definition for τ for the generalised case, consider the following approach where the inverse adjoint linear operator is applied to Equation (5.42) [30]:

$$\tilde{\mathscr{L}}^{-1}\tilde{\mathscr{L}}g_e(x,s) = \tilde{\mathscr{L}}^{-1}\delta(x-s) \tag{5.52}$$

$$g_e(x,s) = \tilde{\mathscr{L}}^{-1}\delta(x-s). \tag{5.53}$$

Now applying the assumption that the inverse adjoint operator can be expressed as a polynomial $\tau(x,s)$:

$$g_e(x,s) \approx \tau(x,s)\,\delta(x-s) \tag{5.54}$$

$$\int_{\Omega_e} g_e(x,s)\,\mathrm{d}s \approx \tau(x). \tag{5.55}$$

Considering the polynomial $\tau(x)$ to be expressed using the *1-form* edge basis functions $e_i(x)$ over each of the N elements yields the following definition for $\tau(x)$.

$$\tau(x) := \sum_{k=0}^{N}\sum_{i=1}^{p}\tau_i^k e_i^k(x), \tag{5.56}$$

$$\tau_i^k := \int_{x_{i-1}^k}^{x_i^k}\int_0^{h^k} g(x,s)\,\mathrm{d}s\mathrm{d}x \tag{5.57}$$

The expression for u' can then be written in the same form as Equation (5.51) using this new definition of $\tau(x)$,

$$u' \approx -\tau(x)\mathscr{R}u_h. \tag{5.58}$$

If this new generalised approach is applied to the $p = 1$ case, one arrives back to the element averaged Greens' function estimate. This is due to the fact that the expansion coefficients τ_i^k simply becomes the integral of the Greens' function over the entire element, and the sole edge basis for $p = 1$ is a constant function $e_1(x) = \frac{1}{h}$.

Employing the same degrees of freedom as the classical SEM case, the resolved scale equation becomes:

$$\underbrace{\int_\Omega \mathscr{L} u_h \wedge \star\, v_h}_{\boldsymbol{Au}} + \underbrace{\int_\Omega (-\tau \mathscr{R}_h u_h) \wedge \star\, \tilde{\mathscr{L}} v_h}_{\text{Multiscale term}} = \underbrace{\int_\Omega f_h \wedge \star\, v_h}_{\hat{\boldsymbol{f}}}. \tag{5.59}$$

The discrete form of the operator $\mathscr{L}$ is represented by $\boldsymbol{A}$, and its adjoint or dual operator ($\tilde{\mathscr{L}}$) can be proven to be $-\boldsymbol{A}^T$. The discrete equation is then given by:

$$\boldsymbol{Au} + \boldsymbol{A}^T \boldsymbol{\tau} \mathscr{R}_h u_h = \hat{\boldsymbol{f}}, \tag{5.60}$$

where $\boldsymbol{\tau}$ is a diagonal matrix containing the evaluation of the polynomial in Equation (5.56) at the Gauss-Lobatto integration nodes and $\mathscr{R}_h$ is the discrete residual operator. This residual operator takes the form:

$$\mathscr{R}_h u_h = \boldsymbol{\psi}^{(1)}(\boldsymbol{x}) \left(c\, \mathbb{E}^{1,0}\right) - \boldsymbol{\psi}^{(0)}(\boldsymbol{x}) \mathbb{M}^{(0)^{-1}} \left(\nu \left(-\mathbb{E}^{1,0^T} \mathbb{M}^{(1)} + \mathbb{N}_1 \mathbb{B}\right) \mathbb{E}^{1,0}\right) \boldsymbol{u} - \boldsymbol{f}, \tag{5.61}$$

where $\boldsymbol{\psi}^{(0)}(\boldsymbol{x})$ and $\boldsymbol{\psi}^{(1)}(\boldsymbol{x})$ are matrices containing the evaluation of the *0-form* and the *1-form* basis functions respectively at the Gauss-Lobatto integration points ($\boldsymbol{x}$). It is important to note that the solution at boundaries is not driven by PDE, hence, evaluating the residual at the boundaries is not sensible. Thus, the residual must be forced to zero at the boundaries. This, however, is not possible for the $p = 1$ case as the residual will be a constant function over each element. If the residual is set to zero for this case, it would be zero throughout the element thereby negating the effect of the VMS. For $p > 1$ on the other hand, it is possible to force this zero residual value at the domain boundaries and the presented implementation does employ this concept. Noting this and bringing everything together into a single system yields:

$$\left(\boldsymbol{A} + \boldsymbol{A}^T \boldsymbol{\tau} \underbrace{\left(\boldsymbol{\psi}^{(1)}(\boldsymbol{x}) \left(c\, \mathbb{E}^{1,0}\right) - \boldsymbol{\psi}^{(0)}(\boldsymbol{x}) \mathbb{M}^{(0)^{-1}} \left(\nu \left(-\mathbb{E}^{1,0^T} \mathbb{M}^{(1)} + \mathbb{N}\right) \mathbb{E}^{1,0}\right)\right)}_{\boldsymbol{\mathcal{R}}}\right) \boldsymbol{u} = \hat{\boldsymbol{f}} + \boldsymbol{A}^T \boldsymbol{\tau} \boldsymbol{f} \tag{5.62}$$

$$\left(\boldsymbol{A} + \boldsymbol{A}^T \boldsymbol{\tau} \boldsymbol{\mathcal{R}}\right) \boldsymbol{u} = \hat{\boldsymbol{f}} + \boldsymbol{A}^T \boldsymbol{\tau} \boldsymbol{f}. \tag{5.63}$$

Using the previously described Lagrange multiplier approach to enforce continuity and boundary conditions gives:

$$\begin{bmatrix} \boldsymbol{A} + \boldsymbol{A}^T \boldsymbol{\tau} \boldsymbol{\mathcal{R}} & \mathbb{E}^{\lambda,0^T} \\ \mathbb{E}^{\lambda,0} & \varnothing \end{bmatrix} \begin{bmatrix} \boldsymbol{u} \\ \boldsymbol{\lambda} \end{bmatrix} = \begin{bmatrix} \hat{\boldsymbol{f}} + \boldsymbol{A}^T \boldsymbol{\tau} \boldsymbol{f} \\ \boldsymbol{0} \end{bmatrix}. \tag{5.64}$$

Comparing this system to the base Galerkin method, it is clear that the VMS simply introduces additional terms to the left and right-hand sides of the linear system. Moreover, these additional terms do not change the number of degrees of freedom being solved which adds no significant additional costs (apart from the evaluation of the additional terms) for solving when compared with the Galerkin method.

5.1.5. Numerical experiments with VMS

The solutions obtained using the derived VMS approaches are plotted in Figure 5.5 and Figure 5.6 alongside the base Galerkin solution and the H_0^1 Projection for different degree polynomials. Considering the solution corresponding to $p = 1$ in Figure 5.5a, it is observed that both the Classical and High-order VMS solutions exactly coincide with the optimal H_0^1 projection. This is due to the fact that the constant u' estimate provided by the element averaged Greens' function captures just the essential component of the exact u' to produce the correct weighted integral of u' in the resolved scale equation. The observation also confirms the fact that the Classical VMS and the new proposed High-order VMS do indeed equate to one another for the $p = 1$ case.

For larger p, the Classical VMS behaves rather poorly by being too diffusive as apparent though Figure 5.5b, Figure 5.5c, and Figure 5.5d. The general behaviour of the Classical VMS solution is that it behaves fairly similar to the High-order VMS and the H_0^1 Projection in the linear regime, however, it tends to fall short to capture the sharp gradient at $x = 1$ even when sufficiently refined. The reason the Classical VMS behaves so poorly for $p > 1$ is due to the invalid assumption of u' being constant over each element. This leads to the Classical VMS being inconsistent for $p > 1$. In contrast, the High-order VMS closely follows the exact solution and behaves similarly to the H_0^1 Projection although it is no longer exact as for the $p = 1$ case. The addition

of the High-order VMS also shows its effect in the solution gradient prediction as seen in Figure 5.6. The close likeness between the High-order VMS and the H_0^1 Projection results in the two solutions behaving in a very similar manner.

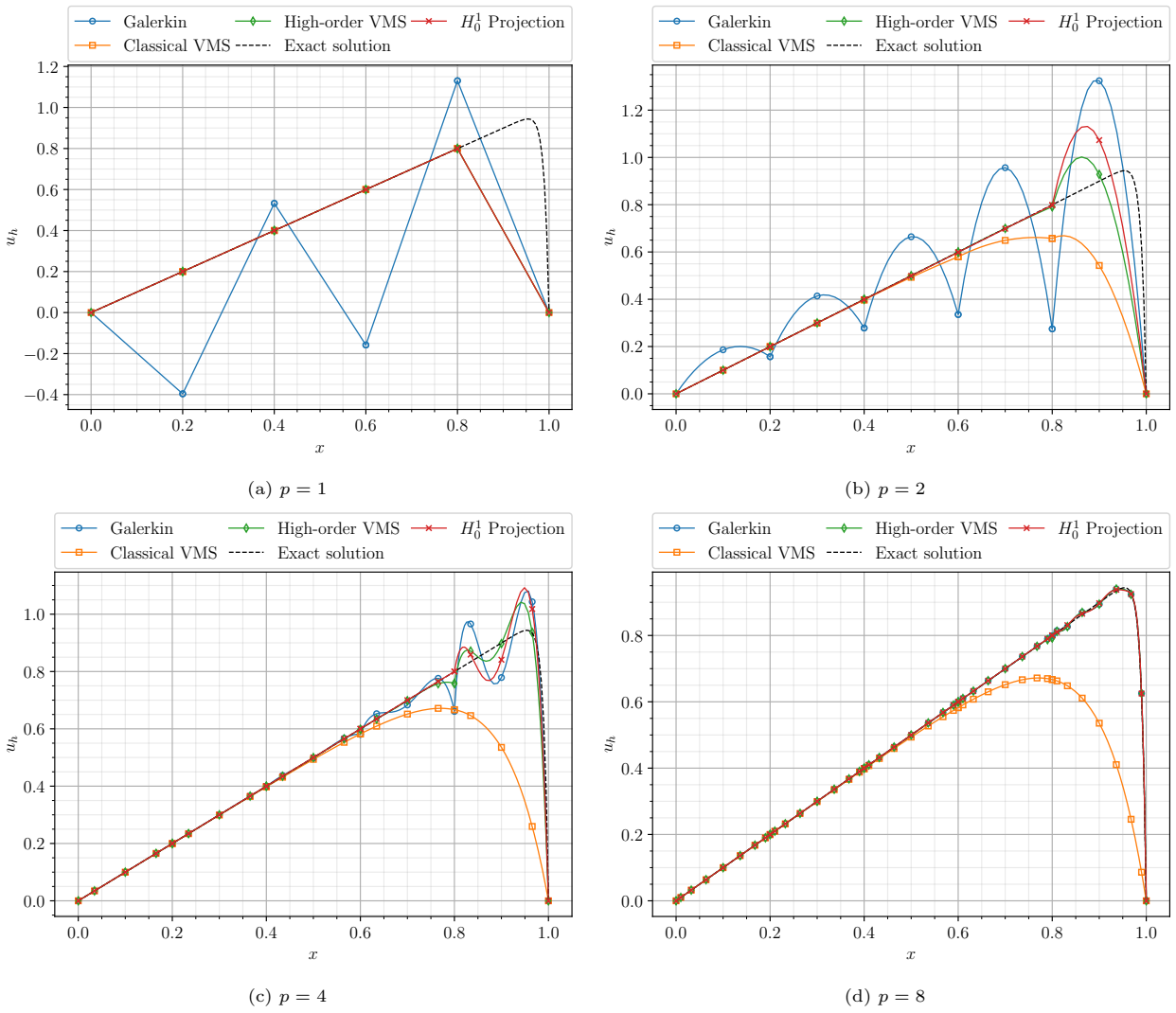

(a) $p = 1$

(b) $p = 2$

(c) $p = 4$

(d) $p = 8$

Figure 5.5: Solution to the steady advection-diffusion using the Galerkin and multiscale formulation for different order polynomials with $N = 5$ uniform elements

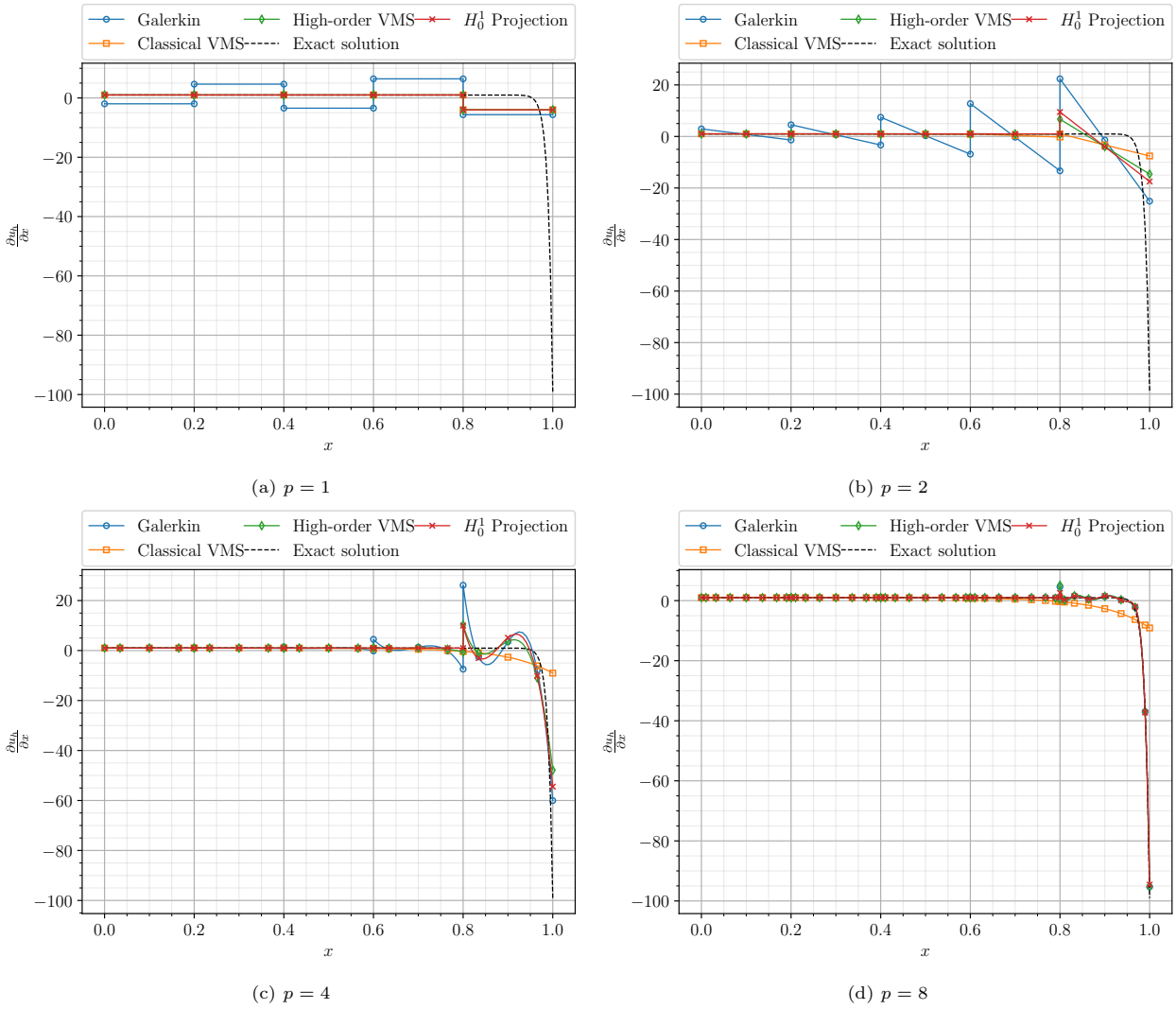

(a) $p = 1$

(b) $p = 2$

(c) $p = 4$

(d) $p = 8$

Figure 5.6: Derivative of the solution to the steady advection-diffusion using the Galerkin and multiscale formulation for different order polynomials with $N = 5$ uniform elements

The reason for the High-order VMS no longer coinciding with the H_0^1 Projection can be found by analysing the localised version ($u' = 0$ at $\partial\Omega_k$) of the un-resolved scale equation in Equation (5.41). This un-resolved scale equation can be numerically solved using high-degree polynomials to obtain an approximate u'. For this problem, a polynomial space of degree 12 polynomials is used and the residual of the resolved scales computed using the High-order VMS method is considered. The numerically computed estimate u' for each of the residuals from the different VMS cases (using the aforementioned different polynomial degrees) are plotted in Figure 5.7. It must be noted, however, that this pointwise evaluation of u' is not required and only its integral is of interest. Hence, the integral of the computed u' over each element is plotted in a bar graph alongside the integral of $\tau\mathscr{R}u_h$ in Figure 5.7. As seen through Figure 5.7a, the integral of $\tau\mathscr{R}u_h$ exactly matches up with the integral of the exact u'. As such, the effect of the exact u' required for the H^1 projection is obtained for the $p = 1$ case. For the other values of p, it can be seen that the integral values of $\tau\mathscr{R}u_h$ do not necessarily match with the exact u' where it is under-approximated in some cases and overestimated in others. This leads to the High-order VMS approach for $p > 1$ only being close to the exact H_0^1 Projection, but not exact.

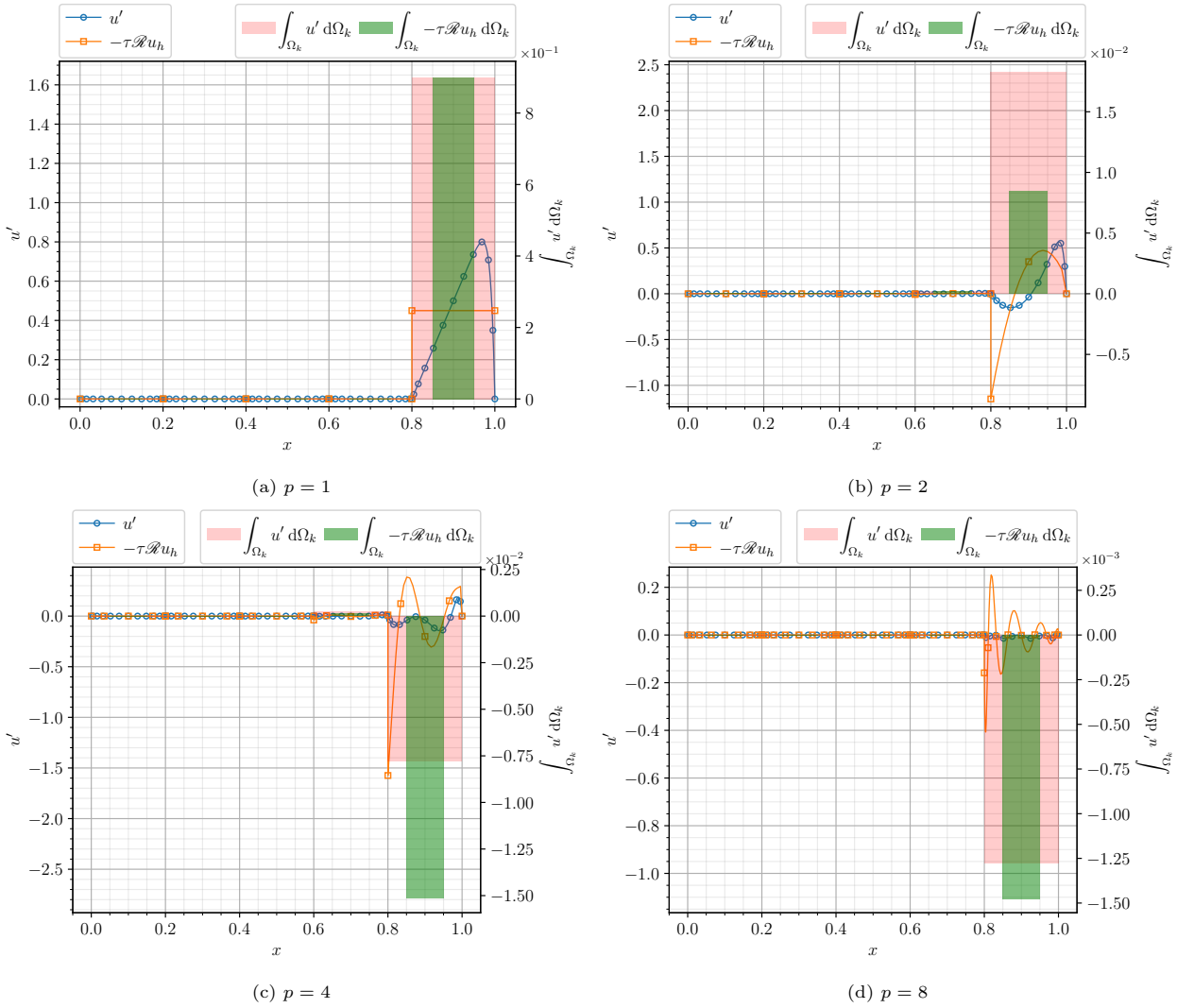

(a) $p = 1$

(b) $p = 2$

(c) $p = 4$

(d) $p = 8$

Figure 5.7: Prediction of the un-resolved scales using $\tau\mathscr{R}u_h$ compared to the exact un-resolved scales of steady advection-diffusion for different order polynomials with $N = 5$ elements

On another note, an interesting component of the solution that is yet to be considered is the Lagrange multipliers λs used to enforce solution continuity over the elements and the boundary conditions. As highlighted earlier, these Lagrange multipliers physically represent the diffusive flux $\nu\dfrac{\partial u}{\partial x}$ at the element boundaries. Consequently, the computed Lagrange multipliers for the different methods and mesh refinements are plotted in Figure 5.8 alongside the exact diffusive flux. Concerning the predictions of the diffusive flux through the Lagrange multipliers, it is observed that the base Galerkin scheme yields poor predictions on coarse meshes as seen through Figure 5.8a and Figure 5.8b. However, the predictions do improve for finer meshes. The two VMS approaches on the other hand closely follow exact diffusive flux with the High-order variant naturally performing better for higher-order polynomials. The nature of these Lagrange multipliers has the potential to be used in post-processing routines to improve the scheme's prediction of the solution gradient which would omit the discontinuous jumps in the gradient. This, however, was not used in the present work.

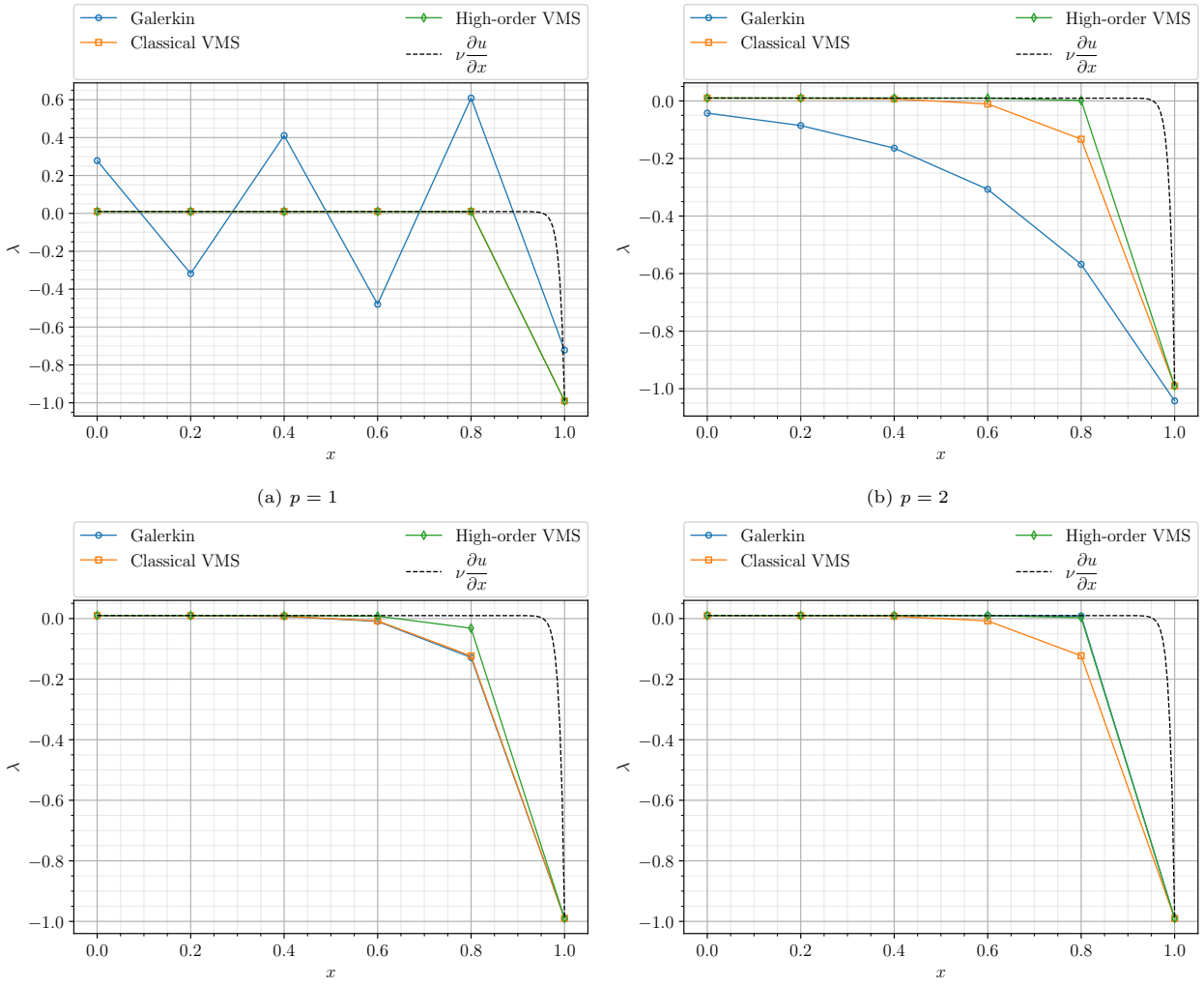

(a) $p = 1$

(b) $p = 2$

(c) $p = 4$

(d) $p = 8$

Figure 5.8: Lagrange multipliers to the steady advection-diffusion problem for different order polynomials with $N = 5$ elements

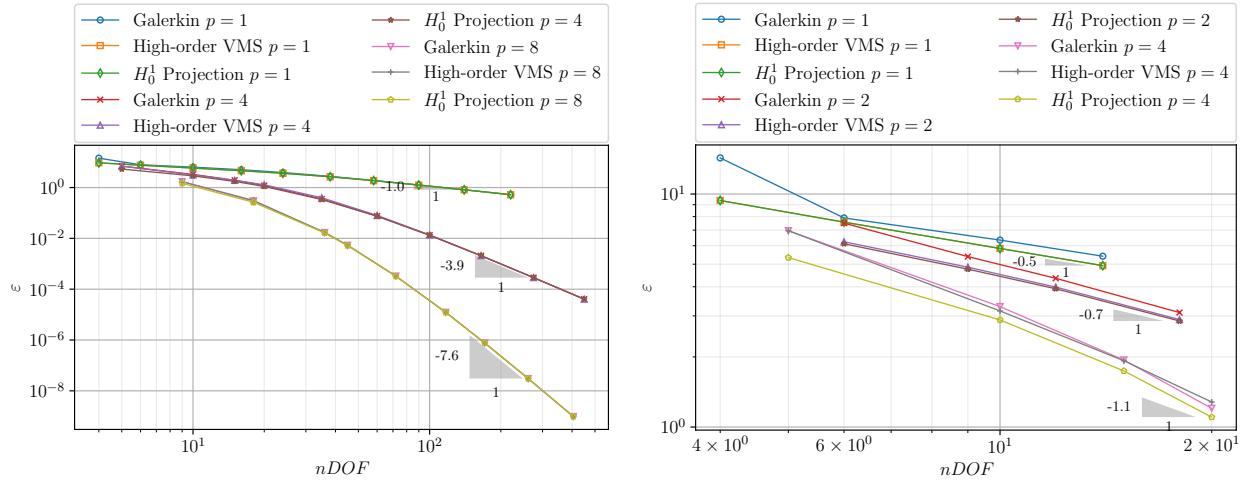

(a) H^1 error

(b) H^1 error in the non-asymptotic region

Figure 5.9: h-convergence of the Galerkin and multiscale solutions to the steady advection-diffusion computed in the H^1 error norm using the exact solution

Concerning the error behaviour of the High-order VMS scheme, the H^1 errors of the VMS and Galerkin schemes for different degree polynomials are plotted in Figure 5.9 for varying number of degrees of freedom. As indicated by Figure 5.9a, both the Galerkin and High-order VMS schemes tend to converge at the same

rate which confirms the consistency of the VMS approach. Moreover, the difference between the Galerkin, H_0^1 Projection, and the High-order VMS is most prominent when very few number of degrees of freedom are used. As such, H^1 errors for the different schemes in the non-asymptotic region of the convergence curve are plotted in Figure 5.9b. Through this plot, it is apparent that the H^1 errors of the High-order VMS scheme are closer to that of the optimal H_0^1 Projection. More specifically, the errors of the two schemes are exactly coincident for $p = 1$, reasonably close for $p = 2$, and only a slight improvement over the Galerkin scheme for $p = 4$. This suggests that, while the newly proposed High-order VMS does improve the Galerkin solution by bringing it closer to the optimal H_0^1 Projection, it is not capable of reproducing the H_0^1 Projection itself.

In summary, it can be concluded that an improvement is achieved by incorporating multiscale theory into the Galerkin approach. The addition of the multiscale term associates no additional computational costs over the base Galerkin scheme and tends to provide a consistent approach that reduces the absolute error of the numerical solution in coarse meshes. It is noted that the proposed VMS approach does not produce the exact optimal H_0^1 Projection for arbitrary degree polynomials. This is attributed to the fact that u' is only obtained as an estimate for $p > 1$.

5.2. 1D unsteady advection-diffusion

Having concluded the section on the steady problem, the focus is now set on the full unsteady advection-diffusion equation in 1D. The considered domain for this problem is taken to be a periodic domain ranging between 0 and 1 where the governing equation and problem setup reads as follows:

$$\frac{\partial u}{\partial t} + c\frac{\partial u}{\partial x} - \nu\frac{\partial^2 u}{\partial x^2} = 0, \qquad x \in \Omega \in]0,1[\tag{5.65}$$

$$u(0,t) = u(1,t), \qquad \forall t \geq 0 \tag{5.66}$$

$$u(x,0) = f(x). \tag{5.67}$$

This particular model equation describes the transport and diffusion of a quantity u over time where the initial distribution of the quantity is described by $f(x)$. Like for the steady case, the advection speed c and the diffusion coefficient ν are considered to be constant values. This linear problem is characterised as a second-order parabolic equation for $\nu > 0$. In the case where $\nu = 0$, the problem then becomes hyperbolic where the exact solution can be found in the following form:

$$u(x,t) = u(x - ct, 0) = f(x - ct). \tag{5.68}$$

A crucial thing to note about the physical behaviour of the solution for this hyperbolic case is that the integral of the solution and the integral of the squared solution are preserved over time. To demonstrate this, consider the integral of the PDE over the periodic domain:

$$\int_\Omega \frac{\partial u}{\partial t}\,\mathrm{d}\Omega = -c\int_\Omega \frac{\partial u}{\partial x}\,\mathrm{d}\Omega = -cu\big|_{\partial\Omega} = 0, \tag{5.69}$$

where the resulting boundary evaluation cancels due to periodic boundaries leading to the integral of u being preserved. Similarly, multiplying the PDE by u and integrating gives:

$$\int_\Omega u\frac{\partial u}{\partial t}\,\mathrm{d}\Omega = -c\int_\Omega u\frac{\partial u}{\partial x}\,\mathrm{d}\Omega \tag{5.70}$$

$$\frac{1}{2}\int_\Omega \frac{\partial u^2}{\partial t} = -\frac{c}{2}\int_\Omega \frac{\partial u^2}{\partial x}\,\mathrm{d}\Omega = -\frac{c}{2}u^2\big|_{\partial\Omega} = 0, \tag{5.71}$$

where periodicity leads to the right-hand side cancelling, which shows the conservation of the integral of u^2 in time. In the parabolic case, the integral of u is conserved, however, u^2 decays over time.

For the numerical tests considered in this section, both the parabolic and hyperbolic cases are considered. First, the Galerkin weak forms are derived in Section 5.2.1 for a number of formulations of the continuous equation with the solution represented as different *k-forms*. These continuous formulations are thereafter discretised in Section 5.2.2 using the mimetic method which aims to preserve the aforementioned integral of u in both parabolic and hyperbolic cases along with conserving the integral of u^2 for the hyperbolic case. This is then followed by the results of the test cases including both parabolic and hyperbolic problems in Section 5.2.3 and Section 5.2.4 respectively. Lastly, the integration of multiscale theory into the Galerkin formulation, along with its results are presented in Section 5.2.5 and Section 5.2.6.

5.2.1. Continuous form

Like for the steady case, the Galerkin weak form of the governing equation for u expressed as a *k-form* is derived by testing Equation (5.65) with a test function $v^{(k)}$:

$$\int_\Omega \left(\frac{\partial u^{(k)}}{\partial t} + \mathscr{L} u^{(k)} \right) \wedge \star\, v^{(k)} = 0, \qquad \forall v^{(k)} \in \Lambda^{(k)}(\mathcal{M}) \qquad \text{where } \mathscr{L} := c\frac{\partial}{\partial x} - \nu \frac{\partial^2}{\partial x^2}. \tag{5.72}$$

The quantity u can be expressed as any generic *k-form* in 1D where each representation can be associated with a physical interpretation. For instance, expressing u as a *0-form* corresponds to the solution being defined in points. Whereas, u as a *1-form* corresponds to the solution being defined along edges (1D volumes). The latter case can be argued to present a more physical solution representation for advection cases. This is attributed to the fact that advection problems deal with the transport of quantities such as mass (density) or momentum which are typically associated with volumetric quantities. Nonetheless, both representations are equally reasonable to be used, at least in the 1D setting. Hence both representations are considered in this section.

Starting off with u defined as a *0-form* in the primal space yields the following weak form:

$$\int_\Omega \frac{\partial u^{(0)}}{\partial t} \wedge \star\, v^{(0)} + c \int_\Omega \mathrm{d}u^{(0)} \wedge \star\, v^{(0)} + \nu \int_\Omega \mathrm{d}u^{(0)} \wedge \star\, \mathrm{d}v^{(0)} = 0, \tag{5.73}$$

where the advection term is simply computed by taking the exterior derivative of u and the diffusion term is computed by moving the second exterior derivative to the test function yielding the adjoint operator. It must be noted here that the boundary terms emerging from the adjoint operator are neglected given that the periodic domain has no boundaries. The advection and diffusion terms in the above weak form can be recognised as being the same as for the steady case where the unsteady case simply adds a temporal derivative term to the equation.

In a similar manner, u can be defined as a *1-form* in the dual space. For this representation of the solution, the exterior derivative of the quantity does not exist. As such, the derivatives are computed by first mapping the solution to its dual *0-form* and then applying the exterior derivative. The corresponding weak form thus reads:

$$\int_\Omega \frac{\partial \tilde{u}^{(1)}}{\partial t} \wedge \star\, \tilde{v}^{(1)} + c \int_\Omega \mathrm{d} \star \tilde{u}^{(1)} \wedge \star\, \tilde{v}^{(1)} + \nu \int_\Omega \mathrm{d} \star \tilde{u}^{(1)} \wedge \star\, \mathrm{d} \star \tilde{v}^{(1)} = 0. \tag{5.74}$$

Again, the boundary terms for the adjoint operator in the diffusion term are neglected given the periodic boundary condition. Alternatively, instead of taking the derivative of the solution for the advection term, the derivative could be moved to the test function which yet again yields the adjoint operator (where boundary terms are neglected) and the weak form reads as follows:

$$\int_\Omega \frac{\partial \tilde{u}^{(1)}}{\partial t} \wedge \star\, \tilde{v}^{(1)} - c \int_\Omega \tilde{u}^{(1)} \wedge \star\, \mathrm{d} \star \tilde{v}^{(1)} + \nu \int_\Omega \mathrm{d} \star \tilde{u}^{(1)} \wedge \star\, \mathrm{d} \star \tilde{v}^{(1)} = 0. \tag{5.75}$$

Given that the advection terms in both Equation (5.74) and Equation (5.75) are exactly equivalent at the continuous level, one can take a linear combination of the two as shown below to arrive at a new formulation for the advection term.

$$\begin{aligned} \int_\Omega \frac{\partial \tilde{u}^{(1)}}{\partial t} \wedge \star\, \tilde{v}^{(1)} - a \left(c \int_\Omega \tilde{u}^{(1)} \wedge \star\, \mathrm{d} \star \tilde{v}^{(1)} \right) + (1-a) \left(c \int_\Omega \mathrm{d} \star \tilde{u}^{(1)} \wedge \star\, \tilde{v}^{(1)} \right) + \\ \nu \int_\Omega \mathrm{d} \star \tilde{u}^{(1)} \wedge \star\, \mathrm{d} \star \tilde{v}^{(1)} = 0. \end{aligned} \tag{5.76}$$

A commonly used formulation of the above equation is the Skew-Symmetric (S-S) form which entails taking $a = 0.5$. As the name suggests, this form of the advection term yields a skew-symmetric advection operator when discretised as will be later presented in Section 5.2.2.

Lastly, consider u to be defined as a *1-form* in the primal space. Since the exterior derivative does not exist for a *1-form*, the derivatives of the solution are computed by first mapping the solution to a *0-form* through the interior product and then applying the exterior derivative. For the advection term, the vector quantity used for the interior product is the advection speed $\boldsymbol{c} := c\partial_x$ where ∂_x is the basis vector in the tangent space. Similarly, the vector quantity for the interior product in the diffusion term is solely the basis vector ∂_x. This approach thus yields the following weak form:

$$\int_\Omega \frac{\partial u^{(1)}}{\partial t} \wedge \star\, v^{(1)} + \int_\Omega \mathrm{d} \circ i_{\boldsymbol{c}} u^{(1)} \wedge \star\, v^{(1)} + \nu \int_\Omega \mathrm{d} \circ i_{\partial_x} u^{(1)} \wedge \star\, \mathrm{d} \circ i_{\partial_x} v^{(1)} = 0. \tag{5.77}$$

The advection term for this case can be recognised to be the Lie derivative of a *1-form*.

5.2.2. Discrete form

Having derived the weak forms for the numerous different continuous formulations of the linear advection-diffusion equation, their respective discrete forms are derived in this subsection. Firstly the semi-discrete system is derived for each of the different weak forms. Thereafter, the fully discrete system is derived by discretising the time derivative.

Starting with the first weak form in Equation (5.73), the corresponding discrete representation of the solution and test functions are as follows:

$$u_h := \boldsymbol{\psi}^{(0)}\boldsymbol{u}, \quad \in \Lambda_h^{(0)}(\boldsymbol{\mathcal{M}}) \tag{5.78}$$

$$v_h := \boldsymbol{\psi}^{(0)}\boldsymbol{v}, \quad \in \Lambda_h^{(0)}(\boldsymbol{\mathcal{M}}). \tag{5.79}$$

Substituting these discrete forms into Equation (5.73) and applying the discrete exterior derivative in the form of the incidence matrix $\mathbb{E}^{1,0}$ yields the following:

$$\boldsymbol{v}^T \left[\int_{\Omega_h} \boldsymbol{\psi}^{(0)^T}\boldsymbol{\psi}^{(0)}\,\mathrm{d}\Omega_h\right]\frac{\partial \boldsymbol{u}}{\partial t} + c\,\boldsymbol{v}^T\left[\int_{\Omega_h}\boldsymbol{\psi}^{(0)^T}\boldsymbol{\psi}^{(1)}\,\mathrm{d}\Omega_h\right]\mathbb{E}^{1,0}\boldsymbol{u} + \nu\,\boldsymbol{v}^T\mathbb{E}^{1,0^T}\left[\int_{\Omega_h}\boldsymbol{\psi}^{(1)^T}\boldsymbol{\psi}^{(1)}\,\mathrm{d}\Omega_h\right]\mathbb{E}^{1,0}\boldsymbol{u} = 0 \tag{5.80}$$

$$\mathbb{M}^{(0)}\frac{\partial \boldsymbol{u}}{\partial t} + c\,\mathbb{M}^{(0,1)}\mathbb{E}^{1,0}\boldsymbol{u} + \nu\,\mathbb{E}^{1,0^T}\mathbb{M}^{(1)}\mathbb{E}^{1,0}\boldsymbol{u} = 0 \tag{5.81}$$

$$\frac{\partial \boldsymbol{u}}{\partial t} = -\mathbb{M}^{(0)^{-1}}\left(c\,\mathbb{M}^{(0,1)}\mathbb{E}^{1,0} + \nu\,\mathbb{E}^{1,0^T}\mathbb{M}^{(1)}\mathbb{E}^{1,0}\right)\boldsymbol{u}. \tag{5.82}$$

The resulting semi-discrete system can be expressed in the following way for compactness:

$$\frac{\partial \boldsymbol{u}}{\partial t} = \boldsymbol{A}^{(0)}\boldsymbol{u}. \tag{5.83}$$

This particular scheme is henceforth referred to as the "nodal" scheme. With the derived semi-discrete system, the types of operators appearing in the system and their properties can be assessed. Firstly it can be recognised that the terms inside the brackets in Equation (5.82) are identical to the ones for the steady advection-diffusion case. This comes as no surprise as the spatial operator and the choice of degrees of freedom are the same in both cases. In this unsteady case, however, there is the inverse of the mass matrix ($\mathbb{M}^{(0)^{-1}}$) appearing in the equation. This inclusion of the inverse mass matrix naturally changes the mappings associated with the advection and diffusion term compared to the steady case. Upon distributing the inverse mass matrix over the two terms, it is evident that the advection term includes the discrete Lie derivative of the *0-form*. The sequence of applying the Lie derivative to a *0-form* can be schematically shown in the discrete De Rham complex as depicted in Figure 5.10a. Similarly, the sequence of mappings corresponding to the diffusion term is shown in Figure 5.10b. Like in the previous depiction of the De Rham sequence, the green links show the metric-free operations and the red links show the metric-dependent ones.

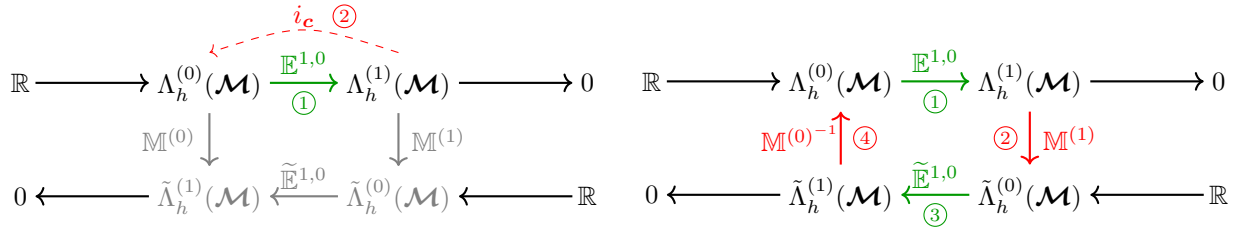

(a) Advection term (b) Diffusion term

Figure 5.10: The path followed in the discrete De Rham sequence for the advection and diffusion terms for the unsteady advection-diffusion equation with the solution expressed as a *0-form* on the primal mesh

Starting with the advection term, one can observe it comprises the metric-free incidence matrix and a metric-dependent interior product. The interior product actually contains a metric free term which is the $\mathbb{M}^{(0,1)}$ matrix that was described in the steady case, however, this matrix is accompanied by $\mathbb{M}^{(0)^{-1}}$ though which the metric dependence is introduced. The diffusion term again consists of the two topological incidence matrices along with the two metric-dependent mass matrices creating a full loop around the De Rham sequence.

Next, the weak form in Equation (5.74) is considered where the following discrete representation is substituted

into the equation:

$$u_h := \tilde{\boldsymbol{\psi}}^{(1)} \tilde{\boldsymbol{u}}, \quad \in \tilde{\Lambda}_h^{(1)}(\boldsymbol{\mathcal{M}}) \tag{5.84}$$

$$v_h := \tilde{\boldsymbol{\psi}}^{(1)} \tilde{\boldsymbol{v}}, \quad \in \tilde{\Lambda}_h^{(1)}(\boldsymbol{\mathcal{M}}). \tag{5.85}$$

The resulting discrete system reads as follows:

$$\tilde{\boldsymbol{v}}^T \left[\int_{\Omega_h} \tilde{\boldsymbol{\psi}}^{(1)^T} \tilde{\boldsymbol{\psi}}^{(1)} \, \mathrm{d}\Omega_h \right] \frac{\partial \tilde{\boldsymbol{u}}}{\partial t} + c \, \tilde{\boldsymbol{v}}^T \left[\int_{\Omega_h} \tilde{\boldsymbol{\psi}}^{(1)^T} \boldsymbol{\psi}^{(1)} \, \mathrm{d}\Omega_h \right] \mathbb{E}^{1,0} \star \tilde{\boldsymbol{u}} + \nu \, \tilde{\boldsymbol{v}}^T \star \mathbb{E}^{1,0^T} \left[\int_{\Omega_h} \boldsymbol{\psi}^{(1)^T} \boldsymbol{\psi}^{(1)} \, \mathrm{d}\Omega_h \right] \mathbb{E}^{1,0} \star \tilde{\boldsymbol{u}} = 0. \tag{5.86}$$

Replacing the continuous Hodge $\star$ operator with its discrete counterpart in the form of the mass matrix and employing the concept presented in [11], the dual polynomials can be expressed as the mass matrix times the primal polynomials, $\tilde{\boldsymbol{\psi}}^{(1)} = \boldsymbol{\psi}^{(0)} \mathbb{M}^{(0)^{-1}}$:

$$\tilde{\boldsymbol{v}}^T \left(\mathbb{M}^{(0)^{-1}} \right)^T \left[\int_{\Omega_h} \boldsymbol{\psi}^{(0)^T} \boldsymbol{\psi}^{(0)} \, \mathrm{d}\Omega_h \right] \mathbb{M}^{(0)^{-1}} \frac{\partial \tilde{\boldsymbol{u}}}{\partial t} + c \, \tilde{\boldsymbol{v}}^T \left(\mathbb{M}^{(0)^{-1}} \right)^T \left[\int_{\Omega_h} \boldsymbol{\psi}^{(0)^T} \boldsymbol{\psi}^{(1)} \, \mathrm{d}\Omega_h \right] \mathbb{E}^{1,0} \mathbb{M}^{(0)^{-1}} \tilde{\boldsymbol{u}} + \nu \, \tilde{\boldsymbol{v}}^T \left(\mathbb{M}^{(0)^{-1}} \right)^T \mathbb{E}^{1,0^T} \left[\int_{\Omega_h} \boldsymbol{\psi}^{(1)^T} \boldsymbol{\psi}^{(1)} \, \mathrm{d}\Omega_h \right] \mathbb{E}^{1,0} \mathbb{M}^{(0)^{-1}} \tilde{\boldsymbol{u}} = 0 \tag{5.87}$$

$$\tilde{\boldsymbol{v}}^T \cancel{\left(\mathbb{M}^{(0)^{-1}} \right)^T} \cancel{\mathbb{M}^{(0)} \mathbb{M}^{(0)^{-1}}} \frac{\partial \tilde{\boldsymbol{u}}}{\partial t} + c \, \tilde{\boldsymbol{v}}^T \cancel{\left(\mathbb{M}^{(0)^{-1}} \right)^T} \mathbb{M}^{(0,1)} \mathbb{E}^{1,0} \mathbb{M}^{(0)^{-1}} \tilde{\boldsymbol{u}} + \nu \, \tilde{\boldsymbol{v}}^T \cancel{\left(\mathbb{M}^{(0)^{-1}} \right)^T} \mathbb{E}^{1,0^T} \mathbb{M}^{(1)} \mathbb{E}^{1,0} \mathbb{M}^{(0)^{-1}} \tilde{\boldsymbol{u}} = 0 \tag{5.88}$$

$$\frac{\partial \tilde{\boldsymbol{u}}}{\partial t} + c \, \mathbb{M}^{(0,1)} \mathbb{E}^{1,0} \mathbb{M}^{(0)^{-1}} \tilde{\boldsymbol{u}} + \nu \, \mathbb{E}^{1,0^T} \mathbb{M}^{(1)} \mathbb{E}^{1,0} \mathbb{M}^{(0)^{-1}} \tilde{\boldsymbol{u}} = 0 \tag{5.89}$$

$$\frac{\partial \tilde{\boldsymbol{u}}}{\partial t} = - \left(c \, \mathbb{M}^{(0,1)} \mathbb{E}^{1,0} + \nu \, \mathbb{E}^{1,0^T} \mathbb{M}^{(1)} \mathbb{E}^{1,0} \right) \mathbb{M}^{(0)^{-1}} \tilde{\boldsymbol{u}} \tag{5.90}$$

$$\frac{\partial \tilde{\boldsymbol{u}}}{\partial t} = \tilde{\boldsymbol{A}}^{(1)} \tilde{\boldsymbol{u}} \tag{5.91}$$

This derived scheme is subsequently referred to as the "edge" scheme. Considering the discrete operators that appear in the semi-discrete system for this dual *1-form* representation, it is evident that these are identical to the ones in Equation (5.82). The difference, however, lies in the order that these operators are applied. In Equation (5.90) the inverse mass matrix is the first operation applied whereafter the previously established advection-diffusion operator is applied. As a consequence, the sequence of mappings in the discrete De Rham sequence changes to the one depicted in Figure 5.11.

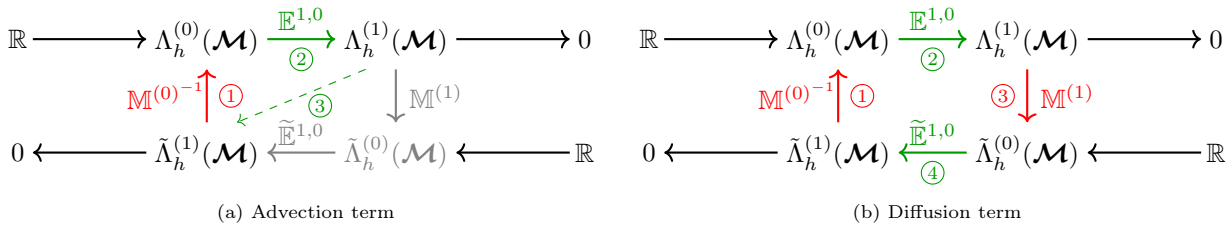

(a) Advection term

(b) Diffusion term

Figure 5.11: The path followed in the discrete De Rham sequence for the advection and diffusion terms for the unsteady advection-diffusion equation with the solution expressed as a *1-form* on the dual mesh

At this point, it is worth addressing an intriguing characteristic of the discrete systems in Equation (5.82) and Equation (5.90) arising from the choice of degrees of freedom. When u is expressed as a *0-form*, the degrees of freedom correspond to nodal values on the mesh, much like the classical Finite-Difference method. Applying the incidence matrix is effectively applying a differencing operator as commonly done in the Finite-Difference case. Lastly, the projection of the derivative back to the original space of nodal values is done using a metric-dependent term involving the mesh spacing for the Finite-Difference case whereas the described formulation in Equation (5.82) uses the interior product. Thus, in essence, Equation (5.82) acts as an extension of the

simple Finite-Difference method to higher-order. Similarly, for u expressed as a dual *1-form*, a connection can be made between Equation (5.90) and the well-known Finite-Volume method. As Finite-Volume methods are associated with their degrees of freedom defined within volumes where an initial metric-dependent operation is applied to reconstruct the flux/nodal values after which the derivative is applied. The sequence of operations seen in Equation (5.90) shows a close resemblance to this process where the initial discrete Hodge operator in the form of the inverse mass matrix acts as the flux reconstruction process and the remaining operators compute the derivative and project it back to the initial space. This connection between the SEM and central Finite Difference/Volume method is shown in Appendix .5.

Moving further with the derivations of the discrete systems, the weak form in Equation (5.75) is considered. Substituting in the same discrete dual *1-form* representations from Equation (5.84) and Equation (5.85) gives:

$$\frac{\partial \tilde{\boldsymbol{u}}}{\partial t} - c\,\mathbb{E}^{1,0^T}\mathbb{M}^{(1,0)}\mathbb{M}^{(0)^{-1}}\tilde{\boldsymbol{u}} + \nu\,\mathbb{E}^{1,0^T}\mathbb{M}^{(1)}\mathbb{E}^{1,0}\mathbb{M}^{(0)^{-1}}\tilde{\boldsymbol{u}} = 0 \tag{5.92}$$

$$\frac{\partial \tilde{\boldsymbol{u}}}{\partial t} = -\left(-c\,\mathbb{E}^{1,0^T}\mathbb{M}^{(1,0)} + \nu\,\mathbb{E}^{1,0^T}\mathbb{M}^{(1)}\mathbb{E}^{1,0}\right)\mathbb{M}^{(0)^{-1}}\tilde{\boldsymbol{u}} \tag{5.93}$$

$$\frac{\partial \tilde{\boldsymbol{u}}}{\partial t} = \tilde{\boldsymbol{A}}^{(1)}_{\text{SBP}}\tilde{\boldsymbol{u}}. \tag{5.94}$$

This scheme with the adjoint advection operator is referred to as the Summation By Parts ("SBP") scheme, which is a nomenclature borrowed from literature where similar adjoint operators are applied.

Similarly, the discrete system of the Skew-Symmetric ("S-S") form of Equation (5.76) is found as follows:

$$\frac{\partial \tilde{\boldsymbol{u}}}{\partial t} + \frac{1}{2}\left(c\,\mathbb{M}^{(0,1)}\mathbb{E}^{1,0}\mathbb{M}^{(0)^{-1}}\mathbb{M}^{(0)^{-1}}\tilde{\boldsymbol{u}} - c\,\mathbb{E}^{1,0^T}\mathbb{M}^{(1,0)}\mathbb{M}^{(0)^{-1}}\tilde{\boldsymbol{u}}\right) + \nu\,\mathbb{E}^{1,0^T}\mathbb{M}^{(1)}\mathbb{E}^{1,0}\mathbb{M}^{(0)^{-1}}\tilde{\boldsymbol{u}} = 0 \tag{5.95}$$

$$\frac{\partial \tilde{\boldsymbol{u}}}{\partial t} = -\left(\frac{1}{2}\left(c\,\mathbb{M}^{(0,1)}\mathbb{E}^{1,0} - c\,\mathbb{E}^{1,0^T}\mathbb{M}^{(1,0)}\right) + \nu\,\mathbb{E}^{1,0^T}\mathbb{M}^{(1)}\mathbb{E}^{1,0}\right)\mathbb{M}^{(0)^{-1}}\tilde{\boldsymbol{u}} \tag{5.96}$$

$$\frac{\partial \tilde{\boldsymbol{u}}}{\partial t} = \tilde{\boldsymbol{A}}^{(1)}_{\text{S-S}}\tilde{\boldsymbol{u}}. \tag{5.97}$$

Lastly, considering Equation (5.77) with the following representations:

$$u_h := \boldsymbol{\psi}^{(1)}\boldsymbol{u}, \quad \in \Lambda^{(1)}_h(\boldsymbol{\mathcal{M}}) \tag{5.98}$$

$$v_h := \boldsymbol{\psi}^{(1)}\boldsymbol{v}, \quad \in \Lambda^{(1)}_h(\boldsymbol{\mathcal{M}}) \tag{5.99}$$

gives the following discrete system:

$$\begin{aligned}\boldsymbol{v}^T\left[\int_{\Omega_h}\boldsymbol{\psi}^{(1)^T}\boldsymbol{\psi}^{(1)}\,\mathrm{d}\Omega_h\right]\frac{\partial \boldsymbol{u}}{\partial t} + \boldsymbol{v}^T\left[\int_{\Omega_h}\boldsymbol{\psi}^{(1)^T}\boldsymbol{\psi}^{(1)}\,\mathrm{d}\Omega_h\right]\mathbb{E}^{1,0}\mathbb{M}^{(0)^{-1}}\mathbb{M}^{(0,1)}_{\boldsymbol{c}}\boldsymbol{u} + \\ \nu\,\boldsymbol{v}^T(\mathbb{M}^{(0,1)}_{\partial_x})^T(\mathbb{M}^{(0)^{-1}})^T\mathbb{E}^{1,0^T}\left[\int_{\Omega_h}\boldsymbol{\psi}^{(1)^T}\boldsymbol{\psi}^{(1)}\,\mathrm{d}\Omega_h\right]\mathbb{E}^{1,0}\mathbb{M}^{(0)^{-1}}\mathbb{M}^{(0,1)}_{\partial_x}\boldsymbol{u} = 0\end{aligned} \tag{5.100}$$

$$\mathbb{M}^{(1)}\frac{\partial \boldsymbol{u}}{\partial t} + \mathbb{M}^{(1)}\mathbb{E}^{1,0}\mathbb{M}^{(0)^{-1}}\mathbb{M}^{(0,1)}_{\boldsymbol{c}}\boldsymbol{u} + \nu\,(\mathbb{M}^{(0,1)}_{\partial_x})^T(\mathbb{M}^{(0)^{-1}})^T\mathbb{E}^{1,0^T}\mathbb{M}^{(1)}\mathbb{E}^{1,0}\mathbb{M}^{(0)^{-1}}\mathbb{M}^{(0,1)}_{\partial_x}\boldsymbol{u} = 0 \tag{5.101}$$

$$\frac{\partial \boldsymbol{u}}{\partial t} = -\left(\mathbb{E}^{1,0}\mathbb{M}^{(0)^{-1}}\mathbb{M}^{(0,1)}_{\boldsymbol{c}} + \nu\,\mathbb{M}^{(1)^{-1}}(\mathbb{M}^{(0,1)}_{\partial_x})^T(\mathbb{M}^{(0)^{-1}})^T\mathbb{E}^{1,0^T}\mathbb{M}^{(1)}\mathbb{E}^{1,0}\mathbb{M}^{(0)^{-1}}\mathbb{M}^{(0,1)}_{\partial_x}\right)\boldsymbol{u} \tag{5.102}$$

$$\frac{\partial \boldsymbol{u}}{\partial t} = \boldsymbol{A}^{(1)}\boldsymbol{u}. \tag{5.103}$$

This scheme is henceforward referred to as the "Lie" scheme. For this scheme, the corresponding path followed in the discrete De Rham sequence is depicted in Figure 5.12.

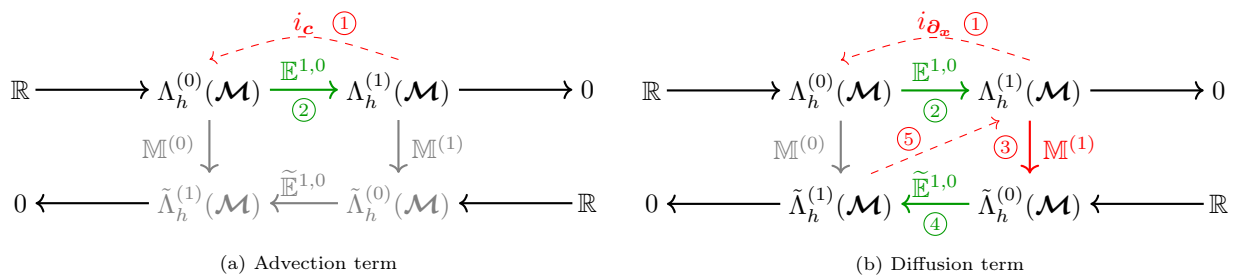

(a) Advection term (b) Diffusion term

Figure 5.12: The path followed in the discrete De Rham sequence for the advection and diffusion terms for the unsteady advection-diffusion equation with the solution expressed as a *1-form* on the primal mesh

The advection term simply involves the Lie derivative much like the case for the nodal expansion of u. However, the order of applying the incidence matrix and the interior product is reversed given that u is defined as a *1-form* on the primal.

With all the semi-discrete systems in place, a fully discrete system is obtained by discretising the temporal derivative using the Crank-Nicolson time march scheme as follows:

$$\frac{\partial \boldsymbol{u}}{\partial t} = \boldsymbol{A}\boldsymbol{u} \tag{5.104}$$

$$\frac{\boldsymbol{u}^{n+1} - \boldsymbol{u}^n}{\Delta t} = \boldsymbol{A}\boldsymbol{u}^{n+\frac{1}{2}} \tag{5.105}$$

$$\frac{\boldsymbol{u}^{n+1} - \boldsymbol{u}^n}{\Delta t} = \frac{1}{2}\boldsymbol{A}\boldsymbol{u}^{n+1} + \frac{1}{2}\boldsymbol{A}\boldsymbol{u}^n \tag{5.106}$$

$$\boldsymbol{u}^{n+1} - \frac{\Delta t}{2}\boldsymbol{A}\boldsymbol{u}^{n+1} = \boldsymbol{u}^n + \frac{\Delta t}{2}\boldsymbol{A}\boldsymbol{u}^n \tag{5.107}$$

$$\left[\boldsymbol{I} - \frac{\Delta t}{2}\boldsymbol{A}\right]\boldsymbol{u}^{n+1} = \left[\boldsymbol{I} + \frac{\Delta t}{2}\boldsymbol{A}\right]\boldsymbol{u}^n \tag{5.108}$$

$$\boldsymbol{L}\boldsymbol{u}^{n+1} = \boldsymbol{R}\boldsymbol{u}^n \tag{5.109}$$

Since this time march approach simply involves solving a linear system every time step, the verification of the time march scheme implementation is done for a generic case which is shown in Appendix .3.

Note that up until this point, no continuity between the elements or boundary conditions have been imposed on the discrete system. Imposing the required constraints via the Lagrange multipliers yields a linear system in the following form to be solved every time step:

$$\begin{bmatrix} \boldsymbol{L} & \boldsymbol{\Lambda}^T \\ \boldsymbol{\Lambda} & \varnothing \end{bmatrix} \begin{bmatrix} \boldsymbol{u}^{n+1} \\ \boldsymbol{\lambda} \end{bmatrix} = \begin{bmatrix} \boldsymbol{R}\boldsymbol{u}^n \\ \boldsymbol{0} \end{bmatrix}. \tag{5.110}$$

The goal of the Lagrange multipliers is to constrain the solution such that the nodal values are matched at the element boundaries. This approach is identical to the steady case. However, the composition of the matrix $\boldsymbol{\Lambda}$ must be adjusted based on the representation of u. When u is expressed as a *0-form*, the $\boldsymbol{\Lambda}$ matrix is the aforementioned topological $\mathbb{E}^{\lambda,0}$ matrix which is adjusted for the periodic boundaries. If u is represented as a dual *1-form*, then it must be first mapped to the points before applying the continuity constraint which results in $\boldsymbol{\Lambda} = \mathbb{E}^{\lambda,0}{\mathbb{M}^{(0)}}^{-1}$. Lastly, when u is expressed as a *1-form* in the primal space, a special treatment is required. This *1-form* representation's dual is the dual *0-form* which does not include the (element) boundary points. As such, the approach followed to overcome this was to interpolate the solution at the element boundaries using the *1-form* basis functions and constrain that pointwise value to be continuous over the elements. This gives $\boldsymbol{\Lambda} = \mathbb{E}^{\lambda,0}\boldsymbol{\psi}^{(1)}(x)$ where $\boldsymbol{\psi}^{(1)}(x)$ is a matrix containing the evaluation of the edge basis at the mesh nodes. One thing to note here is that this presented "Lie" scheme in the current formulation does not produce a solution for $p = 1$. This is down to the fact that the bases for this scheme are edge basis functions which are constant functions when $p = 1$. This results in the solution being represented as element-wise constants which have a derivative of zero. As such, this particular case with $p = 1$ is ignored when presenting results for this scheme.

Alternatively, one can apply a different approach by generating a time evolution equation for the Lagrange multipliers, see Appendix .4. While this approach is practically feasible it is not very desirable as it involves unwanted and unnecessary dynamics of the Lagrange multipliers. As such, the use of this formulation was disregarded. Nonetheless, it serves as a useful tool to analyse the properties of the full (coupled) global system and was used to check the energy conservation property of the numerical scheme.

5.2.3. Numerical experiments with diffusion

For the numerical tests in this subsection, a truncated Fourier series of a square wave is used. The corresponding equation for the initial condition reads:

$$\begin{aligned} f(x) = u(x,0) = d + &\sum_{n=1}^{m} \frac{1}{n\pi i}((1 - e^{-n\pi id}) - (1 - e^{n\pi id}))\cos\left(n\frac{2\pi}{(x_1 - x_0)}x\right) + \\ &\sum_{n=1}^{m} \frac{i}{n\pi i}((1 - e^{-n\pi id}) + (1 - e^{n\pi id}))\sin\left(n\frac{2\pi}{(x_1 - x_0)}x\right), \end{aligned} \tag{5.111}$$

where i is the imaginary number $i = \sqrt{-1}$, d is the duty cycle of the square wave, and $(x_1 - x_0)$ is the difference between the domain endpoints, which for the considered case is 1. All the tests considered in this section use a

duty cycle $d = 0.25$ and truncated series at $m = 4$. Expressing the initial condition as a Fourier series has the advantage that the exact solution for the unsteady advection-diffusion can be found by simply phase shifting the different wave numbers in time and damping each wave number by ν times the square of the wave number. The exact solution thus reads:

$$u_{exact}(x,t) = d + \sum_{n=1}^{m} \frac{1}{n\pi i}((1 - e^{-n\pi id}) - (1 - e^{n\pi id})) \cos\left(n\frac{2\pi}{(x_1 - x_0)}(x - ct)\right) e^{-\nu\left(n\frac{2\pi}{(x_1-x_0)}\right)^2 t} + \sum_{n=1}^{m} \frac{i}{n\pi i}((1 - e^{-n\pi id}) + (1 - e^{n\pi id})) \sin\left(n\frac{2\pi}{(x_1 - x_0)}(x - ct)\right) e^{-\nu\left(n\frac{2\pi}{(x_1-x_0)}\right)^2 t}. \tag{5.112}$$

Using this exact solution, each of the derived numerical schemes was verified by computing the L^2 error between the numerical and exact solution after one complete period ($t = 1$). Plotting this L^2 error for all the derived schemes with different degree polynomials varying the number of degrees of freedom yields the plots in Figure 5.13. Since only the spatial convergence is being tested, the time step size has to be sufficiently small to ensure that the temporal errors are significantly smaller than the spatial ones. As such, a different time step size was used for each polynomial degree. For the cases in Figure 5.13a, time step sizes of $\Delta t = 5 \times 10^{-3}$, $\Delta t = 1 \times 10^{-3}$, and $\Delta t = 2 \times 10^{-5}$ were used for $p = 1$, $p = 2$, and $p = 4$ cases respectively. The $p = 2$, $p = 3$, and $p = 4$ cases in Figure 5.13b use the same three time step sizes. Starting off with the error curves

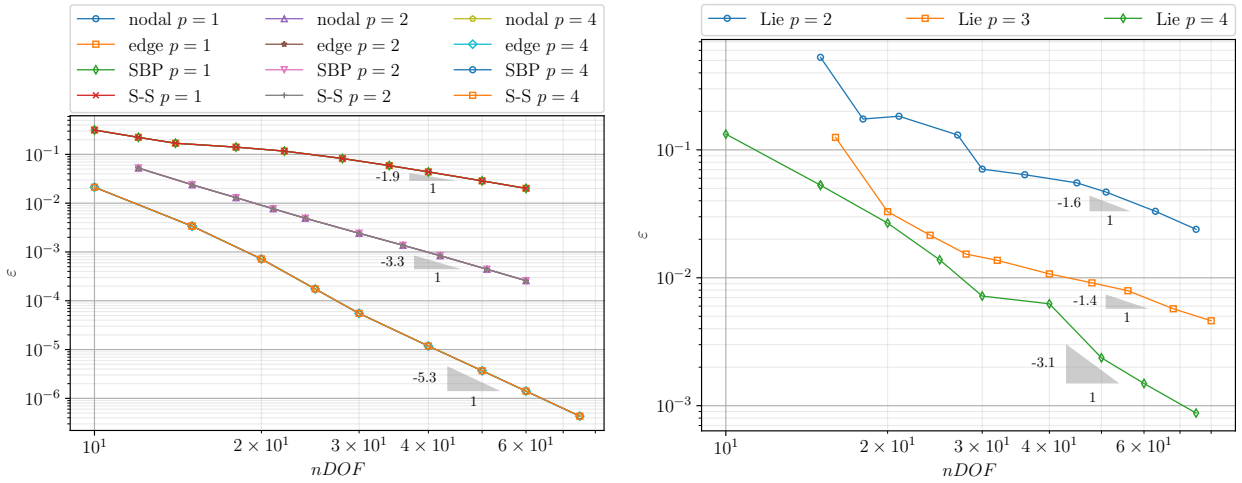

(a) h-convergence of the consistent schemes

(b) h-convergence of the inconsistent "Lie" scheme

Figure 5.13: h-convergence of the different numerical schemes for the unsteady advection-diffusion problem computed in the L^2 error norm against the exact solution at $t = 1$

in Figure 5.13a it can be seen that the rate of convergence is of order $p + 1$. This rate is in line with the expected rate as all the schemes shown in Figure 5.13a express the discrete solution as p^{th} degree polynomials. In general, all the different schemes behave in a very similar manner as suggested by the error curves being nearly indistinguishable in the plot. Considering Figure 5.13b on the other hand, fairly unusual behaviour is observed where, apart from the $p = 2$ case, the rate of convergence does not come close to the expected rate. The expected rate of convergence for this "Lie" scheme is order p given that the solution is expressed using the *1-form* edge basis functions which include polynomials of degree $p - 1$. The fact that the two curves in Figure 5.13b attain a slope that does not match the expected rate of convergence combined with the large error values for a sufficiently large number of degrees of freedom, suggests that there are exist some form of inconsistency in the approach.

The source of the inconsistency is apparent when considering the time evolution of the solution shown in Figure 5.14 in Figure 5.15. Through these plots, it can be observed that all the consistent numerical schemes (nodal, edge, etc) behave as expected by closely following the exact solution. However, the "Lie" scheme seems to produce significant over and undershoots at the element boundaries as seen in Figure 5.14. This poor approximation may seem like it is attributed to the lower order polynomial space ($p - 1$ degree polynomials) used in this discretisation, however, similar observations are made for the case where $p = 8$ in Figure 5.15 albeit to a lesser extent. These observations clearly indicate that the continuity constraint forced through the Lagrange multipliers is the source of the inconsistency. As noted earlier when the scheme was derived, the continuity constraint for this scheme was set up by interpolating the solution to the boundary nodes and forcing these interpolated values to be continuous at the boundaries. The relatively poorer solutions obtained

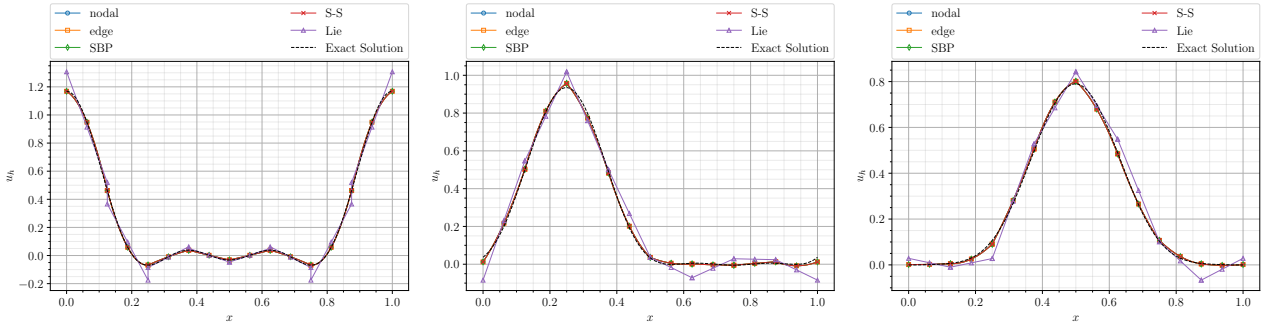

(a) $t = 0.0$ (b) $t = 0.25$ (c) $t = 0.5$

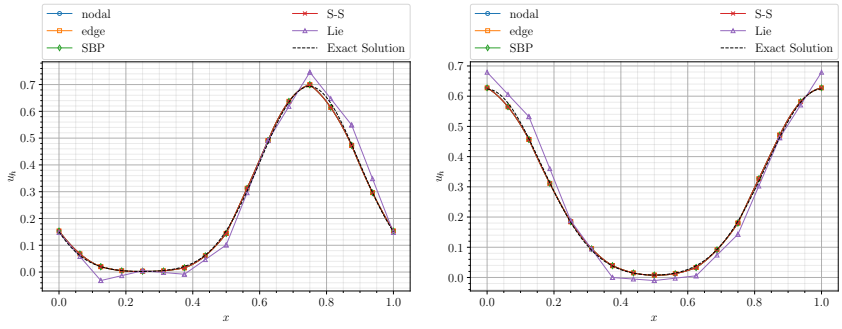

(d) $t = 0.75$ (e) $t = 1.0$

Figure 5.14: Time evolution of the numerical solutions to the linear advection-diffusion problem for $N = 8$, $p = 2$, and $\Delta t = 1 \times 10^{-3}$

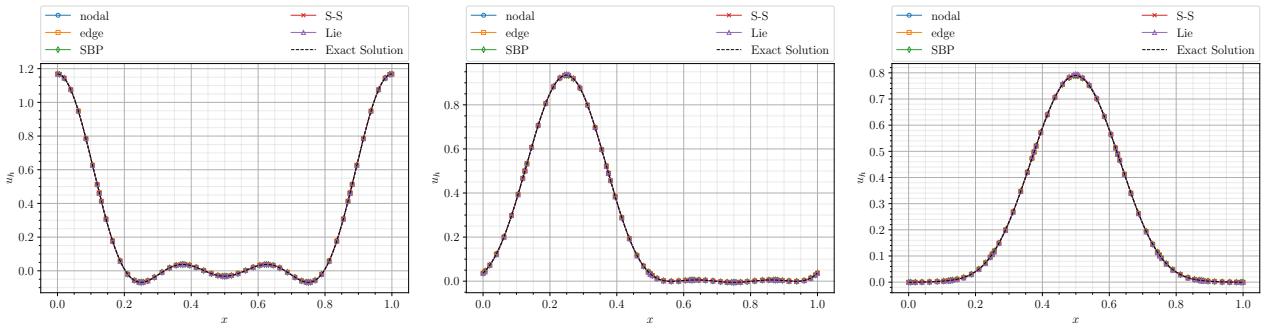

(a) $t = 0.0$ (b) $t = 0.25$ (c) $t = 0.5$

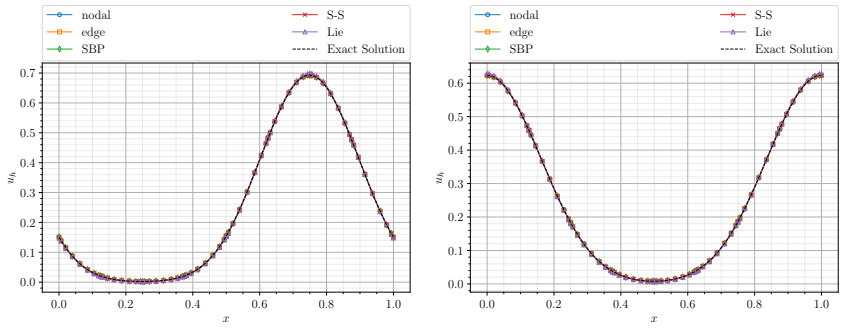

(d) $t = 0.75$ (e) $t = 1.0$

Figure 5.15: Time evolution of the numerical solutions to the linear advection-diffusion problem for $N = 8$, $p = 8$, and $\Delta t = 1 \times 10^{-3}$

using this technique which show no clear sign of convergence, suggest that this approach is unsuitable. While the over and undershoots at the element boundaries tend to decrease when using higher-degree polynomials, it does not completely vanish. In this discussion about the continuity constraints, it can be noted that even the other consistent schemes produce poorer solution predictions at the element boundaries given that the current formulation only ensures C^0 continuity. However, these errors are of a much lesser extent compared to the Lie scheme and more importantly, there are nearly eliminated for larger p. Concerning the Lagrange multiplier, it can be shown that they physically represent boundary terms emerging from the adjoint operator used in the weak form alike the steady case. However, it must be noted that the Lagrange multipliers are scaled by the time step size (Δt) and other components of the matrices used in the semi-discrete system. For instance, consider the semi-discrete system of the "nodal" scheme in its complete form:

$$\frac{\partial \boldsymbol{u}}{\partial t} = -\mathbb{M}^{(0)^{-1}} \left(c\, \mathbb{M}^{(0,1)} \mathbb{E}^{1,0} + \nu\, \mathbb{E}^{1,0^T} \mathbb{M}^{(1)} \mathbb{E}^{1,0} - \nu\, \mathbb{N}_1 \mathbb{B}\, \mathbb{E}^{1,0} \right) \boldsymbol{u}, \tag{5.113}$$

where the boundary term can be seen to be expressed as $\nu \mathbb{M}^{(0)^{-1}} \mathbb{N}_1 \mathbb{B}\, \mathbb{E}^{1,0} \boldsymbol{u}$. Given the inclusion of the inverse mass matrix, the boundary term is scaled differently than in the steady case. More specifically, the scaling factor is $\mathbb{M}^{(0)^{-1}} \mathbb{N}_1$ which ends up being one over the first (or last) weight of the Gauss-Lobatto quadrature $\left(\frac{1}{w_0}\right)$ given that $\mathbb{M}^{(0)^{-1}}$ is a diagonal matrix with the inverse of the Gauss-Lobatto quadrature weights in its entries. Combined with the time step size Δt emerging from the time discretisation, the complete scaling term is $\frac{\Delta t}{w_0}$. Thus, the Lagrange multipliers for the "nodal" scheme are given by:

$$\lambda_{\text{nodal}} = \frac{\Delta t}{w_0}\, \nu \frac{\partial u}{\partial x}. \tag{5.114}$$

Similarly, the physical representation of the Lagrange multipliers for the "edge" scheme can be found to be:

$$\lambda_{\text{edge}} = \Delta t\, w_0\, \nu \frac{\partial u}{\partial x}. \tag{5.115}$$

Applying this procedure allows one to obtain the physical interpretation of the Lagrange multipliers for any given scheme that includes the boundary terms from the adjoint operator. One important remark is that there might be multiple boundary terms appearing from the weak form, for instance, the "SBP" scheme has boundary terms emerging from both the advection and diffusion terms. In such cases, the terms are first scaled like shown before and added appropriately to their appearance in the weak form.

Correspondingly, the time evolution of the scaled Lagrange multipliers $\tilde{\lambda}$ is plotted for the different schemes below. The scaling is done in such a manner that the resulting quantity only contains the physical quantity of interest such as the diffusive flux. For example, the scaled Lagrange multipliers for the "nodal" scheme are computed as follows:

$$\tilde{\lambda}_{\text{nodal}} = \frac{w_0}{\Delta t}\, \lambda_{\text{nodal}}. \tag{5.116}$$

The plots in Figure 5.16 show the scaled Lagrange multipliers of the "nodal", "edge", and "Lie" schemes at different time instances for $p = 8$ and $N = 20$[2]. It can be seen that the Lagrange multipliers start off as all zeros given that they are initialised as such, and then they closely follow the exact solution which is physically the diffusive flux at each time instance. Similar observations can be made for the plots in Figure 5.17 and Figure 5.17 which show the (scaled) Lagrange multipliers for the "SBP" and "S-S" schemes where the exact solution is given by $-cu + \nu \frac{\partial u}{\partial x}$ and $-\frac{1}{2} cu + \nu \frac{\partial u}{\partial x}$ for the two respective formulations.

[2]Note, all the shown cases use $N = 20$ elements simply to be able to sample the values at sufficiently many points to be compared to the exact solution.

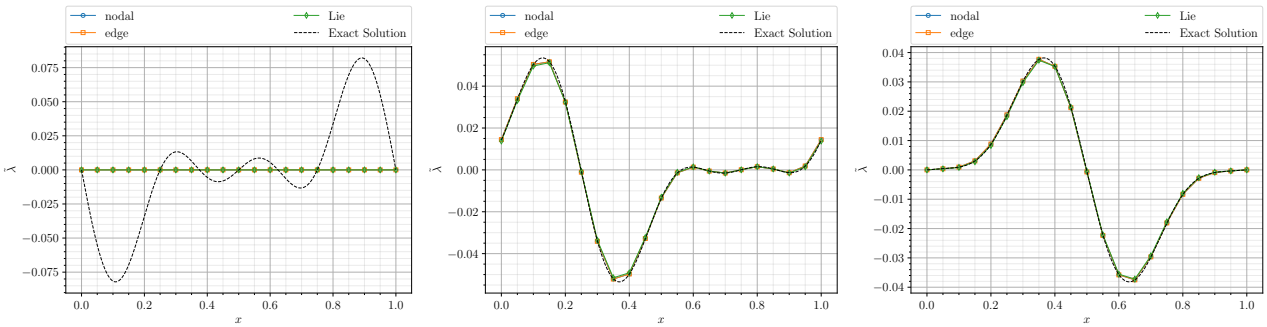

(a) $t = 0.0$ (b) $t = 0.25$ (c) $t = 0.5$

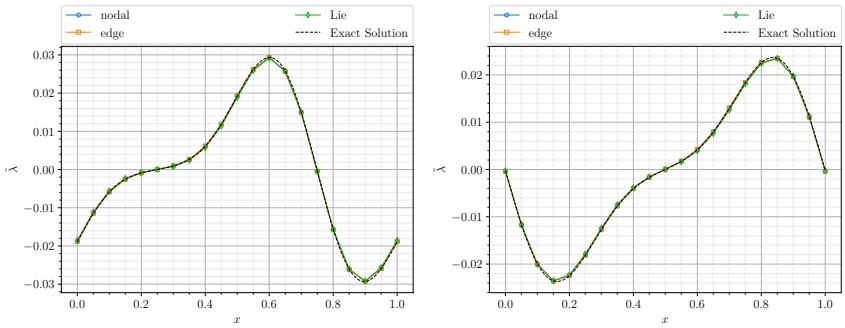

(d) $t = 0.75$ (e) $t = 1.0$

Figure 5.16: Time evolution of the (scaled) Lagrange multipliers to the linear advection-diffusion problem for $N = 20$, $p = 8$, and $\Delta t = 1 \times 10^{-3}$ where the exact solution is the exact diffusive flux $\nu \dfrac{\partial u}{\partial x}$

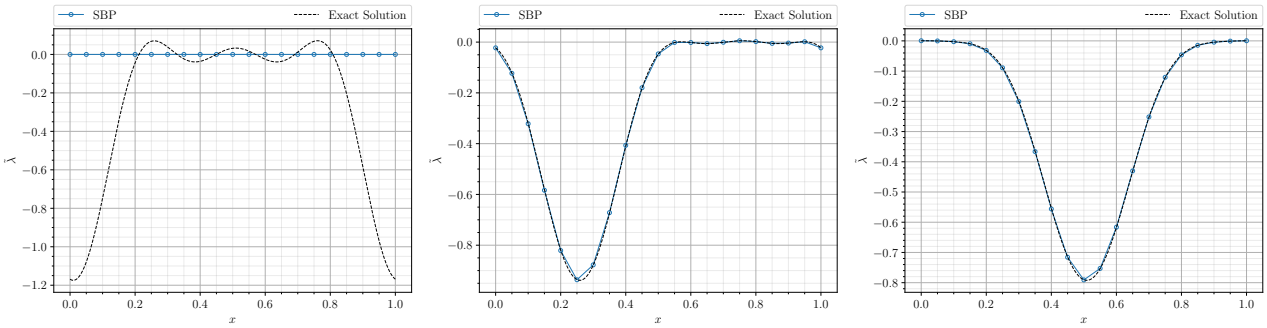

(a) $t = 0.0$ (b) $t = 0.25$ (c) $t = 0.5$

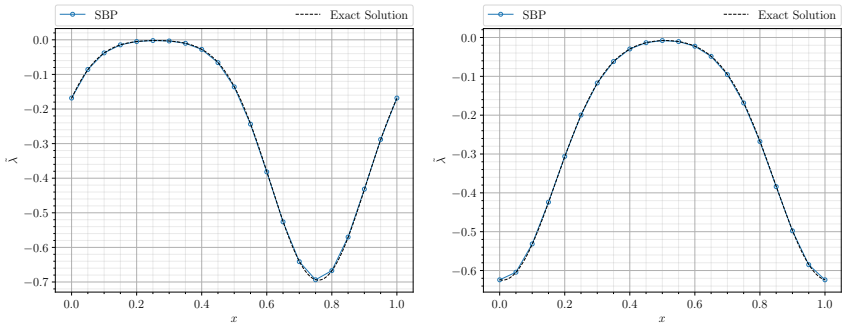

(d) $t = 0.75$ (e) $t = 1.0$

Figure 5.17: Time evolution of the (scaled) Lagrange multipliers to the linear advection-diffusion problem for $N = 20$, $p = 8$, and $\Delta t = 1 \times 10^{-3}$ where the exact solution is $-cu + \nu \dfrac{\partial u}{\partial x}$

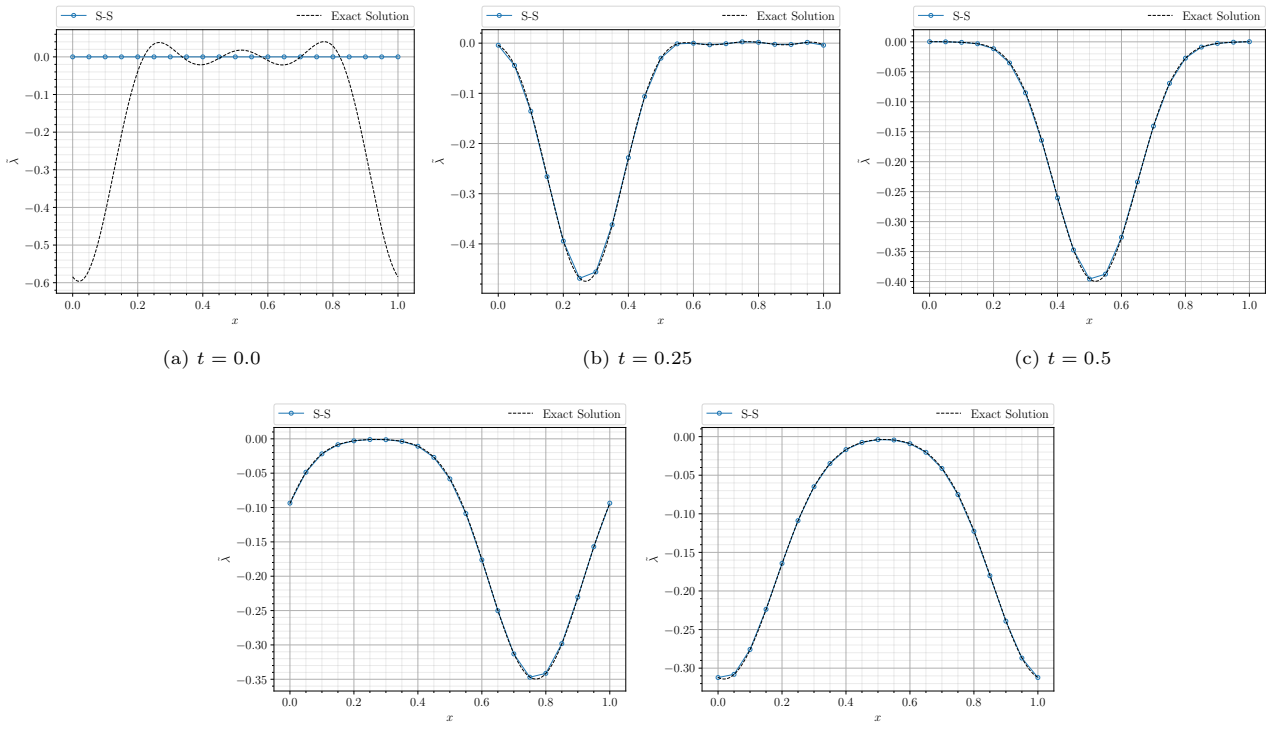

(a) $t = 0.0$ (b) $t = 0.25$ (c) $t = 0.5$

(d) $t = 0.75$ (e) $t = 1.0$

Figure 5.18: Time evolution of the (scaled) Lagrange multipliers to the linear advection-diffusion problem for $N = 20$, $p = 8$, and $\Delta t = 1 \times 10^{-3}$ where the exact solution is $-\frac{1}{2}cu + \nu\frac{\partial u}{\partial x}$

Now the focus is turned to the conservation qualities of the derived schemes. It is well established that the continuous level solution to the unsteady advection-diffusion problem in Equation (5.65) conserves the total integral of the solution over time. This conservation property is physically analogous to conserving mass (density), or momentum, where the advection term transports the quantity and the diffusion term spreads it over the domain all the while ensuring the total amount of the quantity is unchanged over time. For this conservation property to be achieved at the discrete level, the semi-discrete system must satisfy a specific property. To demonstrate this property, consider the conservation property expressed in a mathematical sense as follows:

$$\frac{\partial}{\partial t}\int_{\Omega} u_h \, \mathrm{d}\Omega = 0. \tag{5.117}$$

Given that integration and differentiation commute, the above expression can be rewritten as:

$$\int_{\Omega} \frac{\partial u_h}{\partial t} \, \mathrm{d}\Omega = 0. \tag{5.118}$$

The above condition may be assessed by replacing the test vector $\boldsymbol{v}$ with a row vector of 1s ($\boldsymbol{v}^T = [1, 1, ...1] = \mathbf{1}^T$) in the above derived weak forms. To demonstrate this, consider the semi-discrete system in Equation (5.82) re-written below:

$$\boldsymbol{v}^T \mathbb{M}^{(0)} \frac{\partial \boldsymbol{u}}{\partial t} = -\boldsymbol{v}^T \left(c\, \mathbb{M}^{(0,1)} \mathbb{E}^{1,0} \boldsymbol{u} + \nu\, \mathbb{E}^{1,0^T} \mathbb{M}^{(1)} \mathbb{E}^{1,0} \right) \boldsymbol{u}. \tag{5.119}$$

Substituting in the row vector of 1s gives:

$$\mathbf{1}^T \mathbb{M}^{(0)} \frac{\partial \boldsymbol{u}}{\partial t} = -\mathbf{1}^T \left(c\, \mathbb{M}^{(0,1)} \mathbb{E}^{1,0} \boldsymbol{u} + \nu\, \mathbb{E}^{1,0^T} \mathbb{M}^{(1)} \mathbb{E}^{1,0} \right) \boldsymbol{u}, \tag{5.120}$$

where the term on the left represents the sum of the time derivatives of the dual *1-form* degrees of freedom ($\sum_i \tilde{u}_i$, with $\tilde{\boldsymbol{u}} = \mathbb{M}^{(0)}\boldsymbol{u}$). Given the fact that the *1-form* degrees of freedom represent integral values of the quantity between the mesh nodes, the left-hand side term exactly reflects integral in Equation (5.118). Thus, for the discretisation to conserve the integral of the solution over time, the right-hand side term must equal

zero for all $\boldsymbol{u}$:

$$\mathbf{1}^T \left(c\, \mathbb{M}^{(0,1)} \mathbb{E}^{1,0} \boldsymbol{u} + \nu\, \mathbb{E}^{1,0^T} \mathbb{M}^{(1)} \mathbb{E}^{1,0} \right) \boldsymbol{u} = 0, \qquad \forall \boldsymbol{u} \in \mathbb{R}^n \tag{5.121}$$

$$\mathbf{1}^T \left(c\, \mathbb{M}^{(0,1)} \mathbb{E}^{1,0} \boldsymbol{u} + \nu\, \mathbb{E}^{1,0^T} \mathbb{M}^{(1)} \mathbb{E}^{1,0} \right) = \mathbf{0}. \tag{5.122}$$

The generalised condition for achieving the conservation property for an arbitrary semi-discretised weak form is thus given by:

$$\mathbf{1}^T \boldsymbol{A} = \mathbf{0}, \tag{5.123}$$

where $\boldsymbol{A}$ is the matrix representing the discrete spatial operators appearing in the semi-discrete system. The property in Equation (5.123) is satisfied up to the level of round-off errors for all the derived semi-discrete systems which thus proves that the derived schemes attain the conservation of the solution integral at the discrete level[3]. Moreover, since the proof never involved time discretisation, this discrete conservation property can be achieved for any arbitrary stable time march scheme.

To assess this conservation property, the conservation error is computed by taking the absolute difference between the discrete solution's integral at the initial condition and at time t, giving the error curves shown in Figure 5.19. Note, all the integrals are computed using a high degree of precision Gauss-Lobatto quadrature, hence the notation in the integrals uses Ω as opposed to the discrete Ω_h.

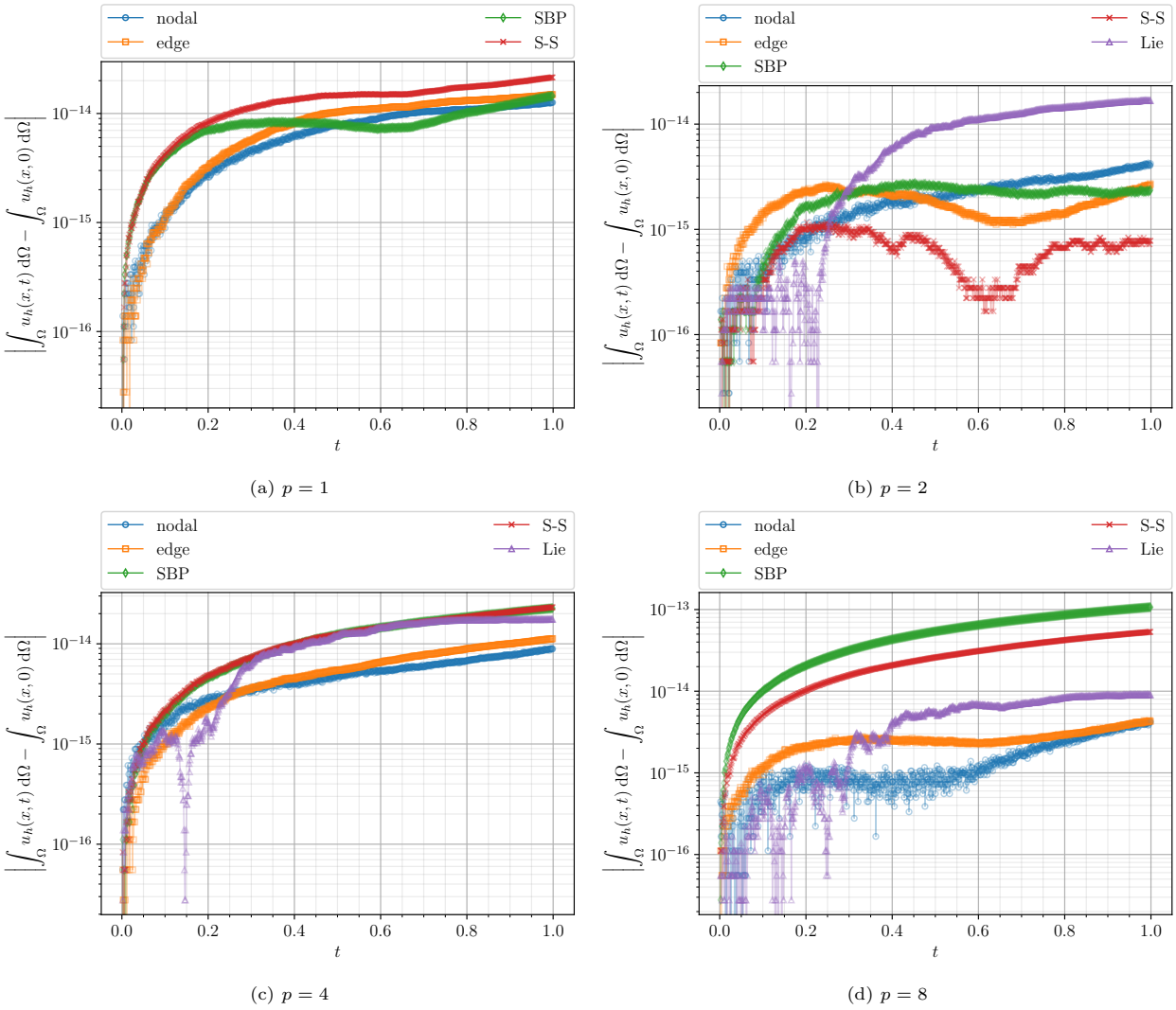

(a) $p = 1$

(b) $p = 2$

(c) $p = 4$

(d) $p = 8$

Figure 5.19: Conservation of the integral of the solution over time for the unsteady advection-diffusion equation with different degree polynomials where $N = 8$ and $\Delta t = 1 \times 10^{-3}$

[3]Note that in the hybrid case, $\mathbf{1}^T \boldsymbol{A}$ will return non-zero values at the element boundaries. The non-zero values are positive on one boundary and negative the same number on the other boundary which causes them to exactly cancel when continuity and periodicity are imposed

As seen in the plots in Figure 5.19, the conservation error is generally observed to be in the order of 1×10^{-14} – 1×10^{-13}. This error value is approaching the level of machine round-off errors which are to be expected. However, the error is seen to steadily grow over time which is not particularly ideal. The exact reason for this growth is uncertain at this stage leading to a postulation that there is some form of error accumulation over each time step caused by the conservation condition in Equation (5.123) is being satisfied up to the level of round-off errors. Following this reasoning, one can expect to observe smaller errors when fewer time steps are taken. This is confirmed when considering Figure 5.20 where the conservation errors for the cases with $\Delta t = 1\times10^{-2}$ are shown. Thus, as the number of time steps is reduced by one order of magnitude, so is the conservation error. While this observation confirms that the error is accumulated over the number of time steps, it does not explain why there is a bias. This concept is naturally encountered in the hyperbolic case as well and further discussion pertaining to this error accumulation behaviour is presented in the subsequent subsection.

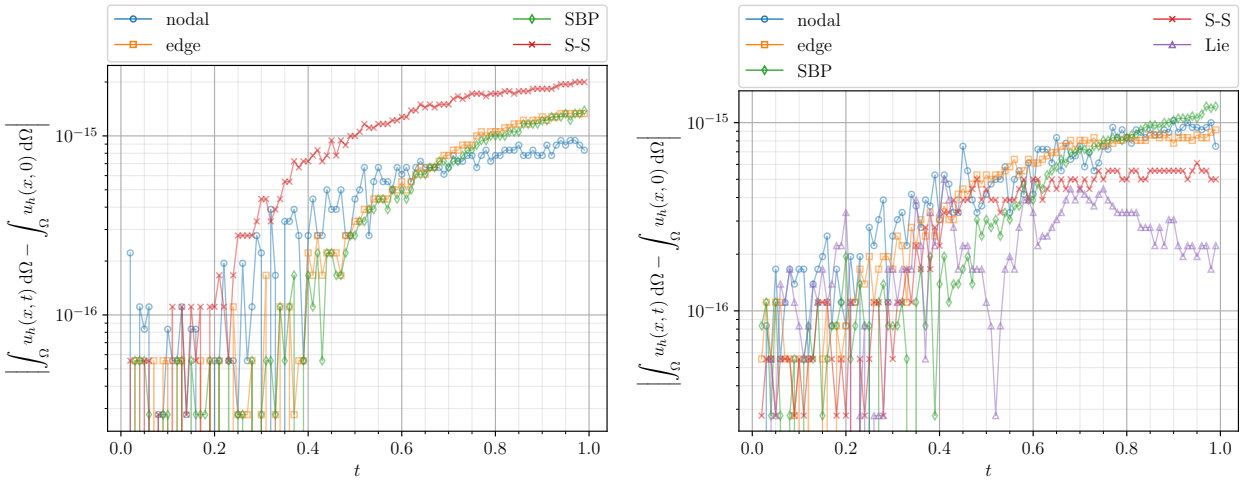

(a) $p = 1$ (b) $p = 2$

Figure 5.20: Conservation of the integral of the solution over time for the unsteady advection-diffusion equation with different degree polynomials where $N = 8$ and $\Delta t = 1\times10^{-2}$

Another property of the advection-diffusion to be assessed is the decay of the squared solution over time. This is physically analogous to the diffusion of kinetic energy over time. To derive this kinetic energy evolution equation, one can replace the test function in the weak form with the solution itself. In the discrete setting, this is achieved by pre-multiplying the generic fully discrete system from Equation (5.106) by $\boldsymbol{u}^{n+\frac{1}{2}} = \frac{1}{2}\left(\boldsymbol{u}^{n+1} + \boldsymbol{u}^{n}\right)$ as follows[4]:

$$\frac{\boldsymbol{u}^{n+1} - \boldsymbol{u}^{n}}{\Delta t} = \frac{1}{2}\boldsymbol{A}^{(k)}\left(\boldsymbol{u}^{n+1} + \boldsymbol{u}^{n}\right) \tag{5.124}$$

$$\frac{1}{2}\left(\boldsymbol{u}^{n+1} + \boldsymbol{u}^{n}\right)^{T}\frac{\boldsymbol{u}^{n+1} - \boldsymbol{u}^{n}}{\Delta t} = \frac{1}{4}\left(\boldsymbol{u}^{n+1} + \boldsymbol{u}^{n}\right)^{T}\boldsymbol{A}^{(k)}\left(\boldsymbol{u}^{n+1} + \boldsymbol{u}^{n}\right) \tag{5.125}$$

$$\frac{1}{2}\frac{\left(\boldsymbol{u}^{n+1}\right)^{2} - \left(\boldsymbol{u}^{n}\right)^{2}}{\Delta t} = \left(\boldsymbol{u}^{n+\frac{1}{2}}\right)^{T}\boldsymbol{A}^{(k)}\boldsymbol{u}^{n+\frac{1}{2}}. \tag{5.126}$$

The matrix $\boldsymbol{A}^{(k)}$ can be expressed as a combination of a symmetric and skew-symmetric component as follows:

$$\boldsymbol{A}^{(k)} = \underbrace{\frac{1}{2}\left(\boldsymbol{A}^{(k)} + \boldsymbol{A}^{(k)^{T}}\right)}_{\text{symmetric}} + \underbrace{\frac{1}{2}\left(\boldsymbol{A}^{(k)} - \boldsymbol{A}^{(k)^{T}}\right)}_{\text{skew-symmetric}}. \tag{5.127}$$

Substituting this back into Equation (5.126) gives:

$$\frac{1}{2}\frac{\left(\boldsymbol{u}^{n+1}\right)^{2} - \left(\boldsymbol{u}^{n}\right)^{2}}{\Delta t} = \left(\boldsymbol{u}^{n+\frac{1}{2}}\right)^{T}\left(\frac{1}{2}\left(\boldsymbol{A}^{(k)} + \boldsymbol{A}^{(k)^{T}}\right) + \frac{1}{2}\left(\boldsymbol{A}^{(k)} - \boldsymbol{A}^{(k)^{T}}\right)\right)\boldsymbol{u}^{n+\frac{1}{2}} \tag{5.128}$$

$$\frac{1}{2}\frac{\left(\boldsymbol{u}^{n+1}\right)^{2} - \left(\boldsymbol{u}^{n}\right)^{2}}{\Delta t} = \frac{1}{2}\left(\boldsymbol{u}^{n+\frac{1}{2}}\right)^{T}\left(\boldsymbol{A}^{(k)} + \boldsymbol{A}^{(k)^{T}}\right)\boldsymbol{u}^{n+\frac{1}{2}} + \frac{1}{2}\left(\boldsymbol{u}^{n+\frac{1}{2}}\right)^{T}\cancel{\left(\boldsymbol{A}^{(k)} - \boldsymbol{A}^{(k)^{T}}\right)}\boldsymbol{u}^{n+\frac{1}{2}}, \tag{5.129}$$

[4]Note that this analysis procedure does not work for the hybrid case where $\boldsymbol{A}^{(k)}$ is a block diagonal matrix. Thus, the constrained global system shown in Appendix .4 was used whenever this analysis technique was invoked.

where the last term cancels due to the property of skew-symmetric matrices. The remaining symmetric component is an $n \times n$ matrix which has n orthonormal set of eigenvectors $\boldsymbol{V} = [\mathbf{v}_0, \mathbf{v}_1, \dots \mathbf{v}_{n-1}]$ and n distinct real eigenvalues $\{\lambda_0^{\text{sym}}, \lambda_1^{\text{sym}}, \dots \lambda_{n-1}^{\text{sym}}\}$[5]. Subsequently, the symmetric component may be expressed as follows:

$$\boldsymbol{A}^{(k)} + \boldsymbol{A}^{(k)^T} = \boldsymbol{V}^{-1}\boldsymbol{\Lambda}\boldsymbol{V} = \boldsymbol{V}^T\boldsymbol{\Lambda}\boldsymbol{V}, \tag{5.130}$$

where $\boldsymbol{\Lambda}$ is a diagonal matrix containing the eigenvalues. Finally, substituting this back to the energy evolution equation and defining a new variable $\boldsymbol{w} := \boldsymbol{V}\boldsymbol{u}$ leads to:

$$\frac{1}{2}\frac{\left(\boldsymbol{u}^{n+1}\right)^2 - \left(\boldsymbol{u}^n\right)^2}{\Delta t} = \frac{1}{2}\left(\boldsymbol{u}^{n+\frac{1}{2}}\right)^T \boldsymbol{V}^T\boldsymbol{\Lambda}\boldsymbol{V}\boldsymbol{u}^{n+\frac{1}{2}} \tag{5.131}$$

$$\frac{1}{2}\frac{\left(\boldsymbol{u}^{n+1}\right)^2 - \left(\boldsymbol{u}^n\right)^2}{\Delta t} = \frac{1}{2}\left(\boldsymbol{w}^{n+\frac{1}{2}}\right)^T \boldsymbol{\Lambda}\boldsymbol{w}^{n+\frac{1}{2}} = \frac{1}{2}\sum_{i=0}^{n}\lambda_i^{\text{sym}}\left(w_i^{n+\frac{1}{2}}\right)^2. \tag{5.132}$$

Equation (5.132) thus shows that the eigenvalues of the symmetric component of $\boldsymbol{A}^{(k)}$ dictate the energy evolution in time. In the parabolic case where $\nu > 0$, the sum in Equation (5.132) produces a negative number indicating a decay in the integral of u^2 over time. This is thus consistent with the physical diffusion process. Computing the integral of the squared discrete solution for each scheme and plotting its evolution over time against the time evolution of the exact solution yields the plots shown in Figure 5.21.

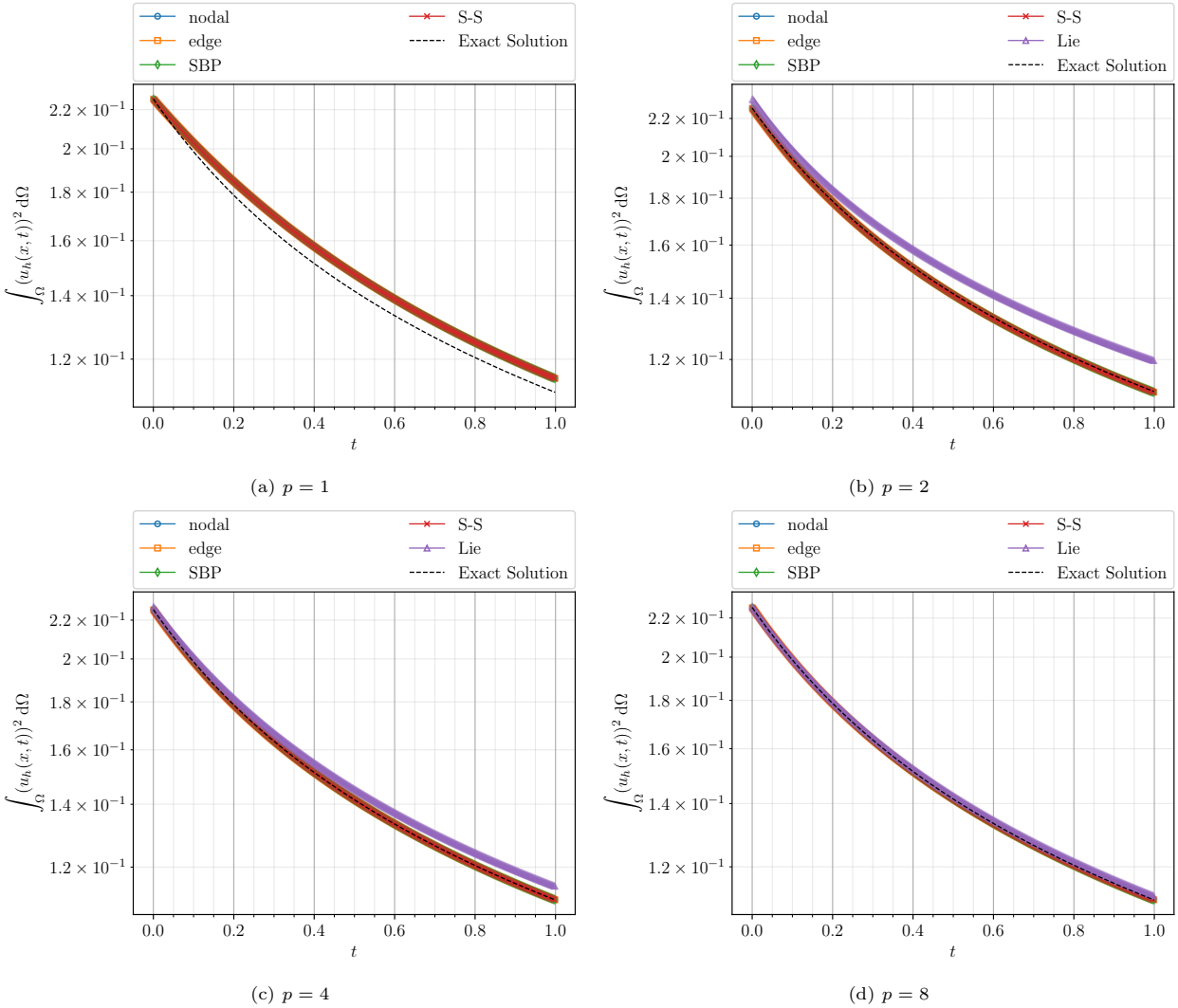

(a) $p = 1$ (b) $p = 2$

(c) $p = 4$ (d) $p = 8$

Figure 5.21: Time evolution of the integral of the square of the solution to the unsteady advection-diffusion equation with different degree polynomials where $N = 8$

The decay rate observed through Figure 5.21a with lower order polynomials does not match that of the exact solution. However, this rate is better matched when higher-degree polynomials are used. The cause of this

[5]Not to be confused with the Lagrange multipliers $\boldsymbol{\lambda}$

mismatch in coarse meshes is attributed to the fact that these meshes do not resolve all wave numbers of the solution. Given that the decay rate is proportional to the wave number squared, when the highest wave numbers are not resolved, only the decay rate associated with the smaller resolved wave numbers is observed. On another note, one can clearly see that the decay rate for the "Lie" scheme does not quite match the one of the exact solution even for relatively finer meshes. This could again be due to the oscillations caused by inconsistent boundary continuity treatment used in the "Lie" scheme. These oscillations cause over and undershoot of the solution which seems to integrate to zero as seen in Figure 5.19 but naturally does not cancel when it is squared and then integrated. Analogous to the integral of the sin function over 1 period, where the integral is zero, but the squared integral is not zero.

5.2.4. Numerical experiments without diffusion

With the numerical tests completed for the parabolic case, the same set of tests are considered here for the hyperbolic case by turning off the diffusion term ($\nu = 0$). To start off, consider the time evolution of the numerical solutions shown in Figure 5.22 and Figure 5.23. Due to the absence of diffusion, the dispersive errors of the scheme along with the effect of the weak C^0 inter-element continuity are more prominent in the coarser mesh. These errors are naturally reduced when using higher degree polynomials as apparent through Figure 5.23. However, the "Lie" scheme behaves significantly poorer as compared to the other (consistent) schemes in this hyperbolic case by dispersing more and producing significant jumps at the element boundaries as seen through Figure 5.22. These issues with the "Lie" scheme do tend to minimise, although not completely vanish when the mesh is refined (need to zoom in the plots in Figure 5.23 to see the effect).

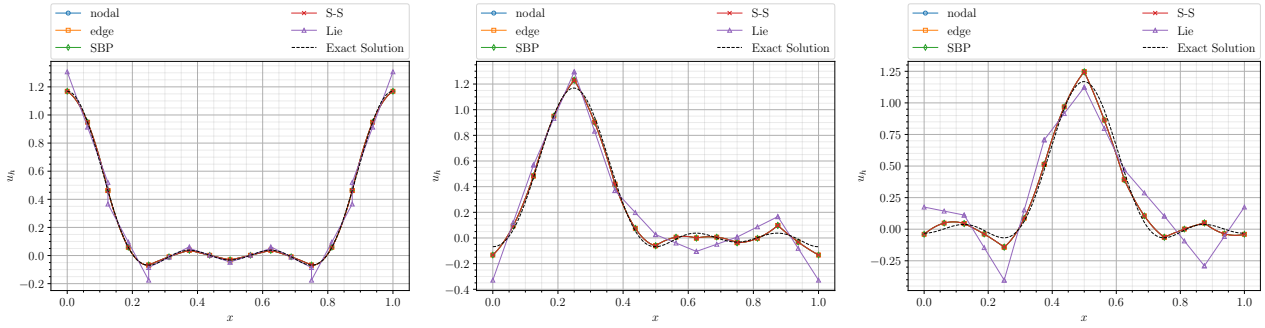

(a) $t = 0.0$ (b) $t = 0.25$ (c) $t = 0.5$

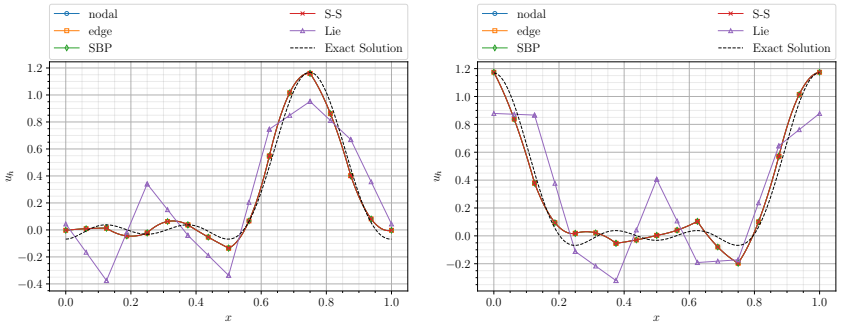

(d) $t = 0.75$ (e) $t = 1.0$

Figure 5.22: Time evolution of the numerical solutions to the linear advection problem for $N = 8$, $p = 2$, and $\Delta t = 1 \times 10^{-3}$

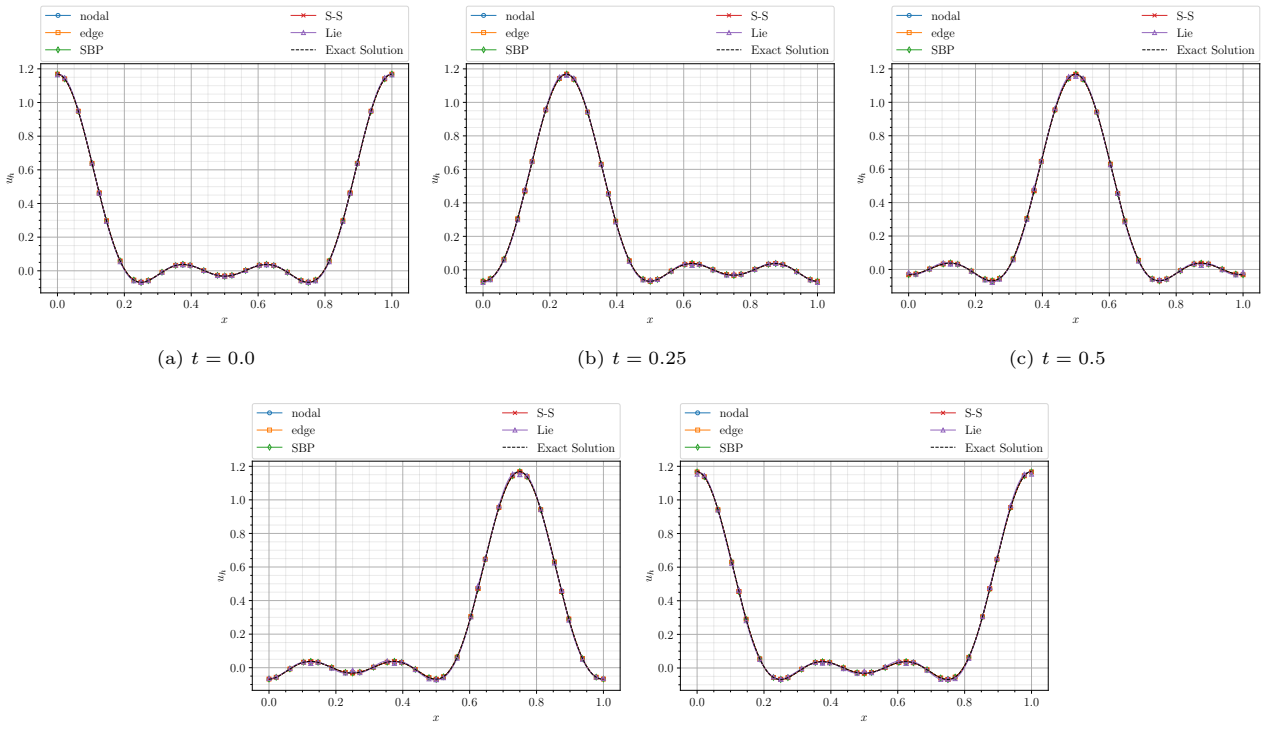

(a) $t = 0.0$ (b) $t = 0.25$ (c) $t = 0.5$

(d) $t = 0.75$ (e) $t = 1.0$

Figure 5.23: Time evolution of the numerical solutions to the linear advection problem for $N = 8$, $p = 4$, and $\Delta t = 1 \times 10^{-3}$

Moving on to the discussion on the physical analogue to the Lagrange multipliers for this hyperbolic case. Unlike the parabolic case where the diffusion term always produces a boundary term in the weak form, the general hyperbolic case does not produce any additional boundary terms with the exception of the cases where the adjoint advection operator is used (eg the "SBP" and "S-S" schemes). As such, the physical interpretation of the Lagrange multipliers is not easily obtained for the general hyperbolic problem. Only the "SBP" and "S-S" schemes have boundary terms which included the solution value itself and thus the Lagrange multipliers for these schemes represent the scaled version of the solution at the element boundaries, effectively the plots in Figure 5.18 and Figure 5.17 with ν set to zero. For the other schemes, however, it is not trivial what the Lagrange multipliers physically represent. For $p = 1$ it was found that the Lagrange multipliers represent some scaled version of the second derivative of the solution as seen in Figure 5.24. However, this does not generalise for any arbitrary p as the Lagrange multipliers for $p = 2$ appear dissimilar to the exact second derivative seen through Figure 5.25.

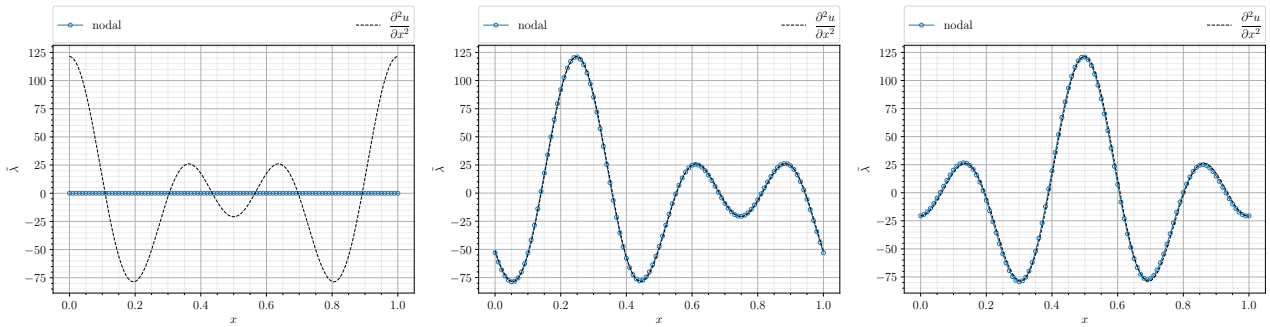

(a) $t = 0.0$ (b) $t = 0.25$ (c) $t = 0.5$

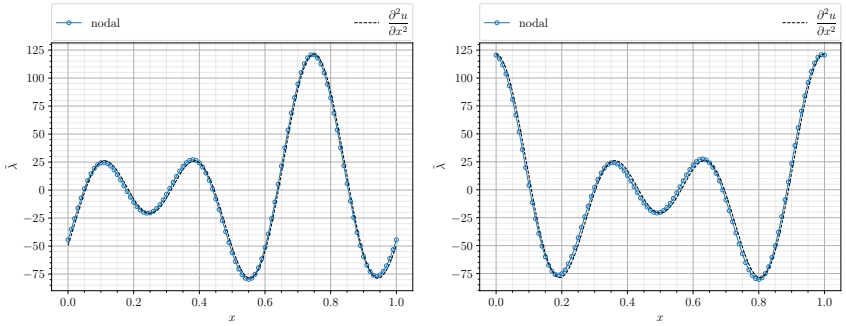

(d) $t = 0.75$ (e) $t = 1.0$

Figure 5.24: Time evolution of the (scaled) Lagrange multipliers for the linear advection problem with $N = 100$, $p = 1$, and $\Delta t = 1 \times 10^{-3}$

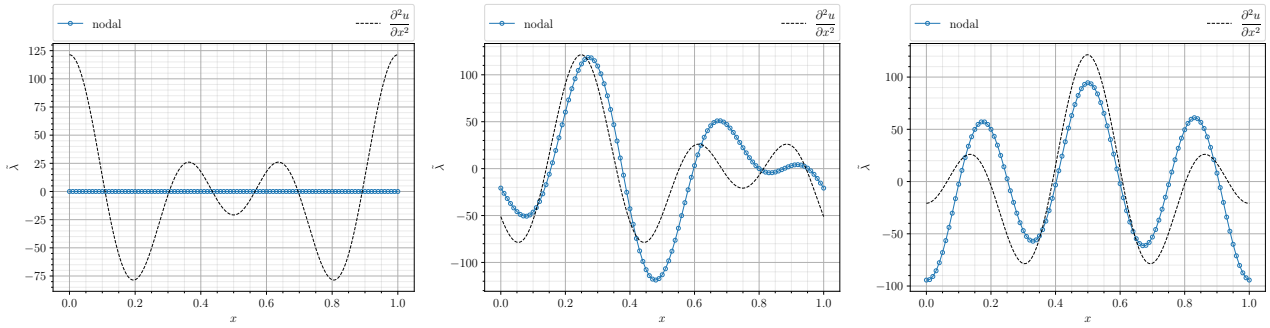

(a) $t = 0.0$ (b) $t = 0.25$ (c) $t = 0.5$

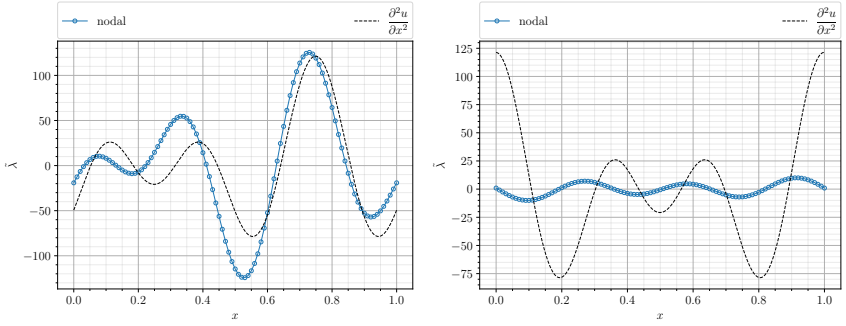

(d) $t = 0.75$ (e) $t = 1.0$

Figure 5.25: Time evolution of the (scaled) Lagrange multipliers for the linear advection problem with $N = 100$, $p = 2$, and $\Delta t = 1 \times 10^{-3}$

Following this discussion, the focus is now set on the conservation properties of the derived schemes. The conditions the (semi) discrete systems must satisfy to achieve discrete conservation of u and u^2 have already

been introduced in Equation (5.123) and Equation (5.132). The condition in Equation (5.123) is satisfied up to round-off errors for both parabolic and hyperbolic cases which guarantees the conservation of u in time. The conservation of u^2 on the other hand depends on the eigenvalues of the semi-discrete system to ensure that Equation (5.132) equates to zero. All the derived schemes produce a semi-discrete system with all imaginary (complex conjugate pairs) eigenvalues. This results in Equation (5.132) equating to zero (close to round-off errors) which therefore ensures the conservation of u^2 in time. An alternative way to view this conservation property is by recognising that the stability contour corresponding to $\frac{\boldsymbol{u}^{n+1}}{\boldsymbol{u}^n} = 1$ for the Crank-Nicolson scheme is the imaginary axis. This means that when a semi-discrete system with purely imaginary eigenvalues is marched in time using the Crank-Nicolson scheme, the amplitude of the solution is unchanged (no diffusive errors) which leads to the scheme conserving u^2 over time.

To assess these conservation properties of the numerical schemes, the conservation errors at each time step were computed and are shown in Figure 5.26 and Figure 5.27. Considering that the value of the conservation errors seen in Figure 5.26 is close to the level of machine round-off errors, it suggests that the schemes conserve the integral of u over time. However, like the parabolic case, a steady increase in the conservation error is observed due to some form of error accumulation.

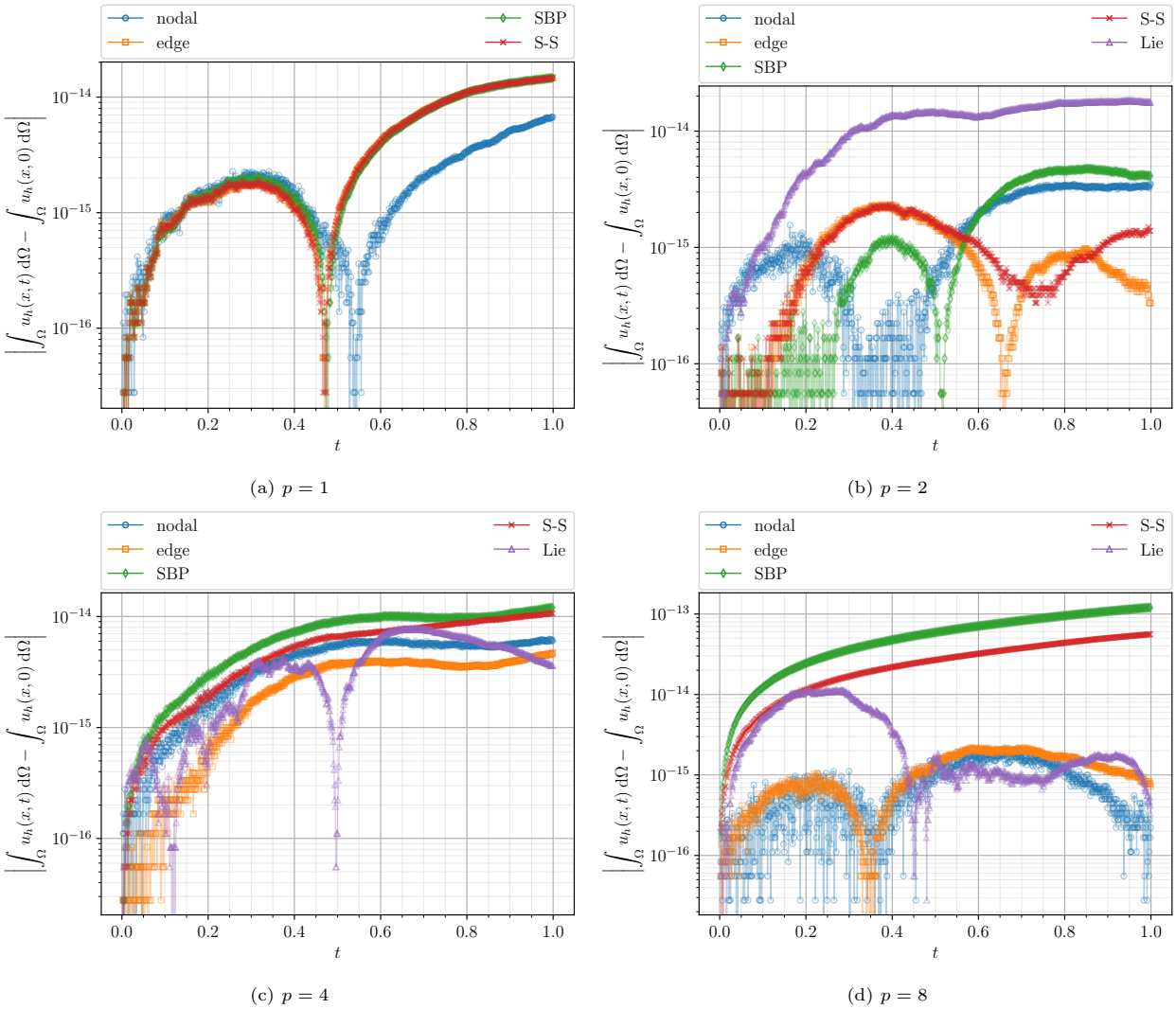

(a) $p = 1$

(b) $p = 2$

(c) $p = 4$

(d) $p = 8$

Figure 5.26: Conservation of the integral of the solution over time for the linear advection equation with different degree polynomials where $N = 8$ and $\Delta t = 1 \times 10^{-3}$

The conservation errors for u^2 have similar behaviour as for the conservation of u for the consistent schemes. Even the "Lie" scheme with $p = 2$ shows comparable conservation qualities as seen in Figure 5.27b. For larger p however, the conservation error of the "Lie" scheme is considerably higher than the rest. This error does tend to decrease for larger p but still significantly larger than the other schemes as seen through Figure 5.27c and Figure 5.27d.

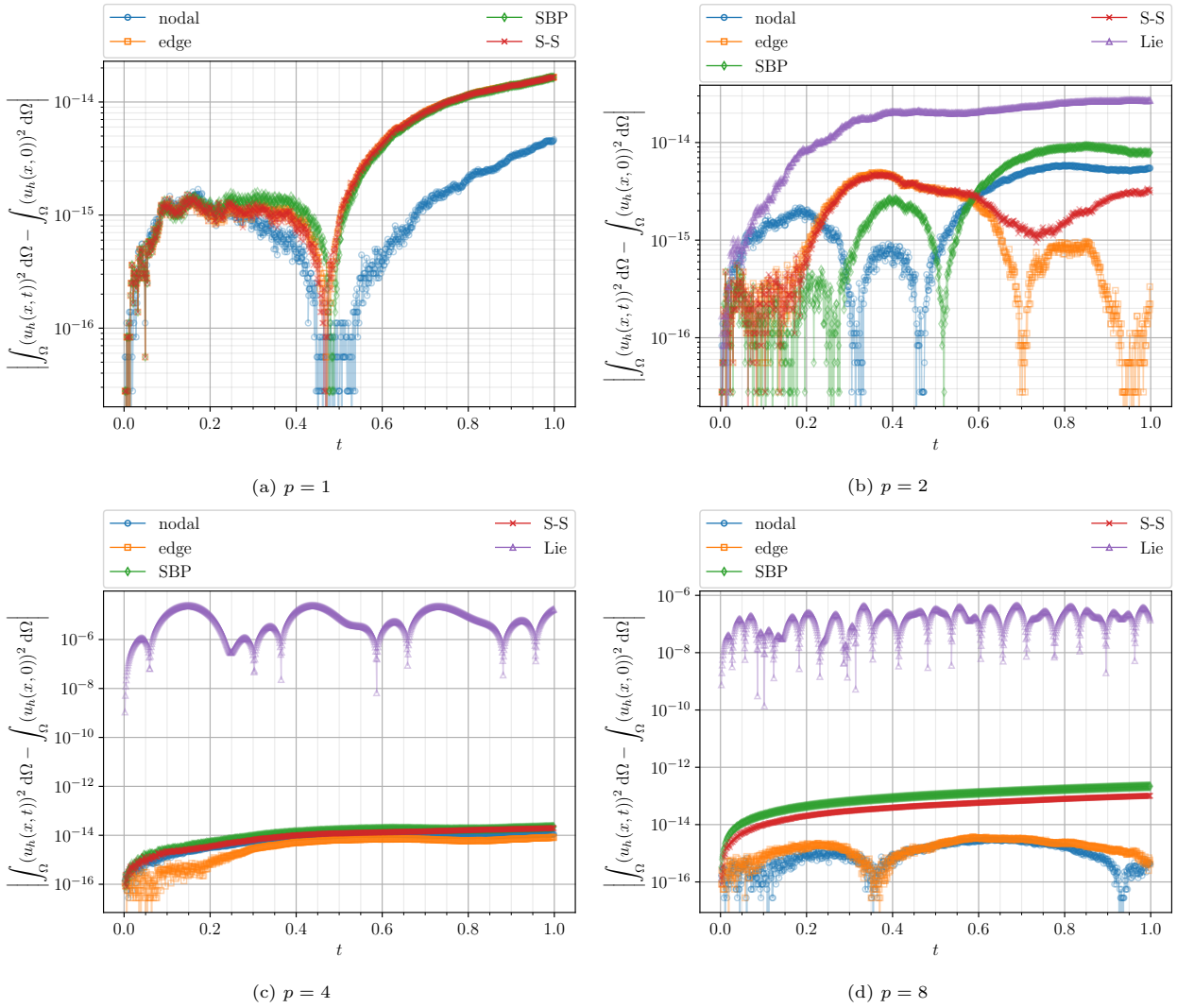

(a) $p = 1$

(b) $p = 2$

(c) $p = 4$

(d) $p = 8$

Figure 5.27: Conservation of the integral of the squared solution over time for the linear advection equation with different degree polynomials where $N = 8$ and $\Delta t = 1 \times 10^{-3}$

Once again, steady growth of the conservation error is observed. As previously mentioned, this growth is likely attributed to the conservation property of the discrete system being satisfied only up to machine round-off errors. As such the time march process accumulates some error in each time step. In Figure 5.20 this fact was highlighted by considering a test with a larger time step (taking fewer time steps). In a similar fashion, the same kind of observations can be made by considering many time steps as shown in Figure 5.28. Here, the schemes are marched in time up to $t = 100$ and the conservation errors appear to steadily grow to considerable values albeit at a slow rate.

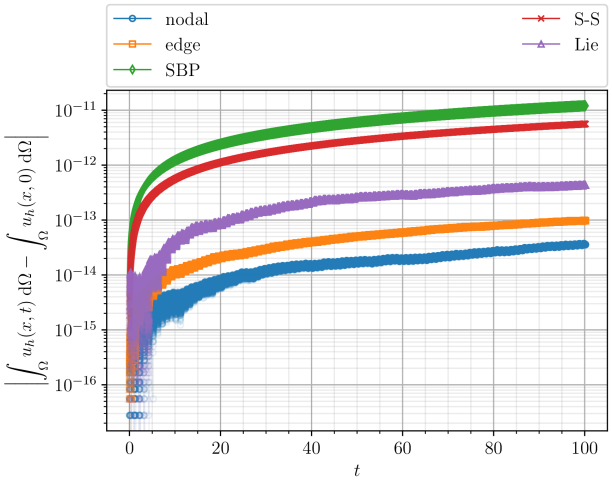

(a) Conservation of the integral of the solution

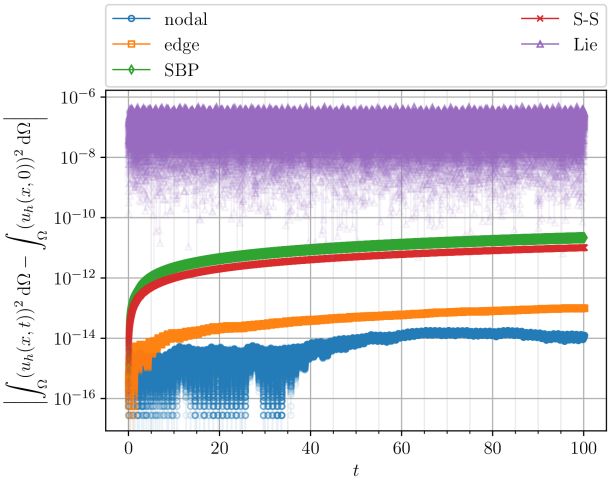

(b) Conservation of the integral of the squared solution

Figure 5.28: Conservation of the integral of the solution and the squared solution over a large time period for the linear advection equation with $N = 8$, $p = 8$, and $\Delta t = 1 \times 10^{-3}$

To further assess this idea of error accumulation, the conservation error between two consecutive time steps (t^{n+1} and t^n) are computed and plotted in Figure 5.29.

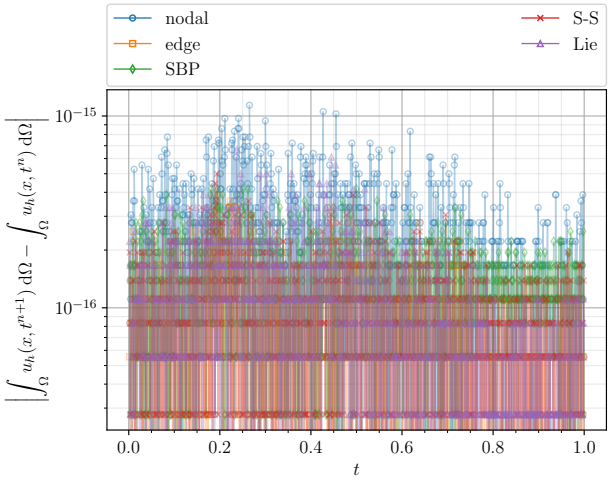

(a) Conservation of the integral of the solution over consecutive time steps

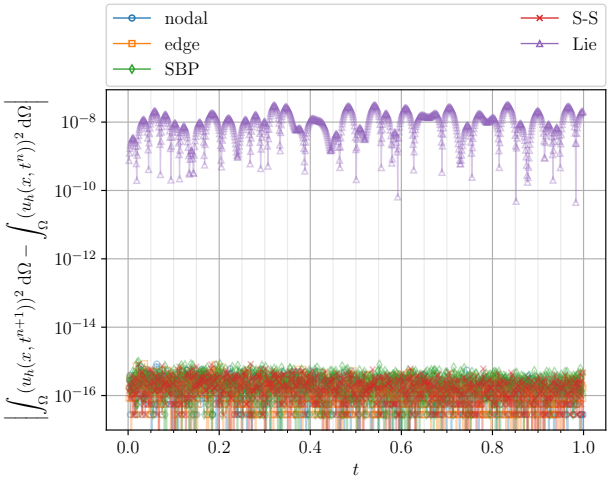

(b) Conservation of the integral of the squared solution over consecutive time steps

Figure 5.29: Conservation of the integral of the solution and the squared solution over each time step for the linear advection equation with $N = 8$, $p = 8$, and $\Delta t = 1 \times 10^{-3}$

As opposed to the error computed with respect to the initial condition, the error at each consecutive time step is always at the level of machine round-off error (except the conservation error of u^2 for the "Lie" scheme due to the aforementioned boundary inconsistency). An important thing to note here is that taking the sum of all these errors at each consecutive time step yields the exact conservation error value with respect to the initial condition at the final time level.

$$\sum_{n=0}^{N_{\Delta t}-1} \int_\Omega u_h(x,t^{n+1})\,\mathrm{d}\Omega - \int_\Omega u_h(x,t^n)\,\mathrm{d}\Omega = \int_\Omega u_h(x,t^{N_{\Delta t}})\,\mathrm{d}\Omega - \int_\Omega u_h(x,0)\,\mathrm{d}\Omega \tag{5.133}$$

Considering the sign of the error at each consecutive time step, one finds a bias in the sign of the error, that is the error is more often positive than it is negative or vice versa. This amounts to adding an error every time step in the order of machine round-off errors that has one specific sign (positive or negative) more often than the other, which causes an accumulation of errors over the time march. The exact origin for this positive bias is yet unknown, however, it can be speculated that it has something to do with the element-wise continuity constraint. Hyperbolic problems have their preferential direction of information transfer which is determined

by the characteristic lines. The current approach of transferring information between elements through the Lagrange multipliers does not consider this characteristic direction and therefore is capable of transferring information in any direction. Consequently, this multi-direction information transfer naturally tampers with the physics of the equations and is likely to be the cause of the observed error bias. This was found to have a more significant effect on non-linear problems than on linear problems thus, a more elaborate discussion on this topic is presented in the subsequent chapter. While this error growth issue may seem alarming, by simply taking a step back and considering the relative orders of magnitude reassures the quality of the derived schemes. Considering the fact that the sought solution and its integral properties are of order $1 \times 10^0 - 1 \times 10^1$ and the largest observed conservation error growth rate in Figure 5.28 is in the order of 1×10^{-16} per time step[6], it is safe to say that the error growth does not pose any significant threat to any practical application.

5.2.5. Variational Multiscale

Having concluded the results for both the parabolic and hyperbolic cases in the previous subsection, this subsection presents the discussion regarding the inclusion of VMS theory in the unsteady case. For this incorporation of multiscale theory into the derived Galerkin schemes, the standard multiscale split is applied:

$$\Lambda^{(k)}(\boldsymbol{\mathcal{M}}) = \Lambda_h^{(k)}(\boldsymbol{\mathcal{M}}) \oplus \Lambda^{(k)'}(\boldsymbol{\mathcal{M}}) \tag{5.134}$$

$$u^{(k)} := u_h + u' \tag{5.135}$$

$$v^{(k)} := v_h + v'. \tag{5.136}$$

Inserting this split into Equation (5.72) yields:

$$\int_\Omega \left(\frac{\partial (u_h + u')}{\partial t} + \mathscr{L}(u_h + u') \right) \wedge \star \, (v_h + v') = 0. \tag{5.137}$$

The equation can be simplified using the linearity of the time derivative and $\mathscr{L}$ which gives:

$$\int_\Omega \left(\frac{\partial u_h}{\partial t} + \frac{\partial u'}{\partial t} + \mathscr{L} u_h + \mathscr{L} u' \right) \wedge \star \, (v_h + v') = 0. \tag{5.138}$$

Alike the steady case, resolved scale equation is derived by setting $v' = 0$ and replacing the linear operator acting on u' with its adjoint[7]:

$$\int_\Omega \frac{\partial u_h}{\partial t} \wedge \star \, v_h + \int_\Omega \frac{\partial u'}{\partial t} \wedge \star \, v_h + \int_\Omega \mathscr{L} u_h \wedge \star \, v_h + \int_\Omega \mathscr{L} u' \wedge \star \, v_h = 0 \tag{5.139}$$

$$\int_\Omega \frac{\partial u_h}{\partial t} \wedge \star \, v_h + \int_\Omega \frac{\partial u'}{\partial t} \wedge \star \, v_h + \int_\Omega \mathscr{L} u_h \wedge \star \, v_h + \int_\Omega u' \wedge \star \, \tilde{\mathscr{L}} v_h = 0, \quad \text{where } \tilde{\mathscr{L}} := -c\frac{\partial}{\partial x} - \nu \frac{\partial^2}{\partial x^2}. \tag{5.140}$$

Similarly, setting $v_h = 0$ to derive un-resolved scale equation:

$$\int_\Omega \frac{\partial u_h}{\partial t} \wedge \star \, v' + \int_\Omega \frac{\partial u'}{\partial t} \wedge \star \, v' + \int_\Omega \mathscr{L} u_h \wedge \star \, v' + \int_\Omega \mathscr{L} u' \wedge \star \, v' = 0 \tag{5.141}$$

$$\int_\Omega \frac{\partial u'}{\partial t} \wedge \star \, v' + \int_\Omega \mathscr{L} u' \wedge \star \, v' = -\int_\Omega \left(\frac{\partial u_h}{\partial t} + \mathscr{L} u_h \right) \wedge \star \, v' \tag{5.142}$$

$$\int_\Omega \frac{\partial u'}{\partial t} \wedge \star \, v' + \int_\Omega \mathscr{L} u' \wedge \star \, v' = -\int_\Omega \mathscr{R} u_h \wedge \star \, v'. \tag{5.143}$$

Looking at the form of the un-resolved scale equation, it is evident that it involves the unsteady advection-diffusion operator acting on u' with the residual of the resolved scales as the source term. The issue here is that, unlike the steady case, a generic Greens' function for the unsteady case is not easily found. A slightly heuristic approach that can be applied is the assumption that the un-resolved scales' time derivative is zero which implies that these scales respond instantaneously and thus have no dynamics of their own. This assumption is commonly referred to as the quasi-steady sub-scales assumption [32, 43] and is described below.

[6] $\frac{10^{-11}}{10^5}$ given that there were 100,000 time steps

[7] the boundary terms are ignored due to periodic boundary conditions

Quasi-steady sub-scales

Invoking the quasi-steady sub-scale assumption, $\frac{\partial u'}{\partial t} = 0$, the un-resolved scale equation simplifies to the following:

$$\int_\Omega \mathscr{L}u' \wedge \star v' = -\int_\Omega \mathscr{R}u_h \wedge \star v' \tag{5.144}$$

$$\int_\Omega u' \wedge \star \tilde{\mathscr{L}}v' = -\int_\Omega \mathscr{R}u_h \wedge \star v'. \tag{5.145}$$

This form of the un-resolved scale equation is identical to the steady case presented earlier in the chapter. As such, the approximation for u' can be found in the same way by employing the element's Greens' function resulting in the expression for u' in the previously established form:

$$u' \approx -\tau(x)\mathscr{R}u_h. \tag{5.146}$$

Substituting this estimation for u' into the resolved scale equation and ignoring the temporal gradient of the un-resolved scales gives:

$$\underbrace{\int_\Omega \frac{\partial u_h}{\partial t} \wedge \star v_h + \int_\Omega \mathscr{L}u_h \wedge \star v_h}_{\mathbb{M}^{(k)}\frac{\partial \boldsymbol{u}}{\partial t} - \boldsymbol{A}\boldsymbol{u}} + \int_\Omega (-\tau\mathscr{R}_h u_h) \wedge \star \tilde{\mathscr{L}}v_h = 0. \tag{5.147}$$

The discrete form of the resolved component of the solution expressed as any *k-form* can be written as a semi-discrete system involving the *k-form* mass matrix and a discrete advection-diffusion operator like the one in Equation (5.82). Since the operator $\mathscr{L}$ is represented in the discrete setting by $\boldsymbol{A}$, and its adjoint operator ($\tilde{\mathscr{L}}$) can be proven to be $\tilde{\boldsymbol{A}} = -\boldsymbol{A}^T$. Thus, the semi-discrete system incorporating the multiscale term is then given by:

$$\frac{\partial \boldsymbol{u}}{\partial t} = \mathbb{M}^{(k)^{-1}}\left(\boldsymbol{A}\boldsymbol{u} - \tilde{\boldsymbol{A}}(-\boldsymbol{\tau}\mathscr{R}_h u_h)\right), \tag{5.148}$$

where $\mathscr{R}_h$ is the discrete residual operator. For the sake of demonstration, consider u to be expressed as a *0-form* which gives the following form for the residual operator:

$$\mathscr{R}_h u_h = \frac{\boldsymbol{u}^{n+1} - \boldsymbol{u}^n}{\Delta t} + \underbrace{\left[\boldsymbol{\psi}^{(1)}(\boldsymbol{x})\left(c\,\mathbb{E}^{1,0}\right) - \boldsymbol{\psi}^{(0)}(\boldsymbol{x})\mathbb{M}^{(0)^{-1}}\left(\nu\left(-\mathbb{E}^{1,0^T}\mathbb{M}^{(1)} + \mathbb{N}_1\mathbb{B}\right)\mathbb{E}^{1,0}\right)\right]}_{\boldsymbol{\mathcal{R}}}\boldsymbol{u}^{n+\frac{1}{2}}. \tag{5.149}$$

Discretising $\frac{\partial \boldsymbol{u}}{\partial t}$ using the Crank-Nicolson scheme gives the following fully discrete system:

$$\frac{\boldsymbol{u}^{n+1} - \boldsymbol{u}^n}{\Delta t} = \frac{1}{2}\boldsymbol{A}^{(0)}\left(\boldsymbol{u}^{n+1} + \boldsymbol{u}^n\right) + \frac{1}{\Delta t}\tilde{\boldsymbol{A}}^{(0)}\boldsymbol{\tau}\left(\boldsymbol{u}^{n+1} - \boldsymbol{u}^n\right) + \frac{1}{2}\tilde{\boldsymbol{A}}^{(0)}\boldsymbol{\tau}\boldsymbol{\mathcal{R}}\left(\boldsymbol{u}^{n+1} + \boldsymbol{u}^n\right). \tag{5.150}$$

At this point, the conservation properties of the discrete system can already be assessed using the criteria stated in Equation (5.123) and Equation (5.126). The derived system satisfies Equation (5.123) which ensures that the scheme will preserve the integral of u over time. The evolution u^2 on the other hand proves to be suboptimal for the hyperbolic case. Considering the evolution equation u^2 derived by testing Equation (5.150) with $\boldsymbol{u}^{n+\frac{1}{2}}$ gives:

$$\begin{aligned}\frac{1}{2}\left(\boldsymbol{u}^{n+1} + \boldsymbol{u}^n\right)^T \frac{\boldsymbol{u}^{n+1} - \boldsymbol{u}^n}{\Delta t} = \cancel{\frac{1}{4}\left(\boldsymbol{u}^{n+1} + \boldsymbol{u}^n\right)^T \boldsymbol{A}^{(0)}\left(\boldsymbol{u}^{n+1} + \boldsymbol{u}^n\right)} + \\ \frac{1}{2\Delta t}\left(\boldsymbol{u}^{n+1} + \boldsymbol{u}^n\right)^T \tilde{\boldsymbol{A}}^{(0)}\boldsymbol{\tau}\left(\boldsymbol{u}^{n+1} - \boldsymbol{u}^n\right) + \frac{1}{4}\left(\boldsymbol{u}^{n+1} + \boldsymbol{u}^n\right)^T \tilde{\boldsymbol{A}}^{(0)}\boldsymbol{\tau}\boldsymbol{\mathcal{R}}\left(\boldsymbol{u}^{n+1} + \boldsymbol{u}^n\right)\end{aligned} \tag{5.151}$$

$$\frac{1}{2}\frac{(\boldsymbol{u}^{n+1})^2 - (\boldsymbol{u}^n)^2}{\Delta t} = \frac{1}{\Delta t}\left(\boldsymbol{u}^{n+\frac{1}{2}}\right)^T \tilde{\boldsymbol{A}}^{(0)}\boldsymbol{\tau}\left(\boldsymbol{u}^{n+1} - \boldsymbol{u}^n\right) + \left(\boldsymbol{u}^{n+\frac{1}{2}}\right)^T \tilde{\boldsymbol{A}}^{(0)}\boldsymbol{\tau}\boldsymbol{\mathcal{R}}\boldsymbol{u}^{n+\frac{1}{2}}, \tag{5.152}$$

where the first term on the right cancels given that the base Galerkin scheme conserves the integral of u^2 for hyperbolic cases. The additional terms introduced through multiscale theory do not cancel in the hyperbolic case suggesting that the conservation of u^2 is destroyed. Moreover, numerical tests with this scheme showed growth of u^2 over time which is far from ideal. The cases in the literature that do employ the quasi-steady

sub-scales assumption eg [28, 32, 43] do not address this energy-conserving property for the hyperbolic case. Instead, they focus predominately on parabolic problems where the multiscale term acts to add artificial viscosity to stabilise the system.

This issue of conserving u^2 in time in the hyperbolic case can be attributed to the fact that the construction of u' is incorrect since the exact u' would have the conservation properties. The main culprit of the incorrect u' can be thought to be the quasi-steady sub-scales assumption. Hence, an alternative formulation must be considered in order to satisfy the desired conservation properties. For ease of implementation, it would be ideal to have a formulation where neglecting the time derivative is mathematically justified.

Dynamic orthogonal sub-scales

The work in [44] on orthogonal sub-scales is a promising approach to consider where the time derivative exactly cancels from the resolved scale equation. In this framework, u' is constrained to be orthogonal to the resolved space $\Lambda_h^{(k)}(\boldsymbol{\mathcal{M}})$ in a L^2 sense as follows:

$$\int_\Omega v_h u' \,\mathrm{d}\Omega = -\int_\Omega v_h \tau \mathscr{R} u_h \,\mathrm{d}\Omega + \int_\Omega v_h \tau \boldsymbol{V}_{h,ort} \,\mathrm{d}\Omega = 0, \qquad \forall v_h \in \Lambda_h^{(k)}(\boldsymbol{\mathcal{M}}), \tag{5.153}$$

where $\boldsymbol{V}_{h,ort}$ is the projection of the residual onto the test space. The orthogonal u' is thus given by:

$$u' \approx -\tau(\mathscr{R} u_h - \boldsymbol{V}_{h,ort}) = -\tau \Pi_\tau^\perp \mathscr{R} u_h. \tag{5.154}$$

Since energy conservation in the hyperbolic case is the problem of interest, diffusion shall be ignored and the orthogonal residual operator for the linear hyperbolic problem reads:

$$\mathscr{R}_h u_h = \frac{\boldsymbol{u}^{n+1} - \boldsymbol{u}^n}{\Delta t} + \underbrace{\left[\boldsymbol{\psi}^{(1)}(\boldsymbol{x}) \left(c\, \mathbb{E}^{1,0}\right)\right]}_{\boldsymbol{\mathcal{R}}} \frac{1}{2}(\boldsymbol{u}^{n+1} + \boldsymbol{u}^n) \tag{5.155}$$

$$\Pi_\tau^\perp \mathscr{R} u_h = \left[\boldsymbol{\mathcal{R}} - c\, \mathbb{M}_\tau^{(0)^{-1}} \mathbb{M}_\tau^{(0,1)} \mathbb{E}^{1,0}\right] \frac{1}{2}(\boldsymbol{u}^{n+1} + \boldsymbol{u}^n). \tag{5.156}$$

Constructing this residual operator for the linear problem where the matrices $\mathbb{M}_\tau^{(0)^{-1}}$ and $\mathbb{M}_\tau^{(0,1)}$ are computed using a high degree of precision quadrature, leads to the residual operator attaining zeros in all its entries for all τ:

$$\Pi_\tau^\perp \mathscr{R} u_h = 0. \tag{5.157}$$

Consequently, the use of this orthogonal residual in the unresolved scale equation gives:

$$\int_\Omega \frac{\partial u'}{\partial t} \wedge \star\, v' + \int_\Omega \mathscr{L} u' \wedge \star\, v' = -\int_\Omega \Pi_\tau^\perp \mathscr{R} u_h \wedge \star\, v' = 0, \tag{5.158}$$

of which the corresponding strong form of the un-resolved scale equation reads:

$$\frac{\partial u'}{\partial t} + \mathscr{L} u' = 0. \tag{5.159}$$

This equation simply describes the transport of u' over time with no energy exchange with the resolved scales as the source term is zero. This is a physically sound result as the linear advection equation simply acts to advect (phase shift) the different wave numbers independently without exchanging any energy between the wave numbers. This holds true in the discrete setting as well given that the base Galerkin scheme is energy-conserving.

Given that this orthogonal sub-scales approach yields the correct physical behaviour of the un-resolved scales, this was the chosen approach to be studied. Applying this orthogonal sub-scale approach yields the following resolved scale equation:

$$\int_\Omega \frac{\partial u_h}{\partial t} \wedge \star\, v_h + \cancel{\int_\Omega \frac{\partial u'}{\partial t} \wedge \star\, v_h} + \int_\Omega \mathscr{L} u_h \wedge \star\, v_h + \int_\Omega u' \wedge \star\, \tilde{\mathscr{L}} v_h = 0. \tag{5.160}$$

Given the simplicity of this linear problem, the modelling of u' was done using the strong form itself. For modelling u', the following two questions need answering:

- How to represent u' such that it is orthogonal to the resolved test space?

- How to evolve u' in time?

The first question inevitably determines the desired spatial projection of the exact solution. A suitable projection for this advection case is the L^2 projection which is one that was chosen. Given the solution (test) space comprises Lagrange polynomials of degree p, it is known that Legendre polynomials of degree $p+1$ and above are exactly orthogonal to the solution space. Thus, u' may be expressed using the set of Legendre polynomials of degree greater than or equal to $p+1$. Obtaining this representation requires interpolation of the initial condition. Consider two methods to interpolate the initial condition for u_h and u'. **Method 1:** First interpolate the initial condition with the resolved function space (Lagrange polynomials of p^{th} degree) to obtain u_h, then compute u' by taking the difference between the exact u and u_h. Finally, interpolate this u' using the orthogonal subspace of the un-resolved scales (Legendre polynomials of degree $p+1$ and higher); **Method 2:** First interpolate the initial condition using the full set of Legendre polynomials, then find u' by setting the coefficients of the non-orthogonal functions (polynomials of degree p and lower) to zero. Next, find u_h by taking the difference between u and u' and interpolating using Lagrange polynomials (resolved function space). The interpolated (discrete) u' is referred to as $\tilde{u}'$ where Legendre polynomials of degree $p+1$ up-to $p+3$ were used for both interpolation methods.

The two methods yield different solutions for the interpolation of the initial condition. The corresponding discrete representations of the resolved and un-resolved components found using the two methods are shown in Figure 5.30 and Figure 5.31.

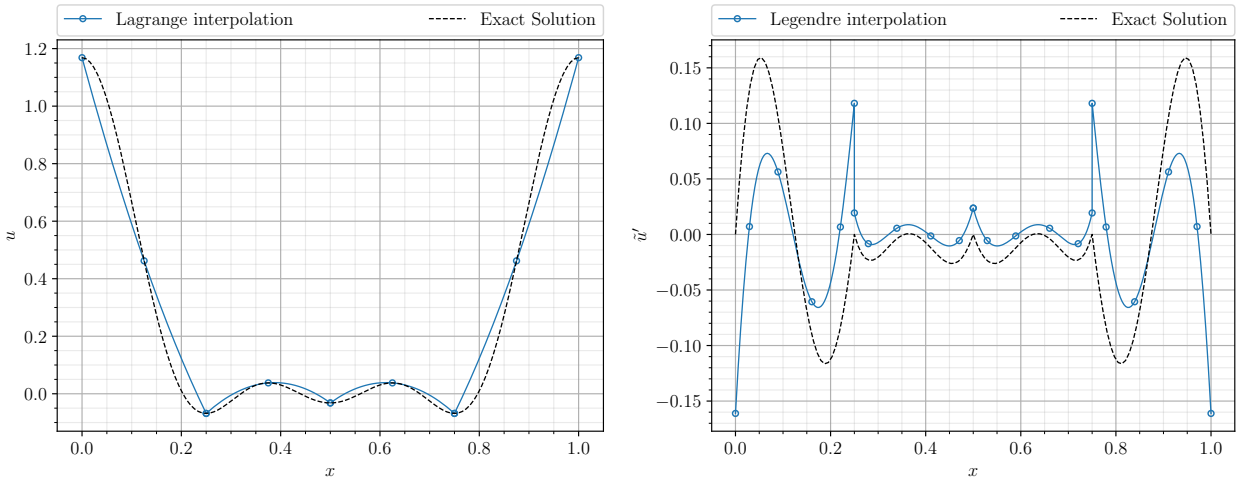

(a) Resolved component of the initial condition

(b) Un-resolved component of the initial condition

Figure 5.30: Interpolation of the resolved and un-resolved components of the initial condition using Method 1

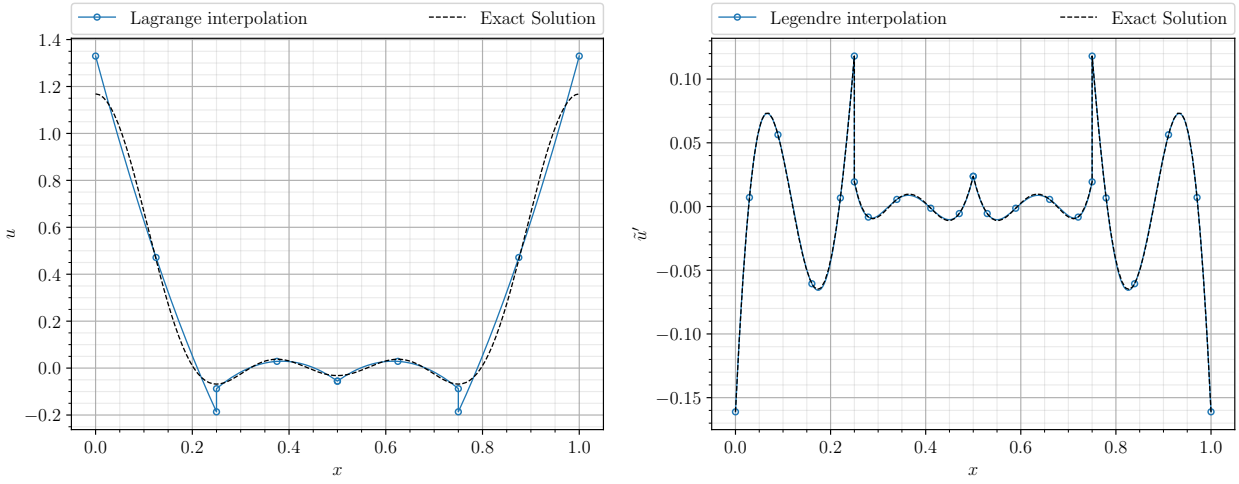

(a) Resolved component of the initial condition

(b) Un-resolved component of the initial condition

Figure 5.31: Interpolation of the resolved and un-resolved components of the initial condition using Method 2

Comparing the total solution $u_h + \tilde{u}'$ produced by the two methods in Figure 5.32 below, clearly shows that Method 2 is the better approach. The reason for Method 1 being worse is due to the fact that it attempts to interpolate u' using purely higher degree polynomials which results in the Galerkin (L^2) interpolation missing the low order components of the solution.

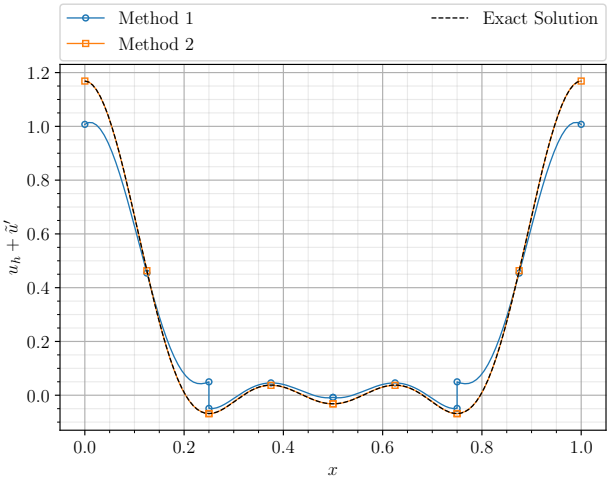

Figure 5.32: Comparison of the total solution $u_h + \tilde{u}'$ produced by the two methods for the interpolation of the initial condition

With the approach for representing u' established, the next step was to tackle the second question for modelling u' in time. This step may be viewed as selecting the desired projection of the solution in time. This, however, is a difficult task as there is no natural/generalisable way to link the resolved scale's time march with the time evolution of the un-resolved scales in the current framework. More specifically, the point to consider here is that the Galerkin scheme with the Crank-Nicolson time march on coarse meshes is subject to dispersive errors along with the poor transfer of information at the element boundaries through the Lagrange multipliers. Without a general approach to pass the mentioned deficiencies to the un-resolved scale time evolution while conserving u and u^2, the time evolution approach for u' was chosen to be the one that reflects the (uncoupled) strong form in Equation (5.159). This was achieved by employing a simple phase shift operator over time which first evaluates u' at the nodes $c\Delta t$ upstream of the collocation nodes (integration points for interpolation) and puts that value as the new solution value at the collocation point. This phase shift operation is simply mimicking the method of characteristics approach.

Bringing everything together into a discrete setting where u_h is simply expressed as a *0-form* yields:

$$\frac{\partial \boldsymbol{u}}{\partial t} = -c\,\mathbb{M}^{(0)^{-1}}\mathbb{M}^{(0,1)}\mathbb{E}^{1,0}\boldsymbol{u} + c\,\mathbb{M}^{(0)^{-1}}\mathbb{E}^{1,0^T}\mathbb{M}^{(1,\mathcal{P})}\tilde{\boldsymbol{u}}' \tag{5.161}$$

$$\frac{\boldsymbol{u}^{n+1} - \boldsymbol{u}^n}{\Delta t} = \boldsymbol{A}\boldsymbol{u}^{n+\frac{1}{2}} + \boldsymbol{B}\tilde{\boldsymbol{u}}'^{n+\frac{1}{2}} \tag{5.162}$$

$$\tilde{\boldsymbol{u}}'^{n+\frac{1}{2}} = \mathbb{P}_{\frac{1}{2}c\Delta t}\tilde{\boldsymbol{u}}'^{n} \tag{5.163}$$

Here, $\mathbb{M}^{(1,\mathcal{P})}$ represents the L^2 inner product between the *1-form* resolved basis and the higher degree Legendre polynomials used to represent u', and $\mathbb{P}_{\frac{1}{2}c\Delta t}$ is the phase shift operator. Analysing the discrete systems at this stage already gives an a priori impression of solution behaviour. Firstly, one finds that $\mathbb{M}^{(1,\mathcal{P})}$ is exactly zero given that un-resolved scales are not only orthogonal to resolved space of p^{th} order polynomials, they are also orthogonal to $p-1$ order polynomials (*1-form* edge basis) used to represent the derivative. This yields two uncoupled sets of time evolution equations for the resolved and un-resolved scales much like how one would expect for the physical continuous case. The issue, however, is that the errors in the discrete resolved scales are not perceived nor accounted for by the un-resolved scales. Naturally, it is possible to employ the method of characteristic approach for the resolved scales as well for this linear problem whereby the aforementioned issues with dispersion and weak continuity constraints can be eliminated. However, that approach is specific to this problem and cannot be generalised.

5.2.6. Numerical experiments with VMS

Having already discussed the solution behaviour of the derived system in the previous subsection, this subsection purely serves as a formality to present the obtained numerical solution and its properties. The test case

considered in this subsection is the same as the previous one with Equation (5.111) as the initial condition and periodic boundaries. Considering the time evolution of the solution with and without VMS in Figure 5.33, there is no significant difference and thus no significant gain. The main difference between the two is seen in the initial condition, and a very short time after. This observation comes as no surprise given that the derived approach for u' is unaware of the time evolution of the resolved scales.

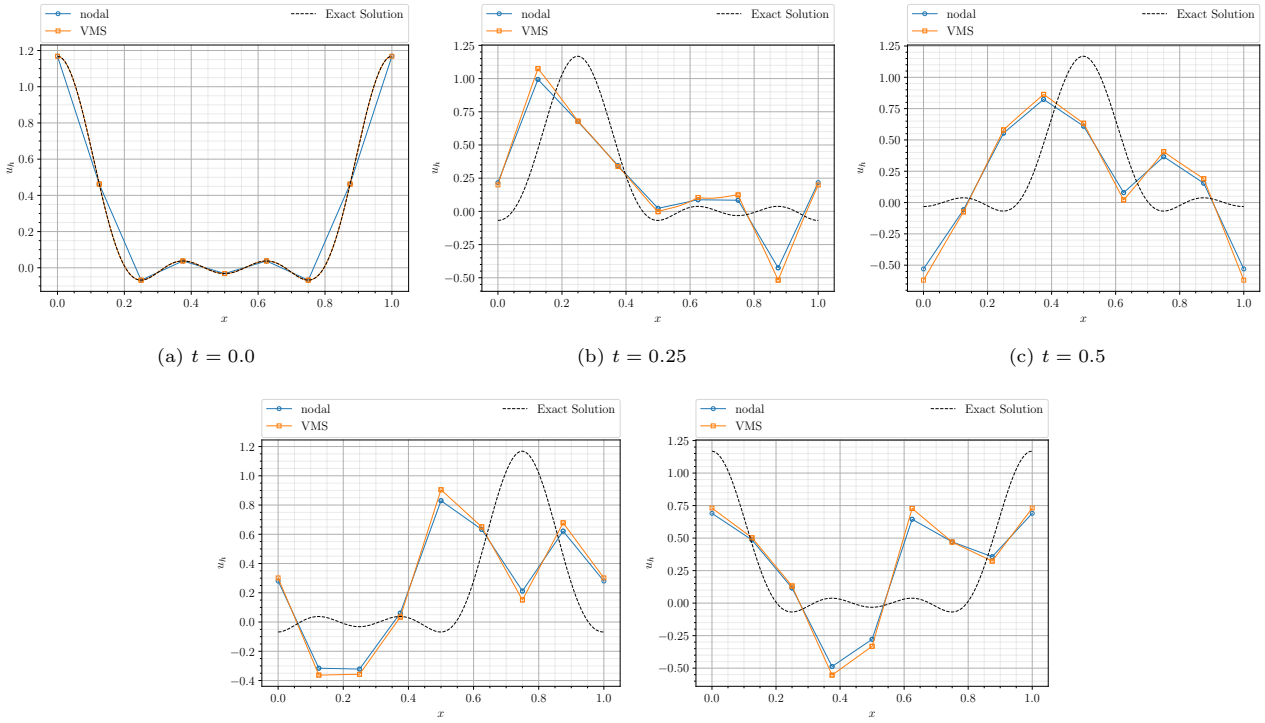

(a) $t = 0.0$ (b) $t = 0.25$ (c) $t = 0.5$

(d) $t = 0.75$ (e) $t = 1.0$

Figure 5.33: Time evolution of the solutions to the linear advection equation with and without VMS for $N = 8$, $p = 1$, and $\Delta t = 1 \times 10^{-3}$

Similarly, considering the L^2 error of the solution with and without VMS in Figure 5.34 shows that there is no significant improvement achieved through multiscale theory in the considered framework. Some cases are marginally worse than the base Galerkin scheme and some are marginally better, but not in a significant amount.

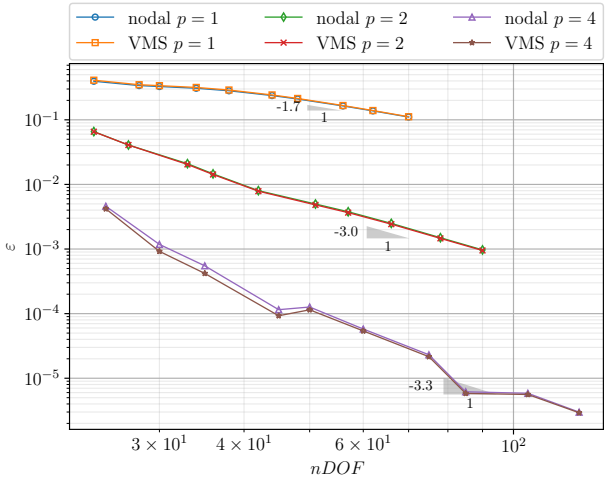

Figure 5.34: h-convergence of the Galerkin and multiscale solutions to the linear advection problem computed in the L^2 error norm using the exact solution at $t = 1$

The advantage of this framework, however, is seen in the conservation qualities of the scheme. As shown in

Figure 5.35 and Figure 5.36, the formulation conserves the integral of the resolved scales as well as the squared resolved scales. Moreover, the plots in Figure 5.37 and Figure 5.38 show the conservation errors of u'. Lastly, the conservation errors of the total solution $u_h + u'$ are shown in Figure 5.39 and Figure 5.40 where both the integral of the solution and the squared integral of the solution are conserved.

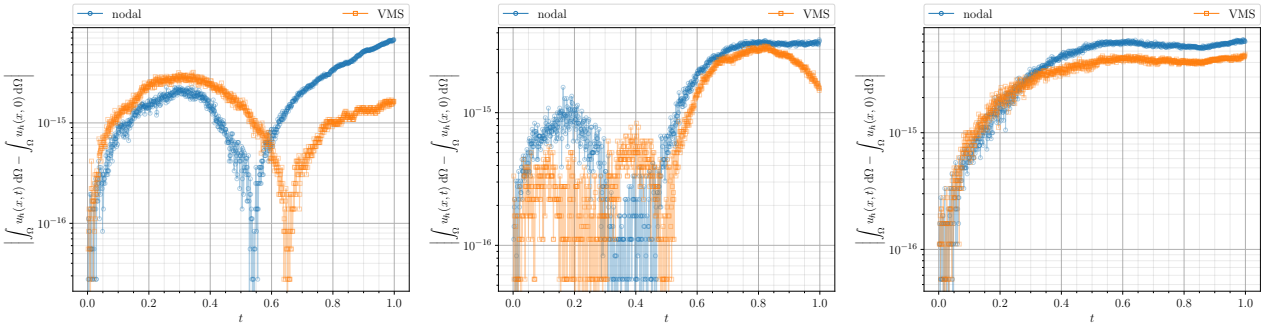

(a) $p = 1$ (b) $p = 2$ (c) $p = 4$

Figure 5.35: Conservation of the integral of the resolved scales over time for the linear advection equation with and without VMS using different degree polynomials where $N = 8$ and $\Delta t = 1 \times 10^{-3}$

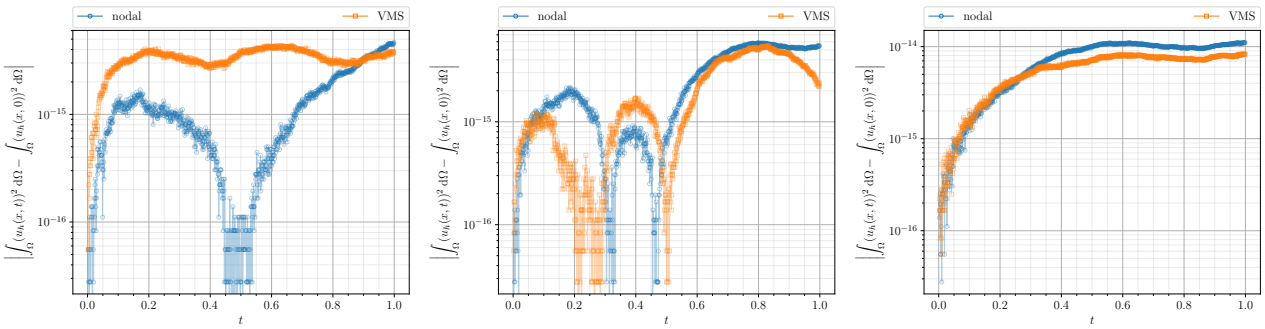

(a) $p = 1$ (b) $p = 2$ (c) $p = 4$

Figure 5.36: Conservation of the integral of the squared resolved scales over time for the linear advection equation with and without VMS using different degree polynomials where $N = 8$ and $\Delta t = 1 \times 10^{-3}$

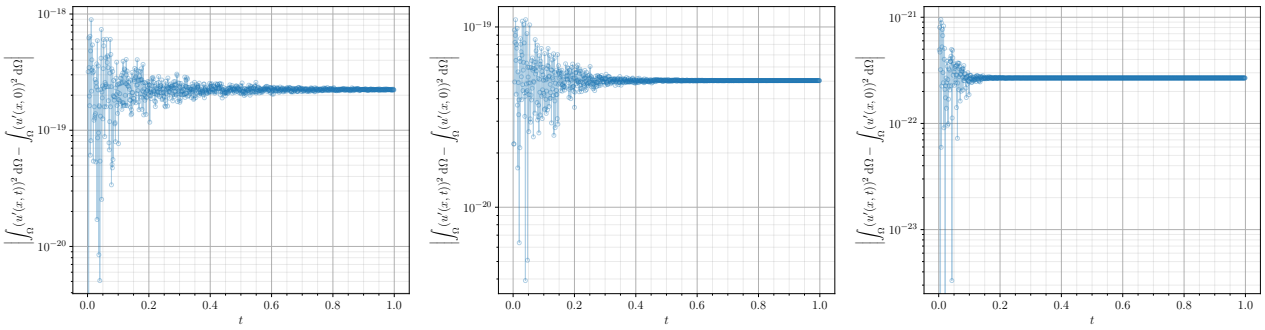

(a) $p = 1$ (b) $p = 2$ (c) $p = 4$

Figure 5.37: Conservation of the integral of the un-resolved scales over time for the linear advection equation using different degree polynomials where $N = 8$ and $\Delta t = 1 \times 10^{-3}$

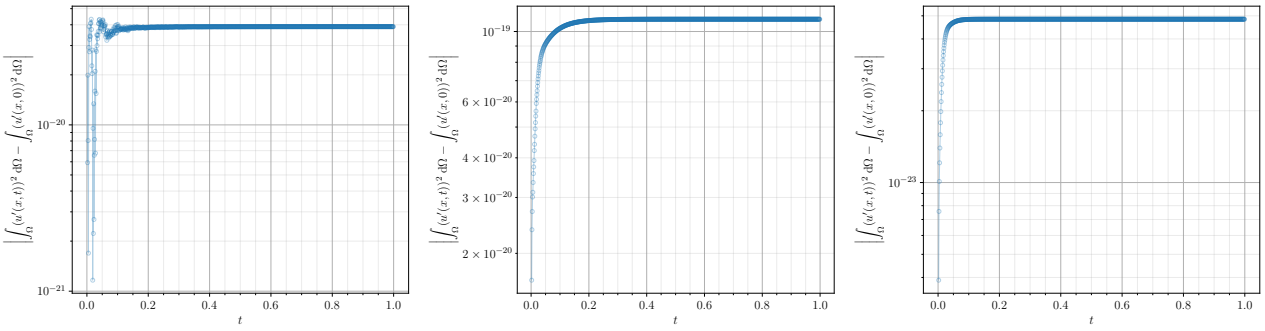

(a) $p = 1$ (b) $p = 2$ (c) $p = 4$

Figure 5.38: Conservation of the integral of the squared un-resolved scales over time for the linear advection equation using different degree polynomials where $N = 8$ and $\Delta t = 1 \times 10^{-3}$

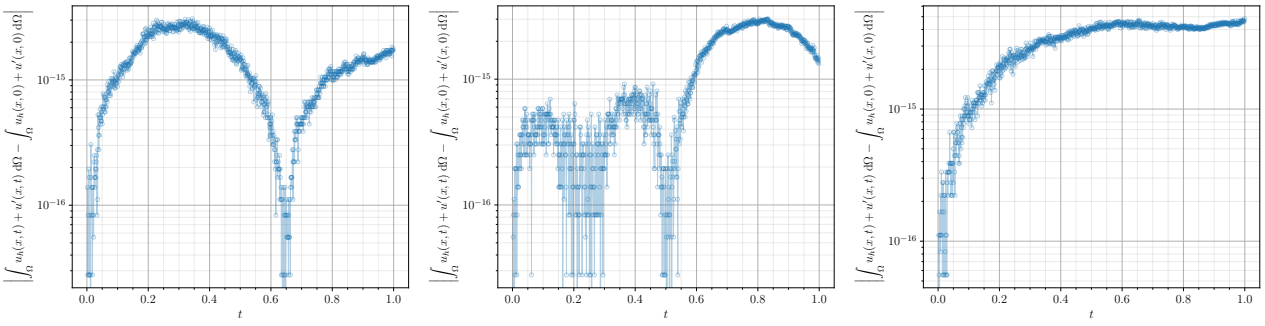

(a) $p = 1$ (b) $p = 2$ (c) $p = 4$

Figure 5.39: Conservation of the integral of the total solution $(u_h + u')$ over time for the linear advection equation using different degree polynomials where $N = 8$ and $\Delta t = 1 \times 10^{-3}$

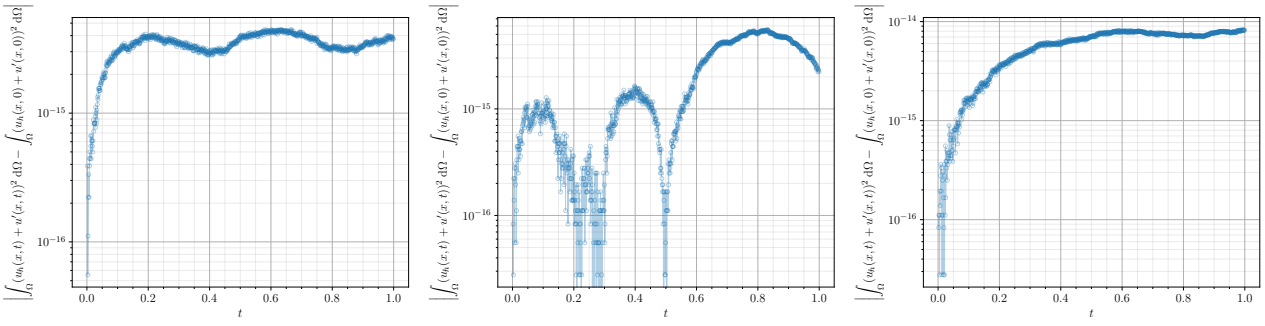

(a) $p = 1$ (b) $p = 2$ (c) $p = 4$

Figure 5.40: Conservation of the integral of the squared total solution $(u_h + u')^2$ over time for the linear advection equation using different degree polynomials where $N = 8$ and $\Delta t = 1 \times 10^{-3}$

6

Non-Linear problems

Having considered the linear advection problems in the preceding chapter, the focus is now turned to slightly more complex non-linear problems. The specific problems considered in this chapter are the 1D Burgers' equation, which is treated in Section 6.1, and the 2D incompressible Navier-Stokes/Euler equations, which is treated in Section 6.2. Note that the incorporation of multiscale theory is excluded for the non-linear problems as the development of sub-scale models for such problems goes out of the scope of the present study. Thus, the primary focus of this chapter is on applying the hybrid mimetic method to non-linear problems.

6.1. 1D Burgers'

The governing equation and problem set up for the 1D Burgers' equation reads:

$$\frac{\partial u}{\partial t} + u\frac{\partial u}{\partial x} = 0, \qquad x \in \Omega \in]0,1[\tag{6.1}$$

$$u(0,t) = u(1,t), \qquad \forall t \geq 0 \tag{6.2}$$

$$u(x,0) = f(x). \tag{6.3}$$

Similar to the linear advection case, the considered domain for this problem is a periodic domain ranging between 0 and 1. This particular problem is characterised as a first-order hyperbolic equation where the exact solution for smooth (shock-free) cases can be found to be the following based on the method of characteristics:

$$u(x,t) = u(x - u(x,0)t, 0) = f(x - f(x)t). \tag{6.4}$$

In contrast to the linear case where the advection speed is a known value that is imposed on the problem, the advection speed for Burgers' equation is the solution itself. As such, this particular model equation describes the self-advection of u over time where the initial distribution of the quantity is described by $f(x)$. This property of the governing equation causes the solution to develop shocks in a finite amount of time even for smooth initial conditions if $\frac{\partial f}{\partial x} < 0$. The exact time instance at which a shock will form for a given initial condition can be computed as follows:

$$T_{shock} = -\frac{1}{\min\left(\frac{\partial f}{\partial x}\right)}. \tag{6.5}$$

The method of characteristics breaks down when shocks are formed, which forces one to seek weak solutions to the governing PDE [45]. Since the weak solutions are not unique, the approach for selecting the most physical weak solution is by employing the concept of entropy. This can be done by selecting a convex entropy function $\eta(u)$ and its corresponding entropy flux $q(u)$ where the physical weak solutions satisfy:

$$\frac{\partial \eta(u)}{\partial t} + \frac{q(u)}{x} \leq 0. \tag{6.6}$$

In the shock-free case, the entropy is conserved, which gives:

$$\frac{\partial \eta(u)}{\partial t} + \frac{q(u)}{x} = 0. \tag{6.7}$$

Despite the simplicity of Burgers' equation, it captures the key essence of non-linear advection typically encountered in the case of Navier-Stokes or Euler equations. Moreover, the non-linear advection term can be expressed in various ways, much like the Navier-Stokes case, of which the two common forms are the conservative and advective forms described below:

$$\textit{Conservative form} : \mathscr{N}(u) := \frac{1}{2}\frac{\partial u^2}{\partial x} \tag{6.8}$$

$$\textit{Advective form} : \mathscr{N}(u) := u\frac{\partial u}{\partial x} \tag{6.9}$$

The two forms are mathematically equivalent to one another based on the product rule applied to $\frac{\partial u^2}{\partial x}$. However, it is worth noting that the two forms are not algebraically similar. To elaborate on that, consider the Navier-Stokes equations where both the conservative $\left(\vec{\nabla} \cdot (\rho \underline{u} \otimes \underline{u})\right)$ and the advective $\left((\underline{u} \cdot \vec{\nabla})(\rho \underline{u})\right)$ forms can be algebraically equated to one another by invoking conservation of mass (density). This algebraic relation between the two advection forms is absent in the case of Burgers', as the governing equation is strictly an advection model and does not represent anything physical.

This section can be viewed as the extension of the linear advection cases presented in Section 5.2, to the non-linear case. Firstly the Galerkin weak forms are derived in Section 6.1.1 for various of formulations of the continuous equation and *k-form* representations of the solution. Thereafter, their discretisation using the mimetic SEM is presented in Section 6.1.2 where the goal is to conserve the integral of u, u^2, and entropy $-\ln(u)$. Lastly, the results of the test cases with and without shocks are discussed in Section 6.1.4 and Section 6.1.3 respectively.

6.1.1. Continuous form

Building on the ideas from the linear advection case, the derivation of the weak form for different formulations of the 1D Burgers' equation is first considered. The weak form for u expressed as a generic *k-form* is found by testing the governing equation with a test function $v^{(k)}$:

$$\int_\Omega \left(\frac{\partial u^{(k)}}{\partial t} + \mathscr{N}(u^{(k)})\right) \wedge \star\, v^{(k)} = 0, \qquad \forall v \in \Lambda^{(k)}(\boldsymbol{\mathcal{M}}). \tag{6.10}$$

Following a similar procedure as for the linear case, u is first expressed as a *0-form* in the primal space. Starting with the advective form, the corresponding Galerkin weak form is given by:

$$\int_\Omega \frac{\partial u^{(0)}}{\partial t} \wedge \star\, v^{(0)} + \int_\Omega i_u \circ \mathrm{d}u^{(0)} \wedge \star\, v^{(0)} = 0, \tag{6.11}$$

where the Lie derivative is used to represent the advection term. Similarly, the weak form for the conservative form of the advection term with u as a *0-form* is given by:

$$\int_\Omega \frac{\partial u^{(0)}}{\partial t} \wedge \star\, v^{(0)} + \frac{1}{2}\int_\Omega \mathrm{d}\left(u^{(0)}\right)^2 \wedge \star\, v^{(0)} = 0. \tag{6.12}$$

As done previously for the linear case, u can also be expressed as a *1-form* in the dual space resulting in the following weak form:

$$\int_\Omega \frac{\partial \tilde{u}^{(1)}}{\partial t} \wedge \star\, \tilde{v}^{(1)} + \frac{1}{2}\int_\Omega \mathrm{d}\left(\star\tilde{u}^{(1)}\right)^2 \wedge \star\, \tilde{v}^{(1)} = 0. \tag{6.13}$$

The advection operator can also be moved to the test function yielding the adjoint operator where, once again, the boundary terms are neglected given the periodic boundary conditions.

$$\int_\Omega \frac{\partial \tilde{u}^{(1)}}{\partial t} \wedge \star\, \tilde{v}^{(1)} - \frac{1}{2}\int_\Omega \left(\tilde{u}^{(1)}\right)^2 \wedge \star\, \mathrm{d} \star\, \tilde{v}^{(1)} = 0. \tag{6.14}$$

Taking the linear combination of Equation (6.13) and Equation (6.14) with a factor $\frac{1}{2}$ applied to each equation yields the Skew-Symmetric form of the advection operator.

$$\int_\Omega \frac{\partial \tilde{u}^{(1)}}{\partial t} \wedge \star\, \tilde{v}^{(1)} + \frac{1}{4}\left(\int_\Omega \mathrm{d}\left(\star\tilde{u}^{(1)}\right)^2 \wedge \star\, \tilde{v}^{(1)} - \int_\Omega \left(\tilde{u}^{(1)}\right)^2 \wedge \star\, \mathrm{d} \star\, \tilde{v}^{(1)}\right) = 0. \tag{6.15}$$

Finally, defining u as a *1-form* in the primal space yields the following weak form where the Lie derivative makes its appearance:

$$\int_\Omega \frac{\partial u^{(1)}}{\partial t} \wedge \star v^{(1)} + \frac{1}{2} \int_\Omega \mathrm{d} \circ i_{\underline{\mathrm{u}}} u^{(1)} \wedge \star v^{(1)} = 0, \qquad \text{where } \underline{\mathrm{u}} := \sharp u^{(1)}. \tag{6.16}$$

The corresponding vector field used in the interior product is the velocity vector $\underline{\mathrm{u}}$ which is found by applying the sharp operator to the *1-form*.

6.1.2. Discrete form

With the weak forms in place, their respective discrete systems are derived in this subsection. Starting off with Equation (6.11), substituting int the following discrete representation:

$$u_h := \boldsymbol{\psi}^{(0)} \boldsymbol{u}, \quad \in \Lambda_h^{(0)}(\boldsymbol{\mathcal{M}}) \tag{6.17}$$

$$v_h := \boldsymbol{\psi}^{(0)} \boldsymbol{v}, \quad \in \Lambda_h^{(0)}(\boldsymbol{\mathcal{M}}), \tag{6.18}$$

yields the following non-linear semi-discrete system:

$$\boldsymbol{v}^T \left[\int_{\Omega_h} \boldsymbol{\psi}^{(0)^T} \boldsymbol{\psi}^{(0)} \, \mathrm{d}\Omega_h \right] \frac{\partial \boldsymbol{u}}{\partial t} + \boldsymbol{v}^T \left[\int_{\Omega_h} \boldsymbol{\psi}^{(0)^T} \boldsymbol{\psi}^{(1)} u \, \mathrm{d}\Omega_h \right] \mathbb{E}^{1,0} \boldsymbol{u} = 0 \tag{6.19}$$

$$\mathbb{M}^{(0)} \frac{\partial \boldsymbol{u}}{\partial t} + \mathbb{M}_{\boldsymbol{u}}^{(0,1)} \mathbb{E}^{1,0} \boldsymbol{u} = 0 \tag{6.20}$$

$$\frac{\partial \boldsymbol{u}}{\partial t} = -\mathbb{M}^{(0)^{-1}} \mathbb{M}_{\boldsymbol{u}}^{(0,1)} \mathbb{E}^{1,0} \boldsymbol{u} \tag{6.21}$$

$$\frac{\partial \boldsymbol{u}}{\partial t} = \boldsymbol{A}_{\mathrm{adv}}^{(0)}(\boldsymbol{u}) \, \boldsymbol{u}. \tag{6.22}$$

Contrary to the linear case where the advection speed was a constant c, the non-linear case involves the construction of the projection matrix $\mathbb{M}^{(0,1)}$ where the solution itself is a part of the integrand. Since the integrals are computed using the Gauss-Lobatto quadrature, the construction of $\mathbb{M}_{\boldsymbol{u}}^{(0,1)}$ needs the evaluation of u at the quadrature nodes which are the degrees of freedom $\boldsymbol{u}$ themselves. This scheme is referred to as the "nodal-adv" scheme in the discussion that follows.

Considering the sequence of operators for this scheme, it simply comprises the topological incidence matrix along with the metric-dependent interior product which forms the discrete Lie derivative of a *0-form*. The corresponding path along the discrete De Rham sequence is depicted in Figure 6.1.

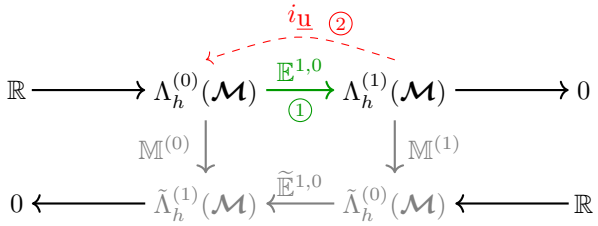

Figure 6.1: The path followed in the discrete De Rham sequence for the advection term for Burgers' equation with nodal degrees of freedom using the advective form

As previously noted, the interior product consists of a metric-free component $\mathbb{M}^{(0,1)}$ and a metric dependent $\mathbb{M}^{(0)^{-1}}$. This fact, however, can be argued to not hold for the presented non-linear case. This is attributed to the solution itself appearing within the integral and thereby scaling the matrix and introducing metric dependence. However, this changes when considering the conservative form of the advection term. Applying the discrete representation from Equation (6.17) and Equation (6.18) into Equation (6.12) gives:

$$\boldsymbol{v}^T \left[\int_{\Omega_h} \boldsymbol{\psi}^{(0)^T} \boldsymbol{\psi}^{(0)} \, \mathrm{d}\Omega_h \right] \frac{\partial \boldsymbol{u}}{\partial t} + \frac{1}{2} \boldsymbol{v}^T \left[\int_{\Omega_h} \boldsymbol{\psi}^{(0)^T} \boldsymbol{\psi}^{(1)} \, \mathrm{d}\Omega_h \right] \mathbb{E}^{1,0} \boldsymbol{u}^2 = 0 \tag{6.23}$$

$$\mathbb{M}^{(0)} \frac{\partial \boldsymbol{u}}{\partial t} + \frac{1}{2} \mathbb{M}^{(0,1)} \mathbb{E}^{1,0} \boldsymbol{u}^2 = 0 \tag{6.24}$$

$$\frac{\partial \boldsymbol{u}}{\partial t} = -\frac{1}{2} \mathbb{M}^{(0)^{-1}} \mathbb{M}^{(0,1)} \mathbb{E}^{1,0} \boldsymbol{u}^2 \tag{6.25}$$

$$\frac{\partial \boldsymbol{u}}{\partial t} = \boldsymbol{A}_{\mathrm{con}}^{(0)}(\boldsymbol{u}) \, \boldsymbol{u}. \tag{6.26}$$

Once again, the discrete Lie derivative makes its appearance. However, this time it acts on $\boldsymbol{u}^2$ and the associated vector for the interior product is just the basis vector of the tangent space (∂_x). The resulting path followed in the discrete De Rham sequence is shown in Figure 6.2.

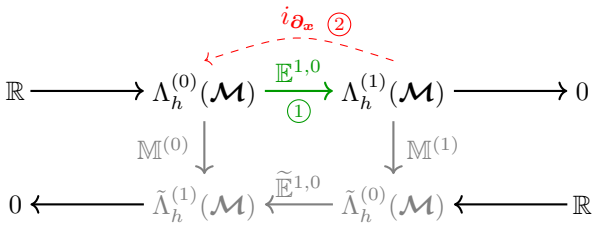

Figure 6.2: The path followed in the discrete De Rham sequence for the advection term for Burgers' equation with nodal degrees of freedom using the conservative form

For this formulation, the aforementioned fact of the interior product comprising a metric-free and a metric-dependent part is again true. This scheme is henceforth referred to as the "nodal-con" scheme.

Moving on with the dual representation of the above formulation in Equation (6.13), the corresponding discrete forms are as follows:

$$u_h := \tilde{\boldsymbol{\psi}}^{(1)} \tilde{\boldsymbol{u}}, \quad \in \tilde{\Lambda}_h^{(1)}(\mathcal{M}) \tag{6.27}$$

$$v_h := \tilde{\boldsymbol{\psi}}^{(1)} \tilde{\boldsymbol{v}}, \quad \in \tilde{\Lambda}_h^{(1)}(\mathcal{M}). \tag{6.28}$$

Substituting these into Equation (6.13) yields:

$$\tilde{\boldsymbol{v}}^T \left[\int_{\Omega_h} \tilde{\boldsymbol{\psi}}^{(1)^T} \tilde{\boldsymbol{\psi}}^{(1)} \, \mathrm{d}\Omega_h \right] \frac{\partial \tilde{\boldsymbol{u}}}{\partial t} + \frac{1}{2} \tilde{\boldsymbol{v}}^T \left[\int_{\Omega_h} \tilde{\boldsymbol{\psi}}^{(1)^T} \boldsymbol{\psi}^{(1)} \, \mathrm{d}\Omega_h \right] \mathbb{E}^{1,0} \left(\star \tilde{\boldsymbol{u}} \right)^2 = 0. \tag{6.29}$$

Replacing the continuous Hodge operator with its discrete form and applying the dual polynomial concept gives the following semi-discrete system:

$$\begin{aligned} \tilde{\boldsymbol{v}}^T \left(\mathbb{M}^{(0)^{-1}} \right)^T \left[\int_{\Omega_h} \boldsymbol{\psi}^{(0)^T} \boldsymbol{\psi}^{(0)} \, \mathrm{d}\Omega_h \right] \mathbb{M}^{(0)^{-1}} \frac{\partial \tilde{\boldsymbol{u}}}{\partial t} + \\ \frac{1}{2} \tilde{\boldsymbol{v}}^T \left(\mathbb{M}^{(0)^{-1}} \right)^T \left[\int_{\Omega_h} \boldsymbol{\psi}^{(0)^T} \boldsymbol{\psi}^{(1)} \, \mathrm{d}\Omega_h \right] \mathbb{E}^{1,0} \left(\mathbb{M}^{(0)^{-1}} \tilde{\boldsymbol{u}} \right)^2 = 0 \end{aligned} \tag{6.30}$$

$$\tilde{\boldsymbol{v}}^T \cancel{\left(\mathbb{M}^{(0)^{-1}} \right)^T} \cancel{\mathbb{M}^{(0)} \mathbb{M}^{(0)^{-1}}} \frac{\partial \tilde{\boldsymbol{u}}}{\partial t} + \frac{1}{2} \tilde{\boldsymbol{v}}^T \cancel{\left(\mathbb{M}^{(0)^{-1}} \right)^T} \mathbb{M}^{(0,1)} \mathbb{E}^{1,0} \left(\mathbb{M}^{(0)^{-1}} \tilde{\boldsymbol{u}} \right)^2 = 0 \tag{6.31}$$

$$\frac{\partial \tilde{\boldsymbol{u}}}{\partial t} = -\frac{1}{2} \mathbb{M}^{(0,1)} \mathbb{E}^{1,0} \left(\mathbb{M}^{(0)^{-1}} \tilde{\boldsymbol{u}} \right)^2 = 0 \tag{6.32}$$

$$\frac{\partial \tilde{\boldsymbol{u}}}{\partial t} = \tilde{\boldsymbol{A}}_{\mathrm{con}}^{(1)}(\tilde{\boldsymbol{u}}) \, \tilde{\boldsymbol{u}}. \tag{6.33}$$

Looking at the above semi-discrete system, it is evident that it contains the same terms as the one in Equation (6.25). However, now the metric-free operators ($\mathbb{E}^{1,0}$ and $\mathbb{M}^{(0,1)}$) can be thought to be separated from the metric-dependent term ($\mathbb{M}^{(0)^{-1}}$) since the latter operator acts as a mapping that transforms the degrees of freedom into a flux. If the flux were to be defined as $\boldsymbol{\mathcal{F}} := \frac{1}{2} \left(\mathbb{M}^{(0)^{-1}} \tilde{\boldsymbol{u}} \right)^2$, then the above semi-discrete system would read:

$$\frac{\partial \tilde{\boldsymbol{u}}}{\partial t} = -\mathbb{M}^{(0,1)} \mathbb{E}^{1,0} \boldsymbol{\mathcal{F}}. \tag{6.34}$$

In essence, this scheme is reminiscent of a Finite-Volume scheme given the flux reconstruction concept. In any case, the corresponding sequence of applying the different operators for this scheme is depicted in Figure 6.3.

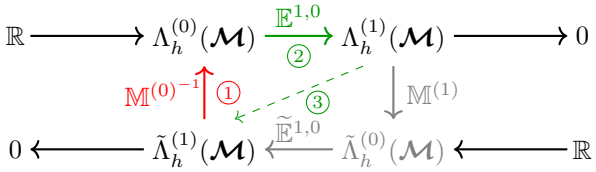

Figure 6.3: The path followed in the discrete De Rham sequence for the advection term for Burgers' equation with edge degrees of freedom on the dual mesh using the conservative form

A reformulation of the above scheme with the adjoint advection operator can be found by substituting the discrete representations in Equation (6.27) and Equation (6.28) into Equation (6.14).

$$\tilde{\boldsymbol{v}}^T \left[\int_{\Omega_h} \tilde{\boldsymbol{\psi}}^{(1)^T} \tilde{\boldsymbol{\psi}}^{(1)} \, \mathrm{d}\Omega_h \right] \frac{\partial \tilde{\boldsymbol{u}}}{\partial t} + \frac{1}{2} \tilde{\boldsymbol{v}}^T \left(\mathbb{M}^{(0)^{-1}} \right) \mathbb{E}^{1,0^T} \left[\int_{\Omega_h} \boldsymbol{\psi}^{(1)^T} \boldsymbol{\psi}^{(0)} \, \mathrm{d}\Omega_h \right] \left(\mathbb{M}^{(0)^{-1}} \tilde{\boldsymbol{u}} \right)^2 = 0 \tag{6.35}$$

$$\cancel{\left(\mathbb{M}^{(0)^{-1}} \right)^T} \frac{\partial \tilde{\boldsymbol{u}}}{\partial t} = \frac{1}{2} \cancel{\left(\mathbb{M}^{(0)^{-1}} \right)^T} \mathbb{E}^{1,0^T} \mathbb{M}^{(1,0)} \left(\mathbb{M}^{(0)^{-1}} \tilde{\boldsymbol{u}} \right)^2 = 0 \tag{6.36}$$

$$\frac{\partial \tilde{\boldsymbol{u}}}{\partial t} = \frac{1}{2} \mathbb{E}^{1,0^T} \mathbb{M}^{(1,0)} \left(\mathbb{M}^{(0)^{-1}} \tilde{\boldsymbol{u}} \right)^2 = 0 \tag{6.37}$$

$$\frac{\partial \tilde{\boldsymbol{u}}}{\partial t} = \tilde{\boldsymbol{A}}^{(1)}_{\mathrm{SBP}}(\tilde{\boldsymbol{u}}) \, \tilde{\boldsymbol{u}}. \tag{6.38}$$

Again, the Summation by Parts ("SBP") nomenclature is used to refer to this scheme. Similarly, the discrete Skew-Symmetric ("S-S") form is found by substituting the discrete representations in Equation (6.27) and Equation (6.28) into Equation (6.15), which gives:

$$\frac{\partial \tilde{\boldsymbol{u}}}{\partial t} = \frac{1}{2} \left(\frac{1}{2} \mathbb{E}^{1,0^T} \mathbb{M}^{(1,0)} - \frac{1}{2} \mathbb{M}^{(0,1)} \mathbb{E}^{1,0} \right) \left(\mathbb{M}^{(0)^{-1}} \tilde{\boldsymbol{u}} \right)^2. \tag{6.39}$$

Lastly, taking the weak form in Equation (6.16) and substituting the following representation:

$$u_h := \boldsymbol{\psi}^{(1)} \boldsymbol{u}, \quad \in \Lambda^{(1)}_h(\boldsymbol{\mathcal{M}}) \tag{6.40}$$

$$v_h := \boldsymbol{\psi}^{(1)} \boldsymbol{v}, \quad \in \Lambda^{(1)}_h(\boldsymbol{\mathcal{M}}), \tag{6.41}$$

gives the following semi-discrete system:

$$\boldsymbol{v}^T \left[\int_{\Omega_h} \boldsymbol{\psi}^{(1)^T} \boldsymbol{\psi}^{(1)} \, \mathrm{d}\Omega_h \right] \frac{\partial \boldsymbol{u}}{\partial t} + \frac{1}{2} \boldsymbol{v}^T \left[\int_{\Omega_h} \boldsymbol{\psi}^{(1)^T} \boldsymbol{\psi}^{(1)} \, \mathrm{d}\Omega_h \right] \mathbb{E}^{1,0} \mathbb{M}^{(0)^{-1}} \mathbb{M}^{(0,1)}_{\underline{\mathbf{u}}} \boldsymbol{u} = 0 \tag{6.42}$$

$$\mathbb{M}^{(1)} \frac{\partial \boldsymbol{u}}{\partial t} + \frac{1}{2} \mathbb{M}^{(1)} \mathbb{E}^{1,0} \mathbb{M}^{(0)^{-1}} \mathbb{M}^{(0,1)}_{\underline{\mathbf{u}}} \boldsymbol{u} = 0 \tag{6.43}$$

$$\frac{\partial \boldsymbol{u}}{\partial t} = -\frac{1}{2} \mathbb{E}^{1,0} \mathbb{M}^{(0)^{-1}} \mathbb{M}^{(0,1)}_{\underline{\mathbf{u}}} \boldsymbol{u} \tag{6.44}$$

$$\frac{\partial \boldsymbol{u}}{\partial t} = \boldsymbol{A}^{(1)}(\boldsymbol{u}) \, \boldsymbol{u}. \tag{6.45}$$

This scheme utilises the Lie derivative which is applied to the discrete *1-form* where the sequence of operations is summarised by Figure 6.4. Alike the linear case, this scheme is also referred to as the "Lie" scheme in the text that follows.

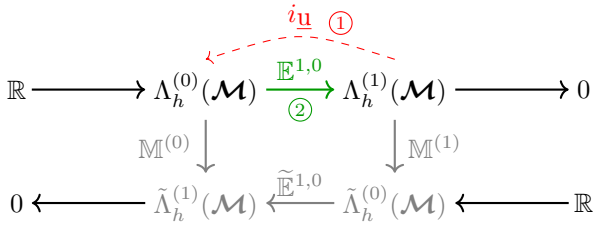

Figure 6.4: The path followed in the discrete De Rham sequence for the advection term for Burgers' equation with edge degrees of freedom on the primal mesh using the advective form

For all the non-linear semi-discrete systems derived, the fully discrete system is derived by employing the

Crank-Nicolson time march. The resulting non-linear algebraic system reads as follows:

$$\frac{\partial \boldsymbol{u}}{\partial t} = \boldsymbol{A}(\boldsymbol{u})\,\boldsymbol{u} \tag{6.46}$$

$$\frac{\boldsymbol{u}^{n+1}-\boldsymbol{u}^{n}}{\Delta t} = \boldsymbol{A}(\boldsymbol{u}^{n+\frac{1}{2}})\,\boldsymbol{u}^{n+\frac{1}{2}} \tag{6.47}$$

$$\frac{\boldsymbol{u}^{n+1}-\boldsymbol{u}^{n}}{\Delta t} = \frac{1}{2}\boldsymbol{A}(\boldsymbol{u}^{n+\frac{1}{2}})\,\boldsymbol{u}^{n+1} + \frac{1}{2}\boldsymbol{A}(\boldsymbol{u}^{n+\frac{1}{2}})\,\boldsymbol{u}^{n} \tag{6.48}$$

$$\boldsymbol{u}^{n+1} - \frac{\Delta t}{2}\boldsymbol{A}(\boldsymbol{u}^{n+\frac{1}{2}})\,\boldsymbol{u}^{n+1} = \boldsymbol{u}^{n} + \frac{\Delta t}{2}\boldsymbol{A}(\boldsymbol{u}^{n+\frac{1}{2}})\,\boldsymbol{u}^{n} \tag{6.49}$$

$$\left[\boldsymbol{I} - \frac{\Delta t}{2}\boldsymbol{A}(\boldsymbol{u}^{n+\frac{1}{2}})\right]\boldsymbol{u}^{n+1} = \left[\boldsymbol{I} + \frac{\Delta t}{2}\boldsymbol{A}(\boldsymbol{u}^{n+\frac{1}{2}})\right]\boldsymbol{u}^{n} \tag{6.50}$$

$$\boldsymbol{L}(\boldsymbol{u}^{n+\frac{1}{2}})\,\boldsymbol{u}^{n+1} = \boldsymbol{R}(\boldsymbol{u}^{n+\frac{1}{2}})\,\boldsymbol{u}^{n}. \tag{6.51}$$

Alike the linear case, element-wise continuity of the solution as well as the boundary conditions are imposed through the introduction of Lagrange multipliers. Thus the full system that is solved every time step reads:

$$\begin{bmatrix} \boldsymbol{L}(\boldsymbol{u}^{n+\frac{1}{2}}) & \boldsymbol{\Lambda}^{T} \\ \boldsymbol{\Lambda} & \varnothing \end{bmatrix} \begin{bmatrix} \boldsymbol{u}^{n+1} \\ \boldsymbol{\lambda} \end{bmatrix} = \begin{bmatrix} \boldsymbol{R}(\boldsymbol{u}^{n+\frac{1}{2}})\,\boldsymbol{u}^{n} \\ \boldsymbol{0} \end{bmatrix}. \tag{6.52}$$

Notice that the non-linear nature of the equations results in the left and right hand side matrices ($\boldsymbol{L}$ and $\boldsymbol{R}$) to be a function of the unknown $\boldsymbol{u}^{n+\frac{1}{2}} = \frac{1}{2}(\boldsymbol{u}^{n+1}+\boldsymbol{u}^{n})$. To solve this non-linear problem, the approach presented in [46] was employed wherein the Picard iteration technique is used. For each time step, a set of iterations are performed where the initial estimate for $\boldsymbol{u}_0^{n+1}$ is made as:

$$\boldsymbol{u}_0^{n+1} = \boldsymbol{u}^{n} + (\boldsymbol{u}^{n} - \boldsymbol{u}^{n-1}), \tag{6.53}$$

using which Equation (6.52) is solved to find the solution at the next iteration level $\boldsymbol{u}_k^{n+1}$. Using the new found $\boldsymbol{u}_k^{n+1}$, a new estimate for $\boldsymbol{u}^{n+\frac{1}{2}}$ is computed and Equation (6.52) is solved repeatedly until the difference between $\boldsymbol{u}_k^{n+1}$ at two successive iteration levels is below a specified tolerance ϵ:

$$\|\boldsymbol{u}_{k+1}^{n+1} - \boldsymbol{u}_k^{n+1}\|_{\infty} < \epsilon. \tag{6.54}$$

Alternatively, taking the L^2 norm of the difference proved to produce near-identical solutions as in the former case.

$$\|\boldsymbol{u}_{k+1}^{n+1} - \boldsymbol{u}_k^{n+1}\|_{L^2} < \epsilon. \tag{6.55}$$

For the cases considered, $\epsilon = 1 \times 10^{-14}$ was taken to be the tolerance value as the work in [46] showed that choosing a large tolerance resulted in poor conservation quality of the scheme.

All the derived schemes in this section generally extend off of the schemes derived for the linear case. Moreover, the "nodal-adv" scheme shares a likeness with the energy and entropy conserving Finite-Volume scheme for Burgers' equation described in [47]. Thus, this scheme acts as a high-order extension of the said Finite-Volume scheme and is thus capable of discretely conserving energy (u^2) and entropy ($\ln(u)$) as will be shortly discussed in the subsequent subsection.

6.1.3. Numerical experiments without shocks

This first set of numerical experiments considered for the discrete systems comprised of a shock-free case. The initial condition used for this shock-free case reads as follows:

$$f(x) = u(x,0) = 0.05\sin(2\pi x) + 1, \tag{6.56}$$

where the time interval was taken to be [0, 1]. Considering the shock formation time for this initial condition using Equation (6.5), one finds that a shock will form at $T_{shock} = \frac{1}{0.314159} \approx 3.18$ which is well beyond the considered time interval of [0, 1]. Given this fact, the exact solution may be computed using the method of characteristics using Equation (6.4).

The first part of the numerical experiments was to assess the convergence of the derived schemes. This was done by computing the L^2 error between the numerical and the exact solution at the final time level for different mesh refinements. The obtained convergence plots are shown in Figure 6.5.

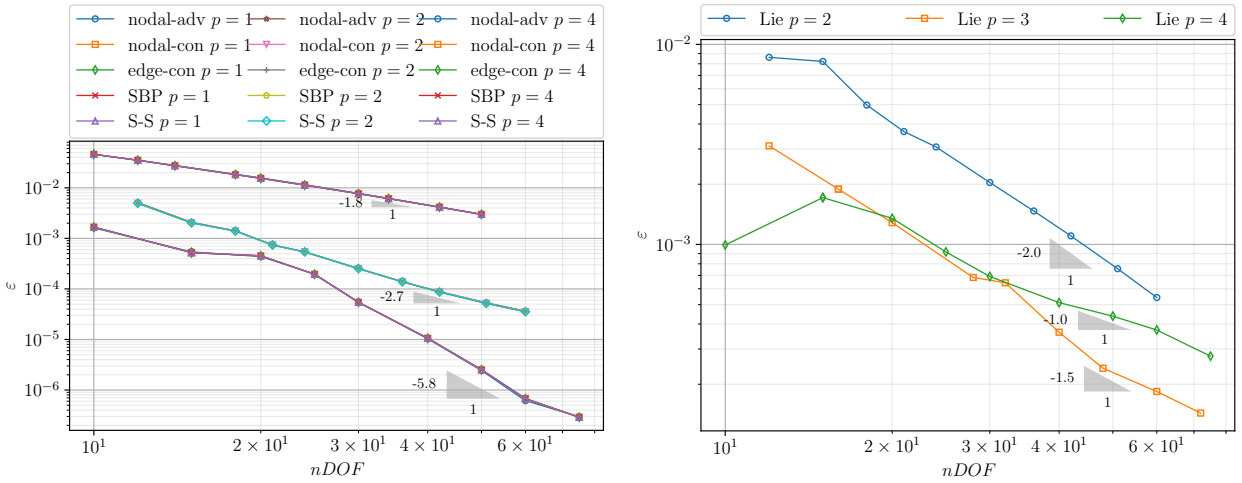

(a) h-convergence of the consistent schemes

(b) h-convergence of the inconsistent "Lie" scheme

Figure 6.5: h-convergence of the different numerical schemes for Burgers' equation computed in the L^2 error norm against the exact solution at $t = 1$

The observations made through the convergence plots are similar to the linear case where all the derived schemes show the expected convergent behaviour apart from the "Lie" scheme for $p > 2$. This is again down to the same issue relating to the incompatible boundary constraint. One remark that can be made for Figure 6.5a is that the curves are not necessarily smooth as seen in Figure 5.13a for the linear case. To further assess the source of the observed errors, the time evolution of the numerical solution for the different schemes is shown Figure 6.6 and Figure 6.7 using different degree polynomials.

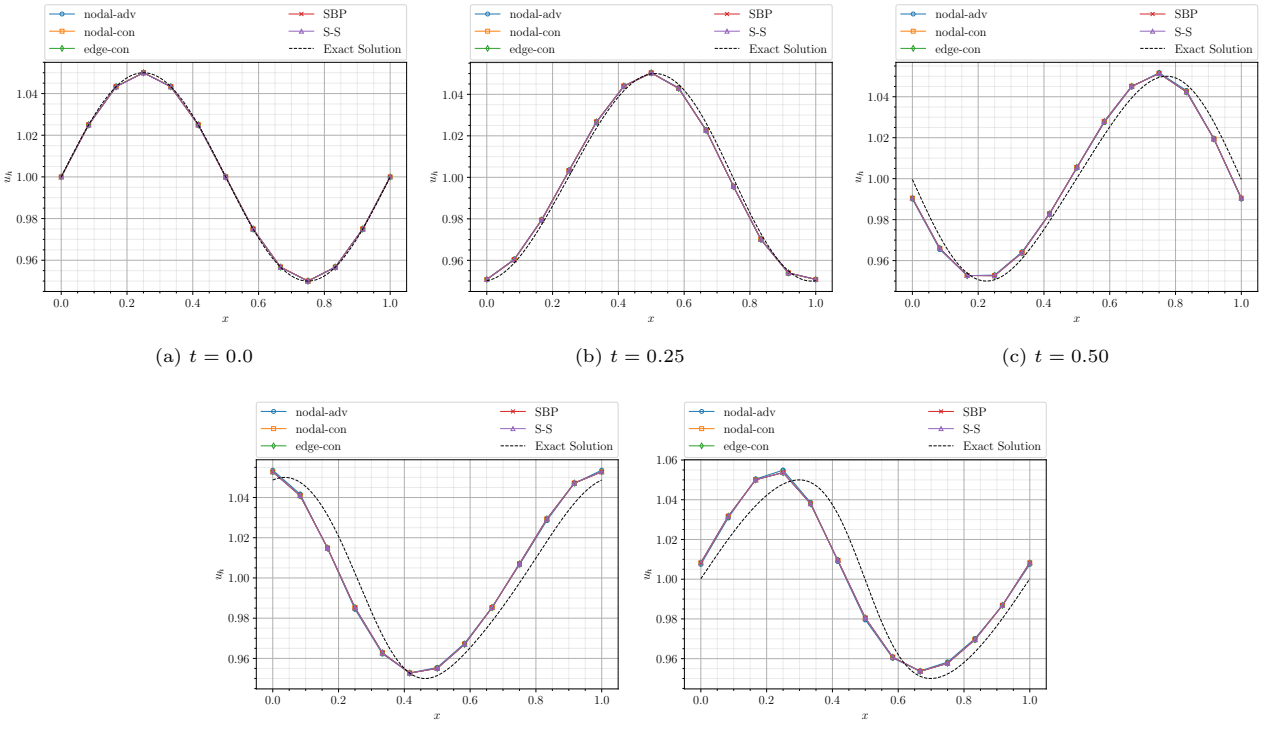

(a) $t = 0.0$

(b) $t = 0.25$

(c) $t = 0.50$

(d) $t = 0.75$

(e) $t = 1.0$

Figure 6.6: Time evolution of the numerical solution to Burgers' equation with $N = 12$, $p = 1$, and $\Delta t = 1 \times 10^{-3}$

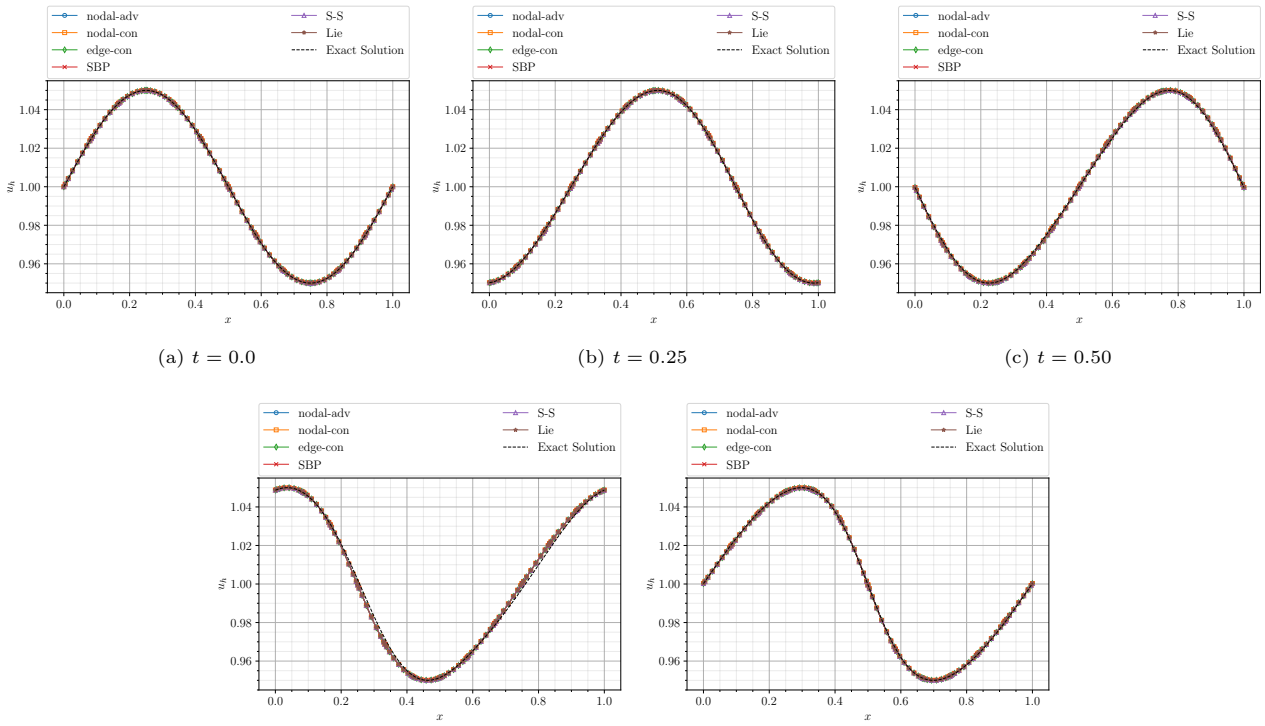

(a) $t = 0.0$ (b) $t = 0.25$ (c) $t = 0.50$

(d) $t = 0.75$ (e) $t = 1.0$

Figure 6.7: Time evolution of the numerical solution to Burgers' equation with $N = 12$, $p = 8$, and $\Delta t = 1 \times 10^{-3}$

Starting with Figure 6.6, it is evident that the numerical solution is slightly lagging behind the exact solution. This clearly indicates the presence of dispersive errors in the numerical solution. This comes as no surprise given that the derived schemes extend off of the energy-conserving linear advection schemes which have semi-discrete systems with purely imaginary eigenvalues. Thus when marched in time with the Crank-Nicolson scheme, the solution disperses in time. This error is of course minimised when using higher order polynomials as seen through Figure 6.7. Viewing the plots for $p = 8$ in Figure 6.7 shows that the numerical solution closely follows the exact solution with the schemes behaving in a very similar to one another. One thing to note here is that the "Lie" scheme still produces unusual behaviour at the element boundaries which are minimised on fine meshes but not totally eliminated.

Regarding the conservation of the integral of the solution, the conservation errors are very similar to the linear case as evident through the plots in Figure 6.8. This boils down to the discrete non-linear semi-discrete system satisfying the condition in Equation (5.123) up to machine precision for all u as checked numerically. The error values are around the order of the round-off errors and are subject to a considerable amount of noise. The noisy behaviour of the error could be attributed to the general round-off error along with the error from the non-linear Picard iteration for each time step. Moreover, the errors also do tend to accumulate every time step although they appear to be ever so slightly less for certain schemes as compared to the linear case.

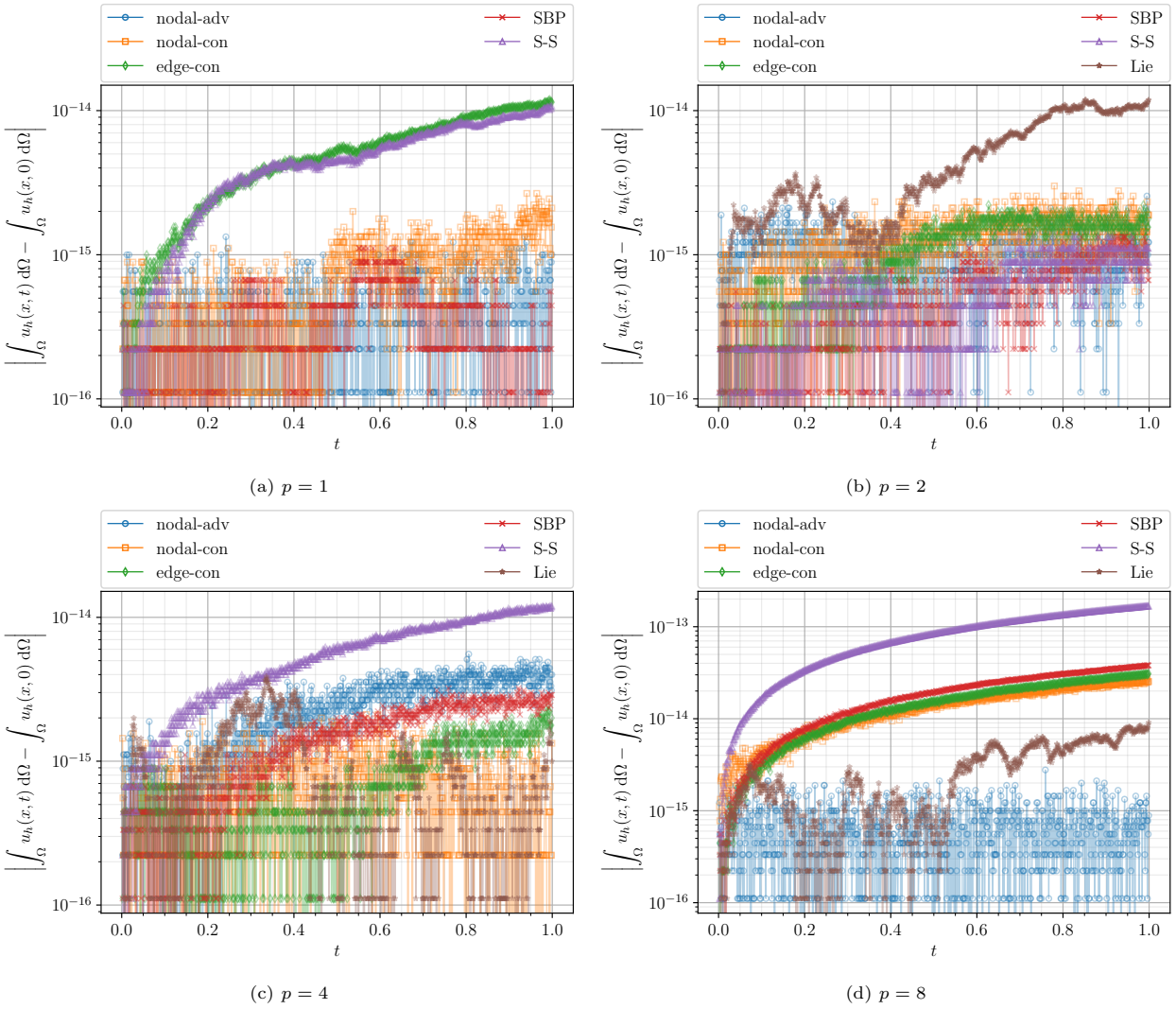

(a) $p = 1$

(b) $p = 2$

(c) $p = 4$

(d) $p = 8$

Figure 6.8: Conservation of the integral of the solution over time for Burgers' equation with different degree polynomials where $N = 12$ and $\Delta t = 1 \times 10^{-3}$

The conservation errors for the integral of u^2, however, behave slightly differently than the linear case as evident through Figure 6.9. There appears to be some form of mesh dependency for this conserved quantity as the errors are considerably larger when using low-order polynomials. Along the same lines, the "Lie" scheme for $p > 2$ generates large conservation errors even for high-order polynomials which are in line with the expectations drawn from the linear case. Similar observations for the conservation of entropy when considering Figure 6.10 with the exception of the "nodal-adv" scheme which remains unchanged for different meshes. As described before, this "nodal-adv" scheme satisfies the property [47] from for discrete conservation of entropy. However, the other schemes also do tend to converge to the same conservation error as the entropy-conserving "nodal-adv" scheme when high-degree polynomials are used.

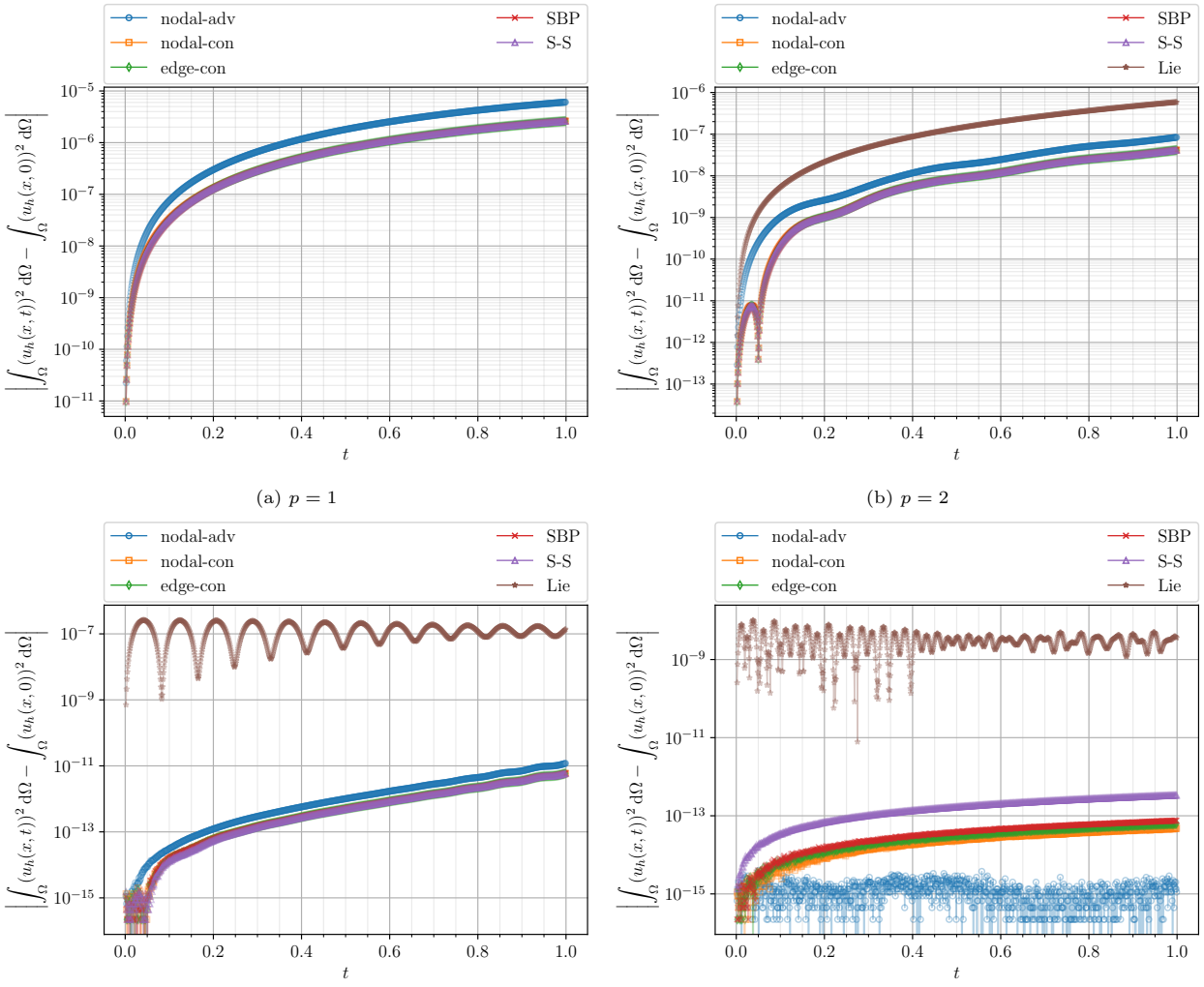

(a) $p = 1$

(b) $p = 2$

(c) $p = 4$

(d) $p = 8$

Figure 6.9: Conservation of the integral of the squared solution over time for Burgers' equation with different degree polynomials where $N = 12$ and $\Delta t = 1 \times 10^{-3}$

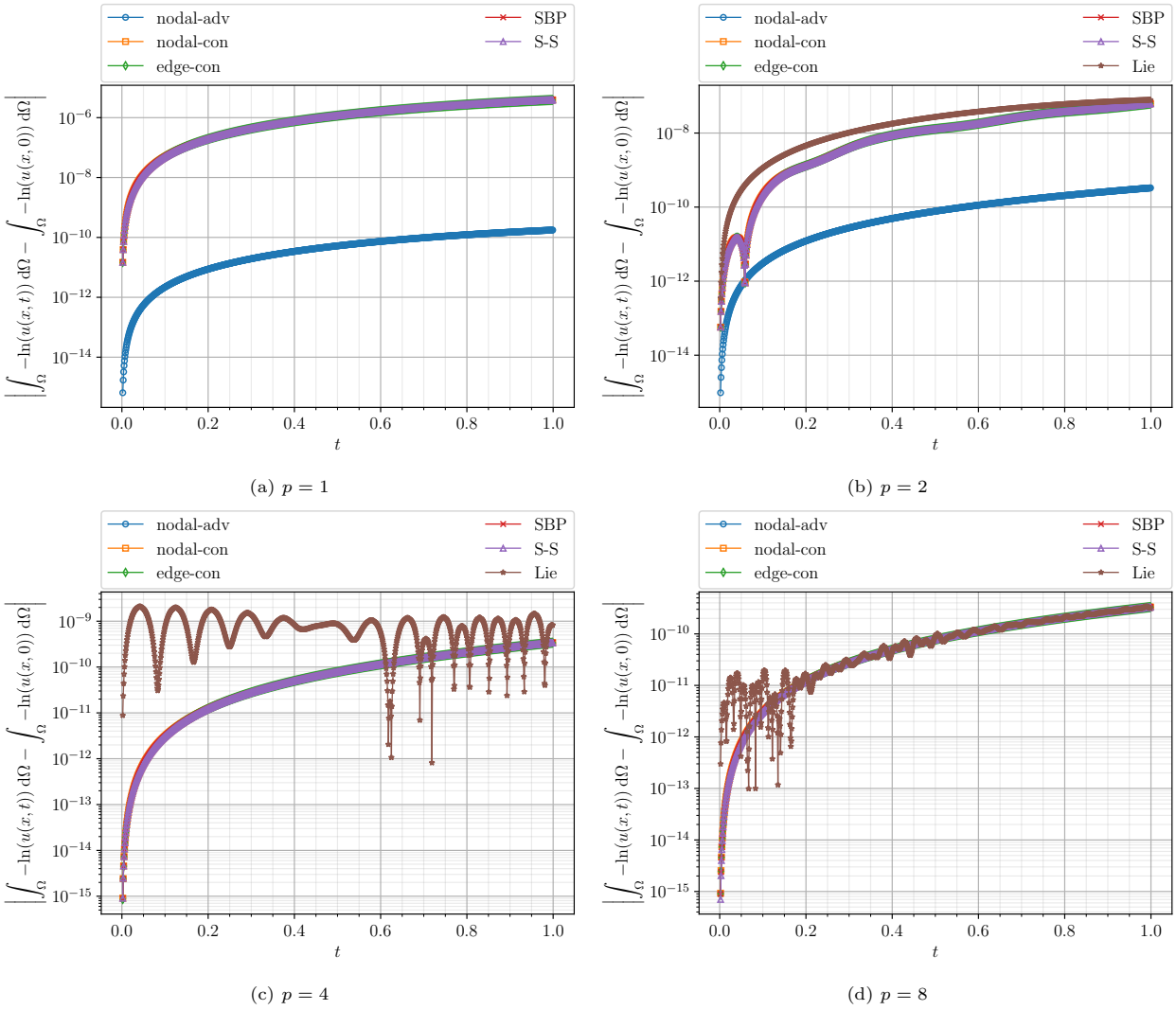

(a) $p = 1$

(b) $p = 2$

(c) $p = 4$

(d) $p = 8$

Figure 6.10: Conservation of the integral of the entropy over time for Burgers' equation with different degree polynomials where $N = 12$ and $\Delta t = 1 \times 10^{-3}$

By numerically analysing the energy conservation property of the discrete system using Equation (5.132) showed that the schemes all start as energy conserving. However, as the solution is evolved in time using low-order polynomials, this conservation property is seen to deteriorate. As briefly discussed in Section 5.2.4 the Lagrange multipliers approach employed to enforce element-wise continuity has no regard for the physical information propagation direction for the hyperbolic case. This is likely to affect the conservation property, especially in this non-linear setting where the solution is advecting itself. Moreover, the weak C^0 continuity imposed at the element boundaries would also constitute to aforementioned effect on the conservation. The "Lie" scheme clearly highlights this argument as it generally has issues trying to conserve u^2 for both linear and non-linear cases due to the forced boundary continuity. It is likely that the standard point-wise continuity constraint is too weak for the non-linear case with low-order polynomials causing a large amount of conservation error for u^2.

Building on this argument, consider the plots in Figure 6.11 where conservation errors are shown for the solutions on two different meshes with comparable number of degrees of freedom but with different polynomial degrees. It is apparent through these figures that the polynomial degree has a significant influence on the conservation properties. Despite the element-wise continuity being the weak C^0 continuity, its appearance in the solution is considerably smoother when using high-degree polynomials as seen in Figure 6.7. This is attributed to the fact the Gauss-Lobatto points used for the mesh nodes are densely spaced around the element boundaries when using high-degree polynomials. This thereby aids the smooth transfer of information between the elements and evidently helps improve the conservation property.

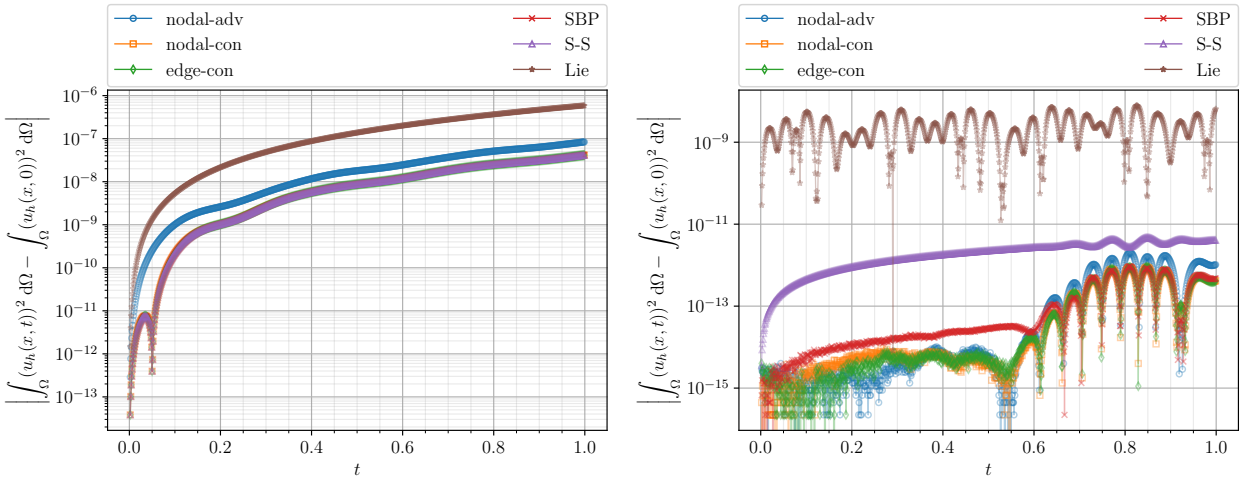

(a) $p = 2,\ N = 12$ (b) $p = 12,\ N = 2$

Figure 6.11: Conservation error of the integral of the squared solution to Burgers' equation on two different meshes with comparable number of degrees of freedom with different order polynomials using a time step of $\Delta t = 1 \times 10^{-3}$

It can further be noted that where sufficiently high-degree polynomials are used, the number of elements on the mesh has little to no influence on the conservation qualities as seen through Figure 6.12.

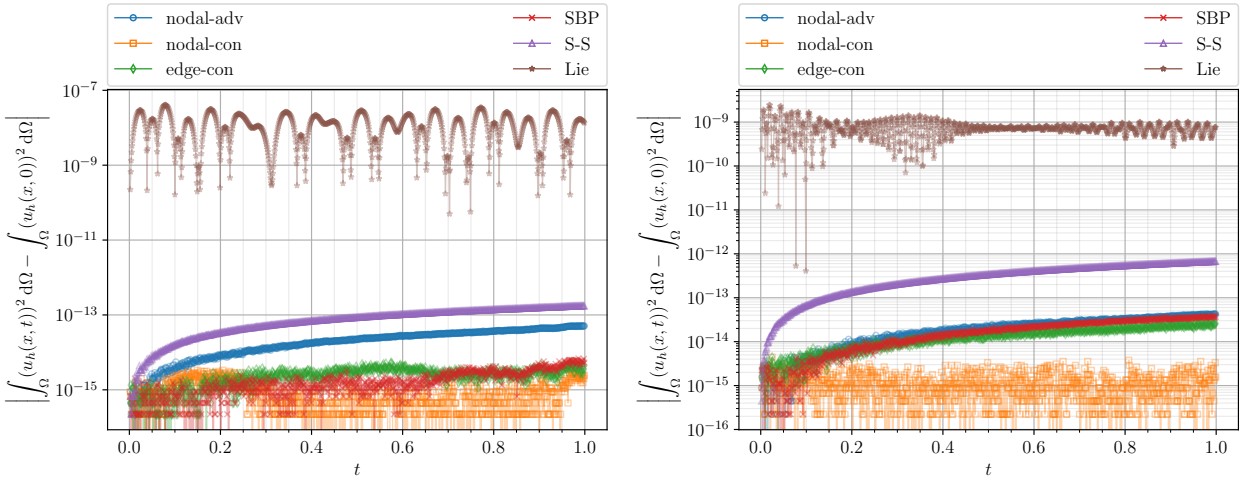

(a) $N = 12$ (b) $N = 24$

Figure 6.12: Conservation error of the integral of the squared solution to Burgers' equation on two different meshes with $p = 8$ and different number of elements using a time step of $\Delta t = 1 \times 10^{-3}$

In summary, the energy conservation property for this Burgers' case is affected by the inter-element continuity constraints. When the weak C^0 continuity is enforced onto the solution, one must use high-degree polynomials in order to ensure a near-smooth transfer of information between the elements. It is, however, important to note that the polynomial degree itself is not the responsible factor for discrete conservation, as a non-conserving scheme will never discretely conserve a quantity regardless of how high a polynomial degree is used. The conservation of entropy on the other hand showed some intriguing behaviour where the entropy conserving "nodal-adv" scheme conserved entropy for all meshes, however, even the non-conserving schemes end up having the same conservation property when sufficiently high polynomials degrees are used.

6.1.4. Numerical experiments with shocks

This subsection addresses a more general case of Burgers' equation wherein a shock is formed in the solution. The considered initial condition for this shock case reads as follows:

$$f(x) = u(x,0) = 0.24 \sin(2\pi x) + 1. \tag{6.57}$$

Subsequently, the time at which the shock forms is found to be $T_{shock} = \frac{1}{1.50796} \approx 0.66$. The solution plots for this shock case found using the different numerical schemes are shown in Figure 6.13. The exact solution for this shock case is taken to be a highly resolved flux-limited Finite-Volume solution.

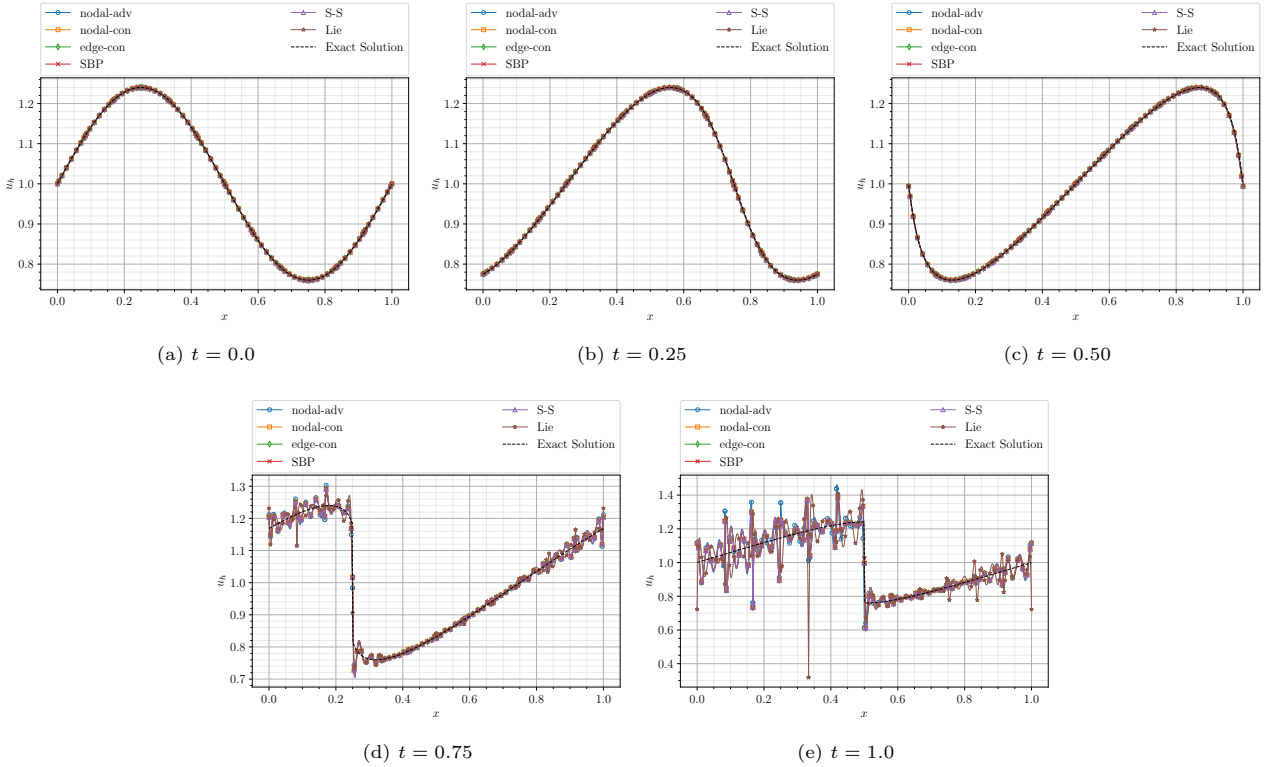

(a) $t = 0.0$ (b) $t = 0.25$ (c) $t = 0.50$

(d) $t = 0.75$ (e) $t = 1.0$

Figure 6.13: Time evolution of the numerical solutions to Burgers' equation with a shock for $N = 12$, $p = 8$, and $\Delta t = 1 \times 10^{-3}$

Considering the solution behaviour from the plots, one finds that the different numerical schemes correctly predict the shock location and speed albeit with considerable oscillations. These oscillations are to be expected as the present formulation seeks to construct continuous functions whereas the exact solution with a shock is in fact discontinuous. The oscillatory solution, however, is the best solution that can be achieved in L^2.

In the presence of shocks, the conservation properties of the equations change, where the energy u^2 and the (mathematical) entropy decrease over the shock, while the integral of u remains unchanged. This physical behaviour is refection by the numerical schemes as seen in Figure 6.14.

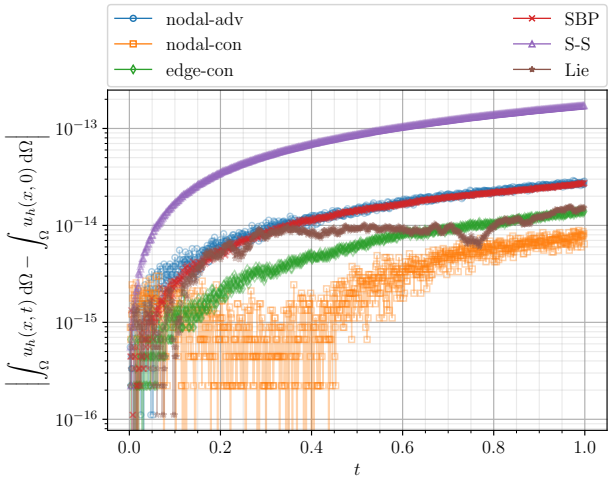

(a) Conservation of the solution

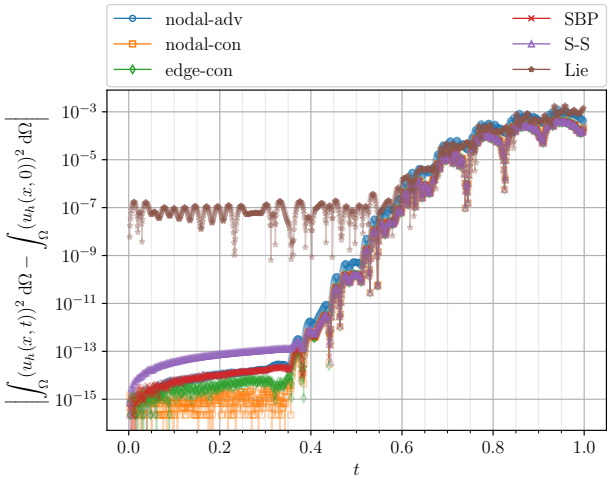

(b) Conservation of the square of the solution

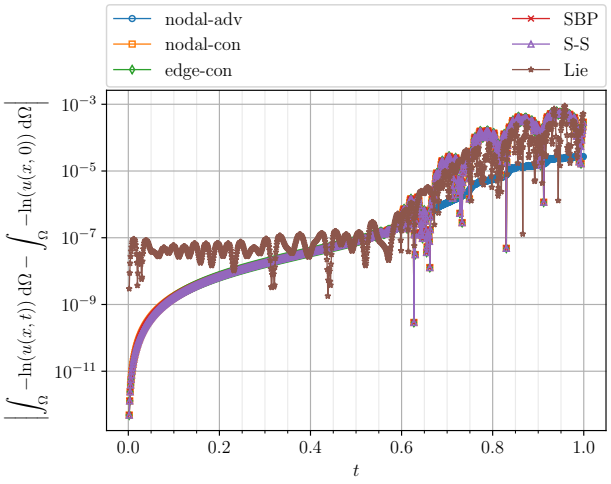

(c) Entropy conservation

Figure 6.14: Conservation of the invariants of Burgers' equation over time for the solution with a shock where $N = 12$, $p = 8$, and $\Delta t = 1 \times 10^{-3}$

As seen through Figure 6.14b and Figure 6.14c the schemes start off by conserving energy and entropy prior to the wave steepening around $t = 0.5$. Thereafter, the wave has steepened considerably and a shock is formed where a clear indication of non-conservation is seen in the plots.

6.2. 2D incompressible Navier-Stokes/Euler equation

Following the initial tests with the non-linear 1D problem, a more complex case namely involving the 2D incompressible Navier-Stokes/Euler equations is considered in this section. The non-dimensional incompressible Navier-Stokes equations are expressed as follows:

$$\vec{\nabla} \cdot \underline{\boldsymbol{u}} = 0 \tag{6.58}$$

$$\frac{\partial \underline{\boldsymbol{u}}}{\partial t} + \left(\underline{\boldsymbol{u}} \cdot \vec{\nabla}\right) \underline{\boldsymbol{u}} + \vec{\nabla} p - \frac{1}{Re} \vec{\nabla}^2 \underline{\boldsymbol{u}} = 0, \tag{6.59}$$

where $\underline{\boldsymbol{u}}$ is the velocity vector [1] which in $\mathbb{R}^2$ comprises of two components $\underline{\boldsymbol{u}} = [u, v]^T$, p is the pressure normalised by the density, and Re is the dimensionless Reynolds number. Equation (6.58) describes the conservation of mass (density) which acts as a constraint that states that the flow field must be divergence-free. On the other hand, Equation (6.59) describes the conservation of momentum which entails a transport equation describing the time evolution of the velocity field. The non-linear advection term in Equation (6.59)

[1] not to be confused with $\boldsymbol{u}$ often used in this report to express the vector containing discrete degrees of freedom

can be expressed in numerous ways which are all equivalent at the continuous level. The following equations show some of the common expressions used to express the advective term ($\mathcal{C}(\underline{\boldsymbol{u}})$):

$$\textit{Conservative form} : \mathcal{C}(\underline{\boldsymbol{u}}) := \vec{\nabla} \cdot (\underline{\boldsymbol{u}} \otimes \underline{\boldsymbol{u}}) \tag{6.60}$$

$$\textit{Advective form} : \mathcal{C}(\underline{\boldsymbol{u}}) := (\underline{\boldsymbol{u}} \cdot \vec{\nabla})\, \underline{\boldsymbol{u}} \tag{6.61}$$

$$\textit{Skew-symmetric form} : \mathcal{C}(\underline{\boldsymbol{u}}) := \frac{1}{2}\,(\underline{\boldsymbol{u}} \cdot \vec{\nabla})\, \underline{\boldsymbol{u}} + \frac{1}{2}\,\vec{\nabla} \cdot (\underline{\boldsymbol{u}} \otimes \underline{\boldsymbol{u}}) \tag{6.62}$$

$$\textit{Rotational form} : \mathcal{C}(\underline{\boldsymbol{u}}) := \underline{\boldsymbol{\omega}} \times \underline{\boldsymbol{u}} + \frac{1}{2}\,\vec{\nabla}\,(\underline{\boldsymbol{u}} \cdot \underline{\boldsymbol{u}}). \tag{6.63}$$

For the proceeding work, the advection term will be expressed using the Rotational form where the vorticity $\underline{\boldsymbol{\omega}}$ is defined as the curl of the velocity, $\underline{\boldsymbol{\omega}} = \vec{\nabla} \times \underline{\boldsymbol{u}}$. Furthermore, the diffusion term $\vec{\nabla}^2\, \underline{\boldsymbol{u}}$ is also rewritten as $-\,\vec{\nabla} \times \underline{\boldsymbol{\omega}}$ using the vector property $\vec{\nabla}^2\, \underline{\boldsymbol{u}} = \vec{\nabla}\,(\vec{\nabla} \cdot \underline{\boldsymbol{u}}) - \vec{\nabla} \times \underline{\boldsymbol{\omega}}$ where the divergence-free constraint is invoked to eliminate the first term. The governing equations are thus rewritten as follows:

$$\vec{\nabla} \cdot \underline{\boldsymbol{u}} = 0 \tag{6.64}$$

$$\underline{\boldsymbol{\omega}} = \vec{\nabla} \times \underline{\boldsymbol{u}} \tag{6.65}$$

$$\frac{\partial \underline{\boldsymbol{u}}}{\partial t} + \underline{\boldsymbol{\omega}} \times \underline{\boldsymbol{u}} + \vec{\nabla} P + \frac{1}{Re}\,\vec{\nabla} \times \underline{\boldsymbol{\omega}} = 0, \tag{6.66}$$

where $P := p + \frac{1}{2}\,\vec{\nabla}\,(\underline{\boldsymbol{u}} \cdot \underline{\boldsymbol{u}})$ is defined as the total pressure normalised by the density.

Note that the incompressible form of the Navier-Stokes does not have an explicit pressure update equation. In order to arrive at the pressure update equation, one can take the divergence of the momentum equation as shown below:

$$\vec{\nabla} \cdot \left[\frac{\partial \underline{\boldsymbol{u}}}{\partial t} + \underline{\boldsymbol{\omega}} \times \underline{\boldsymbol{u}} + \vec{\nabla} P + \frac{1}{Re}\,\vec{\nabla} \times \underline{\boldsymbol{\omega}}\right] = 0. \tag{6.67}$$

Upon simplification, it can be noted that certain terms cancel, namely, the divergence of the time derivative given the divergence-free constraint, the divergence of the diffusion term given the vector calculus relation, the divergence of the curl ($\vec{\nabla} \cdot \vec{\nabla} \times$) is zero.

$$\cancel{\vec{\nabla} \cdot \frac{\partial \underline{\boldsymbol{u}}}{\partial t}} + \vec{\nabla} \cdot (\underline{\boldsymbol{\omega}} \times \underline{\boldsymbol{u}}) + \vec{\nabla} \cdot \vec{\nabla} P + \cancel{\frac{1}{Re}\,\vec{\nabla} \cdot (\vec{\nabla} \times \underline{\boldsymbol{\omega}})} = 0 \tag{6.68}$$

$$\vec{\nabla} \cdot \vec{\nabla} P = -\,\vec{\nabla} \cdot (\underline{\boldsymbol{\omega}} \times \underline{\boldsymbol{u}}). \tag{6.69}$$

This Poisson equation can further be expressed in a mixed formulation as follows:

$$\underline{\boldsymbol{\sigma}} - \vec{\nabla} P = 0 \tag{6.70}$$

$$\vec{\nabla} \cdot \underline{\boldsymbol{\sigma}} = -\,\vec{\nabla} \cdot (\underline{\boldsymbol{\omega}} \times \underline{\boldsymbol{u}}). \tag{6.71}$$

The Navier-Stokes equation expressed in the Rotational form along with the mixed formulation of the pressure Poisson equation is the formulation that is considered throughout the subsequent subsections. Like previous cases, these equations are first considered in their continuous form to derive the weak form in Section 6.2.1. These weak forms are subsequently discretised in Section 6.2.2 using the 2D hybrid mimetic SEM. The aim here is to discretely conserve mass, vorticity, kinetic energy, and enstrophy (square of vorticity), see [4] for an example of such a scheme. Lastly, the results for some benchmark test cases are presented in Section 6.2.3.

6.2.1. Continuous form

For the derivation of the weak form of the governing equations, the various physical quantities are first expressed as *k-forms*. Given the complexity of the problem, only a single representation is considered wherein the velocity is expressed as a *1-form* in the dual space $\underline{\boldsymbol{u}} \in \tilde{\Lambda}^{(1)}(\boldsymbol{\mathcal{M}})$, the vorticity as a *0-form* $\underline{\boldsymbol{\omega}} \in \Lambda^{(0)}(\boldsymbol{\mathcal{M}})$, the total pressure as a *0-form* in the dual space $P \in \tilde{\Lambda}^{(0)}(\boldsymbol{\mathcal{M}})$, and lastly the pressure gradient as a *1-form* $\underline{\boldsymbol{\sigma}} \in \Lambda^{(1)}(\boldsymbol{\mathcal{M}})$.

Starting with the vorticity equation in Equation (6.65), the Galerkin weak form found by testing the equation with a function $\boldsymbol{\epsilon}^{(0)}$ reads:

$$\int_\Omega \underline{\boldsymbol{\omega}}^{(0)} \wedge \star\, \epsilon^{(0)} = \int_\Omega \mathrm{d}\underline{\boldsymbol{u}}^{(1)} \wedge \star\, \epsilon^{(0)}, \qquad \forall \epsilon^{(0)} \in \Lambda^{(0)}(\boldsymbol{\mathcal{M}}). \tag{6.72}$$

Moving the exterior derivative to the test function gives the following expression where the boundary terms emerging from the adjoint operator are neglected given the periodic boundaries.

$$\int_\Omega \underline{\boldsymbol{\omega}}^{(0)} \wedge \star\, \epsilon^{(0)} = -\int_\Omega \underline{\boldsymbol{u}}^{(1)} \wedge \star\, \mathrm{d}\epsilon^{(0)}, \qquad \forall \epsilon^{(0)} \in \Lambda^{(0)}(\boldsymbol{\mathcal{M}}). \tag{6.73}$$

Similarly, testing the momentum equation in Equation (6.66) with $\tilde{\underline{\boldsymbol{v}}}^{(1)}$ gives:

$$\begin{aligned}\int_\Omega \frac{\partial \underline{\boldsymbol{u}}^{(1)}}{\partial t} \wedge \star\, \tilde{\underline{\boldsymbol{v}}}^{(1)} + \int_\Omega \left(\underline{\boldsymbol{\omega}}^{(0)} \wedge \underline{\boldsymbol{u}}^{(1)}\right) \wedge \star\, \tilde{\underline{\boldsymbol{v}}}^{(1)} + \\ \int_\Omega \star\, \underline{\boldsymbol{\sigma}}^{(1)} \wedge \star\, \tilde{\underline{\boldsymbol{v}}}^{(1)} + \frac{1}{Re}\int_\Omega \mathrm{d}\underline{\boldsymbol{\omega}}^{(0)} \wedge \star\, \tilde{\underline{\boldsymbol{v}}}^{(1)} = 0, \qquad \forall \tilde{\underline{\boldsymbol{v}}}^{(1)} \in \tilde{\Lambda}^{(1)}(\boldsymbol{\mathcal{M}}),\end{aligned} \tag{6.74}$$

where the pressure gradient is replace by $\underline{\boldsymbol{\sigma}}^{(1)}$ based on Equation (6.70).

Finally, moving on to the weak form of the mixed formulation of the pressure Poisson equation gives the following when testing Equation (6.70) with $\underline{\boldsymbol{\eta}}^{(1)}$:

$$\int_\Omega \underline{\boldsymbol{\sigma}}^{(1)} \wedge \star\, \underline{\boldsymbol{\eta}}^{(1)} - \int_\Omega \mathrm{d}P^{(0)} \wedge \star\, \underline{\boldsymbol{\eta}}^{(1)} = 0, \qquad \forall \underline{\boldsymbol{\eta}}^{(1)} \in \Lambda^{(1)}(\boldsymbol{\mathcal{M}}) \tag{6.75}$$

$$\int_\Omega \underline{\boldsymbol{\sigma}}^{(1)} \wedge \star\, \underline{\boldsymbol{\eta}}^{(1)} + \int_\Omega P^{(0)} \wedge \star\, \mathrm{d}\underline{\boldsymbol{\eta}}^{(1)} = 0, \qquad \forall \underline{\boldsymbol{\eta}}^{(1)} \in \Lambda^{(1)}(\boldsymbol{\mathcal{M}}), \tag{6.76}$$

where the adjoint operator is applied and once again the boundary terms are neglected. Similarly, testing Equation (6.71) with $\zeta^{(2)}$ gives the following weak form:

$$\int_\Omega \mathrm{d}\underline{\boldsymbol{\sigma}}^{(1)} \wedge \star\, \zeta^{(2)} = -\int_\Omega \mathrm{d} \star \left(\underline{\boldsymbol{\omega}}^{(0)} \wedge \underline{\boldsymbol{u}}^{(1)}\right) \wedge \star\, \zeta^{(2)}, \qquad \forall \zeta^{(2)} \in \Lambda^{(2)}(\boldsymbol{\mathcal{M}}). \tag{6.77}$$

6.2.2. Discrete form

To arrive at a discrete system for each of the above-derived weak forms, the following discrete representations of the solution and test function are used:

$$\underline{\boldsymbol{u}}_h := \tilde{\boldsymbol{\psi}}^{(1)} \tilde{\boldsymbol{u}} \tag{6.78}$$

$$\underline{\boldsymbol{\omega}}_h := \boldsymbol{\psi}^{(0)} \boldsymbol{\omega} \tag{6.79}$$

$$P_h := \tilde{\boldsymbol{\psi}}^{(0)} \tilde{\boldsymbol{P}} \tag{6.80}$$

$$\underline{\boldsymbol{\sigma}}_h := \boldsymbol{\psi}^{(1)} \boldsymbol{\sigma} \tag{6.81}$$

$$\tilde{\underline{\boldsymbol{v}}}_h := \tilde{\boldsymbol{\psi}}^{(1)} \tilde{\boldsymbol{v}} \tag{6.82}$$

$$\epsilon_h := \boldsymbol{\psi}^{(0)} \boldsymbol{\epsilon} \tag{6.83}$$

$$\underline{\boldsymbol{\eta}}_h := \boldsymbol{\psi}^{(1)} \boldsymbol{\eta} \tag{6.84}$$

$$\zeta_h := \boldsymbol{\psi}^{(2)} \boldsymbol{\zeta}. \tag{6.85}$$

Substituting these representations into the weak form starting with the vorticity equation in Equation (6.73) yields:

$$\boldsymbol{\epsilon}^T \left[\int_{\Omega_h} \boldsymbol{\psi}^{(0)^T} \boldsymbol{\psi}^{(0)}\, \mathrm{d}\Omega_h\right] \boldsymbol{\omega} = \boldsymbol{\epsilon}^T \mathbb{E}^{1,0^T} \left[\int_{\Omega_h} \boldsymbol{\psi}^{(1)^T} \tilde{\boldsymbol{\psi}}^{(1)}\, \mathrm{d}\Omega_h\right] \tilde{\boldsymbol{u}} \tag{6.86}$$

$$\boldsymbol{\epsilon}^T \left[\int_{\Omega_h} \boldsymbol{\psi}^{(0)^T} \boldsymbol{\psi}^{(0)}\, \mathrm{d}\Omega_h\right] \boldsymbol{\omega} = \boldsymbol{\epsilon}^T \mathbb{E}^{1,0^T} \left[\int_{\Omega_h} \boldsymbol{\psi}^{(1)^T} \boldsymbol{\psi}^{(1)}\, \mathrm{d}\Omega_h\right] \mathbb{M}^{(1)^{-1}} \tilde{\boldsymbol{u}} \tag{6.87}$$

$$\mathbb{M}^{(0)} \boldsymbol{\omega} = \mathbb{E}^{1,0^T} \cancel{\mathbb{M}^{(1)} \mathbb{M}^{(1)^{-1}}} \tilde{\boldsymbol{u}} \tag{6.88}$$

$$\mathbb{M}^{(0)} \boldsymbol{\omega} = \mathbb{E}^{1,0^T} \tilde{\boldsymbol{u}}. \tag{6.89}$$

Concerning the mapping involved in the above expression, it is observed that the transposed incidence matrix $-\mathbb{E}^{1,0^T}$ represents the dual curl operator that maps the dual *1-form* velocity into a dual *2-form* which is then mapped back to a *0-form* through the metric dependent mapping in the form of the inverse mass matrix $\mathbb{M}^{(0)^{-1}}$. This sequence is summarised in Figure 6.15 below.

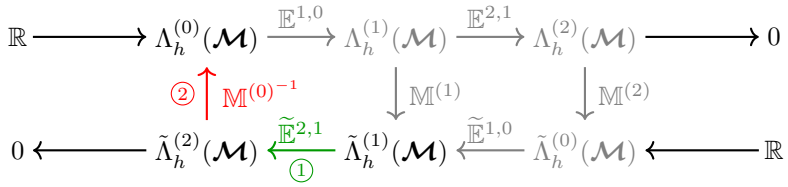

Figure 6.15: The path followed in the De Rham sequence for the vorticity operator

Substituting the discrete representation into the momentum equation in Equation (6.74) and employing the dual polynomial concept yields the following non-linear semi-discrete system:

$$\tilde{\boldsymbol{v}}^T \left[\int_{\Omega_h} \tilde{\boldsymbol{\psi}}^{(1)^T} \tilde{\boldsymbol{\psi}}^{(1)} \, \mathrm{d}\Omega_h\right] \frac{\partial \tilde{\boldsymbol{u}}}{\partial t} + \tilde{\boldsymbol{v}}^T \left[\int_{\Omega_h} \tilde{\boldsymbol{\psi}}^{(1)^T} \boldsymbol{\psi}^{(0)} \, \mathrm{d}\Omega_h\right] \mathbb{C}_{\boldsymbol{\omega}} \mathbb{M}^{(1)^{-1}} \tilde{\boldsymbol{u}} + \tilde{\boldsymbol{v}}^T \left[\int_{\Omega_h} \tilde{\boldsymbol{\psi}}^{(1)^T} \boldsymbol{\psi}^{(1)} \, \mathrm{d}\Omega_h\right] \boldsymbol{\sigma} + \frac{1}{Re} \tilde{\boldsymbol{v}}^T \left[\int_{\Omega_h} \tilde{\boldsymbol{\psi}}^{(1)^T} \boldsymbol{\psi}^{(1)} \, \mathrm{d}\Omega_h\right] \mathbb{E}^{1,0} \boldsymbol{\omega} = 0 \tag{6.90}$$

$$\tilde{\boldsymbol{v}}^T \left(\mathbb{M}^{(1)^{-1}}\right)^T \left[\int_{\Omega_h} \boldsymbol{\psi}^{(1)^T} \boldsymbol{\psi}^{(1)} \, \mathrm{d}\Omega_h\right] \mathbb{M}^{(1)^{-1}} \frac{\partial \tilde{\boldsymbol{u}}}{\partial t} + \tilde{\boldsymbol{v}}^T \left(\mathbb{M}^{(1)^{-1}}\right)^T \left[\int_{\Omega_h} \boldsymbol{\psi}^{(1)^T} \boldsymbol{\psi}^{(0)} \, \mathrm{d}\Omega_h\right] \mathbb{C}_{\boldsymbol{\omega}} \mathbb{M}^{(1)^{-1}} \tilde{\boldsymbol{u}} + \tilde{\boldsymbol{v}}^T \left(\mathbb{M}^{(1)^{-1}}\right)^T \left[\int_{\Omega_h} \boldsymbol{\psi}^{(1)^T} \boldsymbol{\psi}^{(1)} \, \mathrm{d}\Omega_h\right] \boldsymbol{\sigma} + \frac{1}{Re} \tilde{\boldsymbol{v}}^T \left(\mathbb{M}^{(1)^{-1}}\right)^T \left[\int_{\Omega_h} \boldsymbol{\psi}^{(1)^T} \boldsymbol{\psi}^{(1)} \, \mathrm{d}\Omega_h\right] \mathbb{E}^{1,0} \boldsymbol{\omega} = 0 \tag{6.91}$$

$$\cancel{\left(\mathbb{M}^{(1)^{-1}}\right)^T} \cancel{\mathbb{M}^{(1)} \mathbb{M}^{(1)^{-1}}} \frac{\partial \tilde{\boldsymbol{u}}}{\partial t} + \cancel{\left(\mathbb{M}^{(1)^{-1}}\right)^T} \mathbb{M}^{(1,0)} \mathbb{C}_{\boldsymbol{\omega}} \mathbb{M}^{(1)^{-1}} \tilde{\boldsymbol{u}} + \cancel{\left(\mathbb{M}^{(1)^{-1}}\right)^T} \mathbb{M}^{(1)} \boldsymbol{\sigma} + \frac{1}{Re} \cancel{\left(\mathbb{M}^{(1)^{-1}}\right)^T} \mathbb{M}^{(1)} \mathbb{E}^{1,0} \boldsymbol{\omega} = 0 \tag{6.92}$$

$$\frac{\partial \tilde{\boldsymbol{u}}}{\partial t} + \mathbb{M}^{(1,0)} \mathbb{C}_{\omega} \mathbb{M}^{(1)^{-1}} \tilde{\boldsymbol{u}} + \mathbb{M}^{(1)} \boldsymbol{\sigma} + \frac{1}{Re} \mathbb{M}^{(1)} \mathbb{E}^{1,0} \boldsymbol{\omega} = 0. \tag{6.93}$$

The pressure term in the above equation is simply a mapping of the pressure gradient $\boldsymbol{\sigma}$ from its primal *1-form* representation to its dual. The diffusion term involves taking the exterior derivative of the *0-form* vorticity and then mapping that to the space of dual *1-forms*. However, the vorticity itself is computed using the set of projections shown in Figure 6.15. Thus, the sequence of operations for the diffusion term in its entirety includes the vorticity operators where the full sequence is summarised in Figure 6.16.

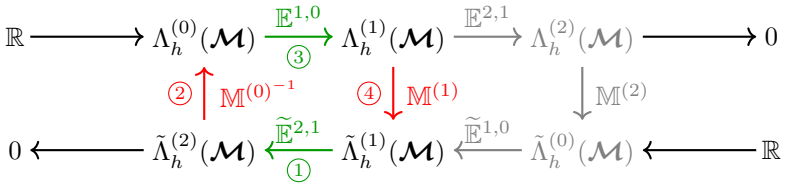

Figure 6.16: Path followed in the De Rham sequence for the diffusion operator

Lastly, the most complex of the terms is the non-linear advection term. This term involves the cross-product of the velocity and the vorticity which is practically computed by evaluating the cross-product as follows in a pointwise sense.

$$(\underline{\boldsymbol{\omega}} \times \underline{\boldsymbol{u}}) = [0, 0, \omega]^T \times [u, v, 0]^T = [-v\,\omega, u\,\omega, 0]^T \tag{6.94}$$

With some abuse of notation, this cross-product operation is summarised by $\mathbb{C}_{\omega}\mathbb{M}^{(1)^{-1}}$. With this term evaluated pointwise, it essentially lives in the space of *0-forms*. Thus, it needs to be mapped back to the space of dual *1-forms* which is done through a component of the co-interior product $\mathbb{M}^{(0,1)}$. Unlike the 1D case, $\mathbb{M}^{(0,1)}$ is no longer metric-free as the Jacobian term scaling the entries of the matrix does not cancel in the 2D case. The process of computing the advection term is summarised in Figure 6.17.

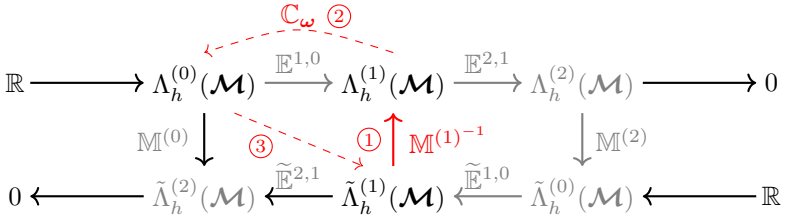

Figure 6.17: Path followed in the De Rham sequence for the advection term

Lastly, the discrete system for the Poisson equation in the mixed formulation can be found to be in the following form [48]:

$$\begin{bmatrix} \mathbb{M}^{(1)} & \mathbb{E}^{2,1^T} \\ \mathbb{E}^{2,1} & \varnothing \end{bmatrix} \begin{bmatrix} \boldsymbol{\sigma} \\ \tilde{\boldsymbol{P}} \end{bmatrix} = \begin{bmatrix} \mathbf{0} \\ -\mathbb{E}^{2,1} \mathbb{M}^{(1)^{-1}} \mathbb{M}^{(1,0)} \mathbb{C}_{\boldsymbol{\omega}} \mathbb{M}^{(1)^{-1}} \tilde{\boldsymbol{u}} \end{bmatrix}. \tag{6.95}$$

It must be noted that the divergence-free constraint is imposed onto the system through this pressure update equation by ignoring the divergence of the temporal gradient of u. In practice, however, the divergence of the solution will not be exactly zero but in the order of 1×10^{-15} given the round-off errors. Neglecting this completely will amount to some error accumulation over the simulation time. Hence the right-hand side source term is adjusted to include the divergence of the solution at the previous time level ($\varepsilon_{\vec{\nabla}\cdot\underline{\boldsymbol{u}}}$) to circumvent any divergence error accumulation.

$$\begin{bmatrix} \mathbb{M}^{(1)} & \mathbb{E}^{2,1^T} \\ \mathbb{E}^{2,1} & \varnothing \end{bmatrix} \begin{bmatrix} \boldsymbol{\sigma} \\ \tilde{\boldsymbol{P}} \end{bmatrix} = \begin{bmatrix} \mathbf{0} \\ \dfrac{\varepsilon_{\vec{\nabla}\cdot\underline{\boldsymbol{u}}}}{\Delta t} - \mathbb{E}^{2,1}\mathbb{M}^{(1)^{-1}}\mathbb{M}^{(1,0)}\mathbb{C}_{\boldsymbol{\omega}}\mathbb{M}^{(1)^{-1}}\tilde{\boldsymbol{u}} \end{bmatrix} \tag{6.96}$$

The Poisson equation can also be expressed in a single system as:

$$\mathbb{E}^{2,1}\mathbb{M}^{(1)^{-1}}\mathbb{E}^{2,1^T}\tilde{\boldsymbol{P}} = \varepsilon_{\vec{\nabla}\cdot\underline{\boldsymbol{u}}} - \mathbb{E}^{2,1}\mathbb{M}^{(1)^{-1}}\mathbb{M}^{(1,0)}\mathbb{C}_{\boldsymbol{\omega}}\mathbb{M}^{(1)^{-1}}\tilde{\boldsymbol{u}}, \tag{6.97}$$

where the mappings involved for the discrete Laplacian operator are summarised as shown in Figure 6.18.

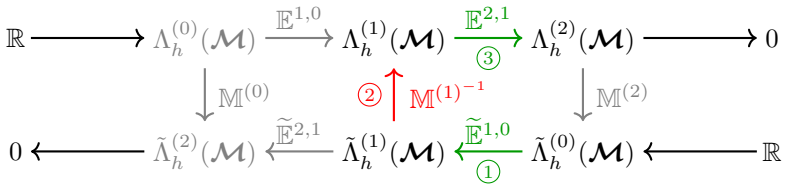

Figure 6.18: Path followed in the De Rham sequence for the Laplacian operator

All the derivations of the discrete systems up until this point have been made for individual elements. To extend the system to the multi-element case, additional degrees of freedom in the form of Lagrange multipliers are introduced. Unlike the simple 1D case, the 2D case requires a few extra Lagrange multipliers to enforce continuity of the various degrees of freedom. This concept was introduced in Section 3.5 and is reiterated here along with a schematic of the mesh in Figure 6.19 with some additional details specific to the considered Navier-Stokes equations.

Figure 6.19: Hybrid 2D periodic mesh

Starting with the continuity of the velocity, recall that the velocity has been chosen to be represented as a dual *1-form* resulting in the degrees of freedom $\tilde{\boldsymbol{u}}$ representing the circulation over the edges. These circulations are dual to the flux over the primal edges and continuity is imposed by using the Lagrange multipliers λ which enforces the two neighbouring element's fluxes to be equal. For the example 2D mesh in Figure 6.19 this condition is achieved by taking the difference of the fluxes as follows:

$$\begin{aligned} u_0 - u_{26} &= 0 \\ u_3 - u_{29} &= 0 \\ u_6 - u_{80} &= 0 \\ &\vdots \\ u_{102} - u_{68} &= 0 \\ u_{107} - u_{71} &= 0. \end{aligned} \tag{6.98}$$

The corresponding constraint expressed in a matrix form reads:

$$\mathbb{E}^{\lambda,1}\boldsymbol{u} = \mathbb{E}^{\lambda,1}\mathbb{M}^{(1)^{-1}}\tilde{\boldsymbol{u}} = 0, \tag{6.99}$$

where $\mathbb{E}^{\lambda,1}$ is a topological differencing matrix containing ± 1 which encapsulates the differencing operation in Equation (6.98). In an identical manner, the continuity of the pressure gradient $\boldsymbol{\sigma}$ in Equation (6.96) is imposed using $\mathbb{E}^{\lambda,1}$ where the condition reads:

$$\mathbb{E}^{\lambda,1}\boldsymbol{\sigma} = 0. \tag{6.100}$$

As previously established, the Lagrange multipliers physically represent the boundary terms appearing in the weak form. Given that $\boldsymbol{\sigma}$ in Equation (6.93) is the pressure gradient that does not include the boundary terms for the adjoint gradient operator $\widetilde{\mathbb{E}}^{1,0}$, the boundary terms are accounted by the Lagrange multipliers λ. This results in λ physically representing the pressure values at the element interfaces.

While the velocity fluxes are constrained to be continuous between the elements, it alone is not sufficient as the tangential velocity or vorticity also needs to be constrained. For this purpose, the Lagrange multipliers γ are used. To impose vorticity continuity constraint, the following condition is applied:

$$\begin{aligned} \omega_0 - \omega_{60} &= 0 \\ -\omega_0 + \omega_{20} &= 0 \\ \omega_1 - \omega_{61} &= 0 \\ &\vdots \\ \omega_{68} - \omega_{75} &= 0 \\ \omega_{71} - \omega_{78} &= 0. \end{aligned} \tag{6.101}$$

Expressing this in a matrix form gives:

$$\mathbb{E}^{\gamma,0}\boldsymbol{\omega} = 0. \tag{6.102}$$

Considering the boundary term of the adjoint curl operator, the Lagrange multipliers γ physically represent the tangential velocities at the element boundaries. However, using these tangential velocities on their own is insufficient when trying to enforce vorticity continuity at the junction points of the elements where more than two pointwise values have to be equated to each other. For instance consider the junction consisting of points 8, 15, 29, and 36 in Figure 6.19. The constraint imposed by γ_{11}, γ_{21}, γ_{24}, and γ_{25} reads as follows:

$$\begin{aligned} \omega_8 - \omega_{15} &= 0 \\ -\omega_8 + \omega_{29} &= 0 \\ -\omega_{15} + \omega_{36} &= 0 \\ \omega_{29} - \omega_{36} &= 0. \end{aligned} \tag{6.103}$$

This system is clearly ill-posed as a unique solution to the problem does not exist. In order to ensure a unique solution, the Lagrange multipliers θ are used to enforce a constraint on γ. The constraint that θ imposes on γ is that the inflow and outflow of the tangential velocities is balanced at the junction point in question. Expressing this condition mathematically for the aforementioned junction point where θ_4 is the additional Lagrange multiplier gives:

$$-\gamma_{11} - \gamma_{21} + \gamma_{24} + \gamma_{25} = 0. \tag{6.104}$$

Expressing this in a generalised matrix form for all the junctions yields:

$$\mathbb{E}^{\theta,\gamma}\boldsymbol{\gamma} = 0, \tag{6.105}$$

where $\mathbb{E}^{\theta,\gamma}$ is a topological differencing matrix. Adding this additional constraint on γ to each of the junctions on the mesh yields a well-posed system that returns a unique system. For this Lagrange multipliers θ, the physical interpretation is not obtained through the weak form. Nonetheless, its interpretation may be obtained by considering the operation that it is mimicking. If the surface created by connecting the four points in a junction is considered to be a ghost surface, then the tangential velocities act as fluxes through the ghost edges enclosing the ghost surface. As such, the inflow-outflow balance of the tangential velocities enforced via θ acts like the divergence operation much like $\mathbb{E}^{2,1}$. Inspecting the values of θ found during post-processing showed that the values were all in the order of machine precision alike the divergence of the solution. This result is in line with the results presented in [12]. Another thing to note is that θ need not impose this specific inflow-outflow constraint. It was found that the following constraint on γ:

$$-\gamma_{11} + \gamma_{21} + \gamma_{24} + \gamma_{25} = 0, \tag{6.106}$$

also produces a unique solution with θ again being in the order of machine precision[2]. Given this fact, the actual physical interpretation of θ is yet unknown.

[2]Both sets of constraints produce the exact same numerical solution

Moving forward with the time discretisation, the Crank-Nicolson scheme is used which gives the following discrete systems to be iteratively solved every time step:

$$\begin{bmatrix} \mathbb{M}^{(0)} & -\mathbb{E}^{\gamma,0^T} & \varnothing \\ -\mathbb{E}^{\gamma,0} & \varnothing & \mathbb{E}^{\theta,\gamma^T} \\ \varnothing & \mathbb{E}^{\theta,\gamma} & \varnothing \end{bmatrix} \begin{bmatrix} \boldsymbol{\omega}^{n+\frac{1}{2}} \\ \boldsymbol{\gamma} \\ \boldsymbol{\theta} \end{bmatrix} = \begin{bmatrix} \mathbb{E}^{1,0^T}\tilde{\boldsymbol{u}}^{n+\frac{1}{2}} \\ \mathbf{0} \\ \mathbf{0} \end{bmatrix} \tag{6.107}$$

$$\begin{bmatrix} \mathbb{M}^{(1)} & \mathbb{E}^{2,1^T} & \mathbb{E}^{\lambda,1^T} \\ \mathbb{E}^{2,1} & \varnothing & \varnothing \\ \mathbb{E}^{\lambda,1} & \varnothing & \varnothing \end{bmatrix} \begin{bmatrix} \boldsymbol{\sigma}^{n+\frac{1}{2}} \\ \tilde{\boldsymbol{P}}^{n+\frac{1}{2}} \\ \boldsymbol{\lambda}_P \end{bmatrix} = \begin{bmatrix} \mathbf{0} \\ \frac{\varepsilon\vec{\nabla}\cdot\underline{\boldsymbol{u}}}{\Delta t} - \mathbb{E}^{2,1}\mathbb{M}^{(1)^{-1}}\mathbb{M}^{(1,0)}\mathbb{C}_{\boldsymbol{\omega}}^{n+\frac{1}{2}}\mathbb{M}^{(1)^{-1}}\tilde{\boldsymbol{u}}^{n+\frac{1}{2}} \\ \mathbf{0} \end{bmatrix} \tag{6.108}$$

$$\begin{bmatrix} \frac{1}{\Delta t}\boldsymbol{I} & \mathbb{E}^{\lambda,1^T} \\ \mathbb{E}^{\lambda,1} & \varnothing \end{bmatrix} \begin{bmatrix} \tilde{\boldsymbol{u}}^{n+1} \\ \boldsymbol{\lambda} \end{bmatrix} = \begin{bmatrix} \frac{\boldsymbol{u}^n}{\Delta t} - \mathbb{M}^{(1,0)}\mathbb{C}_{\boldsymbol{\omega}}^{n+\frac{1}{2}}\mathbb{M}^{(1)^{-1}}\tilde{\boldsymbol{u}}^{n+\frac{1}{2}} - \mathbb{M}^{(1)}\boldsymbol{\sigma}^{n+\frac{1}{2}} - \frac{1}{Re}\mathbb{M}^{(1)}\mathbb{E}^{1,0}\boldsymbol{\omega}^{n+\frac{1}{2}} \\ \mathbf{0} \end{bmatrix} \tag{6.109}$$

6.2.3. Numerical experiments

As the first part of the numerical experiments, the convergence of the derived method was tested. For this, the well-known 2D Taylor-Green Vortex test case was used of which the exact solution is given by:

$$\begin{aligned} u_{exact}(x,y,t) &= -\sin(\pi x)\cos(\pi y)e^{-2\pi^2\nu t} \\ v_{exact}(x,y,t) &= \cos(\pi x)\sin(\pi y)e^{-2\pi^2\nu t}, \end{aligned} \tag{6.110}$$

on a periodic domain $\Omega =]0,2[^2$. The viscosity was set to $\nu = 0.01$ and the solution was evolved to $t = 1$ at which point the L^2 error with respect to the exact solution was computed. The quantity used for this error calculation was the velocity magnitude $\sqrt{u^2+v^2}$. The L^2 errors plots are shown in Figure 6.20 where the following time step sizes were used $\Delta t = 2.5\times10^{-2}$, $\Delta t = 1\times10^{-3}$, and $\Delta t = 1\times10^{-4}$ for $p=1$, $p=2$, and $p=4$ respectively. Concerning the error curves in Figure 6.20a, the curse of dimensionality shows that the rate of convergence is slower when measured in terms of the number of degrees of freedom. When computing the slopes for the error variation with average mesh height, the rate of convergence can be found to be p^{th} order when using polynomials of degree p which is in line with the expected rate.

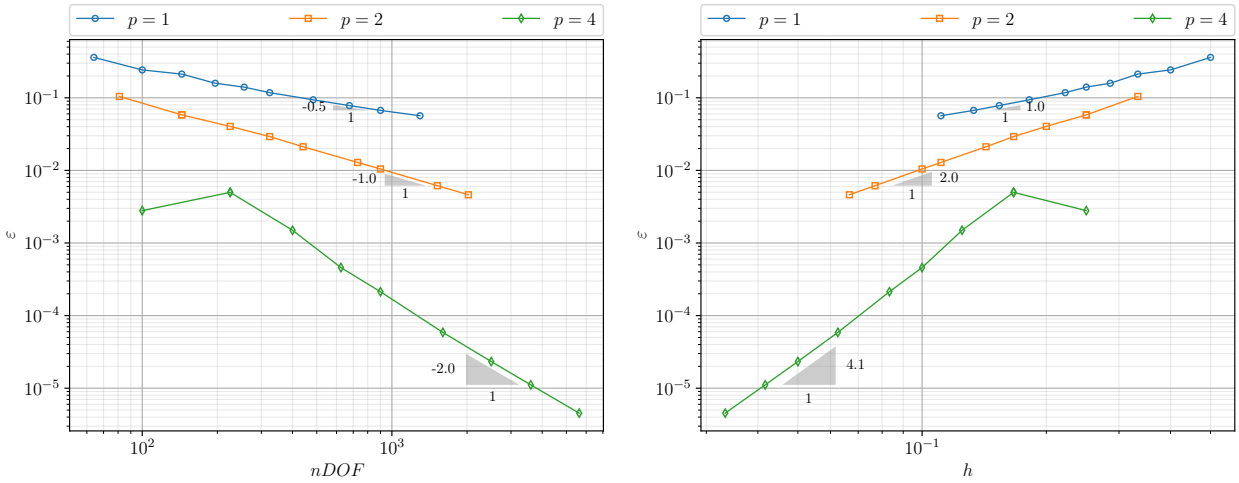

(a) L^2 error vs number of degrees of freedom

(b) L^2 error vs average mesh height

Figure 6.20: h-convergence of the numerical scheme for the incompressible Navier-Stokes equations computed in the L^2 error norm against the exact solution at $t = 1$

Once the scheme was verified, a simple stationary inviscid ($\nu = 0$) vortex test case was considered. The initial condition for this problem is defined as follows:

$$\begin{aligned} u(x,y,0) &= -\frac{\beta}{a}\exp\left(0.5\left(1.0-\frac{(x-0.5)^2+(y-0.5)^2}{a^2}\right)\right)(y-0.5) \\ v(x,y,0) &= \frac{\beta}{a}\exp\left(0.5\left(1.0-\frac{(x-0.5)^2+(y-0.5)^2}{a^2}\right)\right)(x-0.5), \end{aligned} \tag{6.111}$$

with the domain being double periodic $\Omega \in]0, 1[^2$, $\beta = 1$ and $a = 0.05$. This initial condition was interpolated into the dual *1-form* space from which the corresponding initial vorticity was computed and is shown in Figure 6.21 for two different meshes using different degree polynomials.

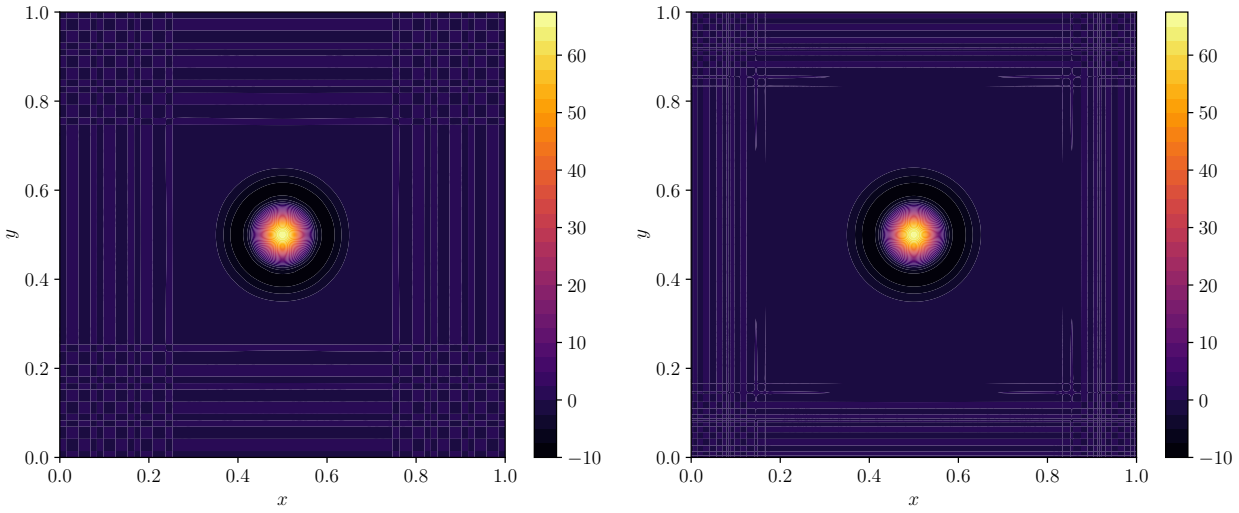

(a) $p = 4$ (b) $p = 8$

Figure 6.21: Initial vorticity distribution for the stationary vortex test case interpolated using different order polynomials with 12×12 elements

The interpolation and mapped initial condition for the vorticity introduces evenly distributed oscillations throughout the domain. It is apparent that these oscillations are naturally reduced with higher degree polynomials. Nonetheless, when evolved over time, the oscillations further disperse throughout the domain given that there is no physical diffusion damping them. This is seen through the solution plot at $t = 1$ in Figure 6.22.

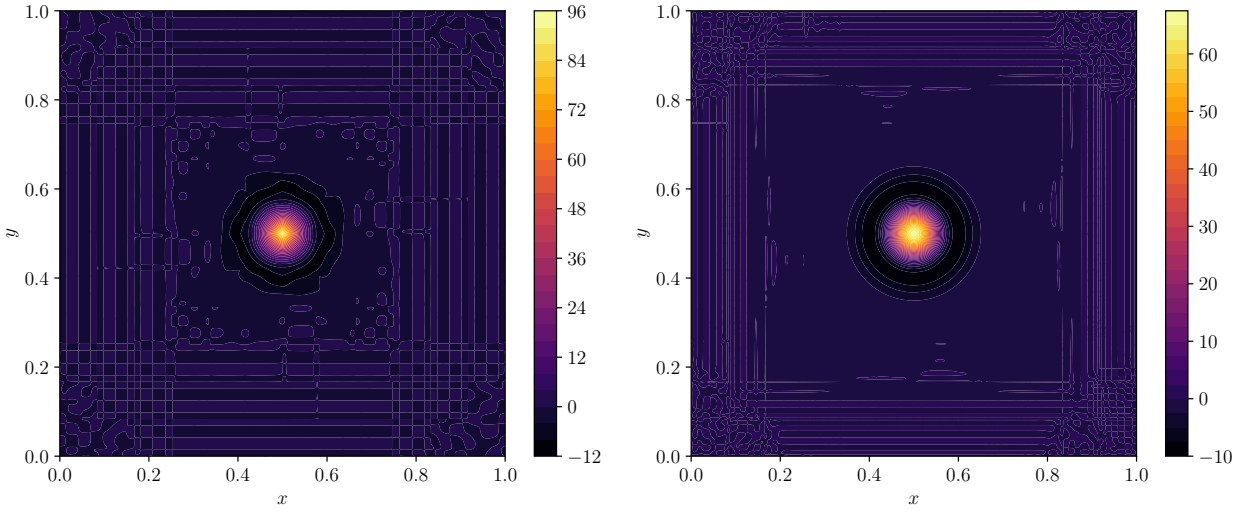

(a) $p = 4$ (b) $p = 8$

Figure 6.22: Vorticity solution of the stationary vortex test case at $t = 1$ using different order polynomials with 12×12 elements wit $\Delta t = 1 \times 10^{-3}$

Considering the conservation qualities of the solution shown in Figure 6.23, it can be found that the scheme exactly conserves mass (the divergence of u) and the total vorticity for both meshes with no sign of error accumulation over time. This is due to the fact that the divergence of the velocity is forced to be equal to zero at every time step through the pressure update equation. For the vorticity, the conservation is purely related to the exactness of the discrete curl operator satisfied through the incidence matrix and is in fact conserved irrespective of the choice of time march scheme.

The conservation of the quadratic invariants, namely the kinetic energy and enstrophy, is found to be poor on

coarse meshes as seen in Figure 6.23c and Figure 6.23d. When the mesh is refined, however, this conservation quality is improved where the error drops to more nominal values. Nonetheless, steady growth is observed for these conservation errors which is again attributed to the concept of error accumulation over each time step discussed for the 1D problems.

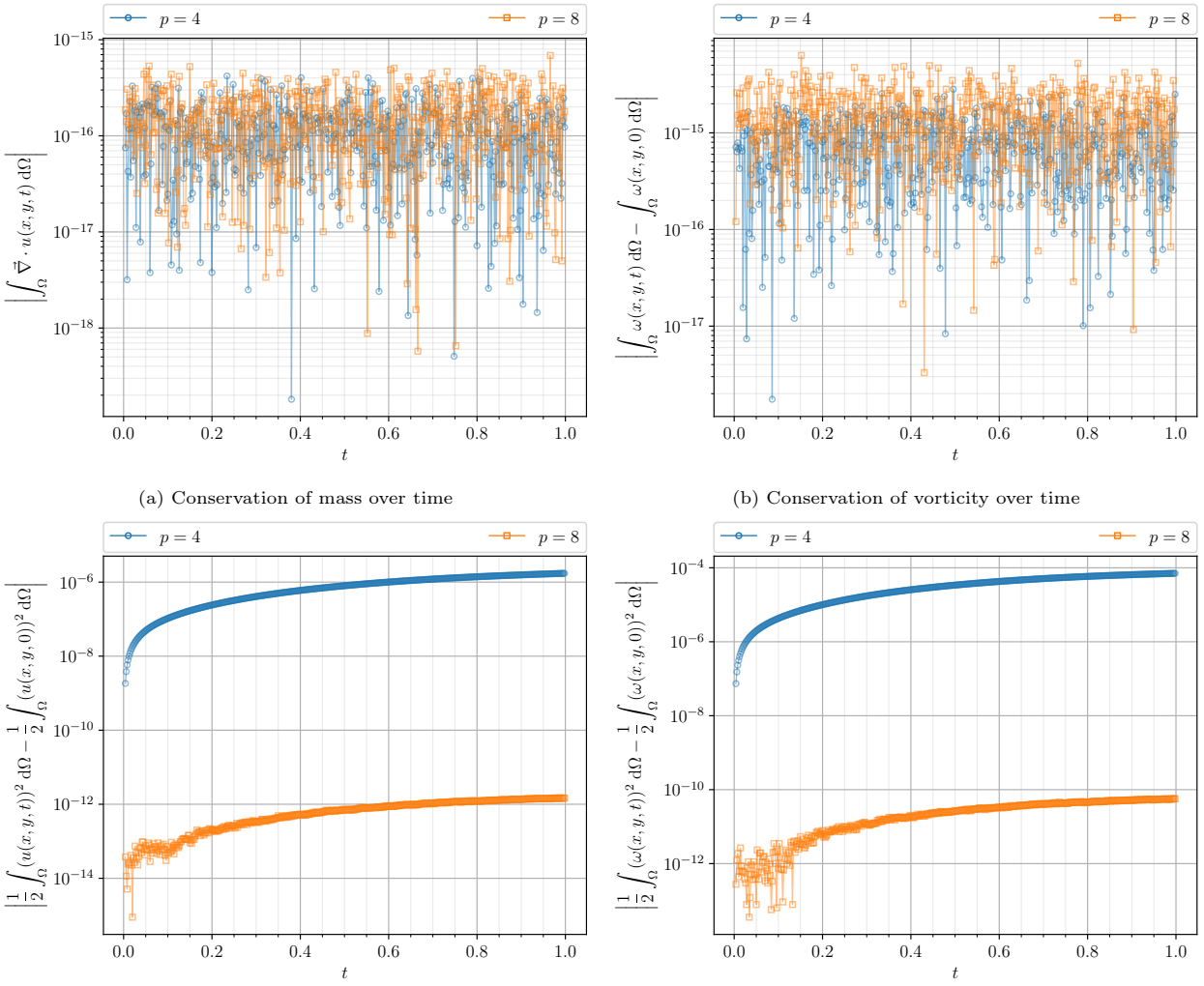

(a) Conservation of mass over time

(b) Conservation of vorticity over time

(c) Conservation of kinetic energy over time

(d) Conservation of enstrophy over time

Figure 6.23: Conservation errors for the stationary vortex test case with 12×12 elements wit $\Delta t = 1 \times 10^{-3}$

The large conservation errors for $p = 4$ could possibly be explained by considering the observed oscillations in the solution. Extending off of the ideas from the 1D problems, the weak C^0 continuity imposed on the solution (velocity flux and vorticity) leads to poor information transfer over elements and even introduces quite some oscillations in the solution for low-order polynomials. This, therefore, contribute to a larger conservation error of the squared invariants for low-order polynomials.

In order to further test the limits of the applied discretisation, a more complex example was considered. This was in the form of a test case involving two co-rotating Taylor Vortices taken from [13] where it was analysed using isogeometric analysis. The domain for this problem is a double period domain $\Omega \in]0, 1[^2$ The initial condition for this problem reads as follows:

$$\begin{aligned} u(x, y, 0) &= -\sum_{i=1}^{2} \frac{\beta}{a} \exp\left(0.5\left(1.0 - \frac{(x - x_i)^2 + (y - 0.5)^2}{a^2}\right)\right)(y - 0.5) \\ v(x, y, 0) &= \sum_{i=1}^{2} \frac{\beta}{a} \exp\left(0.5\left(1.0 - \frac{(x - x_i)^2 + (y - 0.5)^2}{a^2}\right)\right)(x - x_i), \end{aligned} \tag{6.112}$$

with $x_i = \{0.4, 0.6\}$, $\beta = 1$, and $a = 0.075$.

The time evolution of the numerically computed vorticity up to $t = 1$ is shown in Figure 6.24 for the finest mesh with $p = 8$ and 12×12 elements with $\Delta t = 1 \times 10^{-3}$.

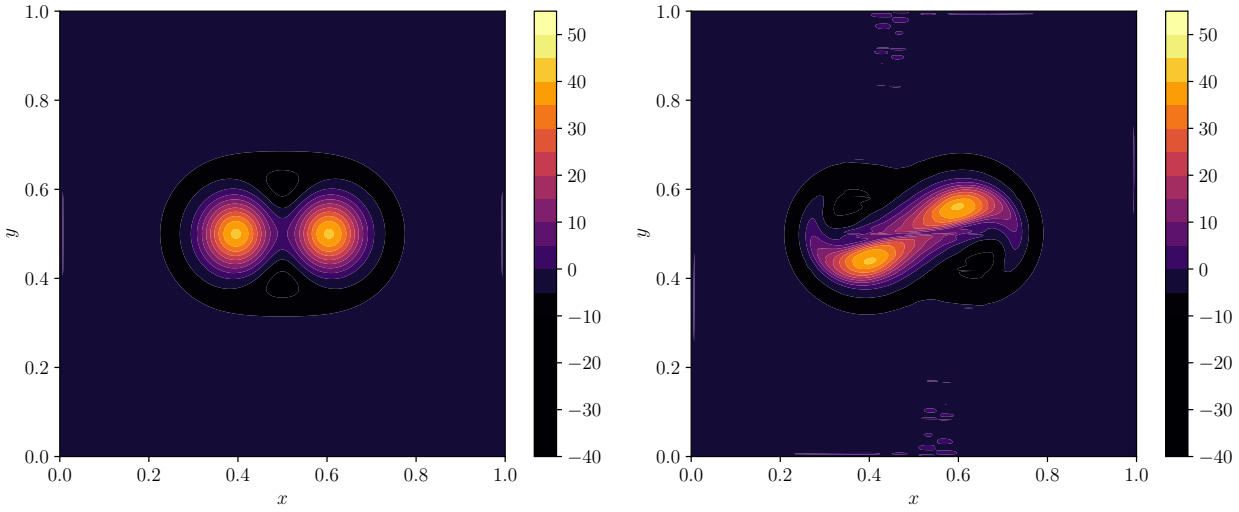

(a) $t = 0$

(b) $t = 0.25$

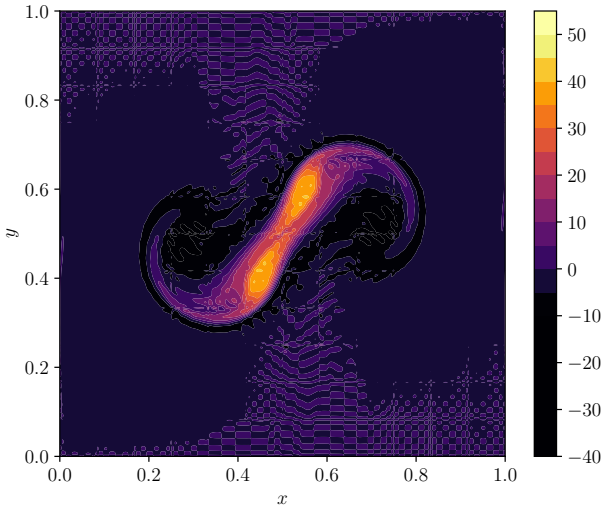

(c) $t = 0.5$

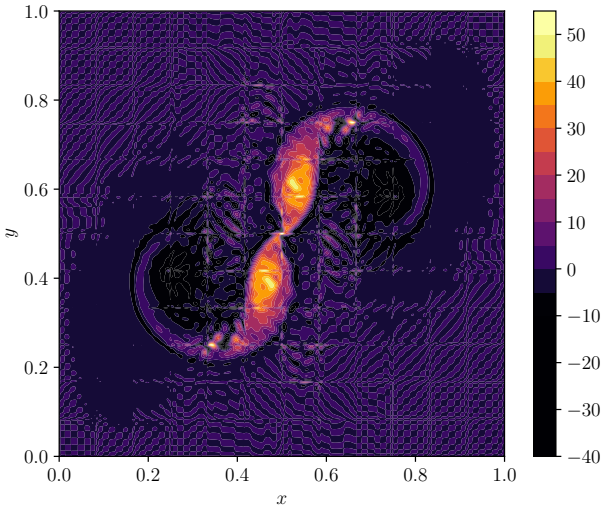

(d) $t = 0.75$

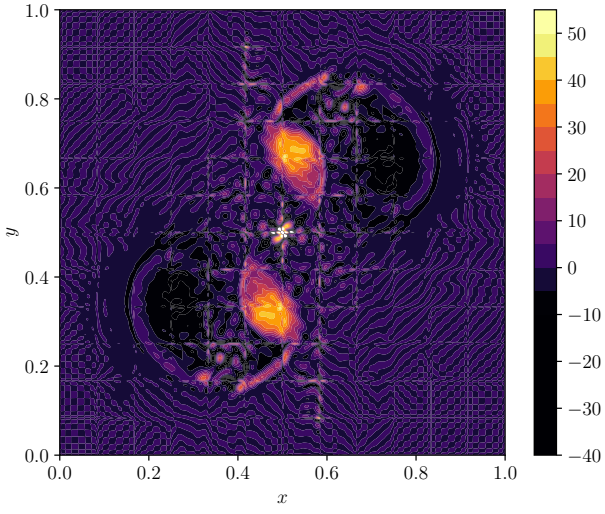

(e) $t = 1.0$

Figure 6.24: Time evolution of the co-rotating vortex test case for $p = 8$, 12×12 elements, and $\Delta t = 1 \times 10^{-3}$

When viewing the solution evolution, significant oscillations can be seen to considerably pollute the solution. The severity of these oscillations is to the point where the element boundaries are clearly visible in the solution as seen in Figure 6.24e. On a more concerning note, the behaviour of the conservation errors for the quadratic invariants is even more severe. The conservation of mass and vorticity are nicely satisfied as seen through Figure 6.25a and Figure 6.25b, however, the conservation of kinetic energy and enstrophy are notably poor for both meshes considered in this example, as evident in Figure 6.25c and Figure 6.25d. Following the line of reasoning from the steady vortex case, a much finer mesh is required to prevent the oscillations from occurring which will then allow the conservation errors for kinetic energy and enstrophy to be reduced to a more favourable level.

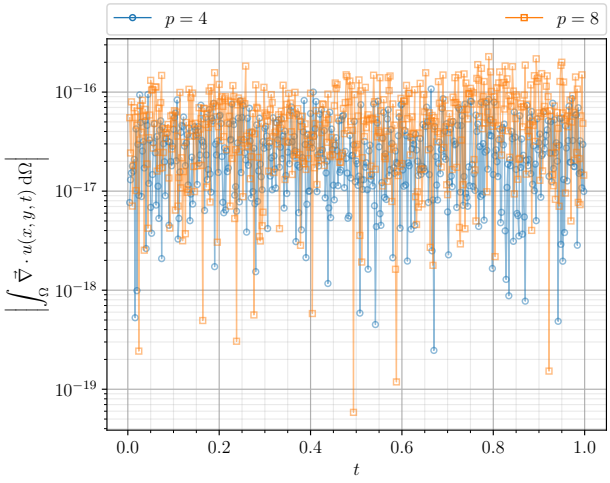

(a) Conservation of mass over time

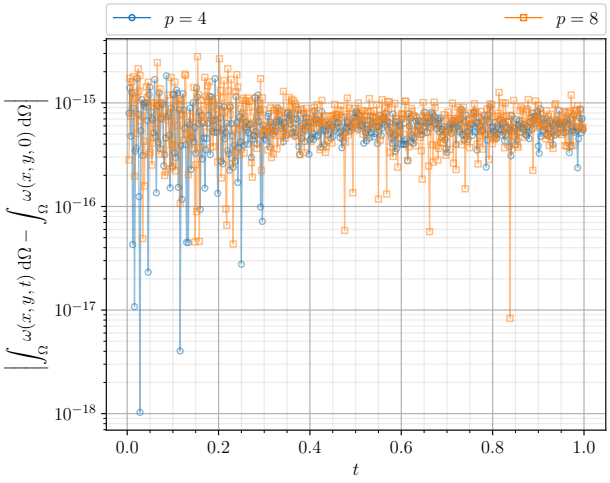

(b) Conservation of vorticity over time

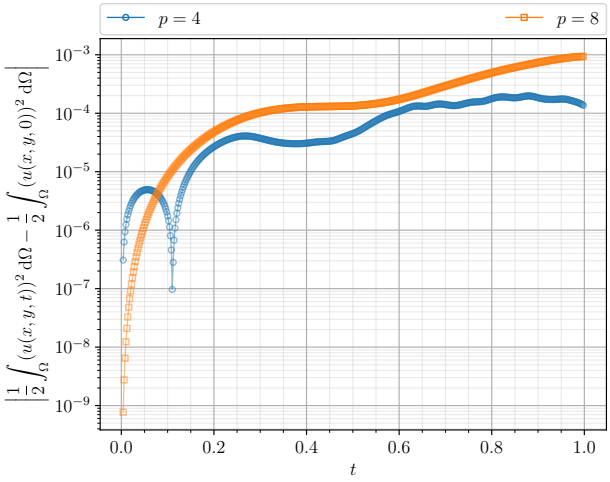

(c) Conservation of kinetic energy over time

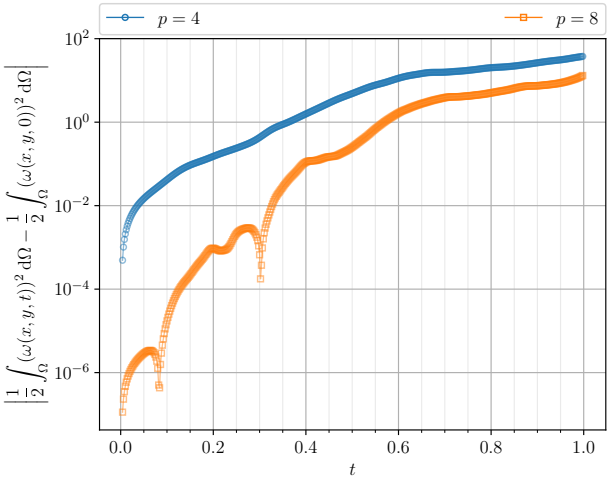

(d) Conservation of enstrophy over time

Figure 6.25: Conservation errors for the co-rotating vortex test case with 12×12 elements with $\Delta t = 1 \times 10^{-3}$

7

Conclusion

The focus of this thesis has been on the hybrid mimetic method along with multiscale theory for advection-dominated problems where the latter aspect was only covered for linear problems. With the aim to extend the hybrid SEM for advection problems and further equip it with multiscale theory, the opening chapters of this report addressed the relevant background theory on mimetic methods and the VMS theory. Thereafter, Chapter 5 included the discussion on the implementation and results of the mimetic discretisation and multiscale theory for 1D linear advection problems. Subsequently, Chapter 6 presented discussions on the implementation and results of the mimetic discretisation on more complex non-linear problems, namely, 1D Burgers' equation and 2D incompressible Euler/Navier-Stokes equations. Taking a step back from these problem-specific discussions, the focus is now set to answering the more general research questions that were posed for the present thesis, which are repeated below for convenience.

1. What do the discrete equations look like for advection-dominated PDEs discretised using the hybrid mimetic method?
    a. What are the terms in the discrete equations and are they metric-free?
    b. What do the Lagrange multipliers physically represent for advection-dominated problems in 1D and 2D?
    c. Does the hybrid formulation conserve continuous-level invariants?
2. What does the multiscale formulation integrated within the hybrid mimetic method for linear PDEs look like?
    a. What is the additional term introduced into the equations with VMS theory?
    b. What is the effect of the multiscale formulation on the discrete solution?
    c. Does the multiscale formulation preserve structures of the continuous equations?

Starting with question 1. a; a generic discrete advection term naturally involves an incidence matrix along with projection matrices which combine to trace out a triangular path in the De Rham sequence. In the 1D cases, the matrices involved for the advection term are the incidence matrix $\mathbb{E}^{1,0}$ and the projection matrix $\mathbb{M}^{(0,1)}$, both of which are found to be metric-free. However, there is also a metric-dependent term, $\mathbb{M}^{(0)^{-1}}$, involved whose operation may be viewed as a constituent relation linking the solution to the advective flux. This relation is best seen when viewing the discrete system for Burgers' equation in Equation (6.34). This general concept also extends to the 2D case to some degree, however, the metric-free nature of the projection matrix $\mathbb{M}^{(0,1)}$ is lost in the 2D case. For the rotational form considered here, the advection term $(\underline{\boldsymbol{\omega}} \times \underline{\boldsymbol{u}})$ involves the incidence matrix $\mathbb{E}^{1,0^T}$ (for computing $\underline{\boldsymbol{\omega}}$), followed by metric-dependent operations for computing the point-wise cross product and projecting the degrees of freedom back to the original space in the De Rham sequence. This general property in 2D will hold for different formulations of the advection term, however, it will include different incidence matrices and projection matrices. On the other hand, the diffusion term has a general structure of completing a loop in the De Rham sequence where two incidence matrices along with the respective mass matrices (Hodges) are involved.

Moving on to question 1. b; the Lagrange multipliers correspond to the boundary terms that appear in the weak form when using adjoint operators. For the steady advection-diffusion problem, the Lagrange multipliers

physically represent the diffusive flux at the element interfaces. For the unsteady advection-diffusion, the Lagrange multipliers correspond to some scaled version of the diffusive flux plus a scaled version of the solution itself if the adjoint advection term is used. In the case of the 2D Navier-Stokes, the λs represent the pressure and the γs represent the tangential velocity. The physical analogue for θ, however, is yet unknown as it always equates to zero leaving no possibility to be compared to other quantities. Moreover, the physical analogue of the Lagrange multipliers for the generic hyperbolic case is also not easily derived due to the absence of any boundary terms in the weak form. Inspecting the results for the considered hyperbolic cases showed signs that the Lagrange multipliers are associated with the second derivation of the solution for $p = 1$. However, its generalisation to higher-order polynomials was not found.

Concerning the answer to question 1. c; the invariants for the 1D advection case, namely, the integral of u (analogous to momentum) and the integral of u^2 (analogous to kinetic energy) are both preserved with the error being in the order of machine round-off errors for all the consistent schemes. However, there is small but steady growth in the conservation error due to some form of error bias that causes the error to accumulate over the time march. Analysing the conservation conditions for the discrete system did confirm that the schemes do have the desired conservation properties, which indicated that there was an external factor causing this error bias leading to an accumulation of conservation errors. Based on the poor behaviour observed for the inconsistent "Lie" scheme due to its incompatible element-wise continuity enforcement, it was deduced that the approach for enforcing element-wise continuity has an effect on the conservation properties. As the Lagrange multiplier approach for ensuring element-wise continuity has no regard for the characteristic direction of information propagating in hyperbolic cases, it could be speculated that this causes the conservation error to grow each time step. Moreover, the fact that the continuity constraint only ensures C^0 at the boundaries showed to have issues in the conservation of certain invariants for non-linear problems. The weak C^0 continuity generally resulted in a poor transfer of information through the element interfaces when low-order polynomials were used, leading to significant conservation errors for invariants such as kinetic energy and enstrophy.

Considering question 2. a; the additional term introduced by the VMS in the steady case is a weighted integral of the scaled version of the solution residual. The residual itself includes the same incidence and projection matrices as the Galerkin weak form. For the unsteady case where the concept of orthogonal sub-scales was used, the additional term is also a weighted integral but this time it is of the discrete representation of the un-resolved scales. Given that the un-resolved scale space was orthogonal to the test space, this additional term vanished which yielded a resolved scale equation that was decoupled with the un-resolved scale equation. While this outcome had consequences on the effectiveness of the VMS incorporation, it resulted in a physically sound formulation describing the independent advection of the different wave numbers of the solution like in the continuous case.

Regarding question 2. b; the inclusion of multiscale theory effectively brings the Galerkin solution closer to the chosen desired projection of the exact solution. For the steady advection-diffusion case, the choice of the projector was the H^1 projection and the results of the VMS showed that the solution gets closer to the optimal H^1_0 Projection. While the exact H^1_0 Projection is achieved for the $p = 1$ case, the more general $p > 1$ cases produced a solution that is similar to the optimal H^1_0 Projection but not exact. This is attributed to the fact that the considered definition of τ is not capable of returning the exact integral effect of the un-resolved scales for $p > 1$. For the unsteady advection case, the additional VMS terms are inactive due to the non-existence of the physical energy exchange between the scales. Note that this energy exchange analogy is through to be in an integral sense, that is conservation of the integral of u^2.

Finally, considering question 2. c; the multiscale formulation for the unsteady linear advection case does preserve the structures of the continuous equations when formulated using the orthogonal sub-scales model. As noted before, the choice of orthogonal sub-scales yields a physically correct formulation of the resolved and un-resolved scales equations, although it does result in the VMS addition having little to no improvement on the solution as the time evolution is decoupled.

8

Recommendation

Over the course of this thesis project, a wide range of aspects pertaining to mimetic methods, multiscale theory, and advection were explored. Undoubtedly, there are still numerous things yet to be explored and improvements that could be applied to the presented work. These future recommendations for this project are discussed below.

- The algebraic multiscale approach considered in this thesis employed the standard Greens' function approach. The issue with this formulation is that the Dirac Delta function cannot be represented in the mesh. Thus, an alternative approach could be to solve a new Greens' problem in the following form:

$$\tilde{\mathscr{L}}\hat{g}_i(x,s) = e_i(x), \tag{8.1}$$

  where $e_i(x)$ is the edge basis function. These functions are well defined in the mesh and they also integrate exactly to 1 over the domain.

- As noted in Section 5.2.6 the current multiscale approach for the unsteady case with orthogonal sub-scales yields negligible improvement over the Galerkin solution. It can be argued that is attributed to the choice of time march and the boundary continuity constraint. As such, it would be beneficial to consider a Galerkin space-time approach wherein a higher-order basis can be applied in the time direction as well, whereby dispersive errors can be minimised. Moreover, stronger element-wise continuity can also be imposed to improve the transfer of information. These additions are expected to improve the scheme's ability to preserve the initial shape of the solution in time whereby the inclusion of the multiscale will be more significant and meaningful.

- Building on the previous point, the next step for the unsteady orthogonal sub-scale approach would be the extension to non-linear problems. While the linear case has the elegance of having an explicit residual operator independent of the solution (un-resolved scales), this is no longer true for the non-linear case. As such, the residual calculation and the estimation of the un-resolved scales must be done iteratively along with the resolved scales.

- The hybridised framework used in this thesis could be further improved by imposing stronger continuity constraints where derivatives of the solution are also continuous over the element boundary. Additionally, an alternative approach could be considered for the "Lie" scheme by employing extended edge basis functions shown in Figure 8.1b. These edge bases have the same properties as the standard ones but are all zero at the element boundaries apart from the first and last ones which are 1 on either boundary.

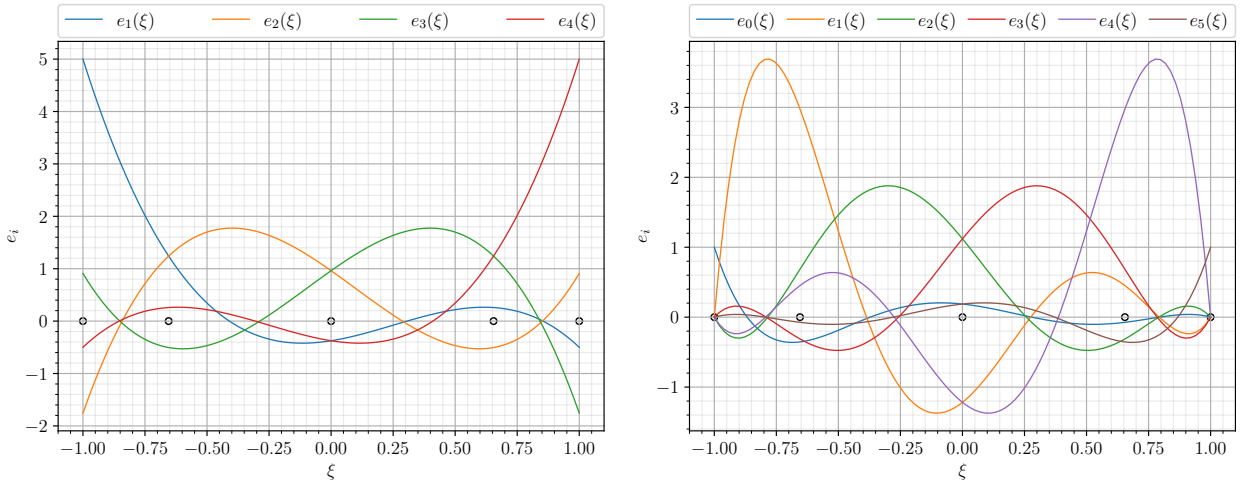

(a) Standard edge basis functions

(b) Extended edge basis functions

Figure 8.1: Standard and extended 1D edge basis functions for $p = 4$

In addition to this, the continuity constraint can be adjusted to account for the preferential (characteristic) direction of information propagation.

- Building on the mimetic hyperbolic framework, the second-order hyperbolic wave equation is an intriguing problem to consider. Take the 1D wave equation in 1D as follows:

$$\frac{\partial^2 \phi}{\partial t^2} - c^2 \frac{\partial^2 \phi}{\partial x^2} = 0, \tag{8.2}$$

and reformulate it as two first-order hyperbolic equations with $u := \dfrac{\partial \phi}{\partial t}$ and $v := \dfrac{\partial \phi}{\partial x}$ gives:

$$\frac{\partial u}{\partial t} - c^2 \frac{\partial v}{\partial x} = 0 \tag{8.3}$$

$$\frac{\partial v}{\partial t} - \frac{\partial u}{\partial x} = 0. \tag{8.4}$$

By selecting u to be a *0-form* and v to be a *1-form* on the primal, one can derive the corresponding weak forms and arrive at the following semi-discrete system:

$$\int_\Omega \frac{\partial u^{(0)}}{\partial t} \wedge \star \varepsilon^{(0)} + c^2 \int_\Omega v^{(1)} \wedge \star \, \mathrm{d}\varepsilon^{(0)} = 0, \qquad \forall \varepsilon^{(0)} \in \Lambda^{(0)}(\boldsymbol{\mathcal{M}}) \tag{8.5}$$

$$\int_\Omega \frac{\partial v^{(1)}}{\partial t} \wedge \star \eta^{(1)} - \int_\Omega \mathrm{d}u^{(0)} \wedge \star \eta^{(1)} = 0, \qquad \forall \eta^{(1)} \in \Lambda^{(1)}(\boldsymbol{\mathcal{M}}) \tag{8.6}$$

$$\frac{\partial \boldsymbol{u}}{\partial t} = -c^2 \mathbb{M}^{(0)^{-1}} \mathbb{E}^{1,0^T} \mathbb{M}^{(1)} \boldsymbol{v} \tag{8.7}$$

$$\frac{\partial \boldsymbol{v}}{\partial t} = \mathbb{E}^{1,0} \boldsymbol{u}. \tag{8.8}$$

Viewing the semi-discrete systems above shows a very elegant property where Equation (8.8) is purely topological and Equation (8.7) may be seen as a constituent relation involving the material parameter c^2 and the metric-dependent Hodges. Thus, this formulation gives a demonstration for further extending the mimetic method for hyperbolic problems.

References

[1] P. R. Spalart and V. Venkatakrishnan. On the role and challenges of cfd in the aerospace industry. *The Aeronautical Journal*, 120(1223):209–232, 2016.

[2] M. N. Dhaubhadel. Review: Cfd applications in the automotive industry. *Journal of Fluids Engineering*, 118(4):647–653, 1996.

[3] Michael L. Minion and David L. Brown. Performance of under-resolved two-dimensional incompressible flow simulations, ii. *Journal of Computational Physics*, 138(2):734–765, 1997.

[4] A. Palha and M. Gerritsma. A mass, energy, enstrophy and vorticity conserving (meevc) mimetic spectral element discretization for the 2d incompressible navier–stokes equations. *Journal of Computational Physics*, 328:200–220, 2017.

[5] Pavel B. Bochev and James M. Hyman. Principles of mimetic discretizations of differential operators. *Compatible Spatial Discretizations*, page 89–119, 2006.

[6] Pavel Bochev and Marc Gerritsma. A spectral mimetic least-squares method. *Computers & Mathematics with Applications*, 68(11):1480–1502, 2014.

[7] T. Frankel. *The geometry of physics: An introduction*. Cambridge University Press, 2011.

[8] Harley Flanders. *Differential forms with applications to the Physical Sciences*. Acad. Pr, 1963.

[9] Jasper Jonas Kreeft. *Mimetic spectral element method: A discretization of geometry and physics*. PhD thesis, Delft University of Technology, 2013.

[10] Marc Gerritsma. Edge functions for spectral element methods. *Lecture Notes in Computational Science and Engineering*, page 199–207, 2010.

[11] V. Jain, Y. Zhang, A. Palha, and M. Gerritsma. Construction and application of algebraic dual polynomial representations for finite element methods on quadrilateral and hexahedral meshes. *Computers & Mathematics with Applications*, 95:101–142, 2021.

[12] Simone Olto. Development of a fully discontinuous hybrid spectral finite element method. Master's thesis, Delft University of Technology, 2019.

[13] Stevie Ray Janssen. Structure-preserving isogeometric analysis for computational fluid dynamics. Master's thesis, Delft University of Technology, 2016.

[14] B. Sanderse. Energy-conserving runge–kutta methods for the incompressible navier–stokes equations. *Journal of Computational Physics*, 233:100–131, 2013.

[15] T.J.R. Hughes and T.E. Tezduyar. Finite element methods for first-order hyperbolic systems with particular emphasis on the compressible euler equations. *Computer Methods in Applied Mechanics and Engineering*, 45(1-3):217–284, 1984.

[16] T.J.R. Hughes, L.P. Franca, and M. Mallet. A new finite element formulation for computational fluid dynamics: I. symmetric forms of the compressible euler and navier-stokes equations and the second law of thermodynamics. *Computer Methods in Applied Mechanics and Engineering*, 54(2):223–234, 1986.

[17] Thomas J.R. Hughes, Michel Mallet, and Mizukami Akira. A new finite element formulation for computational fluid dynamics: Ii. beyond supg. *Computer Methods in Applied Mechanics and Engineering*, 54(3):341–355, 1986.

[18] Thomas J.R. Hughes and Michel Mallet. A new finite element formulation for computational fluid dynamics: Iii. the generalized streamline operator for multidimensional advective-diffusive systems. *Computer Methods in Applied Mechanics and Engineering*, 58(3):305–328, 1986.

[19] Thomas J.R. Hughes and Michel Mallet. A new finite element formulation for computational fluid dynamics: Iv. a discontinuity-capturing operator for multidimensional advective-diffusive systems. *Computer Methods in Applied Mechanics and Engineering*, 58(3):329–336, 1986.

[20] Thomas J.R. Hughes, Leopoldo P. Franca, and Marc Balestra. A new finite element formulation for computational fluid dynamics: V. circumventing the babuška-brezzi condition: a stable petrov-galerkin formulation of the stokes problem accommodating equal-order interpolations. *Computer Methods in Applied Mechanics and Engineering*, 59(1):85–99, 1986.

[21] Thomas J.R. Hughes, Leopoldo P. Franca, and Michel Mallet. A new finite element formulation for computational fluid dynamics: Vi. convergence analysis of the generalized supg formulation for linear time-dependent multidimensional advective-diffusive systems. *Computer Methods in Applied Mechanics and Engineering*, 63(1):97–112, 1987.

[22] Thomas J.R. Hughes and Leopoldo P. Franca. A new finite element formulation for computational fluid dynamics: Vii. the stokes problem with various well-posed boundary conditions: Symmetric formulations that converge for all velocity/pressure spaces. *Computer Methods in Applied Mechanics and Engineering*, 65(1):85–96, 1987.

[23] Thomas J.R. Hughes, Leopoldo P. Franca, and Gregory M. Hulbert. A new finite element formulation for computational fluid dynamics: Viii. the galerkin/least-squares method for advective-diffusive equations. *Computer Methods in Applied Mechanics and Engineering*, 73(2):173–189, 1989.

[24] Farzin Shakib and Thomas J.R. Hughes. A new finite element formulation for computational fluid dynamics: Ix. fourier analysis of space-time galerkin/least-squares algorithms. *Computer Methods in Applied Mechanics and Engineering*, 87(1):35–58, 1991.

[25] Farzin Shakib, Thomas J.R. Hughes, and Zdeněk Johan. A new finite element formulation for computational fluid dynamics: X. the compressible euler and navier-stokes equations. *Computer Methods in Applied Mechanics and Engineering*, 89(1):141–219, 1991. Second World Congress on Computational Mechanics.

[26] Farzin Shakib. *Finite Element Analysis Of The Compressible Euler And Navier-Stokes Equations*. PhD thesis, Stanford University, 1988.

[27] Thomas J.R. Hughes. Multiscale phenomena: Green's functions, the dirichlet-to-neumann formulation, subgrid scale models, bubbles and the origins of stabilized methods. *Computer Methods in Applied Mechanics and Engineering*, 127(1-4):387–401, 1995.

[28] Stein K.F. Stoter, Sergio R. Turteltaub, Steven J. Hulshoff, and Dominik Schillinger. Residual-based variational multiscale modeling in a discontinuous galerkin framework. *Multiscale Modeling & Simulation*, 16(3):1333–1364, 2018.

[29] Thomas J.R. Hughes, Gonzalo R. Feijóo, Luca Mazzei, and Jean-Baptiste Quincy. The variational multiscale method-a paradigm for computational mechanics. *Computer Methods in Applied Mechanics and Engineering*, 166(1-2):3–24, 1998.

[30] Thomas J. Hughes, Guglielmo Scovazzi, and Leopoldo P. Franca. Multiscale and stabilized methods. *Encyclopedia of Computational Mechanics*, 2004.

[31] E Munts, S Hulshoff, and R. de Borst. A space-time variational multiscale discretization for les. *34th AIAA Fluid Dynamics Conference and Exhibit*, 2004.

[32] Thomas J.R. Hughes, Luca Mazzei, and Kenneth E. Jansen. Large eddy simulation and the variational multiscale method. *Computing and Visualization in Science*, 3(1-2):47–59, 2000.

[33] Y. Bazilevs, V. M. Calo, Y. Zhang, and T. J. Hughes. Isogeometric fluid–structure interaction analysis with applications to arterial blood flow. *Computational Mechanics*, 38(4-5):310–322, 2006.

[34] Y. Bazilevs, V.M. Calo, J.A. Cottrell, T.J.R. Hughes, A. Reali, and G. Scovazzi. Variational multiscale residual-based turbulence modeling for large eddy simulation of incompressible flows. *Computer Methods in Applied Mechanics and Engineering*, 197(1-4):173–201, 2007.

[35] M.F.P. ten Eikelder, Y. Bazilevs, and I. Akkerman. A theoretical framework for discontinuity capturing: Joining variational multiscale analysis and variation entropy theory. *Computer Methods in Applied Mechanics and Engineering*, 359:112664, 2020.

[36] Jurijs Bazilevs. *Isogeometric analysis of turbulence and fluid-structure interaction.* PhD thesis, The University of Texas at Austin, 2006.

[37] Bruno Koobus and Charbel Farhat. A variational multiscale method for the large eddy simulation of compressible turbulent flows on unstructured meshes—application to vortex shedding. *Computer Methods in Applied Mechanics and Engineering*, 193(15-16):1367–1383, 2004.

[38] V. Levasseur, P. Sagaut, F. Chalot, and A. Davroux. An entropy-variable-based vms/gls method for the simulation of compressible flows on unstructured grids. *Computer Methods in Applied Mechanics and Engineering*, 195(9-12):1154–1179, 2006.

[39] Aldo Bonfiglioli and Renato Paciorri. Convergence analysis of shock-capturing and shock-fitting solutions on unstructured grids. *AIAA Journal*, 52(7):1404–1416, 2014.

[40] Franco Rispoli, Rafael Saavedra, Alessandro Corsini, and Tayfun E. Tezduyar. Computation of inviscid compressible flows with the v-sgs stabilization and $yz\beta$ shock-capturing. *International Journal for Numerical Methods in Fluids*, 54(6-8):695–706, 2007.

[41] Y. Bazilevs, V. M. Calo, T. E. Tezduyar, and T. J. Hughes. $yz\beta$ discontinuity capturing for advection-dominated processes with application to arterial drug delivery. *International Journal for Numerical Methods in Fluids*, 54(6-8):593–608, 2007.

[42] M.F.P. ten Eikelder and I. Akkerman. Variation entropy: A continuous local generalization of the tvd property using entropy principles. *Computer Methods in Applied Mechanics and Engineering*, 355:261–283, 2019.

[43] Thomas J. Hughes, Assad A. Oberai, and Luca Mazzei. Large eddy simulation of turbulent channel flows by the variational multiscale method. *Physics of Fluids*, 13(6):1784–1799, 2001.

[44] Ramon Codina. Stabilized finite element approximation of transient incompressible flows using orthogonal subscales. *Computer Methods in Applied Mechanics and Engineering*, 191(39-40):4295–4321, 2002.

[45] Randall J. LeVeque. *Numerical Methods for Conservation Laws.* Birkhäuser, 1990.

[46] Sebastiaan Pouwel Carolus van Schie. Mimetic isogeometric modeling & discretization of compressible euler flows. Master's thesis, Delft University of Technology, 2021.

[47] Eitan Tadmor. Entropy stability theory for difference approximations of nonlinear conservation laws and related time-dependent problems. *Acta Numerica 2003*, page 451–512, 2003.

[48] Yi Zhang, Varun Jain, Artur Palha, and Marc Gerritsma. A high order hybrid mimetic discretization on curvilinear quadrilateral meshes for complex geometries. *European Conference on Computational Fluid Dynamics*, 06 2018.

Appendices

.1. 2D basis functions

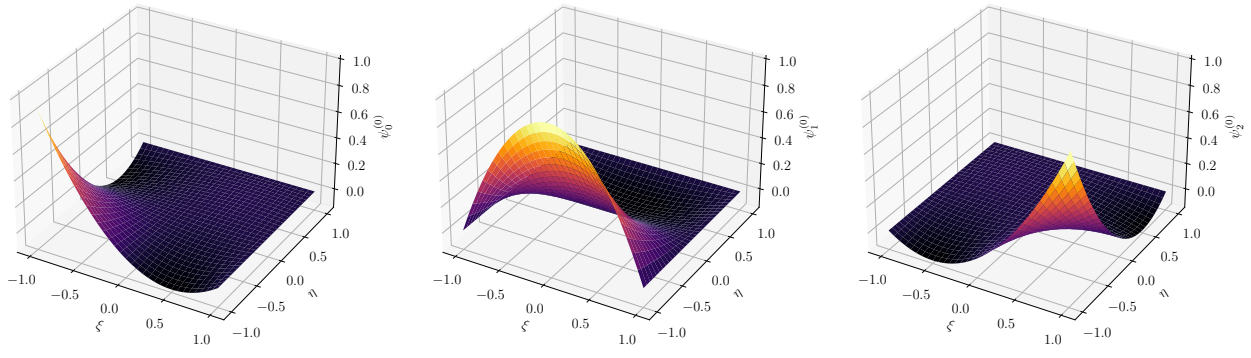

(a) $\psi_0^{(0)}$ (b) $\psi_1^{(0)}$ (c) $\psi_2^{(0)}$

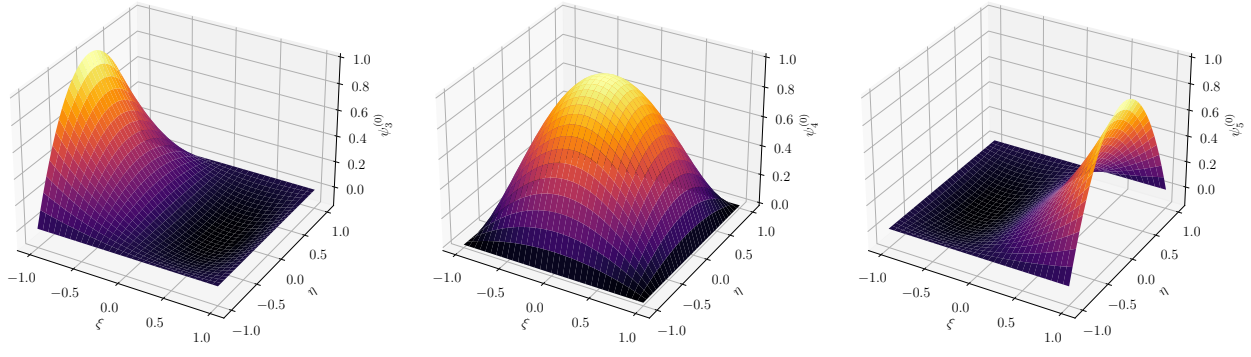

(d) $\psi_3^{(0)}$ (e) $\psi_4^{(0)}$ (f) $\psi_5^{(0)}$

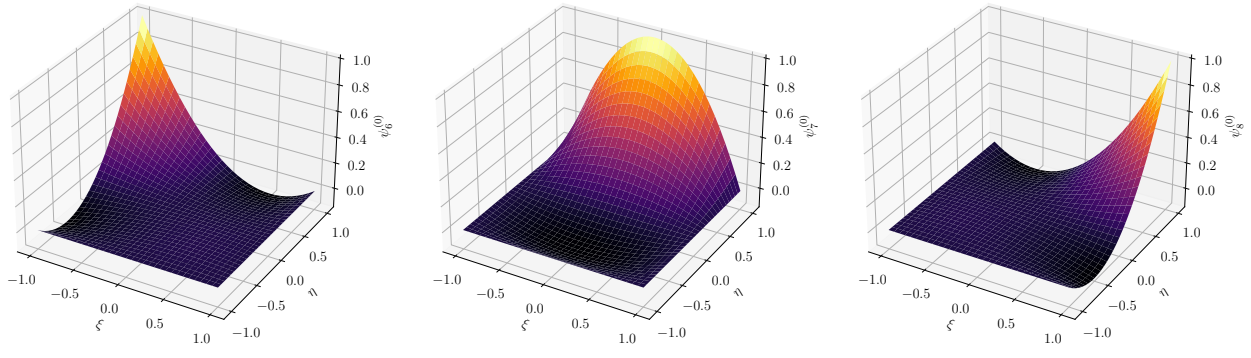

(g) $\psi_6^{(0)}$ (h) $\psi_7^{(0)}$ (i) $\psi_8^{(0)}$

Figure 2: *0-form* basis functions of polynomial degree 2

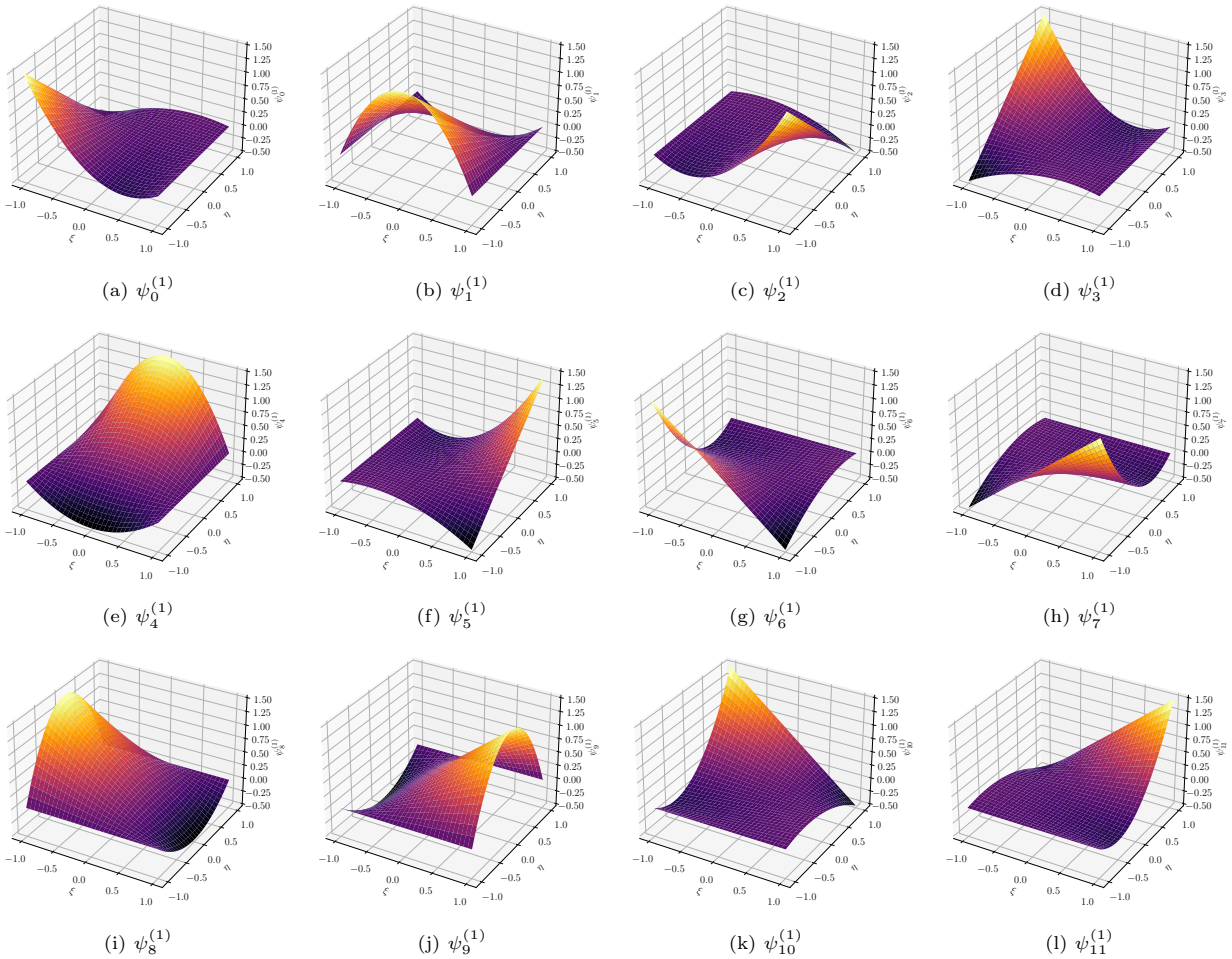

(a) $\psi_0^{(1)}$ (b) $\psi_1^{(1)}$ (c) $\psi_2^{(1)}$ (d) $\psi_3^{(1)}$

(e) $\psi_4^{(1)}$ (f) $\psi_5^{(1)}$ (g) $\psi_6^{(1)}$ (h) $\psi_7^{(1)}$

(i) $\psi_8^{(1)}$ (j) $\psi_9^{(1)}$ (k) $\psi_{10}^{(1)}$ (l) $\psi_{11}^{(1)}$

Figure 3: *1-form* basis functions of polynomial degree 2

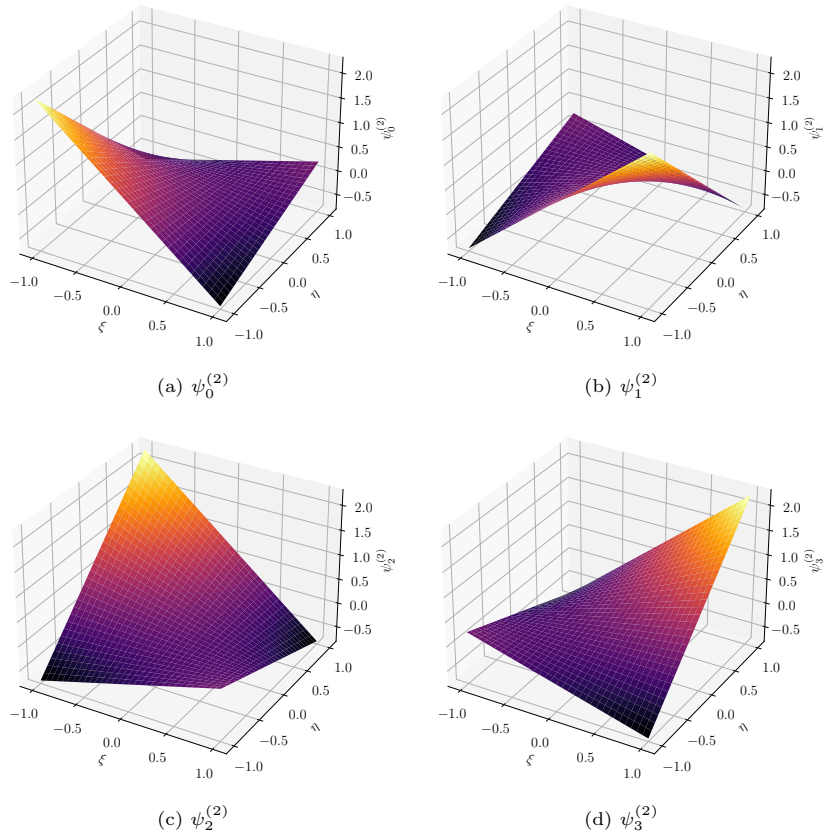

(a) $\psi_0^{(2)}$ (b) $\psi_1^{(2)}$

(c) $\psi_2^{(2)}$ (d) $\psi_3^{(2)}$

Figure 4: *2-form* basis functions of polynomial degree 2

.2. H_0^1 Projection of Steady Advection-Diffusion

To find the H_0^1 projection of the exact solution ($\mathscr{P}u_{exact}$), one must consider the following minimisation problem:

$$\mathscr{P}u_{exact} = \min_{u_h \in H_0^1} \mathcal{F}_{H^1}(u_h - u_{exact}), \tag{9}$$

where $\mathcal{F}_{H^1}$ is a functional that computes the H^1 norm:

$$\mathcal{F}_{H^1}(u) := \frac{1}{2} \|u\|_{L^2}^2 + \frac{1}{2} \left\| \frac{\partial u}{\partial x} \right\|_{L^2}^2. \tag{10}$$

Thus, the minimisation problem reads:

$$\min_{u_h \in H_0^1} \left\{ \frac{1}{2} \|u_h - u_{exact}\|_{L^2}^2 + \frac{1}{2} \left\| \frac{\partial u_h}{\partial x} - \frac{\partial u_{exact}}{\partial x} \right\|_{L^2}^2 \right\}. \tag{11}$$

Considering a second set of the function v_h that live in the same space as u_h then taking the variations of the above equation gives

$$\langle v_h, u_h - u_{exact} \rangle_{L^2} + \left\langle \frac{\partial v_h}{\partial x}, \frac{\partial u_h}{\partial x} - \frac{\partial u_{exact}}{\partial x} \right\rangle_{L^2} = 0, \qquad \forall v_h \in H_0^1 \tag{12}$$

$$\langle v_h, u_h \rangle_{L^2} + \left\langle \frac{\partial v_h}{\partial x}, \frac{\partial u_h}{\partial x} \right\rangle_{L^2} = \langle v_h, u_{exact} \rangle_{L^2} + \left\langle \frac{\partial v_h}{\partial x}, \frac{\partial u_{exact}}{\partial x} \right\rangle_{L^2} \tag{13}$$

If u_h and v_h are both expanded in terms of nodal Lagrange polynomials,

$$u_h := \boldsymbol{\psi}^{(0)} \boldsymbol{u} \tag{14}$$

$$v_h := \boldsymbol{\psi}^{(0)} \boldsymbol{v} \tag{15}$$

then the following system is obtained:

$$\boldsymbol{v}^T \left\langle \boldsymbol{\psi}^{(0)}, \boldsymbol{\psi}^{(0)} \right\rangle_{L^2} \boldsymbol{u} + \boldsymbol{v}^T \mathbb{E}^{1,0^T} \left\langle \boldsymbol{\psi}^{(1)}, \boldsymbol{\psi}^{(1)} \right\rangle_{L^2} \mathbb{E}^{1,0} \boldsymbol{u} = \boldsymbol{v}^T \left\langle \boldsymbol{\psi}^{(0)}, u_{exact} \right\rangle_{L^2} + \boldsymbol{v}^T \mathbb{E}^{1,0^T} \left\langle \boldsymbol{\psi}^{(1)}, \frac{\partial u_{exact}}{\partial x} \right\rangle_{L^2} \tag{16}$$

$$\mathbb{M}^{(0)} \boldsymbol{u} + \mathbb{E}^{1,0^T} \mathbb{M}^{(1)} \mathbb{E}^{1,0} \boldsymbol{u} = \left\langle \boldsymbol{\psi}^{(0)}, u_{exact} \right\rangle_{L^2} + \mathbb{E}^{1,0^T} \left\langle \boldsymbol{\psi}^{(1)}, \frac{\partial u_{exact}}{\partial x} \right\rangle_{L^2} \tag{17}$$

In order to strongly impose the Dirichlet boundary condition and the element-wise continuity, Lagrange multipliers are introduced:

$$\mathbb{M}^{(0)} \boldsymbol{u} + \mathbb{E}^{1,0^T} \mathbb{M}^{(1)} \mathbb{E}^{1,0} \boldsymbol{u} + \mathbb{E}^{\lambda,0^T} \boldsymbol{\lambda} = \left\langle \boldsymbol{\psi}^{(0)}, u_{exact} \right\rangle_{L^2} + \mathbb{E}^{1,0^T} \left\langle \boldsymbol{\psi}^{(1)}, \frac{\partial u_{exact}}{\partial x} \right\rangle_{L^2} \tag{18}$$

$$\mathbb{E}^{\lambda,0} \boldsymbol{u} = 0. \tag{19}$$

.3. Verification of Crank-Nicolson time march

Consider the following semi-discrete system:

$$\begin{bmatrix} \dot{u} \\ \dot{v} \end{bmatrix} = \begin{bmatrix} 0 & -\frac{k}{m} \\ 1 & 0 \end{bmatrix} \begin{bmatrix} u \\ v \end{bmatrix} \tag{20}$$

which represents the dynamics of a mass spring system with mass m and spring stiffness k. The exact solution of the system is given by:

$$u_{exact}(t) = \cos\left(\sqrt{\frac{k}{m}}\, t\right). \tag{21}$$

Solving the system over time with the Crank-Nicolson scheme with $m = 1$, $k = 4\pi^2$, and $[0, 1]^T$ as the initial condition for various different time steps and plotting the L^2 error with the exact solution gives the following:

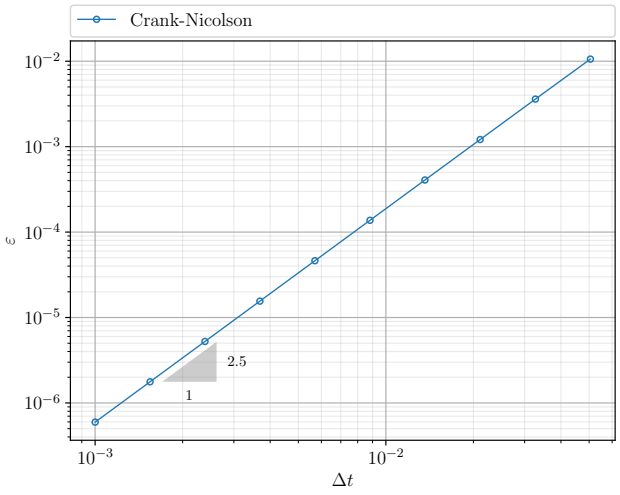

Figure 5: Convergence of Crank-Nicolson scheme

.4. Constrained time march with dynamic Lagrange multipliers

Apply the constraint to the semi-discrete system:

$$\frac{\partial \boldsymbol{u}}{\partial t} = \boldsymbol{A}\boldsymbol{u} + \boldsymbol{\Lambda}^T \boldsymbol{\lambda} \tag{22}$$

$$\boldsymbol{\Lambda}\boldsymbol{u} + \varepsilon \boldsymbol{\lambda} = 0 \tag{23}$$

$$\tag{24}$$

where ε is a small number in the order of 1×10^{-10} or below. Taking the time derivative of the second equation gives the time evolution equation for $\boldsymbol{\lambda}$.

$$\begin{bmatrix} \frac{\partial \boldsymbol{u}}{\partial t} \\ \\ \frac{\partial \boldsymbol{\lambda}}{\partial t} \end{bmatrix} \begin{bmatrix} \boldsymbol{A} & \boldsymbol{\Lambda}^T \\ \\ -\frac{1}{\varepsilon}\boldsymbol{\Lambda}\boldsymbol{A} & -\frac{1}{\varepsilon}\boldsymbol{\Lambda}\boldsymbol{\Lambda}^T \end{bmatrix} \begin{bmatrix} \boldsymbol{u} \\ \\ \boldsymbol{\lambda} \end{bmatrix} \tag{25}$$

.5. Link between 1D SEM and central FDM/FVM

The 1D central Finite Difference/Volume scheme on a uniform mesh with spacing Δx is given by:

$$\frac{\partial u}{\partial x} = \frac{u_{i+1} - u_{i-1}}{2\Delta x} + \mathcal{O}(\Delta x^2). \tag{26}$$

Consider the hybrid SEM mesh with $p = 1$ below.

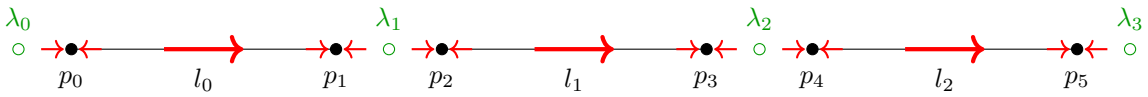

The *0-form* mass matrix for this mesh constructed using the standard Gauss-Lobatto quadrature is a diagonal matrix with the quadrature weights w_i scaled by the element Jacobian J^k:

$$\mathbb{M}^{(0)} = \begin{bmatrix} w_0 J^0 & & & & & & \\ & w_1 J^0 & & & & & \\ & & w_0 J^1 & & & & \\ & & & w_1 J^1 & & & \\ & & & & w_0 J^2 & & \\ & & & & & w_1 J^2 & \end{bmatrix}. \tag{27}$$

The quadrature weights are both equal to 1 for the $p = 1$ case and thus the diagonal simply include the Jacobian of the transformation between the reference element and the physical element. Moreover, the Jacobian is just the ratio between the physical element width h_k and the reference element width 2, $J^k = \frac{h_k}{2}$. Given the staggered nature of the SEM mesh, the physical element width corresponds to twice the mesh spacing Δx for the Finite Difference/Volume method, $h_k = 2\Delta x$. Thus, the *0-form* mass matrix for $p = 1$ is given by:

$$\mathbb{M}^{(0)} = \begin{bmatrix} \Delta x & & & & & & \\ & \Delta x & & & & & \\ & & \Delta x & & & & \\ & & & \Delta x & & & \\ & & & & \Delta x & & \\ & & & & & \Delta x & \end{bmatrix}. \tag{28}$$

Next the projection matrix $\mathbb{M}^{(0,1)}$ for $p = 1$ reads as follows:

$$\mathbb{M}^{(0,1)} = \begin{bmatrix} \frac{1}{2} & & & & \\ \frac{1}{2} & & & & \\ & \frac{1}{2} & & & \\ & \frac{1}{2} & & & \\ & & \frac{1}{2} & & \\ & & \frac{1}{2} & & \end{bmatrix} \tag{29}$$

where the entries of $\frac{1}{2}$ comes from the fact that the *1-form* edge basis for $p = 1$ is a constant function with a value of 1 over the reference element width. Consequently, applying the sequence $\mathbb{M}^{(0)^{-1}}\mathbb{M}^{(0,1)}$ gives:

$$\mathbb{M}^{(0)^{-1}}\mathbb{M}^{(0,1)} = \begin{bmatrix} \frac{1}{2\Delta x} & & & \\ \frac{1}{2\Delta x} & & & \\ & \frac{1}{2\Delta x} & & \\ & \frac{1}{2\Delta x} & & \\ & & \frac{1}{2\Delta x} & \\ & & \frac{1}{2\Delta x} & \end{bmatrix}. \tag{30}$$

Now including the incidence matrix gives:

$$\mathbb{E}^{1,0} = \begin{bmatrix} -1 & 1 & & & & \\ & & -1 & 1 & & \\ & & & & -1 & 1 \end{bmatrix} \tag{31}$$

$$\mathbb{M}^{(0)^{-1}}\mathbb{M}^{(0,1)}\mathbb{E}^{1,0} = \begin{bmatrix} -\frac{1}{2\Delta x} & \frac{1}{2\Delta x} & & & & \\ -\frac{1}{2\Delta x} & \frac{1}{2\Delta x} & & & & \\ & & -\frac{1}{2\Delta x} & \frac{1}{2\Delta x} & & \\ & & -\frac{1}{2\Delta x} & \frac{1}{2\Delta x} & & \\ & & & & -\frac{1}{2\Delta x} & \frac{1}{2\Delta x} \\ & & & & -\frac{1}{2\Delta x} & \frac{1}{2\Delta x} \end{bmatrix}, \tag{32}$$

which can be seen as the operator applying the central difference formula on an element-wise basis. Note that this is in the hybrid setting, thus, continuity must be imposed to either via a gathering matrix or Lagrange multipliers.